FINAL REPORT

Microstructurally Adaptive Constitutive Relations and Reliability Assessment Protocols for Lead Free Solder

SERDP Project WP-1752

MAY 2015

Peter Borgesen
Binghamton University

SERDP
DOD ▪ EPA ▪ DOE

REPORT DOCUMENTATION PAGE

Form Approved
OMB No. 0704-0188

PLEASE DO NOT RETURN YOUR FORM TO THE ABOVE ADDRESS.

1. REPORT DATE *(DD-MM-YYYY)*	2. REPORT TYPE	3. DATES COVERED *(From - To)*
05-05-2015	Final Report	2010 - 2015

4. TITLE AND SUBTITLE

Microstructurally Adaptive Constitutive Relations and Reliability Assessment Protocols for Lead Free Solder

5a. CONTRACT NUMBER

W912HQ-10-C-0041

5b. GRANT NUMBER

5c. PROGRAM ELEMENT NUMBER

6. AUTHOR(S)

Peter Borgesen

5d. PROJECT NUMBER

WP-1752

5e. TASK NUMBER

5f. WORK UNIT NUMBER

7. PERFORMING ORGANIZATION NAME(S) AND ADDRESS(ES)

State University of New York, Binghamton University
PO Box 6000
Binghamton, New York 13902-6000

8. PERFORMING ORGANIZATION REPORT NUMBER

9. SPONSORING/MONITORING AGENCY NAME(S) AND ADDRESS(ES)

Strategic Environmental Research and Development Program
4800 Mark Center Drive, Suite 17D08
Alexandria, VA 22350-3605

10. SPONSOR/MONITOR'S ACRONYM(S)

SERDP

11. SPONSOR/MONITOR'S REPORT NUMBER(S)

12. DISTRIBUTION/AVAILABILITY STATEMENT

DISTRIBUTION A. Approved for public release: distribution unlimited.

13. SUPPLEMENTARY NOTES

14. ABSTRACT

A systematic study of the formation and evolution of realistic lead free solder microstructure and the associated deformation properties led to a general materials science based understanding and the development of constitutive laws for selected alloys. A range of different testing of both assemblies and individual solder joints provides for correlations with the microstructure and the definition of different damage functions for isothermal and thermal cycling. Experiments were conducted to ensure the applicability of these functions under typical service conditions.

15. SUBJECT TERMS

16. SECURITY CLASSIFICATION OF:			17. LIMITATION OF ABSTRACT	18. NUMBER OF PAGES	19a. NAME OF RESPONSIBLE PERSON
a. REPORT	b. ABSTRACT	c. THIS PAGE	none	167	19b. TELEPHONE NUMBER *(Include area code)* 607-777-4437

Reset

Table of Contents

List of Tables

List of Figures

List of Acronyms

AC:	Air-Cooled
AR:	As-Reflowed
BGA:	Ball Grid Array component (like LGA but with pre-attached solder balls)
CSP:	Chip Scale Package
DNP:	Distance to Neutral Point
DSC:	Differential Scanning Calorimetry
EBSD:	Electron Back Scatter Diffraction
EDS:	Energy Dispersive Spectroscopy
LGA:	Land Grid Array component
NEMI:	National Electronics Manufacturing Initiative
No-Pb:	Lead free solder
PCB:	Printed Circuit Board
SAC105:	Solder alloy with 98.5% Sn, 1% Ag, and 0.5% Cu
SAC205:	Solder alloy with 97.5% Sn, 2% Ag, and 0.5% Cu
SAC305:	Solder alloy with 96.5% Sn, 3% Ag, and 0.5% Cu
SAC387:	Solder alloy with 95.5% Sn, 3.8% Ag, and 0.7% Cu
SEM:	Scanning Electron Microscopy
SMT:	Surface Mount Technology
SnPb:	Eutectic tin-lead solder
TC:	Thermal Cycling
TMC:	Thermo Mechanical Cycling
TSOP:	This Small Outline Package (leaded device)
TV64:	Model BGA test vehicle described in Appendix 3.9
WC:	Water-Cooled

Keywords

Constitutive relations; lead free solder; microstructure; reliability; creep; fracture; damage; model

Acknowledgements

This research was supported by the U.S. Department of Defense, through the Strategic Environmental Research and Development Program (SERDP).

Abstract

In the absence of accidents the life of a microelectronics product in long term service under conditions such as those found in many military and aerospace applications is commonly limited by fatigue of the solder joints. The quantitative prediction of solder joint fatigue life under conditions of vibration, shock, and/or thermal excursions is best done by Finite Element (FEM) type modeling to predict stresses and strains in the solder vs. time and temperature while calculating the simultaneous evolution of damage based on these values. In the case of lead free solder this, and even more so simpler approaches to the extrapolation of accelerated test results, is complicated by ongoing thermally and loading induced changes in both deformation properties and damage function.

A systematic study of the formation and evolution of realistic lead free solder microstructure and the associated deformation properties led to a general materials science based understanding and the development of constitutive laws for selected alloys. A range of different testing of both assemblies and individual solder joints provides for correlations with the microstructure and the definition of different damage functions for isothermal and thermal cycling. Experiments were conducted to ensure the applicability of these functions under typical service conditions.

Applications of this research include the accounting for effects of design, assembly processes, and subsequent thermomechanical history in FEM, as well as the definition of simpler estimates of acceleration factors. It also allows for the definition of appropriate accelerated tests protocols.

Objective

The prediction of the life of lead free solder joints under even the simplest long term service conditions cannot be done by following common accelerated test protocols and/or just modifying parameters in current models or expressions for SnPb. Quantitative predictions of long term life under conditions of vibration, shock, and/or thermal excursions may be off by orders of magnitude. This is particularly critical for the long term life required of typical military and aerospace applications.

The present effort led to the development of a quantitative knowledge and understanding of lead free solder joints, as well as lead free joints mixed with SnPb. This is seriously complicated by the ongoing evolution of solder properties over the entire life. Deliverables include test protocols and guidelines for the interpretation of test results in terms of life in long term service and constitutive relations for selected lead free alloys. It was shown that the properties of lead free solder joints under any kind of loading are completely determined by their composition and evolving microstructure, and a quantitative materials science based understanding of these was established. Coupled constitutive relations are ***microstructurally adaptive*** so that they can self-adjust with dynamic changes in solder microstructure.

The present report documents the entire effort.

General Introduction

The present was a coordinated effort between three research groups. The chart below outlines the sub-division on tasks together with the originally planned schedule. Professor Cotts is primarily responsible for Task 1, emphasizing the understanding and prediction of the initial solder microstructure right after reflow. Professor Dutta is primarily responsible for Task 2, emphasizing the understanding and prediction of the subsequent evolution of the solder microstructure and the associated creep properties. A sub-task addresses the fracture properties under high strain rate loading. Professor Borgesen is primarily responsible for Task 3, emphasizing the understanding of the different damage mechanisms in isothermal and thermal cycling, and how these correlate with the evolution of the microstructure. The three Principal Investigators are each responsible for different sections of the present Final Report. Professor Dutta and Professor Borgesen are jointly responsible for work under Task 5 to develop and validate constitutive laws and models. Based on the results of Tasks 2 and 3 Professor Dutta focused on constitutive laws for deformation (Sub-Task 5.1), while Professor Borgesen addressed damage functions. Professor Borgesen is primarily responsible for Task 6, developing protocols for accelerated testing based on the preceding tasks.

After a no-cost extension the work was concluded by September of 2014.

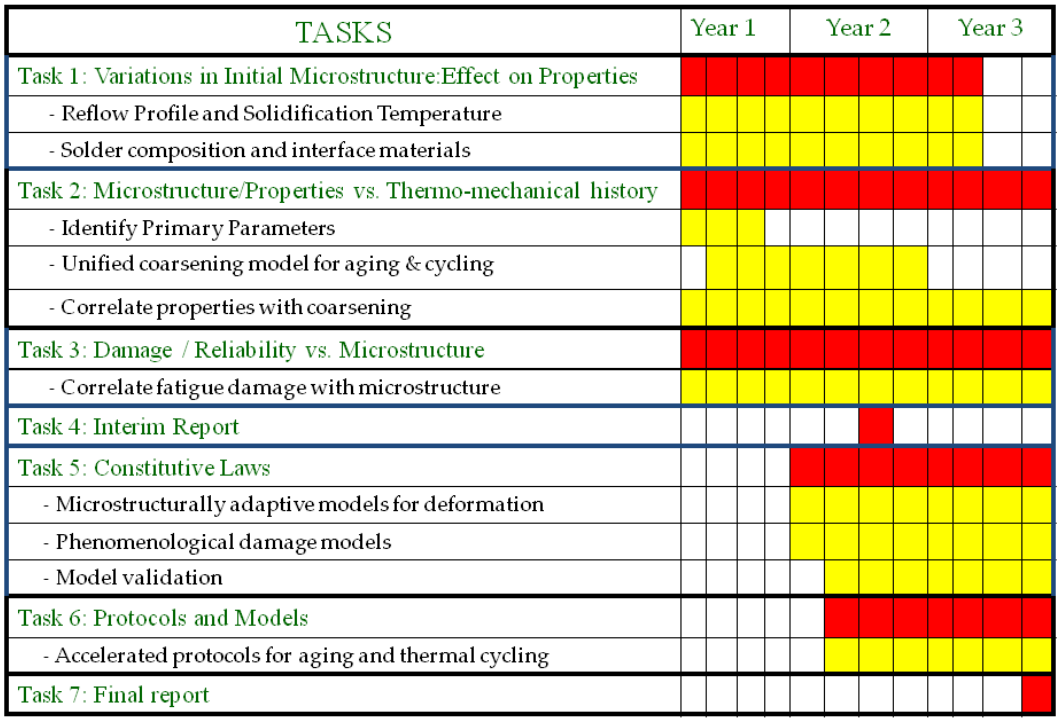

Task 1: Variations in Initial Microstructure

A. Introduction

Overview The goal of this task (Task 1), was to establish a quantitative, predictive capability of the microstructure of near eutectic SnAgCu solder joints, in particular precipitate spacing (Fig. 1.1) and Sn grain morphology (Fig. 1.2). Thus we sought to establish an understanding of the nucleation of Sn in SnAgCu solder joints, including the influence of solder/metallization interfaces on the nucleation processes and associated Sn growth. Our work suggests that the Sn growth proceeds by a six-fold cyclic twinning process which originates at the solder/metallization interface. The nature of this interface and the growth process are such that the solidified solder joint generally contains no more than three Sn orientations, and often only one, although interlacing may make it look like more. We quantified the nucleation process as a function of the impurity chemistry of the solder, the morphology and chemistry of the interface, and temperature and time. Nucleation kinetics were quantified through direct calorimetric measurements in combinatorial experiments at fixed temperatures for a number of different metallizations, solder compositions and geometries.

The effects of reflow times and temperatures, as well as cooling rate, on the size, composition and distribution of precipitates in the bulk of the solder were characterized as well. An understanding of this is linked to the dissolution of metals and formation of intermetallics at interfaces, as these processes tend to add to and/or deplete the solder of certain species. Our studies have shown small variations in peak reflow temperature to lead to marked changes in the precipitate distributions, as do variations in the solidification temperature. Any of these effects may cause significant changes in the initial mechanical properties of the solder. While our understanding of the systematics is still developing, quantitative expressions for precipitate spacing on system parameters are provided.

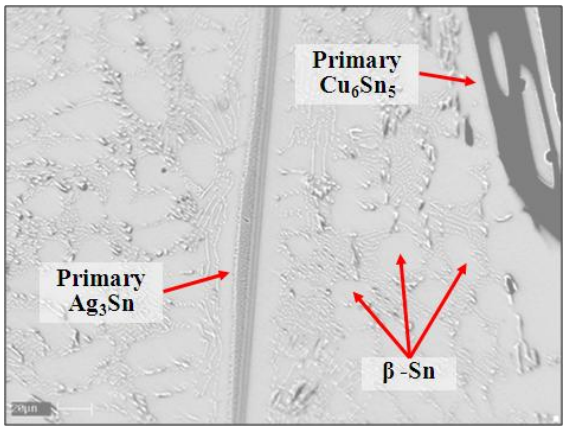

Figure 1.1: Back scattered scanning electron micrographs of Sn-3.0Ag-1.1Cu (wt.%) cooled at 0.1°C/s show typical morphologies of primary Ag_3Sn, Cu_6Sn_5 IMCs and β-Sn dendrites.

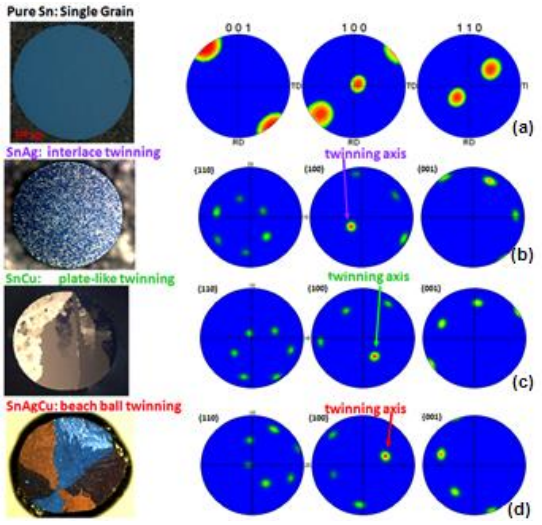

Figure 1.2: Optical micrographs with cross polarizers and pole figures showing the Sn grain morphology and relative orientations of (a) pure Sn, (b) Sn-1Ag, (c) Sn-0.1Cu, and (d) Sn-3.9Ag-0.6Cu, reprinted from Lehman et al.

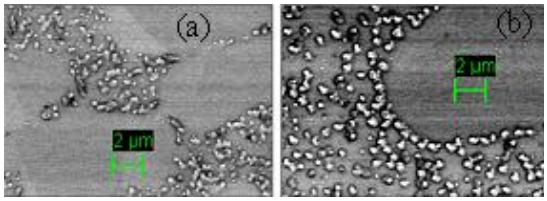

Figure 1.3: Changes in microstructure (precipitate size and number) with cooling rate SAC387 (a) 0.6°C/s cooling rate (b) 1.1°C/s cooling rate.

We systematically examined the nature of the Sn grain morphology and precipitate microstructure as a function of carefully controlled parameters. Thus a number of sample configurations were examined, including reflowed free standing solder balls, solder balls reflowed on contact pads (representative of ball attach to a BGA component), as well as the latter reflowed again in contact with a second set of contact pads on an opposing substrate (representative of BGA attach to a printed circuit board). Substrate metallization, solder composition, solder joint size and aspect ratio, and reflow profile (temperature and time), and solder joint aspect ratio were systematically varied. Reflows were conducted in the differential scanning calorimeter and solidification temperatures were precisely monitored. Samples were cross sectioned and examined by means of optical and electron microscopy (including EBSD), so as to characterize Sn grain size and orientation, as well as mean precipitate size and number (in particular, precipitate spacing).

Reflow Profile A careful study of the effects of reflow temperature and time and cooling rate on the microstructure of SnAgCu solder joints has been conducted, and is detailed in section B, below. Both the reflow time and temperature of near eutectic SnAgCu alloys were observed to strongly affect the solidification temperature, and the final microstructure of samples (Fig.1.3). Sn grain morphology changes were strongly correlated with solidification temperature (please see section C, below). While solidification temperature had a profound effect on precipitate microstructure, reflow time also affected this property in a surprisingly strong fashion.

The dependence of the solidification temperature of SnAgCu alloys on reflow parameters was monitored for a number of different reflow times and temperatures. Near-eutectic SnAgCu samples were produced in different sizes and geometries, with different solidification temperatures. Effects of variations in solidification temperature on Sn grain morphology were consistent with those previously reported by this project, with a transition from beach ball to interlaced Sn grain morphologies as temperature decreased from 205°C to 180°C and below. These Sn grain morphologies were observed to be consistent with a new application of our simple model of Sn nucleation that envisions the nucleus in an undercooled SnAgCu liquid to be Sn atoms clustered around a Ag atom in a hexagonal configuration that allows Sn to grow epitaxially on each of its surfaces. At intermediate degrees of undercooling, a mixed Sn grain morphology is observed, with the interlaced portion associated with the region closer to Sn nucleation in these samples.

A careful study of the effects reflow temperature and time on the microstructure of SnAgCu solder joints was conducted. The reflow time and temperature of near eutectic SnAgCu alloys was observed to strongly affect the solidification temperature, and the final microstructure of samples. Sn grain morphology changes were strongly correlated with solidification temperature. While solidification temperature had a profound effect on precipitate microstructure, reflow time also affected this property in a surprisingly strong fashion (Fig. 1.3).

A strong effect of reflow temperature and time on precipitate microstructure was observed (please see section B). A large source of this effect was a determination of whether or not all primary precipitates (Ag_3Sn and Cu_6Sn_5) dissolved during reflow, or not. Variation of the

reflow parameters affects the dissolution of precipitates, e.g. Ag_3Sn particles. For standard reflow times and temperatures (one minute at 250^{o}C), many large Ag_3Sn primary precipitates generally do not dissolve in the melt. Undissolved Ag_3Sn precipitates begin to grow after cooling below the liquidus. The size of these large Ag_3Sn precipitates in the final solid depends on the time in the melt at temperatures below the liquidus, i.e. on the cooling rate and on the solidification temperature. Thus, intermediate reflow times and temperatures showed the largest Ag_3Sn precipitates in the resulting solids, as these samples had lower solidification temperatures, but Ag_3Sn did not completely dissolve in these samples.

Composition A study of the dependence of the solidification temperature of $SnAg_xCu_yM_z$ alloys on composition was conducted, where M represents metals such as Co, Al, or Ti, added in small amounts ($0.01 < z < 3.0$). In order to separate and understand the effects of different constituents of Sn based alloys, different binary systems were examined in detail. These included both basic systems, $SnAg_x$ and $SnCu_x$, as well as systems based upon certain additives, M, such as Co, Zn, and Al, e.g. $SnCo_x$. Careful measurements of solidification temperature and microstructure as a function of composition have been conducted. We have discovered that the degree of undercooling decreases linearly with concentration of the binary constituent (e.g. Ag) until the nucleation of the first Sn – M alloy in the Sn melt, and then little or no dependence of undercooling on compostion is observed. The slopes of such curves depend on the constituent. For instance, in the $SnAg_x$ system the slope equals -9^{o}C/wt%Ag, until Ag_3Sn nucleates before Sn during solder joint cooling from the melt. In new results, it was shown that Ni is an effective nucleant, and that Co is even more effective. The slope for Ni was found to be -150^{o}C/wt%Ni, and that for Co was found to be even larger -820^{o}C/wt%Co. A concentration of only 0.05wt% Co in Sn reduced the undercooling from 60^{o}C to only 3^{o}C.

Nucleation Rates of Sn in SnAgCu Flip-Chip Solder Joints A new technique was developed to characterize the nucleation rate in commercial solder joints. The nucleation of Sn from the melt in commercial SnAgCu flip chip solder joints was monitored at a number of different temperatures, using a calorimetric technique. Nucleation rates were estimated from measurements of nucleation times for 440 samples after one reflow and were found to be well epitomized by the expression, $I = 1.7 \times 10^9 \exp [(-1.6 \times 10^5) / (T \times (\Delta T)^{\wedge 2})]$ $m^{-3}s^{-1}$, as per classical nucleation theory. After an additional reflow, the nucleation kinetics of the same 440 samples were observed to correspond to $I = 2.2 \times 10^9 \exp [(-8.9 \times 10^4) / (T \times (\Delta T)^{\wedge 2})]$ $m^{-3}s^{-1}$. This change was concluded to correspond to an introduction of Al in the Sn matrix. Distinct changes in Sn grain morphology from beach ball twinning to interlaced twinning upon decreases in solidification temperatures from approximately 200^{o}C to below 180^{o}C were observed. This new approach provides a means to directly calculate and recommend thermal histories which will provide a particular Sn grain morphology for a particular geometry sample. This can be important, as, for instance, in the case of flip chip SnAgCu solder joints, it has been shown that it is important to have an interlaced Sn grain morphology, in order to avoid anomalous damage from electromigration.

Background Material for Task 1

Typical Microstructure of Near Eutectic SnAgCu Alloys The thermomechanical properties of Pb free, near eutectic SnAgCu solder joints are very sensitive to microstructure. Sn is the major

constituent of SnAgCu solder joints, typically comprising more than 95% of the joint. It has been shown in some electronic packages that solder joints with single Sn grain joints fail unexpectedly early as compared to multiple-grained joints, particularly when these Sn grains have particular orientations. [1.1] In a different experiment, distinctly different failure rates where observed for single crystal and tri crystal Sn grain solder joints in room temperature shear fatigue tests. Early and late failing single grain Sn samples were found to have distinct orientations. [1.2] At room temperature, Ag_3Sn, Cu_6Sn_5, exist in equilibrium along with the, β-Sn, in near eutectic SnAgCu. The creep properties of near eutectic SnAgCu solder joints vary distinctly for different secondary Ag_3Sn and Cu_6Sn_5 precipitate size distributions.

The microstructure of near eutectic SnAgCu profoundly affects the properties of a Pb free solder joint. The morphology of Ag_3Sn and Cu_6Sn_5 precipitates, their number and spacing, are important in determining the reliability of SnAgCu solder joints [1.1]. The number and morphology of Sn grains in a SnAgCu solder joint also affect reliability. It has been shown in some electronic packages that solder joints with single Sn grain joints fail unexpectedly early as compared to multiple-grained joints, particularly when these Sn grains have particular orientations [1.2]. In room temperature shear fatigue tests, distinctly different failure rates were observed for solder joints with a single Sn grain, as opposed to those with three Sn grain orientations. Early and late failing, single grain Sn samples were found to have distinct orientations [1.3]. Perhaps the most dramatic effect of Sn grain morphology on SnAgCu solder joint reliability is the strong dependence of electromigration effects on Sn grain orientation. When a SnAgCu solder joint consists of a single Sn grain, the resistance to deleterious electromigration effects depends strongly on the orientation of that grain [1.4, 1.5]. Given the different effects of Sn grain morphology on SnAgCu joint reliability, it is of interest to understand what factors affect Sn grain morphology in SnAgCu solder joints.

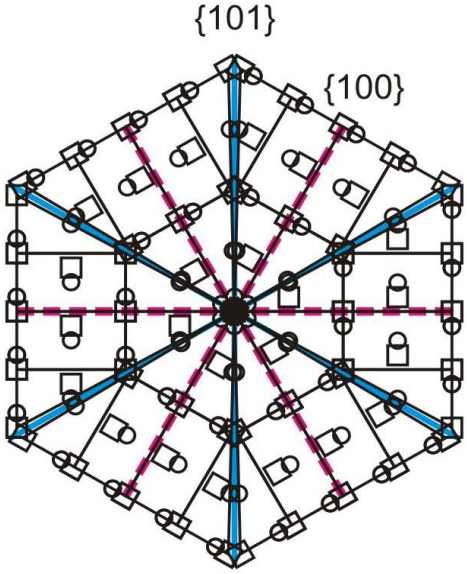

Figure 1.4: Projection view of Sn lattice onto the (010) plane, showing a {101} cyclic twin nucleus.

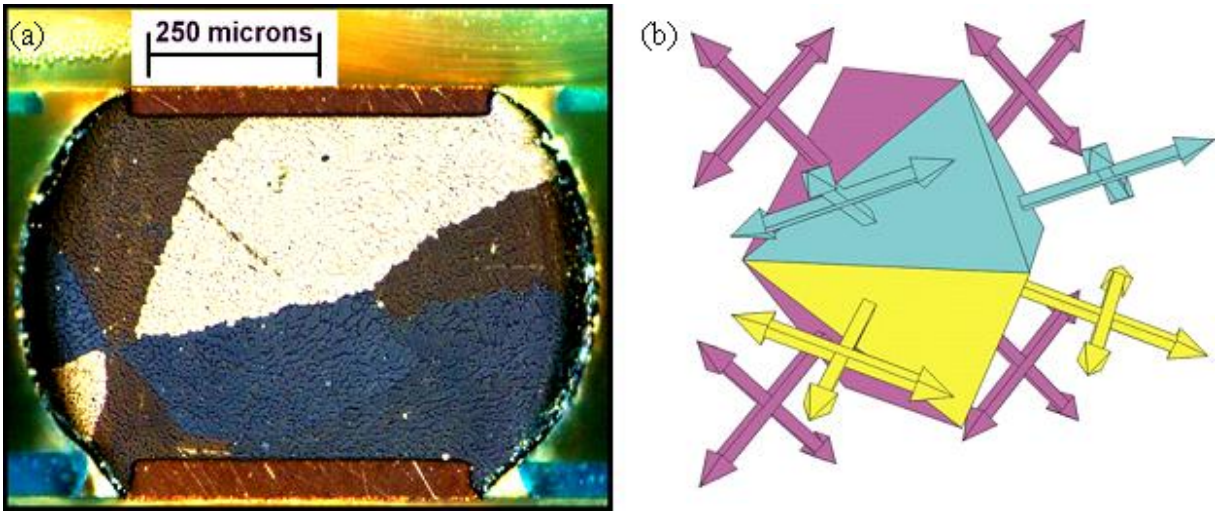

Figure 1.5: (a) Cross polarized optical micrograph of a casting alloy (Sn-2.5Ag-0.8Cu-0.5Sb) solder ball on Ni-plated Cu pas. The Kara's beach ball structure is evident, with three distinct crystal orientations (colors) and six segments. (Sample courtesy of Universal Instruments Corp.) (b) Perspective view of {101} cyclic twin nucleus faceted on {110} planes and rendered as planes.

Nucleation and growth processes after cooling from the melt during standard processing (reflow) strongly affect the Sn grain morphology in SnAgCu solder joints. Often, Sn nucleates from the melt at only one point during SnAgCu solder solidification, even upon undercooling of eighty degrees Celsius and more. When nucleation of Sn does occur, solidification rapidly progresses; a growth rate of 80 cm/s was measured for pure Sn with an undercooling of thirty degrees Celsius (the growth velocity was observed to increase proportionally to the square of the undercooling) [1.6-1.8]. Such rapid growth causes the solder to quickly heat up, generally suppressing additional Sn nucleation sources. The solidification temperature, and thus the growth velocity, also affects the Sn dendrite arm size and the precipitate size and number [1.9].

A model of the nucleation structure of Sn in SnAgCu states that multiple (i.e. two or three) Sn grain orientations in SnAgCu solder are due to the presence of three unique Sn orientations in the nucleus in the solder melt. This model (Fig. 1.4) hypothesizes that the nucleus is a six-fold, multiply twinned β-Sn structure [1.10-1.13]. In fact, {101} twinning occurs in Sn with a twinning angle of 57.2°, consistent with such six fold twinning (twinning is commonly observed in Sn during deformation). The model maintains that a small hexagonal cluster of Sn atoms centered on a Ag or Cu atom forms in the melt (Fig. 1.4). Body centered tetragonal (bct) Sn grows on each face of this hexagonal close-packed (hcp) cluster, meeting at angles of 60^{o}, and forming the six-fold, cyclically twinned pattern of Figure 1.4. The highly anisotropic growth rates [1.14, 1.15] of Sn from the melt, and a six fold twinned Sn nucleus (Fig. 1.4), provide explanation for the observation of extended, beach ball, Sn grain morphologies (cf. Fig. 1.5(a)). Under common conditions, growth of solid Sn from the melt is fastest in the [110] and $\overline{1}10$ directions, while growth in the [001] direction is found to be slower [1.14, 1.15]. Thus, "large, flat Sn dendrites", up to centimeters in length, growing primarily in the [110] and $\overline{1}10$ directions are observed [1.8]. Similar asymmetries in growth velocities exist in a number of Sn rich alloys, including near eutectic SnAgCu (this is in contrast to some other systems where the addition of impurity atoms to the melt results in the change of the preferential growth direction

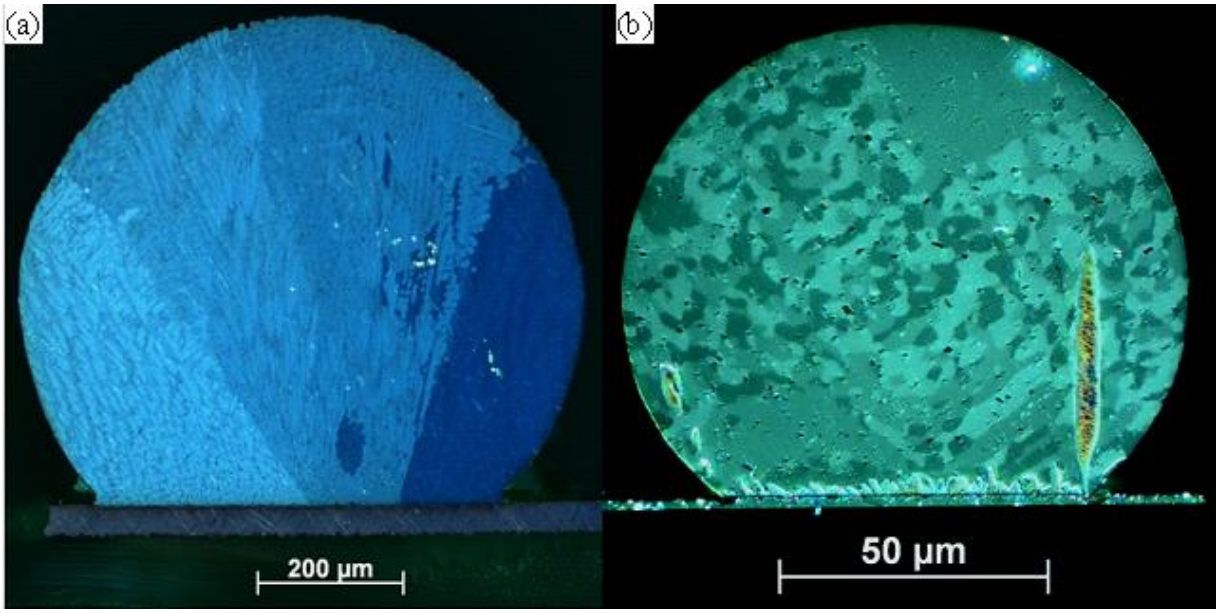

Figure 1.6: Cross polarized micrographs of as reflowed (a) 30mil SAC305 on Cu substrate, (b) 4mil flip chip SAC3510 on Ni(V)/Al substrate.

of dendrites [1.16]). In a novel examination of Sn dendrites in SnAgCu, still liquid solder was separated from solid Sn dendrites using centrifugal force on a solidifying SnAgCu/Cu solder joint. The exposed Sn dendrites in the partially solidified SnAgCu solder joint were characterized using transmission electron microscopy and X-ray diffraction, and found to have been growing primarily in the [110] direction [1.17].

Growth of Sn in a large, flat geometry, in the [110] and $\overline{1}10$ directions, from a nucleus with a dodecahedral geometry as depicted in Figs. 1.4 and 1.5(b), is consistent with the observed beach ball, Sn grain geometry often observed in SnAgCu solder joints (e.g. Fig. 1.5(a)). Figure 1.5(b) illustrates a three dimensional extension of Figure 1.1, faceted on (110) planes. The [110] and $\overline{1}10$ directions, identified as fast growth, are illustrated with arrows (Fig. 1.5(b)). If growth occurs rapidly in the [110] and $\overline{1}10$ directions, with slow growth in the [001] direction, little overlap of the growing three Sn orientations will occur early in the solidification process, and a morphology such as that observed in Figure 1.5(a) can form. While many SnAgCu solder joints (particularly larger solder joints, such as ball grid array (BGA) solder joints) reveal Sn grain, beach ball morphologies similar to those of Figs. 1.5(a) and 1.6(a), some are quite different. Often, particularly in smaller SnAgCu solder joints (such as flip chips), a different, interlaced Sn grain morphology is observed, such as that of Figure 1.6(b). Surprisingly, this interlaced Sn grain morphology also reveals only three Sn grain orientations, with similar relative orientations as those observed in beach ball morphologies.

One may hypothesize that the interlaced Sn grain morphology observed in some SnAgCu solder balls (cf. Fig. 1.6(b)) arises from growth from a nucleus such as depicted in Figure 1.4, in the case when the [110] and $\overline{1}10$ directions are not the preferred growth directions. As can be seen in Figure 1.5(b), if the preferred growth direction of Sn dendrites deviates from the [110] and $\overline{1}10$ directions, these growing dendrites will be more likely to intersect, or interlace. Understanding and predicting dendritic growth patterns is a difficult challenge in thermodynamics; often stability critieria are difficult to formulate on a fundamental basis.

Nevertheless, temperature and concentration gradients can counteract the effects of surface tension, and thus fast growth directions may change. For example, an increase in undercooling may result in higher temperature gradients and a change in fast growth direction. In fact, variations in the fast growth direction of a solidifying material are often reported. It is observed that the direction of dendritic growth is generally highly dependent on factors such as temperature gradient or impurity content. For example, change in the preferred growth direction was reported in Ge-Fe system [1.16]. In the case of Cu rich, Cu-Sn alloys, it was shown that at large undercoolings (more than 90°C) the preferred growth direction changes from [111] to [100] direction [1.18]. In general, under different conditions, such as large thermal gradients, or alloy additions, fast growth directions of dendrites may change, perhaps reverse, in a given system [1.19]. For instance, Lau et al. observed correlations between the direction of dendritic growth and the degree of undercooling of a Ge melt [1.20]. In fact, in the Sn system it has been previously observed that the fast growth direction moves away from the [110] and $\overline{1}10$ directions as the degree of undercooling increases [1.21-1.23].

Variations in the temperature of solidification of Sn from the SnAgCu melt result in significant differences in the size and number of Ag_3Sn and Cu_6Sn_5 precipitates, as well as in the Sn grain morphology [1.4-1.10]. Kinyanjui et al. found that the solidification temperature of SAC solders decreased as the sample size decreased (such as BGA versus flip chip solder joints) [1.4]. Furthermore, the largest Sn dendrites were observed in the biggest solder balls (BGA), i.e. those with the highest solidification temperatures. Lehman et al. showed that the degree of undercooling of Sn will affect the size of the primary precipitates in the solder joint. It was concluded that for larger undercoolings, Ag_3Sn or Cu_6Sn_5 precipitates have a longer time to grow and that the probability of bigger precipitates increases [1.5]. Changes of solidification temperatures result in large differences in the number and size of the secondary Ag_3Sn and Cu_6Sn_5 precipitates [1.4, 1.5].

The temperature of solidification of Sn form the SnAgCu melt depends upon a number of factors, including composition. Previous research in free standing samples indicated that a number of metal impurities facilitate solidification of Sn from the SnAgCu melt [1.25-1.27], while Ag_3Sn and Cu_6Sn_5 precipitates are not effective catalysts for the nucleation of Sn [1.24]. In a study of Sn samples doped with a single element, Ohno et al. reported the undercooling values of Sn alloyed with 0.1% of either Cd, Ag, Zn, Pb, Sb or Bi [1.27]. Their experiment showed that Al, Sb and Zn significantly decreased the undercooling of Sn in SnAgCu undercooled melts. Anderson et al. reported the effect of the addition of 0.05-0.25 wt% of either Fe, Co, Ni, Zn, Mn or Al on the undercooling of SAC 3595 melts [1.25]. He reported Al, Zn and Mn reduced the degree of undercooling of Sn from the SnAgCu melt, while Ni, Co and Fe were less effective. The addition of Al to SAC 3595 in concentrations as low as 0.05 %wt Al was found to lower the undercooling value to 5^oC [1.25]. Thus, consideration of the evolution of intermetallics at solder interfaces, as well as the change of composition of the solder in this system, may provide insight on nucleation mechanisms in this system.

Interfacial reactions between SAC solder and Cu/Ni(V)/Al under bump metallization (UBM) layers in solder joints change the composition of the solder; Ni dissolves in to the SAC solder during the first reflow of solder joints, while Al combines with Sn in the SAC solder joint after additional reflows [1.26-1.28]. The Cu/Ni(V)/Al UBM is often utilized in flip chip SnAgCu solder joints. The Cu acts as a solderable layer during the initial reflow of SnAgCu solder, while the Ni(V) provides a thin (approximately 350 nm) diffusion barrier. The interfacial reactions between SnAgCu solder and Cu/Ni(V)/Al under bump metallization layers (Fig. 1.7) were

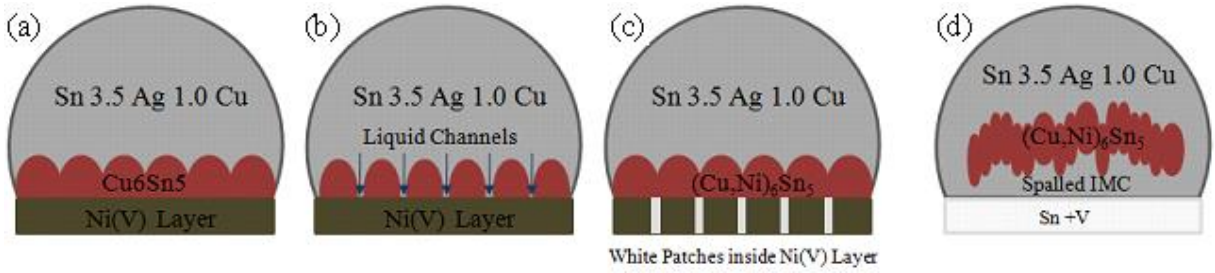

Figure 1.7: A sketch of the evolution of the Sn-3.5Ag-1.0Cu/Ni(V) interface as a function of thermal history (multiple reflows), as determined and presented in Ref. 1.28: (a) after initial reflow (b) during subsequent reflow (c) after solidification of subsequent reflow and (d) IMC spalling after a number of reflows [based on Ref 1.28].

previously examined during multiple reflows (flip chips usually experience three to five reflows during the packaging process) [1.26-1.28]. During the first reflow, some Cu in the UBM was found to dissolve in to the solder, Sn and Cu formed a scalloped layer of Cu_6Sn_5 at the UBM/SAC interface, while some dissolution of the Ni(V) UBM layer occurred (though this Ni(V) layer remained nearly intact) [1.26-1.28]. Upon subsequent reflows, significant interdiffusion between the Ni(V) and the solder was found to occur, including the formation of Ni-Sn intermetallic compounds and their spalling from the UBM surface, such that Sn patches were observed in the Ni layer, in contact with the Al (Fig. 1.7) [1.26-1.28].

In Task 1 we have focused on the effects of reflow profile and composition on the microstructure of SnAgCu near eutectic solder joints (section B). In particular, we have studied the nature of Sn solidification in SnAgCu alloys, with emphasis on the variation of the Sn grain morphology as a function of solidification temperature (section C). We have examined the kinetics of the nucleation of Sn in undercooled SAC solder balls on Cu/Ni(V)/Al under bump metallization layers (section D).

Experimental Details for all sections of Task 1 Reflow temperature has a pronounced influence on the degree of Sn undercooling. In order to investigate the effect of reflow temperature on the degree of Sn undercooling, two commercial available lead free alloys were selected for study: 25mil eutectic Sn-3.5Ag solder balls, and 30mil NEMI (Sn-3.9Ag-0.6Cu) solder balls. Samples were held at 140°C for 1 minute, and then heated at a rate of 0.33°C/s from 140°C to peak reflow temperatures, at which they were held for 1 minute, finally they were cooled at a rate of 1.0°C/s to 140°C. A number of other different SnAgCu Pb free solder samples were examined, including commercial samples, and those fabricated in our laboratory, in both free standing and solder joint forms. Two sets of free standing solder balls (not attached to any substrates) were examined: i) commercial solder balls of 96.5%Sn-3.0%Ag-0.5%Cu (SAC305) of various sizes obtained from a supplier, ii) solder ingots fabricated in house using a vacuum furnace. Lab made samples were prepared using high purity elements of Sn, Ag and Cu, which were placed in a crucible inside a quartz tube vacuum furnace. Generally ingots of SnAgCu alloys of 5g mass were prepared. The samples were heated to 750^{o}C and held for one half hour to achieve homogeneity. Various sizes of solders were cut from the center of a solidified ingot and massed and reflowed using differential scanning calorimetry (DSC). The size of SnAgCu samples was varied between 5 x 10^{-7} and 2 x 10^{-3} cm^3 in order to vary sample solidification temperature upon cooling from the melt.

Solder joint samples were prepared by reflowing 500 micron diameter commercial solder balls on a Cu substrate in a mass convection oven in a nitrogen atmosphere. A tacky flux had been stencil printed onto solder mask openings over larger organic solderability protectant (OSP) coated Cu pads on an flame retardant class 4 (FR-4) substrate. 97.5%Sn-2.0%Ag-0.5%Cu (SAC205) solder balls were placed on 450 micron diameter substrates, and SAC305 solder balls were placed on 550 micron substrates. The reflow profile had a peak temperature of 245^{o}C and a total of 60 seconds above 217^{o}C. A wafer dicing machine was used to cut the substrates so individual joints could be placed in the calorimeter.

Commercially produced flip chip samples consisting of eighty-eight spheres (approximately 100 micron in diameter) of 95.5%Sn-3.5%Ag-1.0%Cu (SAC3510) solder alloy attached to individual pads, each with under bump metallizations (UBM), were examined. The spheres were arranged in a 200 μm pitch, flip chip, peripheral array on a 5mm square Si substrate. The under bump metallization layers between the SnAgCu spheres and Si substrate were Cu, Ni(V) and Al.

The solidification of free standing solder ball and solder joints (on Cu substrate) and flip chip samples was monitored using differential scanning calorimetry. Different means were employed to vary the solidification temperature in order to examine the correlation of the Sn grain structure of SnAgCu samples with their solidification temperature after cooling from the melt. Free standing solder balls were sealed in an Ar atmosphere in a DSC pan while solder joints and flip chip samples were placed directly into the calorimeter and reflowed. Such samples were heated at a rate of 60°C/min to a peak temperature of 250°C, annealed for 2 minutes, and cooled at 60°C/min to room temperature. Each free standing sample was run 12 times with that profile. Argon was flowed throughout the experiment. In a different approach, undercooled liquid samples were held at specific temperatures until solidification ensued. Some selected samples were heated at a rate of 60°C/min to a peak temperature of 250°C, annealed for 2 minutes, and cooled at 60°C/min to a specific isothermal annealing temperature between 185 and 215°C and held at the isothermal annealing temperature for up to 840 minutes. Solidification of a SnAgCu solder sphere during the isothermal anneal generally produced an individual solidification exotherm in the DSC trace.

Selected samples were mounted in epoxy, cross sectioned, and metallographically polished to 0.02 μm colloidal silica. Bright field optical microscopy was used to examine the morphology of samples and the growth of intermetallic compounds after annealing. Cross polarized images of each ball were taken to identify the number of Sn grains in each solder ball. A high resolution Zeiss 55 capable of variable pressure (VP) scanning electron microscope (SEM) equipped with an energy dispersive spectrometer (EDS) was used for backscattered and secondary electron imaging, and for chemical analysis. Electron backscattered diffraction (EBSD) was used to determine the orientations of Sn grains for each individual solder ball. Two different commercial software packages, HKL Channel 5 from Oxford Instruments and orientation imaging microscopy (OIM) from EDAX-TSL, were extensively used for crystallographic texture measurements.

B. Effect of reflow parameters on the degree of Sn undercooling

There are a number of reflow parameters that can be varied in a reflow process; the peak temperature, the hold time at peak temperature or the time above liquidus and the cooling rate. Each of these parameters impacts the solidification behavior and microstructure of a SAC solder joint (Fig. 1.8).

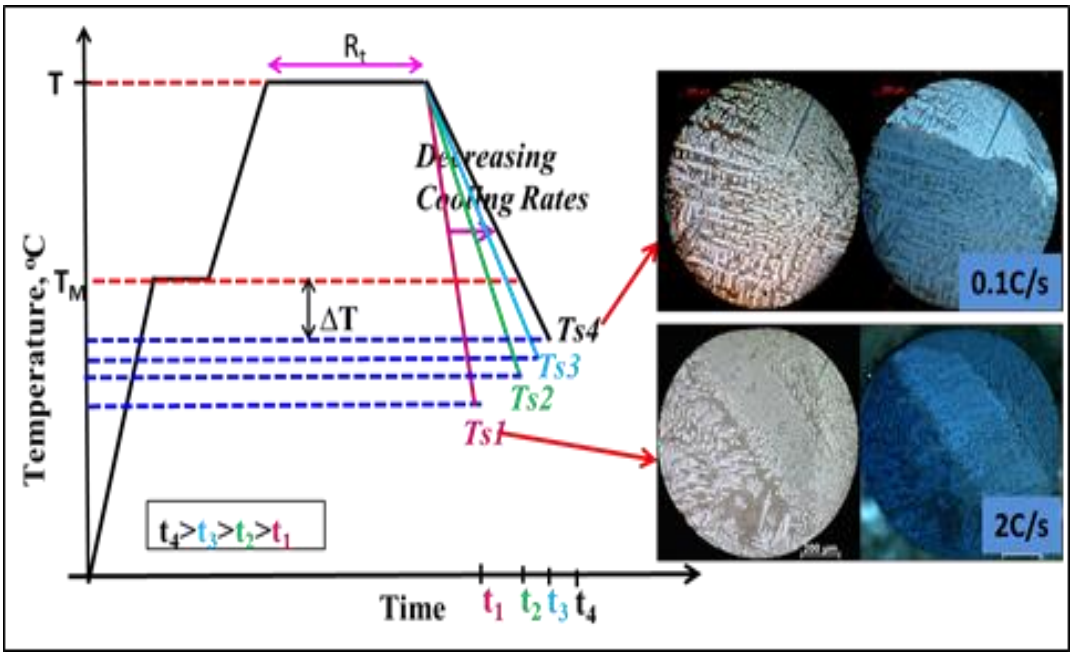

Figure 1.8: Plots of temperature vs time for different reflow profiles. This schematic illustrates the different parameters constitute the reflow profile, including heating rate, hold time, and cooling rate. The optical micrographs illustrate variations in microstructure with changes in reflow profile.

The effects of varying the number and length of reflows at a temperature of 250°C on the solidification temperature of Sn in a SnAgCu alloy were investigated [1.29-1.43]. Individual, as received, 30mil NEMI (Sn-3.9Ag-0.6Cu) solder balls were heated in the DSC at a rate of 1 °C/s to a temperature of 250°C, and then cooled to room temperature. Melting and solidification events were clearly evident in the DSC traces. Solidification temperatures were compared for both one and two reflow cycles with isothermal anneals at 250°C of either one or twenty minutes. Measured solidification temperatures are plotted in Figure 1.9. For identical conditions, variations in solidification temperatures of approximately 10°C were observed. The average undercooling increased slightly (approximately 4°C) for samples reflowed twice (as compared to once). Reflowing for 20 minutes resulted in significant increases in undercooling (10 to 15°C). As can be seen in Figure 1.10, an increase in reflow temperature also had a significant increase, a factor of two, or approximately 15°C, on the degree of undercooling of Sn in these samples. For a one minute reflow at 250°C the mean undercooling was 16°C, while for a one minute reflow at 320°C the mean undercooling was 30°C.

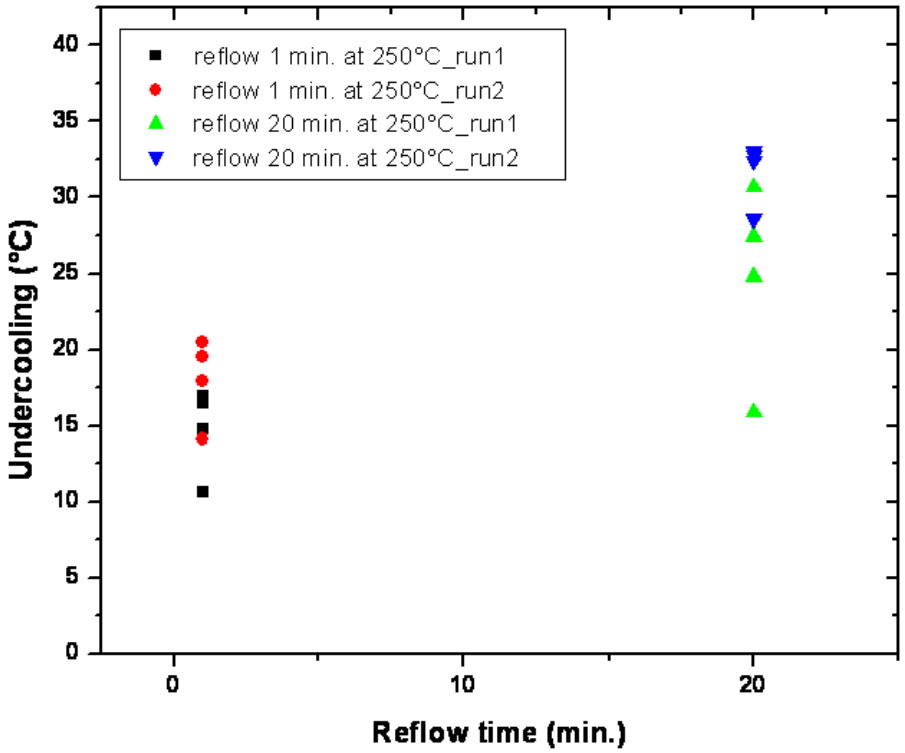

Figure 1.9: 30mil commercial NEMI solder balls: Sn undercooling as a function of holding time.

Systematic examinations of the degree of undercooling of Sn in SnAgCu alloys after reflow of one minute at various temperatures are recorded in Figure 1.11 for three different types of samples. Two commercial samples, Sn3.5Ag and Sn3.9Ag0.6Cu (NEMI) solder balls, were examined, as well as some similar sized Sn3.0Ag1.1Cu samples all cut from the same ingot prepared in our laboratory. For the two commercial samples, the degree of undercooling was rather similar and increased rather systematically with reflow temperature for reflow temperatures up to 325^{o}C, or above. At higher temperatures this trend changed, and decreases in reflow temperature were observed with increasing reflow temperatures (please see Fig. 1.10). Solidification temperatures of Sn in Sn3.0Ag1.1Cu samples produced in our laboratory were generally lower than in the commercial samples. Variations in the degree of undercooling with reflow temperature were observed in these samples as well, with systematic increases with reflow temperature (Fig. 1.11) until 350^{o}C.

In order to examine the possible nucleation and growth of Ag_3Sn upon cooling from the melt, Sn3.5Ag and Sn8.0Ag samples were studied with a differential scanning calorimeter. For Ag fractions close to eutectic concentrations, separate peaks corresponding to Ag_3Sn solidification could not be detected. Measurements of the heat flow versus temperature (Figs. 1.12 and 1.13) for Sn8.0Ag samples revealed a peak associated with the melting of the alloys upon heating, and after reflow and cooling to room temperature, two distinct, separate peaks (Fig. 1.13), one similar to that observed in pure Sn samples, and another, smaller peak at higher temperatures. Measurements of the heat flow versus temperature were conducted for three different reflow temperatures: 400, 500 and 600^{o}C (Fig. 1.13).

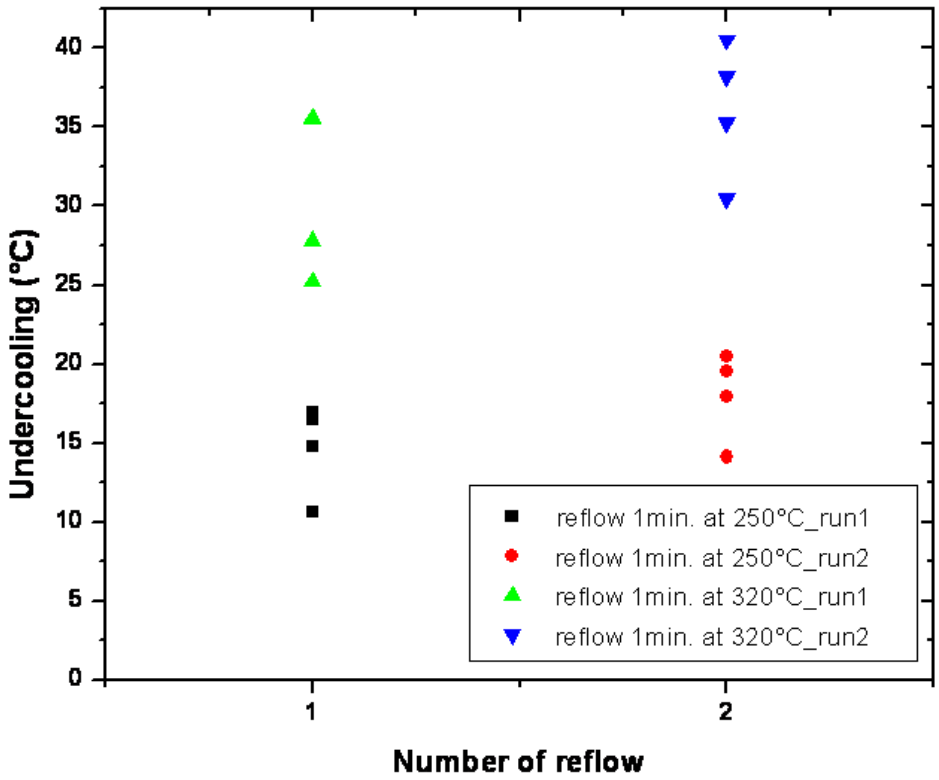

Figure 1.10: 30mil commercial NEMI solder balls: Sn under-cooling as a function of reflow number

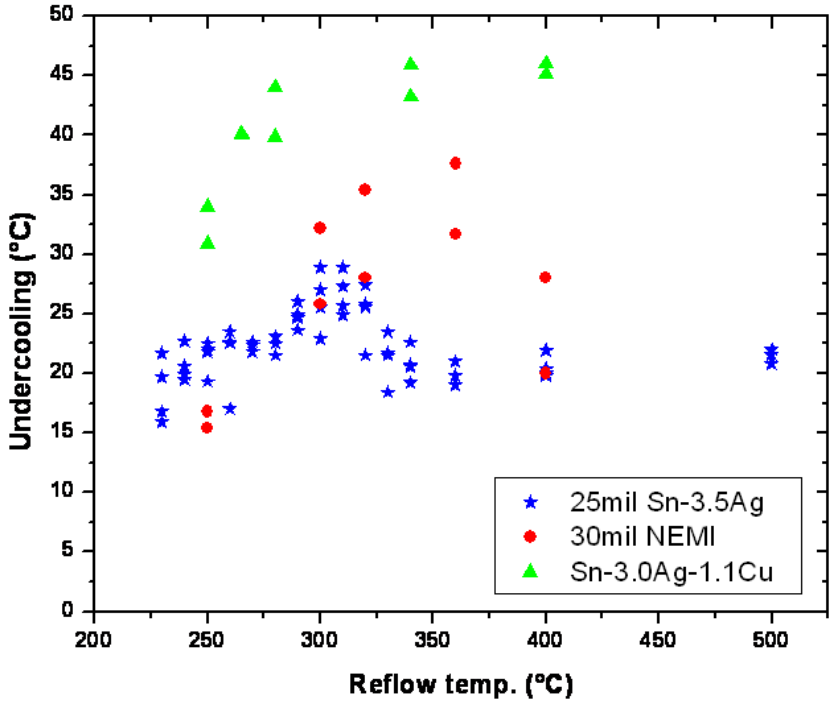

Figure 1.11: Sn undercooling as a function of reflow temperature: 25mil eutectic Sn-3.5Ag commercial solder balls, 30mil NEMI (Sn-3.9Ag-0.6Cu) commercial solder balls and ~10 mg Sn-3.0Ag-1.1Cu sample cut from an arc melted ingot.

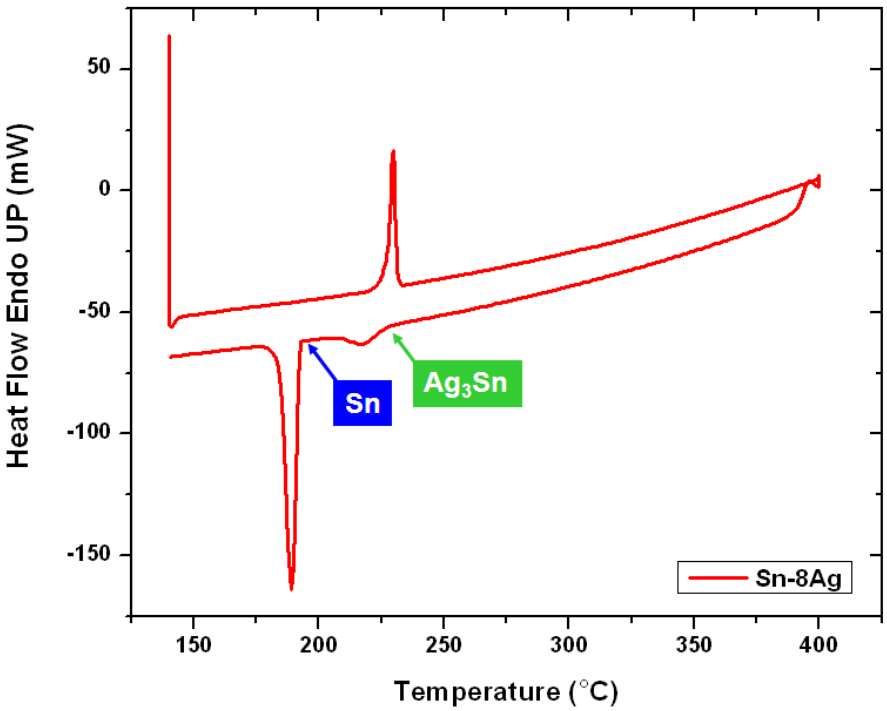

Figure 1.12: DSC trace of a Sn-8Ag sample cooled at 1.0°C/s after reflow 1min. at 400°C: the two solidification peaks in the DSC trace corresponding to the solidification peaks of Ag_3Sn and Sn, respectively

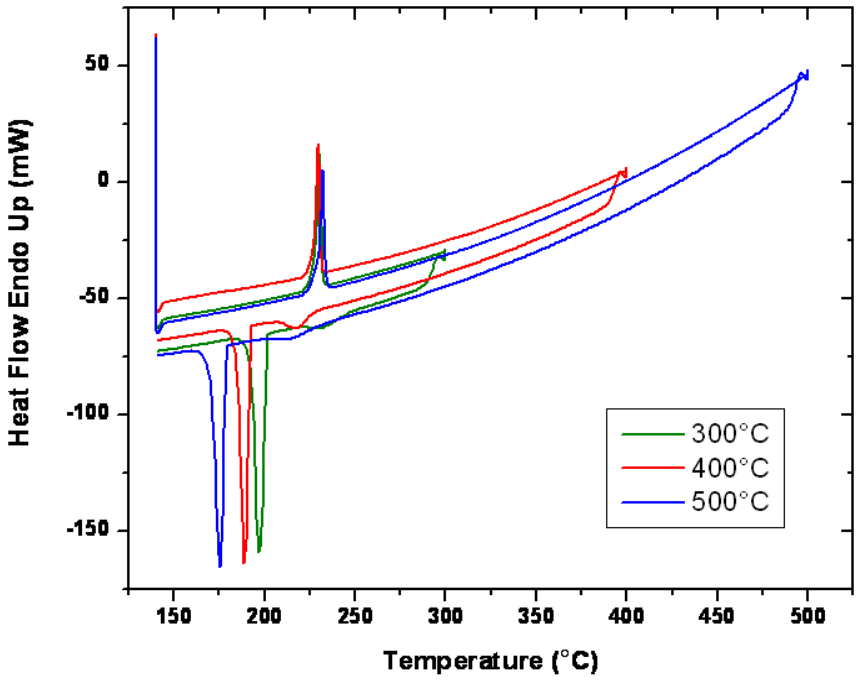

Figure 1.13: DSC trace of a Sn-8Ag sample cooled at 1.0°C/s after reflow 1min. at three reflow temperatures (300°C, 400°C, and 500°C): Both Sn and Ag_3Sn undercooling increase with increasing reflow temperature.

Microstructure of Alloys Variations in the microstructure of SnAg or SnAgCu alloys as a function of solidification temperature and reflow parameters were investigated, with particular focus on commercial solder balls. After measurements (Figs. 1.9-1.13) of solidification temperature upon cooling from the Sn melt after varying reflow profiles, samples were cross sectioned and sample microstructures were examined by means of optical microscopy. Sn grain sizes and relative orientations, secondary and primary precipitate sizes were studied. As would be expected, significant variations of microstructure were observed with changes in solidification temperature. These changes are documented, as are variations in microstructure with changes in reflow profile, for the same solidification temperature.

The microstructure of a commercial Sn3.9Ag0.6Cu (NEMI) solder ball was examined before any reflows, i.e. in the as received state. Fig. 1.14 reveals a bright field optical micrograph of a sample, with a micrograph of the cross section of the entire sample in Fig. 1.12(a) and, in Fig. 1.12(b), a bright field micrograph of higher magnification for the area delineated by the rectangle in Fig. 1.12(a). These micrographs reveal a dispersion of fine secondary Ag_3Sn and Cu_6Sn_5 precipitates between these Sn dendrites. A significant number (approximately ten) of Ag_3Sn precipitates of distinctly larger size (up to 10 micron) were also observed in a cross section as-received samples. As compared to the fine sized precipitates, the locations of these precipitates were less well correlated with the location of Sn dendrites.

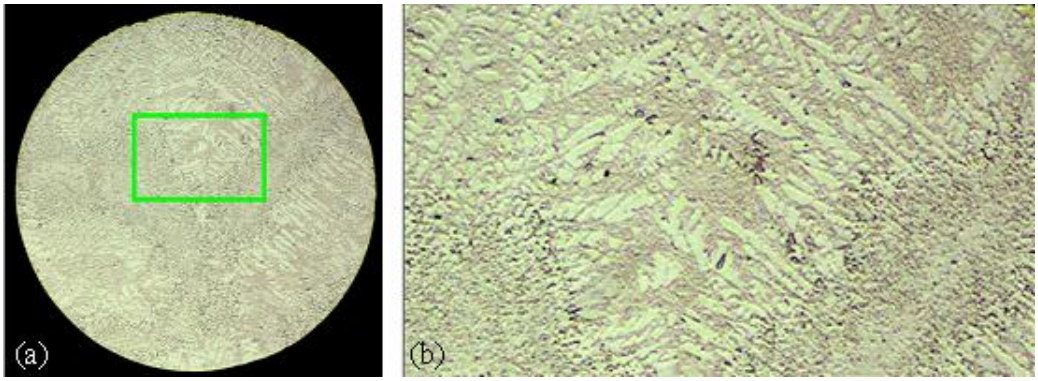

Figure 1.14: Optical micrographs of cross section of an as-received NEMI (Sn-3.9Ag-0.6Cu) solder ball: (a) low magnification showing microstructure of the whole solder ball, and (b) high magnification of the squared region in (a).

Solder balls which had been reflowed for different times and temperatures were examined. Very large primary precipitates of Ag_3Sn were observed in solder balls which had been reflowed at lower temperatures or shorter times. For instance, the bright field micrographs (Fig. 1.15) of cross sections of commercial Sn3.9Ag0.6Cu (NEMI) solder balls which were reflowed at 250^{o}C revealed large (approximately 100 micron) Ag_3Sn plates, with plate sizes generally several times bigger for samples with longer reflow times and larger degrees of undercooling(cf. Figs 1.15(c) and 1.15(d) versus 1.15(a) and 1.15(b)).

Samples which were reflowed at a temperature of 320^{o}C sometimes revealed microstructures with large Ag_3Sn plates. For reflow times of one minute, roughly half the samples examined revealed large (100 micron) plates, while others had no readily discernible Ag_3Sn plates. Micrographs of cross sections of samples annealed at 320^{o}C for twenty minutes did not reveal any Ag_3Sn plates.

Figure 1.15: Optical micrographs of NEMI (Sn-3.9Ag-0.6Cu) solder balls: (a) and (b) cooled at 1.0°C/s after reflow 1min. at 250°C, (c) and (d) cooled at 1.0°C/s after reflow 20min. at 250°C, (e) and (f) cooled at 1.0°C/s after reflow 20min. at 320°C. The solidification temperature and undercooling, respectively, for each sample are as follows: (a) 200°C, 17°C, (b) 202°C, 15°C, (c) 192°C, 25°C, (d) 187°C, 30°C, (e) 184°C, 33°C, and (f) 180°C, 37°C).

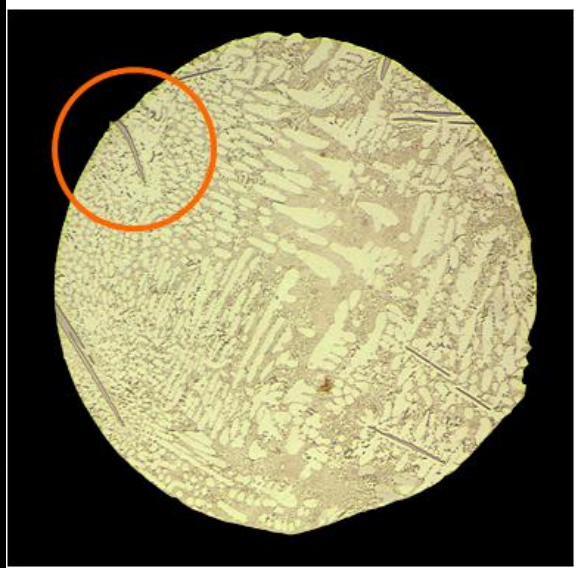

Figure 1.16: A bright field optical micrograph of a NEMI (Sn-3.9Ag-0.6Cu) solder ball after double reflow for 1min. at 250°C: a bent Ag_3Sn plate present in the circle. The solidification temperature after the first reflow was 200.5°C giving and undercooling of 16.5°C and after the second reflow the solidification temperature was 197.5°C giving an undercooling of 19.5°C.

The Sn dendrite arm size varied considerably for different solidification temperatures, and also within a given sample. Sn dendrite arm widths varied between 10 and 50 microns in the sample of Fig. 1.15(a), while in the sample of Fig. 1.15(c), which solidified at a temperature 15 degree lower, Sn dendrite arm widths generally ranged from 5 to 30 microns, with a large fraction near to 5 microns. Sn dendrite arm sizes in a sample which was undercooled 37°C ranged from 1 micron to 20 micron, with most of the visible portion of the sample containing Sn dendrite arm sizes which were quite large (Fig. 1.16(d) and Fig. 1.17).

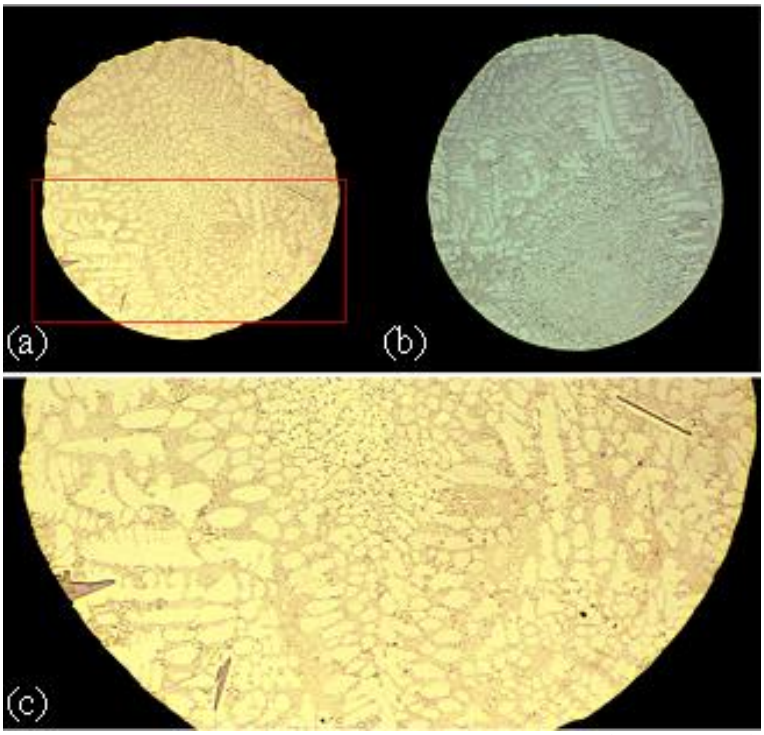

Figure 1.17: 25mil Sn-3.5Ag solder balls: (a) reflow 1min. at 250°C with 22°C Sn undercooling, (b) reflow 1min. at 500°C with 22.0°C Sn undercooling, and (c) high magnification of the squared region in (a) show growth of primary Ag_3Sn plates.

The morphologies of the Sn grains were found to vary distinctly with solidification temperature (Figs. 1.18 and 1.19). Sn grains were delineated in micrographs of cross sections of various samples by use of crossed polarizers. A typical "Kara's beach ball" Sn grain arrangement was observed for Sn3.9Ag0.6Cu (NEMI) solder ball samples which had undercooled approximately 15°C (Fig. 1.18(a), while samples which had undercooled twice as much revealed a distinctly different Sn grain morphology Fig. 1.18(b). While the Sn grain morphology of Fig. 1.18(b) would appear to contain smaller Sn grains, both the beach ball morphology and samples such as those of Fig. 1.19(b) have also been shown to be six fold cyclically twinned. A Sn grain morphology typical of as received samples is shown in Fig. 1.19(c).

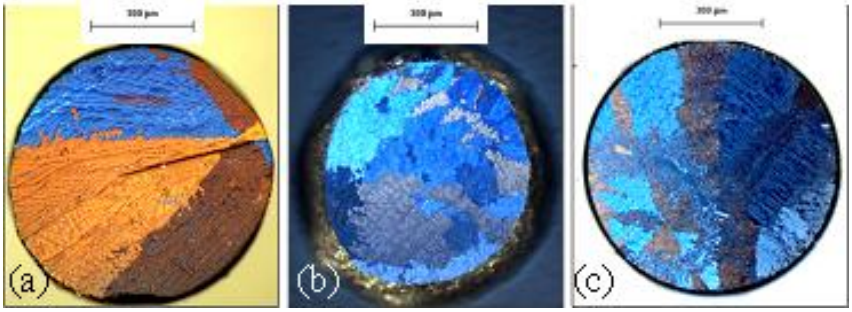

Figure 1.18: Cross-polarized light micrographs of Sn-3.9Ag-0.6Cu: (a) cooled from a temperature of 250°C at a rate of 1°C/s with 16.5°C Sn undercooling, (b) cooled from a temperature of 320°C at a rate of 1°C/s with 34.7°C Sn undercooling, (c) as-received ball.

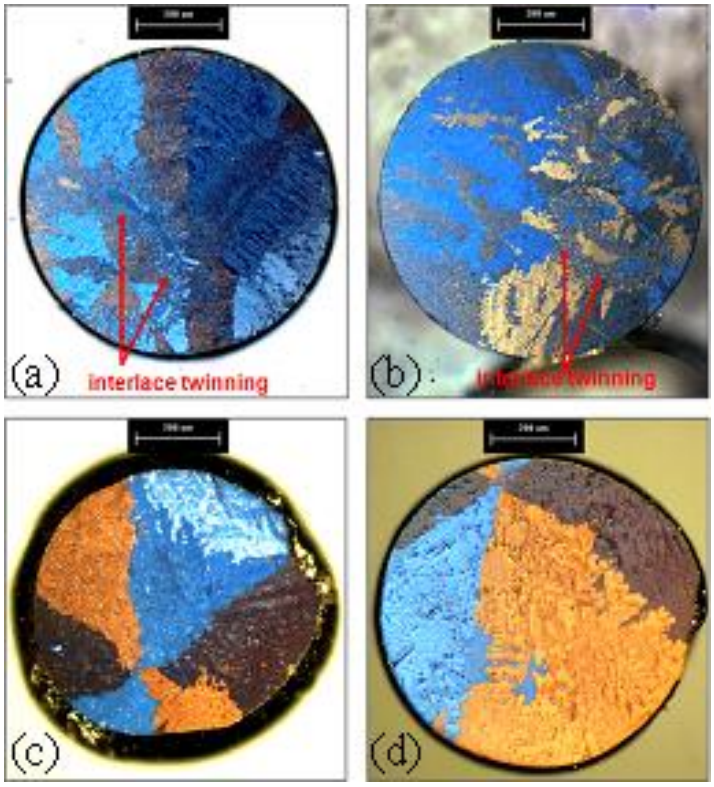

Figure 1.19: Optical micrographs with cross polarizers of 30mil NEMI (Sn-3.9Ag-0.6Cu) solder balls: (a) and (b) as-received (cooling rate > 10^{o}C/s, arrows indicate fine grain interlace twinning region), (c) and (d) cooled at 1.0^{o}C/s after reflow 1 min. at 250^{o}C. The solidification temperature and undercooling is (c) 197^{o}C, 20^{o}C and (d) 201^{o}C, 16^{o}C.

Effect of Reflow on Solder Joint Microstructure Our study indicates that the formation of primary Ag_3Sn plates upon cooling from the melt depends strongly on whether or not the Ag_3Sn precipitates completely dissolve during reflow [1.29-1.39]. This observation is consistent with the fact that growth processes are generally much faster than nucleation rates. If some Ag_3Sn precipitates do not completely dissolve during the reflow process, they will begin growing after cooling below the liquidus temperature. Since Sn typically undercools significantly, a wide temperature range, and thus a relatively long time (a time which depends upon cooling rate!), will be provided for such Ag_3Sn plates to grow in liquid Sn. For a cooling rate of 1^{o}C/s, typical during reflow, and an undercooling of Sn of approximately 30^{o}C, generally more than 50 s would be provided for growth of Ag_3Sn. In this case, one would expect the formation of large Ag_3Sn plates in the solder bulk, as observed in samples which were reflowed at a temperature of 250^{o}C (Figs. 1.15(a) – (d), Fig. 1.16 and Fig 1.17(a)), where Ag_3Sn precipitates with some dimensions over 100 microns are observed.

On the other hand, if all Ag_3Sn precipitates were completely dissolved during reflow, the amount of time for growth of Ag_3Sn precipitates would depend on how quickly Ag_3Sn nucleates as the Sn melt cools. If the degree of Ag_3Sn undercooling is comparable to Sn undercooling, then if no solid Ag_3Sn is present in the melt, any "primary" Ag_3Sn precipitates will be comparable in size to secondary preciptitates; no Ag_3Sn precipitates will be identifiable as plates in the final solidification microstructure (cf. samples reflowed at temperatures of 300^{o}C and above, Figs.

1.15(e), 1.15(f), and 1.17(b)). Thus, determination of the final microstructure depends upon evaluation of whether or not primary precipitates dissolve during reflow.

The data are consistent with a thermally activated dissolution process of Ag_3Sn in the Sn melt which is relatively sluggish at a temperature of 250°C. The rate of dissolution at a temperature of 320°C can be crudely estimated given that the Ag_3Sn particles present in as received NEMI samples were observed to be approximately two micron thick (and much longer) and that some samples show Ag_3Sn plates and some did not after cooling from a temperature of 320°C after one minute of reflow. The working assumption is that these results indicate that the existing Ag_3Sn plates dissolved in approximately one minute at 320°C, some took slightly longer, and so some samples had Ag_3Sn plates. So, the rate at 320°C would be approximately 0.02 micron/s. The rate at 250°C is at least twenty times less, or less than 2nm/s, as samples reflowed for twenty minutes at 250°C generally revealed Ag_3Sn plates. These estimates of rates are reasonably consistent with previous measurements of the rate of dissolution of Ag_3Sn at a temperature of 300°C, where rates between 0.03 and 0.3 micron/s were recorded at a temperature of 300°C.

The presence of Ag_3Sn and Cu_6Sn_5 primary precipitates in the melt has little or no effect on the nucleation of Sn. No correlation was observed between the degree of undercooling of Sn (Figs. 1.9 – 1.11) and the presence and size of Ag_3Sn precipitates in the melt. The solidification temperatures were similar for samples with and without large Ag_3Sn primary precipitates. These precipitates grew in the melt, yet had little or no effect on Sn solidification; no correlation was observed between solidification temperature and the presence of Ag_3Sn. This is consistent with previous research.

The variations in degree of undercooling with reflow profile times and temperatures are consistent with previous research on a general scale. Previous work has indicated that repeated reflow may increase the degree of undercooling of metal samples. It has been speculated that this is due to agglomeration of impurities in the samples, although specific impurities responsible for Sn nucleation and agglomeration mechanisms have not been identified. Such an observation is consistent with an assumption that our laboratory prepared alloys (see Fig. 1.11) have lower impurity contents than industrial samples. The samples prepared in the laboratory showed less dependence of undercooling on reflow temperature (Fig. 1.11). It is less clear why increasing the reflow temperature to 400°C, the degree of Sn undercooling drops, although there is evidence that a reaction occurs between the Sn and the Al DSC sample pan at such elevated temperatures.

The variations in solidification temperature for similar samples attained by varying reflow profiles provides an opportunity to examine variations in microstructure with degree of undercooling for these near eutectic SnAgCu samples. We consider in turn the dependence of Sn grain morphology and the dependence of precipitate morphologies on this parameter. We also examine the effect of cooling rate on Sn grain morphology. The morphology of Sn grains varied from clear cyclic twinning to interlaced twinning as the solidification temperature was lowered. This is clearly illustrated in Figs. 1.18 and 1.19. This dependence is focused on in section C, below.

Effect of Sn Solidification Temperature on Secondary and Primary Precipitate Morphology The solidification temperature affects the size of secondary Ag_3Sn precipitates. These precipitates are generally smaller in samples that undercooled more, as seen in Figs. 1.14-1.16. This effect is muted by the effect of recalescence. Upon nucleation of the Sn phase the heat of fusion of Sn is released. This heat rapidly diffuses through the sample, causing a temperature

increase. For instance, Fig. 1.17 shows a fine structure of secondary precipitates for part of the sample, with larger precipitates and Sn dendrite arm sizes for the rest of the sample. Although overall variation in secondary arm size is observed with variations in undercooling, recalesence results in large variations in secondary arm size in a sample as well.

Effect of Size and Cooling Rate on Sn Solidification Temperature A distinct dependence of the solidification temperature of Sn in near eutectic SnAgCu solder joints is observed (Fig. 1.20). This results in variations in the Sn grain morphology (see section C) and in the precipitate microstructure. It has been observed that variations in the cooling rate affect the precipitate microstructure of these solder joints (see above), but these variations in cooling rate do not directly affect the Sn solidification temperature, as can be seen in Fig. 1.20. The cooling rate is observed to have profound effects upon the precipitate morphology, as noted above (cf. Fig. 1.21).

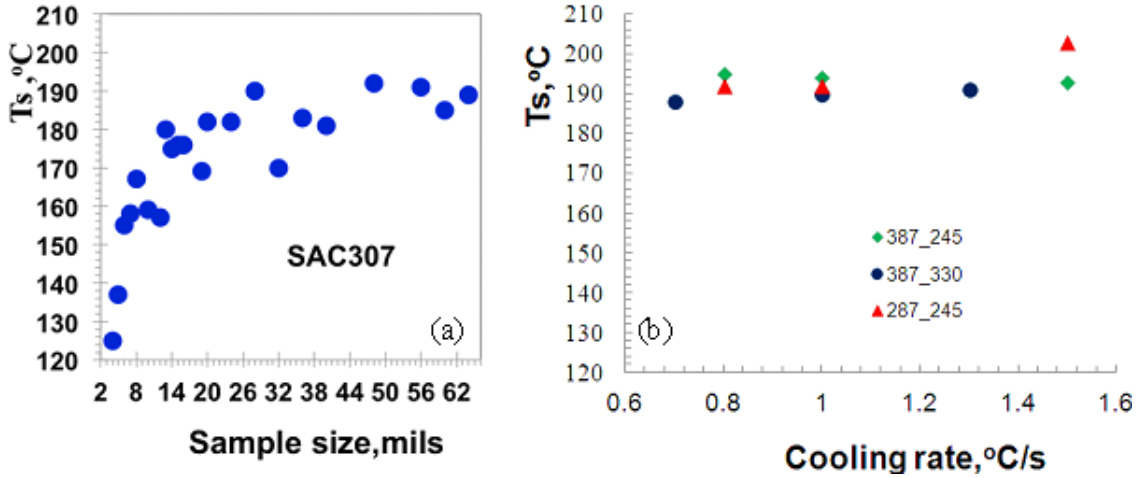

Figure 1.20: (a) The solidification temperature versus sample size for a near eutectic SnAgCu alloy, SAC307. (b) The solidification temperature versus cooling rate for larger samples of near eutectic SnAgCu alloys, SAC387 and SAC287.

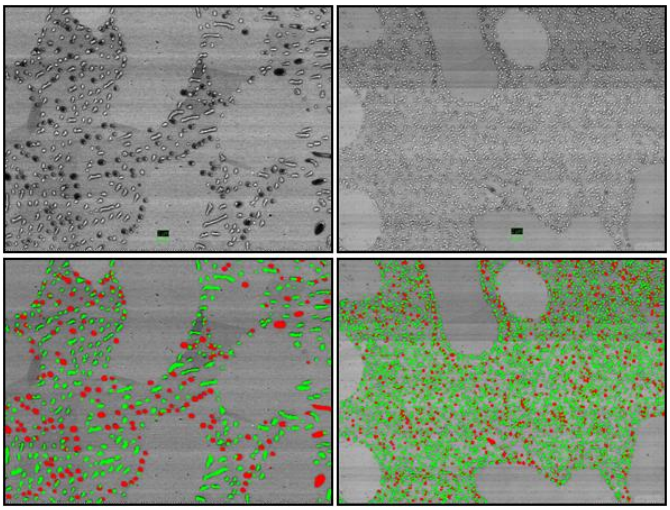

Figure 1.21: Quantitative analysis of secondary precipitates in near eutectic SnAgCu. Ag_3Sn precipitates are shown in green, while Cu_6Sn_5 precipitates are shown in red, for two different cooling rates.

Effect of cooling rate on the precipitate spacing

The inter-particle distance, λ, between Ag_3Sn precipitates in SAC solders shows a dependence on the cooling rate. Previous investigations have shown that cooling rate has a significant effect on the morphology and orientation of Ag_3Sn precipitates. The number density of Ag_3Sn is observed to increase monotonically with increase in the cooling rate (Fig. 1.22). The Ag_3Sn precipitates change in morphology from needlelike at slow cooling rates to relatively spherical shape at fast cooling rates. A decrease in size and an increase in number of Ag_3Sn are observed as the cooling rate increases. The quantitative analysis number density of secondary Ag_3Sn precipitates (Fig. 1.23) shows a monotonic increase with increase in cooling rate. This leads to the relations between the initial particle spacing, λ_o, and cooling rate. For instance, for SAC305 solder $\lambda_o^2 = 0.17 + 0.26/(dT/dt)$.

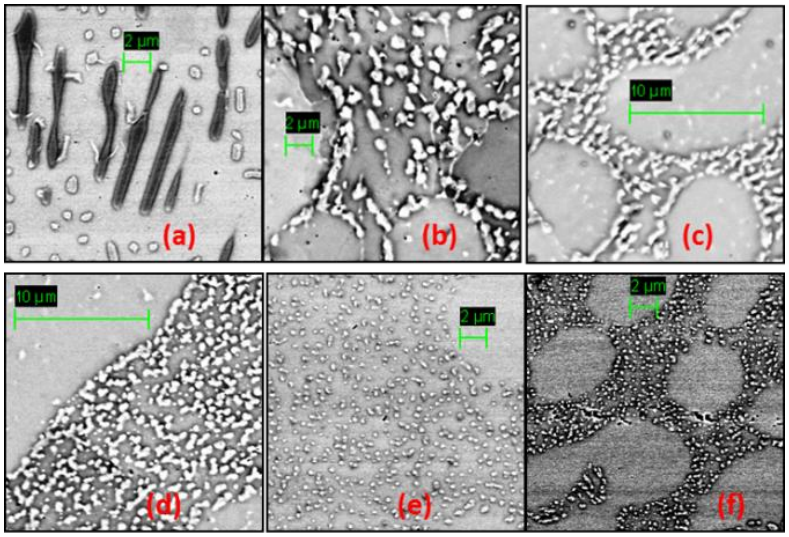

Figure 1.22: Scanning electron micrographs for cooling rates (a) 0.05C/s, (b) 0.1C/s, (c) 0.2C/s, (d) 0.4C/s, (e) 0.8C/s, (f) 1.1C/s).

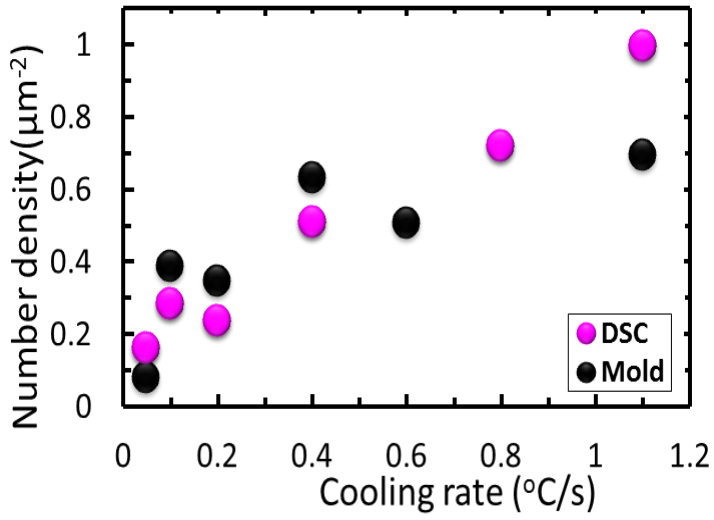

Figure 1.23: Plot of the number density of Ag3Sn precipitates versus cooling rate for near eutectic SnAgCu solder

Reflow Section B Summary The reflow time, temperature, and cooling rate of near eutectic SnAgCu alloys strongly affects the solidification temperature, and the final microstructure of samples. This effect was correlated with the behavior of Sn, independent of any Cu_6Sn_5 or Ag_3Sn precipitates. This effect of reflow parameters on solidification temperature is most probably related to agglomeration of impurities in the sample.

C. Dependence of the Sn Grain Morphology of SnAgCu Solder on Solidification Temperature

This section examines the nature of Sn solidification in SnAgCu alloys, with emphasis on the variation of the Sn grain morphology as a function of solidification temperature [1.44-1.67]. The initial undercooled Sn solidification temperature was varied and carefully monitored. Different means were employed to vary the solidification temperature, in order to examine the correlation of the Sn grain structure of SnAgCu samples with their solidification temperature after cooling from the melt. The size of SnAgCu samples was varied in order to change the sample solidification temperature upon cooling from the melt. In a different approach, the thermal history of SnAgCu samples was varied, in order to change the solidification temperature. For instance, undercooled liquid samples were held at specific temperatures until solidification ensued. Correlations between the Sn grain morphology and SnAgCu sample solidification temperature were carefully characterized. We seek insight into some of the inherent differences in the Sn grain morphologies and properties of different SnAgCu solder joints, such as small (flip chip) versus larger (e.g. BGA) solder joints.

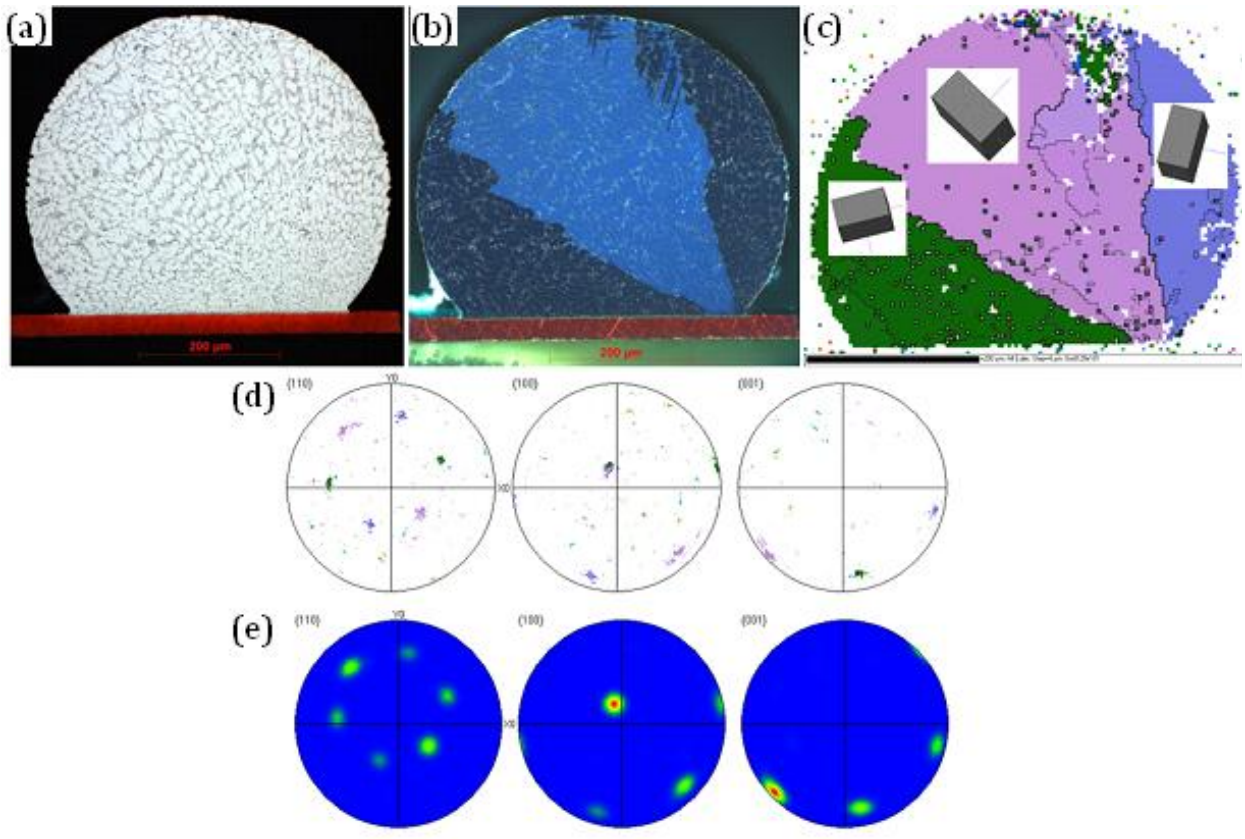

Figure 1.24. (a) Bright field optical micrograph of 500 micron diameter, as reflowed SAC205 on Cu substrate (b) Optical micrograph with crossed polarizers of the sample of (a) showing three large Sn grains. (c) EBSD map for the sample of (a-b), (d) Pole figures, the colors correspond to those of (c), (e) Contour plot of the same data shown in (d), (Half width: 15^{o}, cluster size: 5^{o}, equal area projection, upper hemisphere).

The microstructures of SnAgCu samples of a variety of sizes were examined in the as-received states. Representative optical and electron micrographs for cross sections of such samples are presented in Fig. 1.24(a) and 1.24(b) for a relatively large (500 micron diameter), SAC205 sample, and in Figs. 1.25(a) and 1.25(b) for smaller (100 micron diameter, flip chip) SAC3510 samples. Also included in Figs. 1.24 and 1.25 are EBSD data for these two samples, including orientation maps for each sample, as well as pole figures. Fig. 1.26 provides examples of DSC plots of heat flow versus temperature for the cooling of SnAgCu samples from the melt, including solidification events. In Fig. 1.26(a) the data for the solidification of a large SAC205 sample on Cu is plotted along with that for an assemblage of separate, much smaller SnAgCu samples. In Fig. 1.26 (b) a plot is presented of DSC data for an isothermal anneal of flip chip samples at a temperature of 200°C. Individual solidification events are clearly visible.

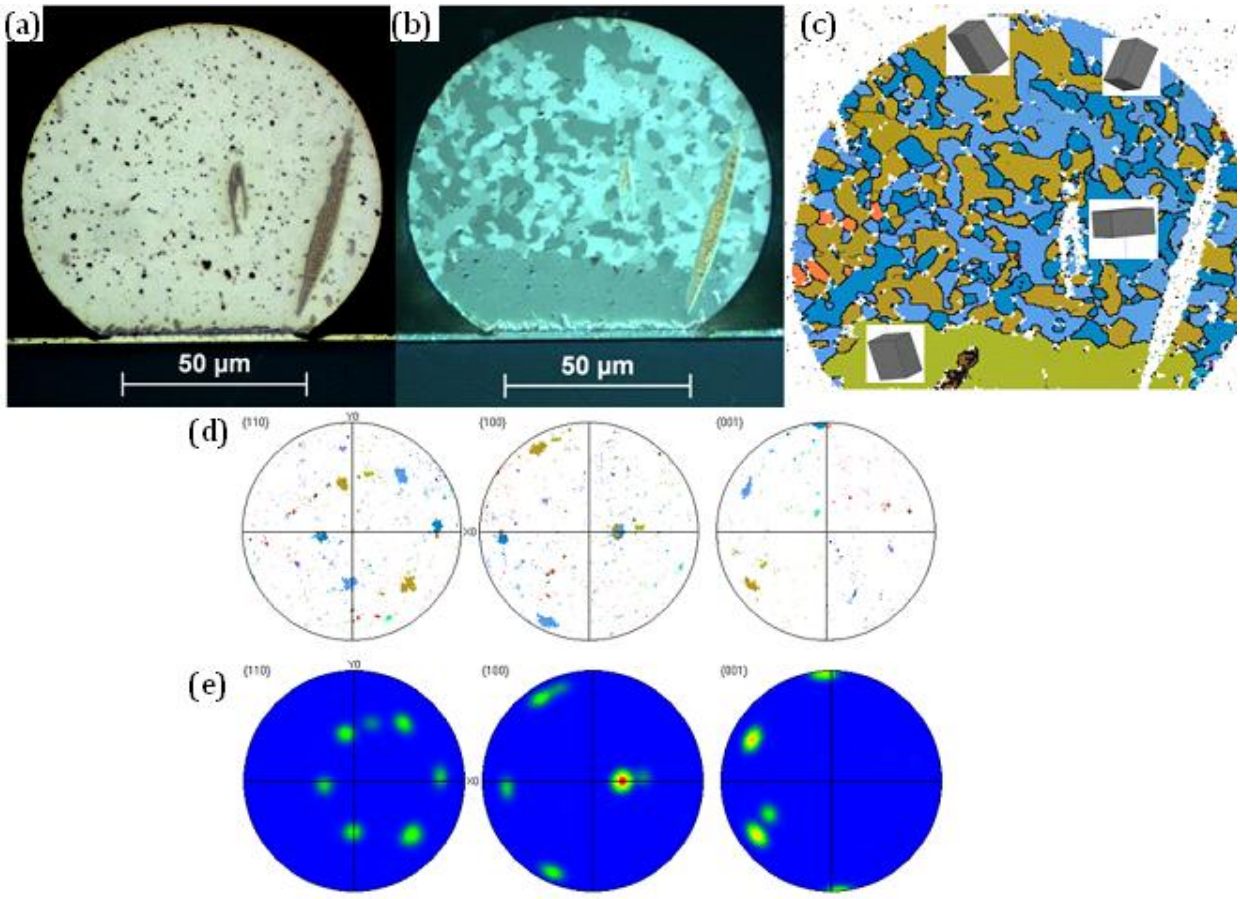

Figure 1.25: (a) Bright field optical micrograph of 100 micron diameter as-received flip chip sample (SAC 2510 on Ni(V)/Al substrate (b) Optical micrograph with crossed polarizers of sample (a), (c) EBSD map for the sample of (a-b), (d) Pole figures, the colors correspond to those of (c), (e) Contour plot of the same data shown in (d), (half width: 15^{o}, cluster size: 5^{o}, equal area projection, upper hemisphere).

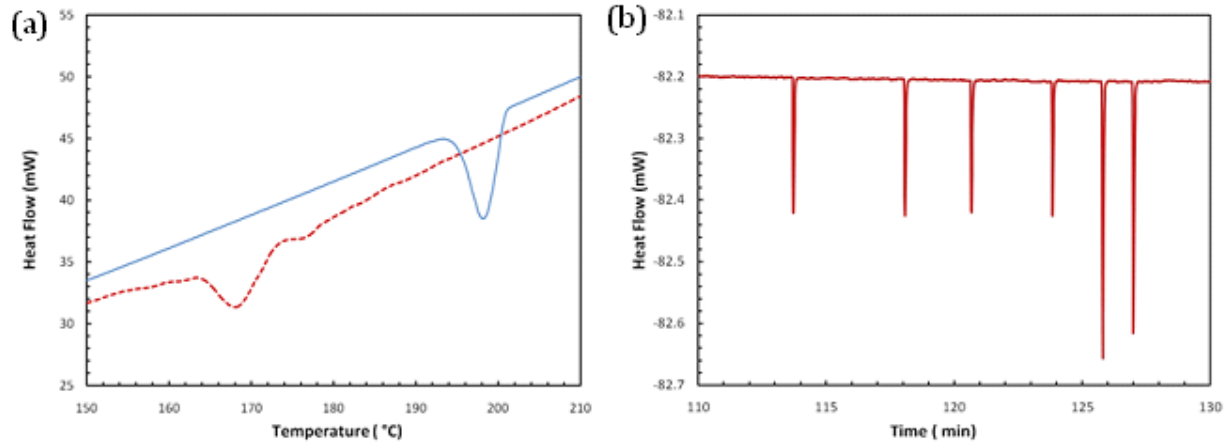

Figure 1.26: (a) Plots of heat flow versus temperature for cooling of an individual SAC205 solder ball on a Cu substrate (solid line), and for cooling 88 flip chip solder balls of SAC3510 on Ni(V)/Al substrates (dashed line). (b) Heat flow versus time during an isothermal hold at a temperature of 200^{o}C, 88 flip chip solder balls of SAC3510 on Ni(V)/Al substrate.

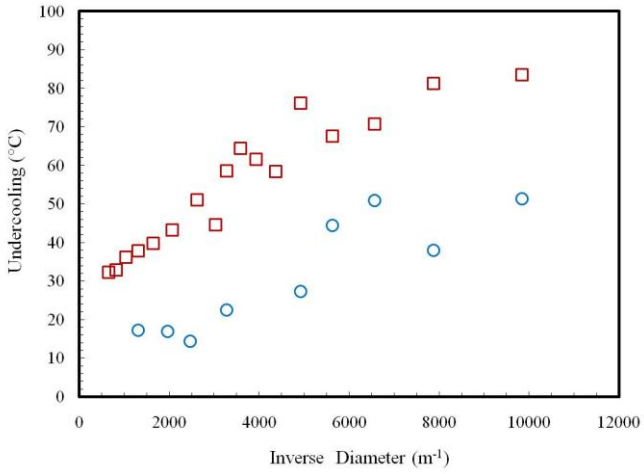

Figure 1.27: Plot of undercooling versus inverse diameter of free standing samples. Each data point represents the average under-cooling for twelve runs. The lab made SAC 305 samples (squares) were prepared in the vacuum tube furnace using high purity ele-ments. The circles show the samples obtained from commercial supplier.

Systematic variation of the solidification temperature with sample size of a particular SnAgCu sample type was observed. Plots of undercooling versus inverse nominal diameter are plotted in Fig. 1.27 for SAC305 samples produced in our laboratory, and for SAC305 samples produced by a commercial supplier. The effects of sample size are apparent. Undercoolings between 30 and 80^{o}C were routinely observed. A number of SnAgCu samples of various solidification temperatures were cross sectioned, polished and examined using optical and electron microscopy, including some from the study of solidification temperature versus sample size (Fig. 1.27). Representative optical micrographs with crossed polarizers are presented in Fig. 1.28. A systematic variation in the degree of interlacing is observed with decreasing temperature. Figure 1.29 includes a bright field optical micrograph for one of the smallest samples which solidified at a temperature of 137^{o}C.

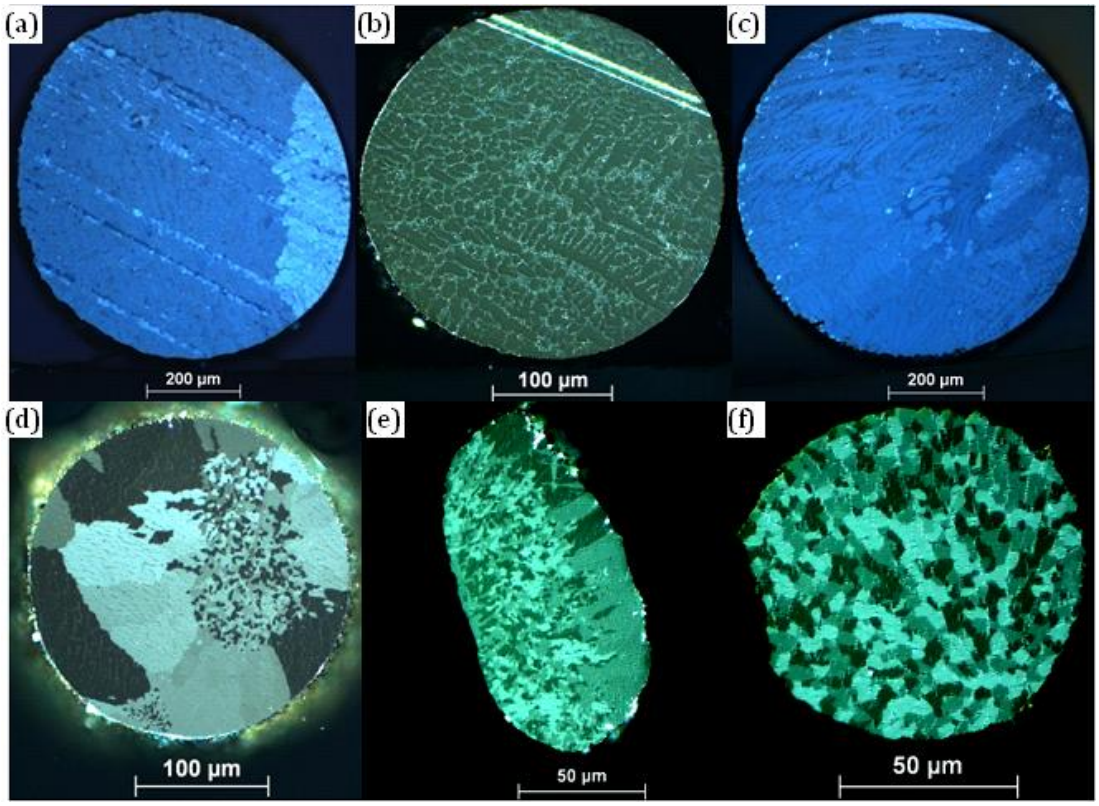

Figure 1.28: Optical micrographs with crossed polarizers for different SAC305 samples of different diameters and solidification temperatures: (a)750 micron, 200^{o}C (b) 300 micron, 195^{o}C (c) 750 micron, 181^{o}C (d) 300 micron, 172^{o}C (e) 100 micron, 165^{o}C (f) 125 micron, 138^{o}C. Samples a, b, and e are from commercial supplier and samples c, d, and f were made in our laboratory.

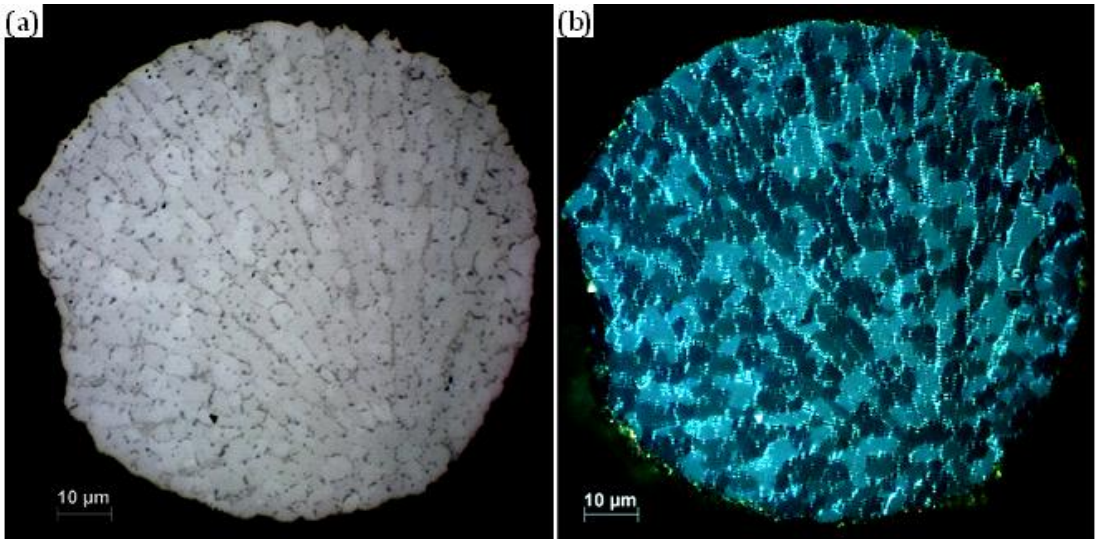

Figure 1.29: Bright field optical micrograph and (b) optical micrograph with crossed polarizers of 125 micron diameter, lab made SAC305 sample. The solidification temperature of this sample was 138^{o}C.

The solidification temperature of a particular sample could be varied by simply cooling to a given temperature (within a certain range) and conducting an isothermal anneal. For temperatures above approximately 205^{o}C degrees, solidification was generally not observed, even for the larger samples, in anneal times less than 10 h. In general, samples could not be cooled much below 185^{o}C degrees and stabilized before solidification occurred. But within the range of 185-205^{o}C degrees, the solidification temperature could be varied. Fig. 1.26(b) provides an example of the measurement of solidification times for samples which were annealed at a constant temperature of 200^{o}C. In this manner, flip chip samples were solidified at various isothermal temperatures between 185 and 205^{o}C. Fig. 1.30 provides a number of optical micrographs with crossed polarizers, for flip chip samples solidified at temperatures of 205, 195, 185^{o}C, as well as samples in the as-received condition. Fig. 1.31 provides additional EBSD data for one of these samples, a flip chip sample which solidified at a temperature of 185^{o}C. An orientation map is provided, as well as pole figures.

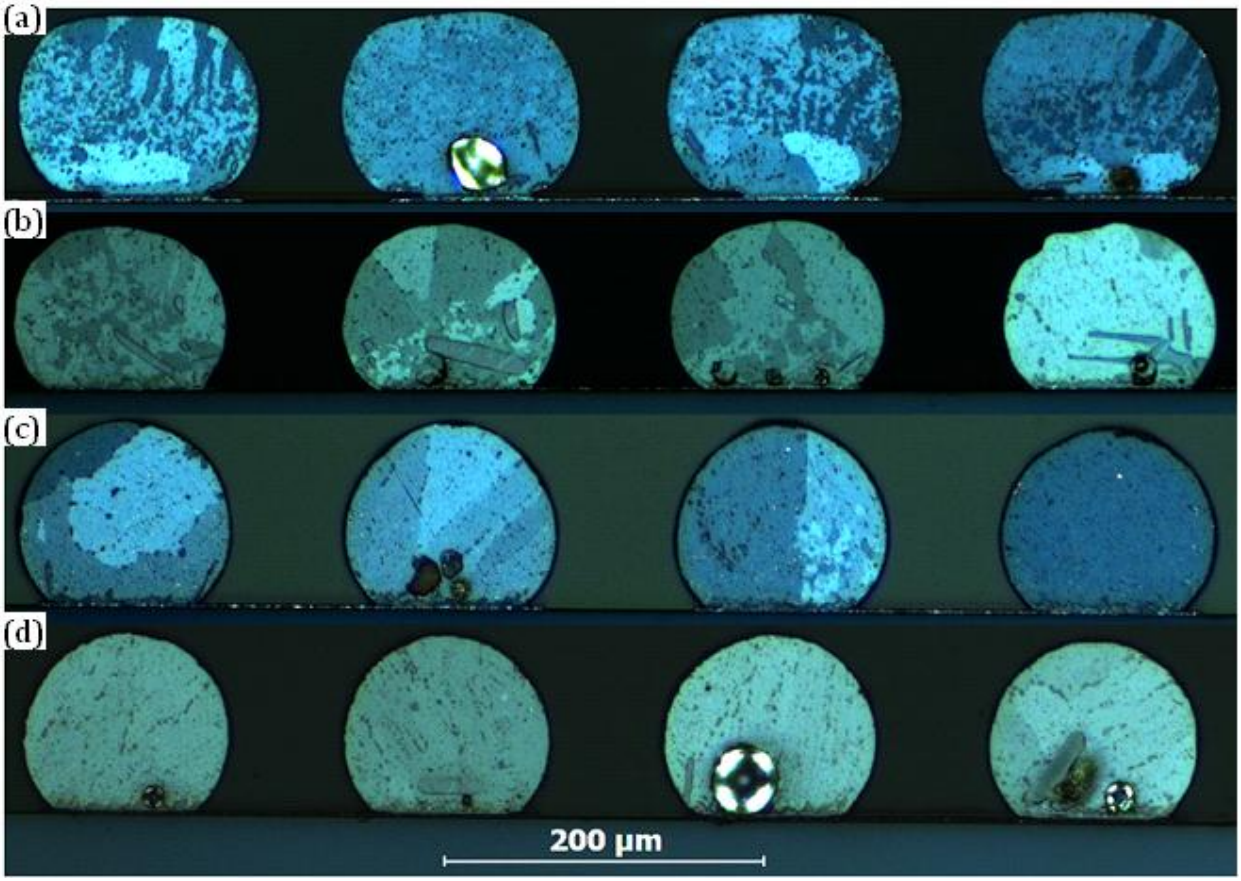

Figure 1.30: Optical micrographs with crossed polarizers of flip chip samples (SAC3105 on Ni(V)/Al substrate) of (a) as received samples that solidified at approximately 172^{o}C. Samples that solidifies at various temperatures during 840 minute isothermal anneal (b) 185^{o}C (c) 195^{o}C (d) 205^{o}C.

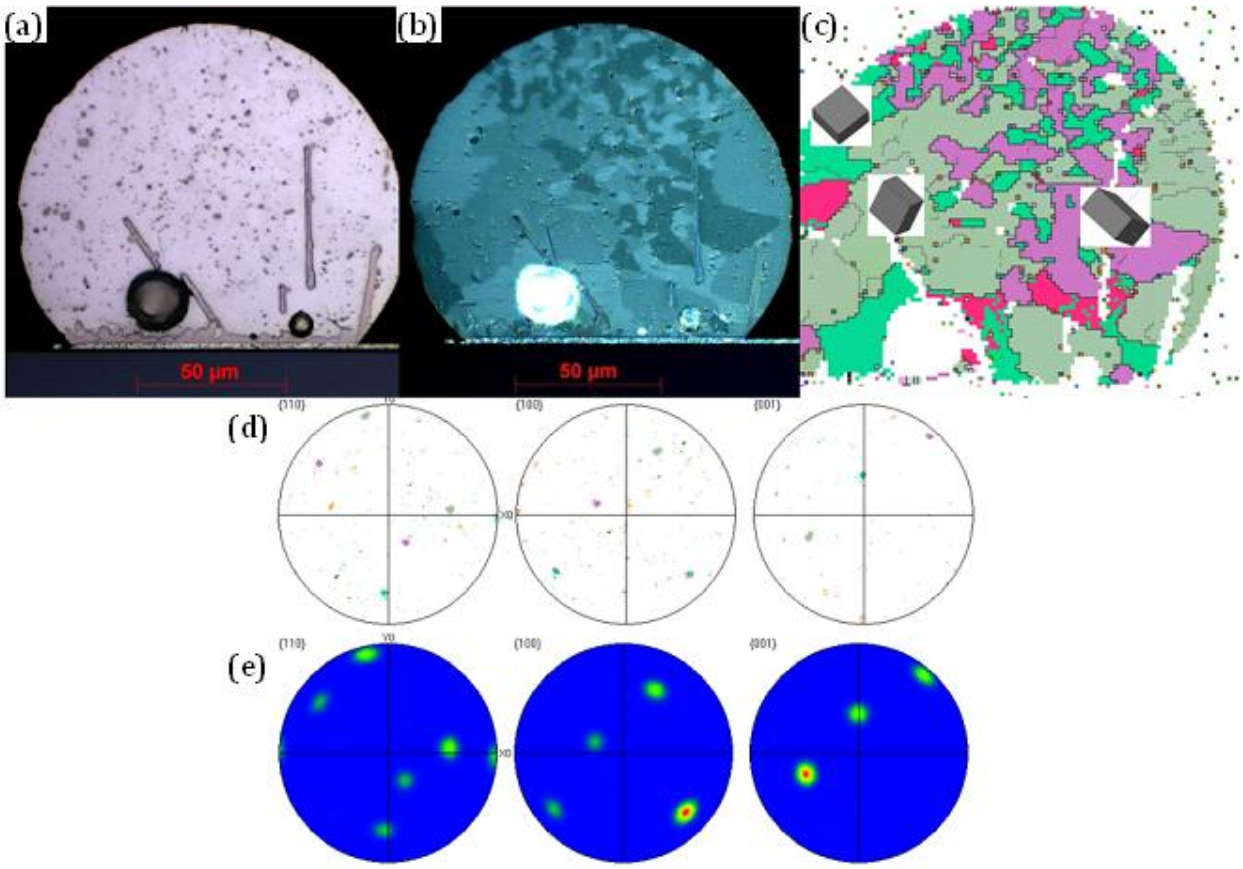

Figure 1.31: (a) Bright field optical micrograph of a flip chip sample (SAC3510) on Ni(V)/Al substrate) which solidified at 185°C during an 840 minute isothermal anneal, (b) Optical micrograph with crossed polarizers of the sample of (a), (c) EBSD map for the sample of (a-b), (d) Pole figures, the colors correspond to those of (c), (e) Contour plot of the same data shown in (d), (half width: 15°, cluster size: 5°, equal area projection, upper hemisphere).

In a similar fashion, larger samples were annealed at various temperatures for 600 minutes, so that they solidified. In Fig. 1.32 optical micrographs of cross sections of a sample solidified at a temperature of 200°C (C9 (a, d)), and a sample solidified at a temperature of 195°C (C9 (b, e)) are provided. Both bright field and crossed polarizer micrographs are displayed. Another large sample was annealed at a temperature of 210°C for 600 minutes in the DSC, without solidifying. This sample was then cooled at a constant rate of 1°C/s from the melt; solidification was observed at a temperature of 171°C (C9 (c, f)). Optical micrographs (bright field and crossed polarizers) for a cross section of this sample are included in Fig. 1.33(a) and (b). Furthermore, in Fig. 1.33, EBSD data for this sample are presented (along with a replication of the bright field optical micrograph, for comparison). In Fig. 1.34 a selected region (near the Cu substrate interface) of the orientation map of Fig. 1.33 is replotted along with a backscattered SEM image of the SAC205 on Cu substrate. Another large SAC205 sample that was solidified at 195°C was cross sectioned parallel to Cu substrate (in the z direction); most of the solder was removed during polishing. Fig. 1.35 shows the cross polarized image of this sample.

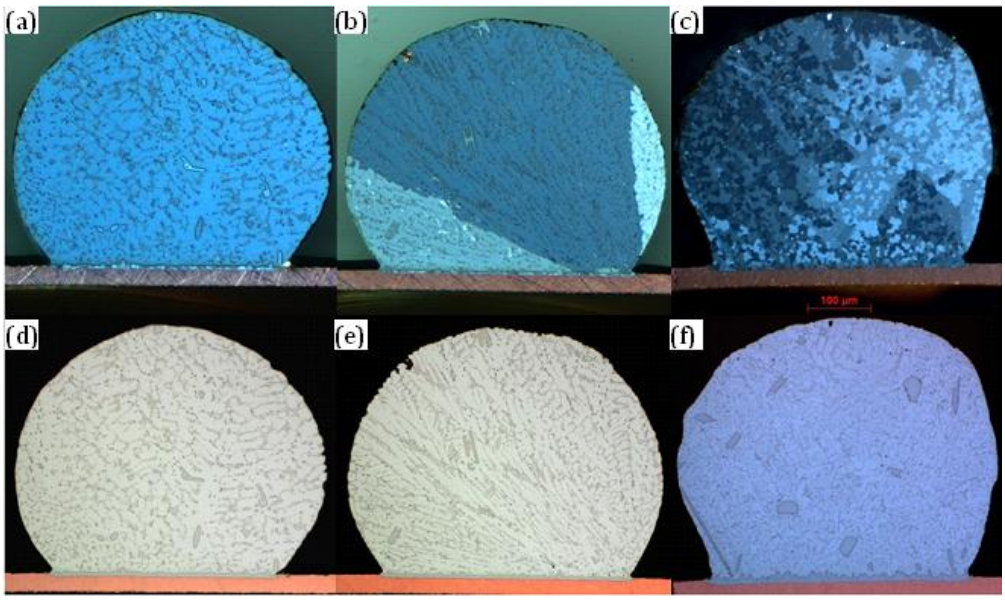

Figure 1.32: Bright field optical micrographs (d-f) and optical micrographs with crossed polarizers (a-c), of 500 micron diameter SAC205 on Cu substrates. The samples were solidified at different temperatures: (a,d) 205^{o}C (b,e) 195^{o}C (c,f) 171^{o}C.

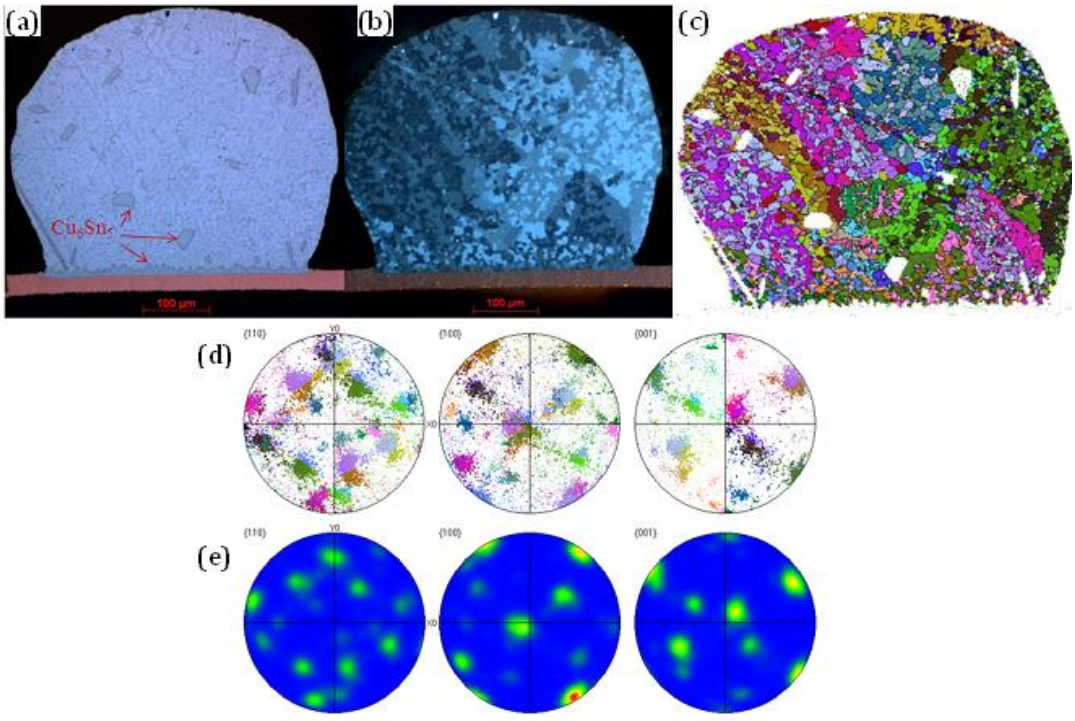

Figure 1.33: (a) Bright field optical micrograph of 500 micron diameter SAC205 sample on a Cu substrate. The sample was annealed at 210^{o}C for 600 minutes, and solidified at a temperature of 171^{o}C during cooling, (b) Optical micrograph with crossed polarizers of the sample of (a), (c) EBSD map for the sample of (a-b), (d) Pole figures, the colors correspond to those of (c), (e) Contour plot of the same data shown in (d), (half width: 15^{o}, cluster size: 5^{o}, equal area projection, upper hemisphere).

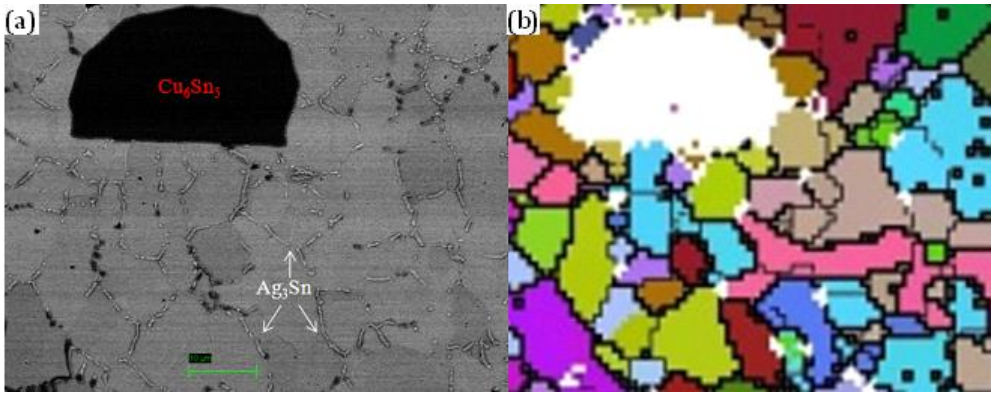

Figure 1.34: (a) Backscattered SEM image of a region of a 500 micron diameter SAC205 sample on a Cu substrate, solidified at 171°C (the same sample as that of Fig. C10). The black precipitates are Cu_6Sn_5 and the bright regions are Ag_3Sn (b) EBSD map of the same region.

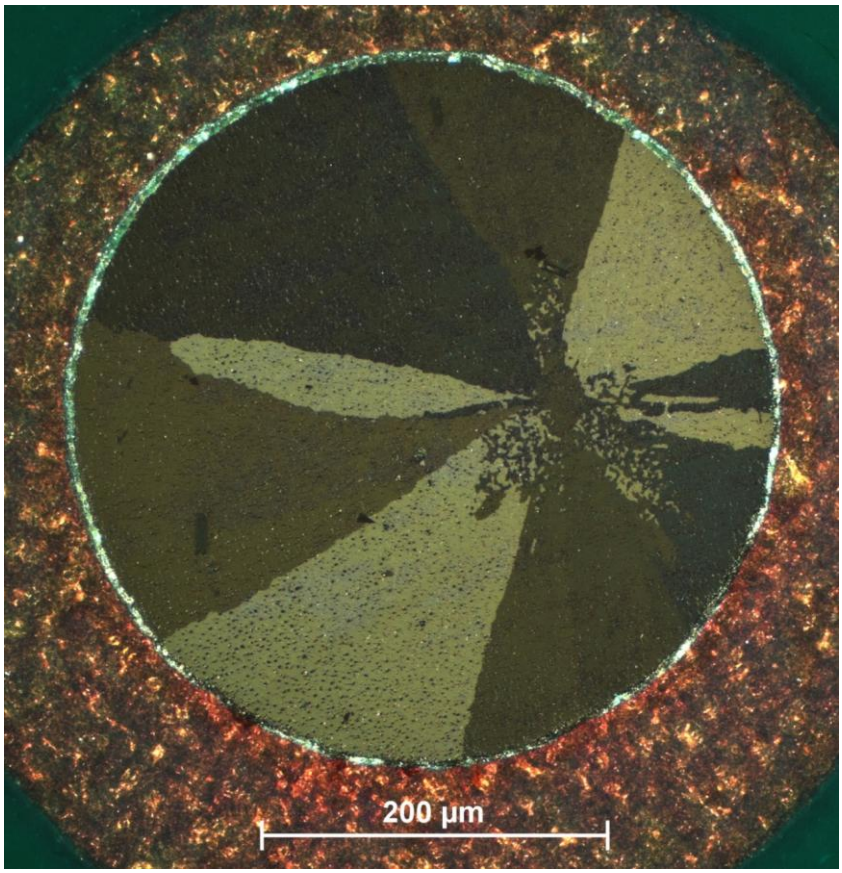

Figure 1.35: Cross polarized image of 500 micron diameter SAC205 sample, as reflowed on a Cu substrate. The sample is sectioned parallel to the substrate.

Quantification of Nucleation Rates in SnAgCu Solder Joints SnAgCu near eutectic alloys were produced over a large range of solidification temperatures (138 to 205oC) and sizes (5 x 10-7 and 2 x 10-3cm3), in free standing, and solder joint, configurations, yet revealed some striking similarities in their microstructures. The Sn grain morphologies of these SnAgCu samples generally revealed only three main Sn grain orientations. Furthermore, these three unique Sn orientations were each rotated sixty degrees around a common <010> axis. The one exception to this behavior was observed for a very large sample which solidified at 171oC (Fig. 1.33), which displayed not one, but two, such Sn grain triplets. The existence of only three main Sn grain orientations was generally observed, regardless of the size of Sn grains in the imaged cross sections, e.g. for Fig. 1.24, where three Sn grains filled the cross section in a 'beach ball' morphology, or e.g. for Fig. 1.25, which revealed an interlaced Sn grain morphology.

A correlation between sample size and the Sn grain morphology in these near eutectic SnAgCu samples is apparent in Figs. 1.24 and 1.25 and Fig. 1.28. For a given thermal history (e.g. for samples which were cooled from the melt at a constant rate of $1^oC/s$), the sample size is correlated with the sample solidification temperature (Fig. 1.27). As sample sizes decrease, solidification temperatures decrease, consistent with classical nucleation theory, for a given sample [1.C13, 1.C24]. Samples of similar nominal compositions (e.g. SAC305 in Fig. 1.27) and size, prepared by different means in several laboratories sometimes display various solidification temperatures. For instance, in Fig. 1.27 samples which were prepared with high purity elements in our laboratory show higher degrees of undercooling than samples obtained from commercial suppliers. But Fig. 1.27 reveals a systematic variation of solidification temperature with sample size for a given set of samples. Thus the samples of Fig. 1.27 include samples of different sizes, but similar degrees of undercooling. A fraction of the samples of Fig. 1.27 were cross sectioned and their Sn grain morphologies were carefully characterized.

The Sn grain morphologies of the SAC305 samples of Fig. 1.27 with different sizes and solidification temperatures were observed to vary systematically from interlaced to beach ball as solidification temperature increased. Representative optical micrographs with crossed polarizers of six different cross sectioned samples, with solidification temperatures ranging from 138 to 200^oC, are displayed in Fig. 1.28. The sample with the lowest solidification temperature, 138^oC, was simply interlaced, while two samples which solidified at 165 and 172^oC revealed a mixture of interlaced and beach ball Sn grain morphologies, while the samples which solidified at a temperature of 181^oC and above were simply beach ball Sn grain morphologies. Thus the correlation between larger samples and beach ball Sn grain morphologies appears to be associated with a correlation between higher solidification temperatures and such microstructures.

To further investigate the correlation between solidification temperature and Sn grain morphology of near eutectic SnAgCu samples, the thermal history of a number of different samples was varied so as to produce distinctly different solidification temperatures for similar samples. For instance, small (approximately 100 micron diameter) flip chip samples of SAC3510 reflowed on a Cu/Ni(V)/Al metallization, which solidify upon being cooled from the melt at a rate of $1^oC/s$ at a temperature near 170^oC, were induced to solidify at higher temperatures. These samples were cooled from the melt at a rate of $1^oC/s$ to a given temperature (205, 195, or 185^oC) and annealed for 840 minutes until they all solidified. Optical micrographs with crossed polarizers of cross sections of such samples are portrayed in Fig. 1.30. It can be seen that the Sn grain morphologies of these samples varied systematically from interlaced to beach ball as solidification temperature increased. Careful examination of the Sn grain morphology of the

samples solidified at 185^{o}C with EBSD revealed that these interlaced samples contained three main Sn grain orientations (e.g. Fig. 1.31). The relation between the orientation of these three orientations was similar to that observed for Sn grains in other samples, the grains were rotated by sixty degrees with respect to each other around a common <010> axis.

In a different approach, but a similar vein, a large sample (approximately 500 micron in diameter, one which when cooled at 1^{o}C/s would solidify above 200^{o}C and display a beach ball Sn grain morphology, cf. Fig. 1.24), was heat treated in order to lower the solidification temperature upon cooling. The 500 micron diameter, SAC205 on a Cu substrate was placed in the DSC, reflowed and cooled to a temperature of 210^{o}C and held for 600 minutes, and then cooled at a rate of 1^{o}C/s. This SnAgCu solder joint was observed to solidify at a temperature of 171^{o}C. Investigation of a cross section of this sample by means of optical microscopy with crossed polarizers and by means of EBSD revealed that the sample was interlaced; it revealed an interlaced Sn grain morphology similar to that of flip chip samples which solidified at the same temperature. In general, a correlation between solidification temperature and Sn grain morphology is observed for these samples.

We note that although hundreds of Sn grains are apparent in the optical micrograph for this large sample which was more deeply undercooled (Fig. 1.32(c)), and in the orientation map determined by EBSD (Fig. 1.33(c)), EBSD analysis reveals that there are a limited number, i.e. six, of primary Sn grain orientations. Such an observation is consistent with the nucleation at two points in this large sample, with nuclei similar in structure to those surmised to have formed in the other samples examined in this study. As classical nucleation theory predicts nucleation rates proportional to sample size and exponentially dependent on degree of undercooling, it is more probable that two nucleation events would occur in a larger sample at greater undercooling [1.67].

One may consider the observed Sn grain morphologies in the context of the simple model of Fig. 1.1 and Fig. 1.2(b). This model is based upon a six fold, multiply twinned Sn nucleus (Fig. 1.1). Growth of Sn dendrites from one such nucleus without growth from any other nuclei, and without growth twinning, should result in a sample with only three unique Sn grain orientations, as is generally observed in the samples examined in this study. In fact, the observed orientations of Sn dendrites in a beach ball configuration (e.g. Fig. 1.24) are consistent with the simple growth model of Fig. 1.2(b). Fig. 1.24(a) is a bright field optical micrograph of a near eutectic, SnAgCu solder joint which was cross sectioned and polished within approximately thirty degrees of the (100) planes of the three, large Sn grains in this sample (cf. Figs 1.24c–e). Fig. 1.24(a) reveals a series of Sn dendrites decorated with Cu_6Sn_5 and Ag_3Sn, all of oval geometry, consistent with fast growth of a parallel array of nearly circular Sn dendrites growing in the [110] and $\bar{1}10$ directions (Figs. 1.24(c), 1.24(d), and 1.24(e) indicate the orientation of these dendrites). Assuming that these dendrites were growing out of the plane of the cross section, growth of the first Sn dendrite probably originated from a point close to the lower right of the cross section (though behind the plane of the cross section, i.e. at some point on the minus Z_0 axis as defined in Fig. 1.24(c)).Thus the Sn dendrites grew in directions oriented approximately thirty five degrees with respect to the plane of the cross section. In Fig. 1.25, optical microscopy with crossed polarizers (Fig. 1.25(b)) and a orientation map (Fig. 1.25 (c)) reveal an interlaced Sn grain morphology. While there are many more grain boundaries in this sample than in a beach ball Sn grain morphology such as that of Fig. 1.24(b), this interlaced Sn grain morphology also reveals only three Sn grain orientations. The pole figures of Fig. 1.25(d) and C2 (e) are similar to those of Fig. 1.24, corresponding to three main Sn grain orientations,

each rotated by sixty degrees about a common <010> axis. The different Sn grain morphologies of Figs. 1.24 and 1.25 are consistent with a similar nucleation process (i.e. the model of Figs. 1.1 and 1.2(b)), but with different preferred dendritic growth directions, due to different solidification temperatures. The fast growth directions of dendrites in Sn moves away from the [110] and $\overline{1}10$ directions as the degree of undercooling increases, apparently due to an increase in thermal gradients in the sample. Then, rather than growing apart, the growing Sn dendrites may intersect, or interlace. A graphic example is provided in Fig 1.29, where in Fig. 1.29(a) the arrangement of secondary precipitates is consistent with growth away from a single nucleation point (a nucleation point somewhere near the lower right hand side of the sample). These secondary precipitates are generally radially arranged, and their spacing increases as the distance from the lower right increases. It is somewhat surprising to note that the regions between these secondary precipitates are not filled with single Sn dendrites, but with a collection of three, interlaced Sn dendrites. Such a configuration is consistent with an average radial growth of the Sn, with the temperature of the liquid increasing with distance from the nucleation point, but with the local preferred direction of growth of the Sn dendrites varying with time and position, and thus interlacing. Careful examination of Fig. 1.29 reveals that there are some secondary precipitates between some Sn grains which are not parallel to the clearly defined radial directions, though these are fewer in number. Fig. 1.33 reveals another interlaced Sn grain morphology, while Fig. 1.34 provides an SEM micrograph and EBSD data at a higher degree of magnification for this sample. The EBSD data of Fig. 1.33, when compared with high resolution SEM data, reveals (Fig. 1.34) a more distinct correlation between precipitate decorated grain boundaries and changes in Sn grain orientation.

Consideration of the model of Fig. 1.1 and 1.2(b) in terms of such a change in the preferred growth direction of Sn dendrites provides some insight into the origin of interlaced Sn grain morphologies, and mixed interlaced/beach ball Sn grain morphologies (e.g. Figs. 1.28(d) and 1.28(e). It is known that growth of Sn from the melt results in release of latent heat of fusion and an associated increase in the temperature of the sample, the magnitude of which depends upon thermal links to other materials, and the rate of growth of Sn. If higher temperatures of Sn dendrite growth may be associated with primary growth in the [110] and $\overline{1}10$ directions, then at some point beach ball type growth may ensue, resulting in a mixture of interlace and beach ball Sn grain morphologies.

Fig. 1.35 shows the cross polarized image of a large sample that was cross sectioned parallel to Cu substrate. It is clear that the morphology of Sn grains varies with position. The area close to the apparent Sn nucleation point shows regions of interlaced Sn structures; however, large Sn grains can be observed further from the nucleation event. This provides support for the contention that the growth pattern of Sn dendrites changes further from the nucleation point.

Solidification Temperature Section C Summary The Sn grain morphologies of near eutectic SnAgCu samples were characterized and found to be correlated with sample solidification temperatures; the lower the solidification temperature, the higher the degree of interlacing observed. These Sn grain morphologies were observed to be consistent with a simple model that envisions the nucleus in an undercooled SnAgCu liquid to be Sn atoms clustered around a Ag or Cu atom in a hcp configuration that allows Sn to grow epitaxially on each of its surfaces. The preferred growth of Sn dendrites in the [110] and $\overline{1}10$ directions at lower degrees of undercooling results in beach ball Sn grain morphologies, while at large degrees of undercooling,

the preferred degree of Sn dendrite growth moves away from the [110] and $\bar{1}10$ directions, and the Sn dendrites interlace. At intermediate degrees of undercooling, a mixed Sn grain morphology is observed, with the interlaced portion associated with the region closer to Sn nucleation in these samples.

D. Quantification of Nucleation Rates of Near Eutectic SnAgCu Solder Joints during Reflow

In this section D we examined the kinetics of the nucleation of Sn in undercooled SAC solder balls on Cu/Ni(V)/Al under bump metallization layers (Fig. 1.36) [1.68-1.102]. Measurements of the nucleation rate of Sn in these SAC 3510 flip chips were conducted at several different temperatures between 185^{o}C and 205^{o}C for separate arrays of 88 similar solder balls. The temperature dependence of the nucleation rate was quantified and compared to rates for high purity Sn. After these measurements, the same sets of solder balls were reflowed again, and the nucleation rates were measured again at the same temperatures. The microstructures of cross sections of solder balls which had been subjected to similar thermal histories were examined by means of optical and electron microscopy. Correlations between the solder ball microstructure, the number of reflows and Sn nucleation rates were examined.

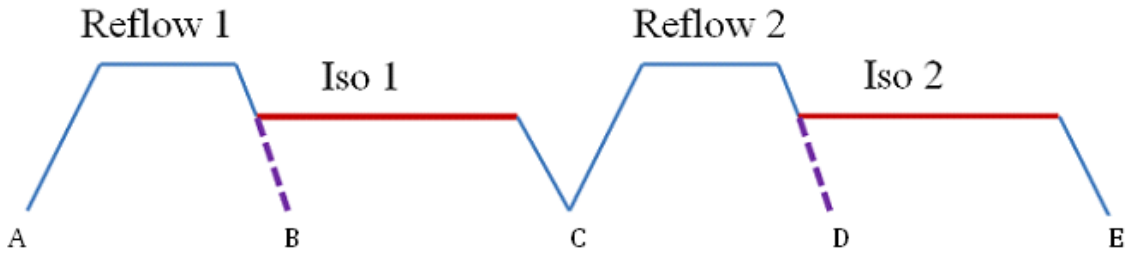

Figure 1.36: Thermal profile of samples prepared using DSC, Reflow Temperature: 250^{o}C, Hold Time: 2 minutes, Isothermal Temperature Range of 185-205^{o}C, Hold Time: 420 minutes.

The effects of solder composition, under bump metallurgy and solder joint geometry on Sn grain morphology in Pb free solder joints were examined. SnAgCu solder joints were examined for near eutectic SnAgCu compositions. The geometries of solder joints were varied: diameters from 10 to 150 microns, and heights between ten and sixty microns were selected.

Solidification temperatures of the samples after various thermal histories were monitored by means of differential scanning calorimetry. Sn grain morphologies were examined by optical microscopy and by scanning electron microscopy and electron backscattered diffraction in order to determine the amount of Sn interlacing. Correlations between the composition, or geometry, and the amount of Sn interlacing are reported. The nucleation rates of Sn from the melt in these Pb solder joints at a number of different temperatures were also measured. An expression for the nucleation rate of Sn in a controlled collapse chip connection solder joint as a function of temperature was thus formulated, providing a predictive capability for Sn solidification temperatures. This focus of this study has shown that variations in the temperature of solidification of Sn from the SnAgCu melt result in significant differences in the Sn grain morphology

Calorimetry Measurements

Plots of heat flow versus temperature are provided in Fig. 1.37 for six different sets of eighty eight flip chip solder balls, three of which (solid lines in Fig. 1.37) had been heated to a reflow temperature of 250^{o}C for 2 min and cooled at a rate of 60^{o}C/min to room temperature (i.e. to point B in Fig. 1.36), and three other samples (dashed lines in Fig. 1.38) had the history leading to point (d) in Fig. 1.36. Clear exothermic signals corresponding to solidification of all the solder balls were observed, upon cooling form the melt at a constant rate, between

temperatures of 195 and 160°C (Fig. 1.37). For the samples which had reached point B in Fig. 1.36 (solid lines in Fig. 1.37), solidification occurred at an average temperature of approximately 172°C, while for the samples which had reached point D in Fig. 1.36 (dashed lines in Fig. 1.37), solidification was observed at an average temperature of approximately 183°C.

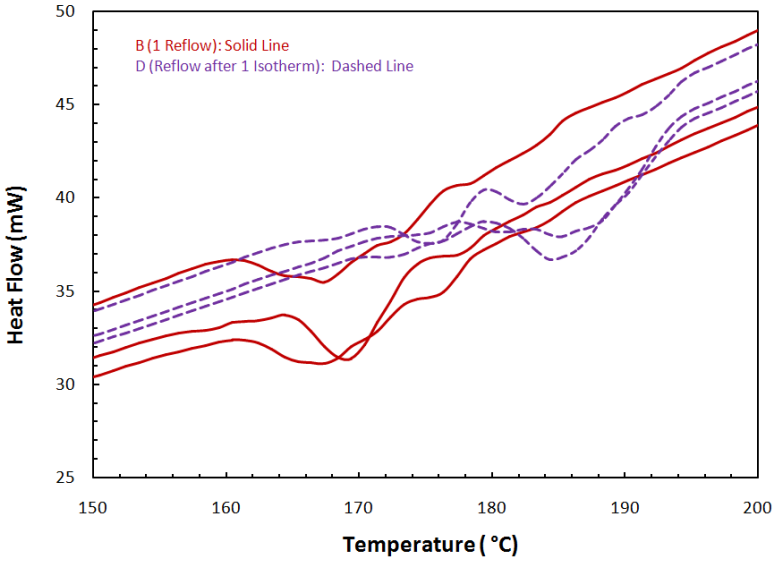

Figure 1.37: DSC plots for cooling of flip chip samples after one reflow (solid lines) and reflowed after one isotherm at 195°C (dashed lines). Three different samples were tested for each condition. Reflow temperature was 250°C, holding time 2 minutes, heating and cooling rate 60°C/min

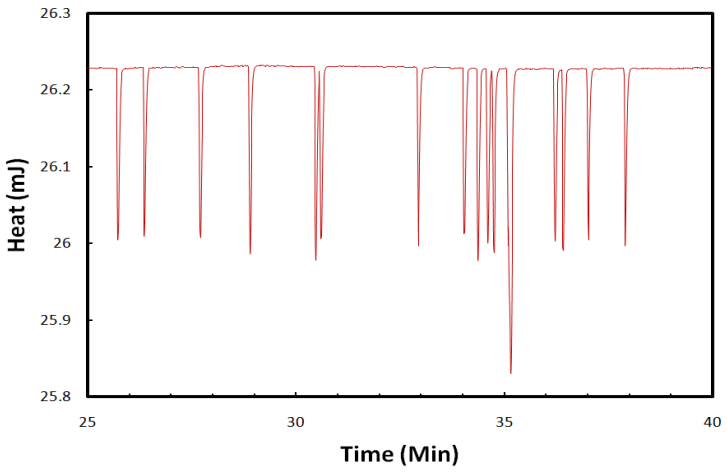

Figure 1.38: Isothermal solidification of flip chip samples with 88 solder balls at 195°C. The samples were held for 420 minutes at temperature range of 185-205°C. Each peak represents at least one solidification event.

Solidification events which occurred during the isothermal holds (cf. Fig. 1.36) were clearly observable in plots of heat flow versus time. An example of such data is provided in Fig. 1.38, heat flow versus time for an isothermal hold at a temperature of 195°C for a set of eighty

eight flip chip solder balls. Solidification times were recorded for solder balls cooled to either a first or second isotherm (cf. Fig. 1.36). Examples of the distribution of solidification times are presented in Fig. 1.39 in plots of number of solder balls solidified versus time. In Fig. 1.39, such plots are provided for data obtained during the first and second isothermal hold at a temperature of 195°C of a set of eighty eight SnAgCu solder balls (cf. Fig. 1.36), and during the first and second isothermal hold at a temperature of 200°C for a different set of eighty eight SnAgCu solder balls.

An increase in the nucleation rate with decreasing temperature was generally observed in these SnAgCu samples. Decreasing the isothermal hold temperature from 200°C to 195°C reduced the time to solidify most of the solder balls by a factor of three (i.e. after one reflow, at a temperature of 200°C, approximately 45 solder balls had solidified after 225 minutes, while at a temperature of 195°C, it took only 75 minutes for the same number of solder balls to solidify; Fig. 1.39). An increase in the isothermal temperature to more than 210ºC resulted in no solidification of solder balls during a seven-hour isothermal hold. On the other hand, at temperatures less than 185ºC, a number of solder balls solidified before time zero of an isothermal hold, i.e. during cooling from the melt (cf. Fig. 1.37).

Solidification rates of Sn in a given set of liquid SnAgCu samples were higher during the second isothermal hold than during the first isotherm. For instance (Fig. 1.39), at a temperature of 195°C, during the first isothermal hold it took approximately 75 minutes for half of the samples to solidify, while during the second isothermal hold (cf. Fig. 1.39) of the same samples, at the same temperature, it took less than thirteen minutes for half of the solder balls to solidify. In a similar vein, Fig. 1.39 shows that during the first isothermal hold at 200°C some solder balls were still in the liquid state after a 400 min isothermal hold, while during the second isotherm all of the solder balls had solidified after 160 min (Fig. 1.39).

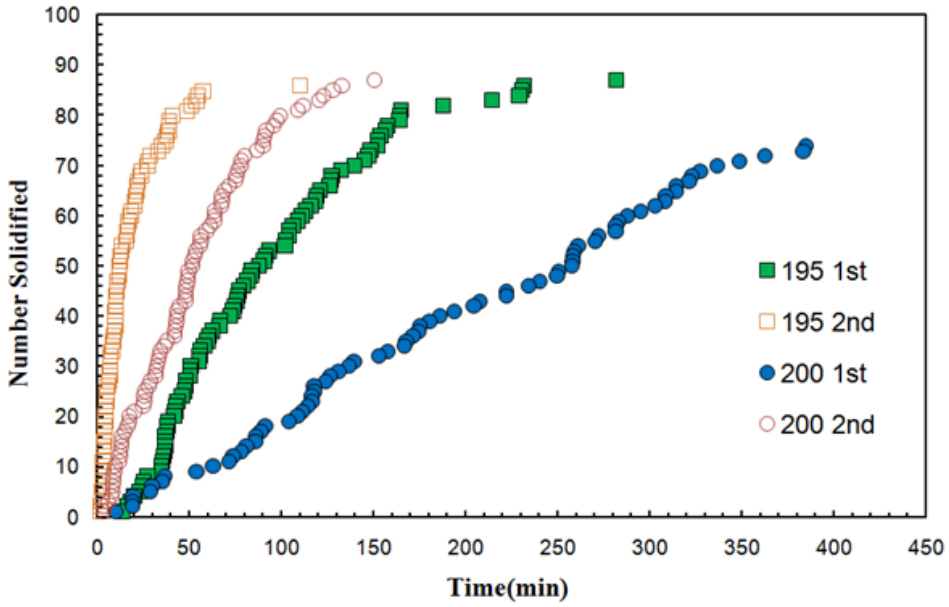

Figure 1.39: Plots of number solidified solder balls versus time for different flip chip samples during isotherm for 420 minutes at temperatures of 195°C and 200°C after first and second isotherms, as noted in the figure.

Optical and Electron Micrographs

Different cross sectioned, SnAgCu flip chip solder balls were examined by means of optical microscopy at five different stages of a given thermal history (e.g. (a) through (e) in Fig. 1.40, corresponding to points A through E in Fig. 1.36, respectively). The optical image of an as received sample in Figure 1.40(a) reveals a microstructure typical of SnAgCu solders (which consist of β-Sn and precipitates of Ag_3Sn and Cu_6Sn_5) [1.68-1.72]. A different phase can be seen at the substrate/SnAgCu solder interface, with indication that this phase grows somewhat thicker during subsequent heating (Figs. 1.40(a) – (e)). Optical micrographs of cross sections of solder balls which had been cooled to room temperature after relatively long, 420 minute isothermal hold at 195°C (Figures 1.40(c) and 1.40(e)), revealed relatively large (approximately 40 micron in length) precipitates.

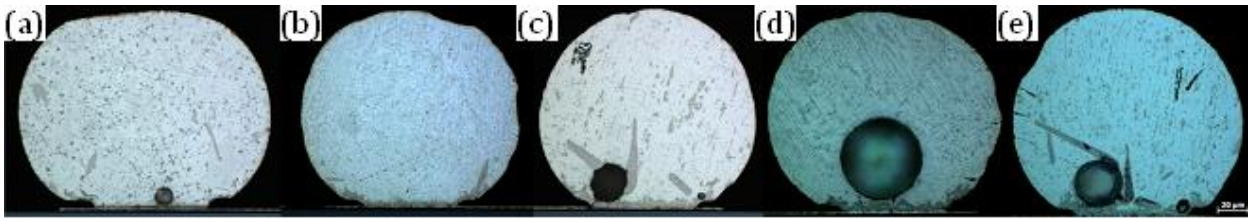

Figure 1.40: Bright field optical micrographs of prepared sample (in Fig 1.38). Few large precipitates are observed in the as received sample (a) and samples after reflow (b and d). On the other hand big precipitates of Ag_3Sn and Cu_6Sn_5 were observed in the matrix of samples after reflow (c and e)

Optical micrographs with crossed polarizers are presented in Figs. 1.41 and 1.42 for cross sections of different solder balls which had been subjected to various thermal histories ((a) through (e) in Fig. 1.41 and 1.42, corresponding to points A through E in Fig. 1.36, respectively). In previous work, similar patterns of contrasting regions in optical micrographs with crossed polarizers for different SnAgCu solder balls have been identified with six-fold, multiply twinned Sn [1.74-1.77]. The finer scale patterns (prevalent in Fig. 1.42(a)) are generally referred to as interlaced Sn, while the Sn grains of larger scale (e.g. in Figs. 1.42(c) and 1.42(e), solder balls isothermally solidified at 195°C) are closer to previously observed beach ball patterns [1.72, 1.74-1.77]. Cross sections of as-received solder balls generally revealed large interlaced regions (Fig. 1.42(a)), while solder balls which had solidified at a temperature of 195°C (Figs. 1.43(c) and 1.43(e)) primarily consisted of relatively large Sn grains. The solder balls which had solidified at lower temperatures during cooling after a reflow (Figs. 1.43(b) and 1.43(d)) revealed a mixture of interlaced and large Sn grains [1.77].

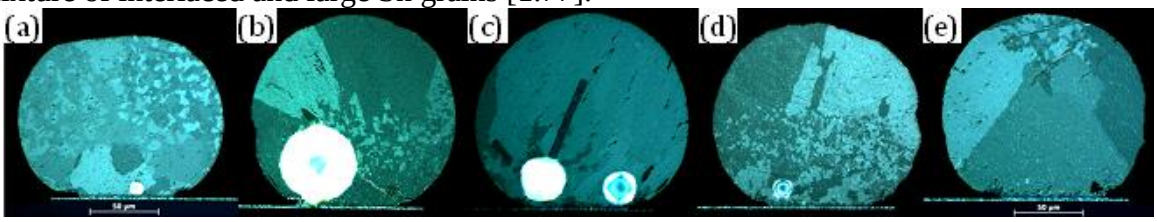

Figure 1.41: Optical micrographs with crossed polarizers of prepared sample (in Fig. 1.38). Samples that were subject to reflow only (a, b, and d) show different microstructures compared to samples that have been isothermally solidified (c and e).

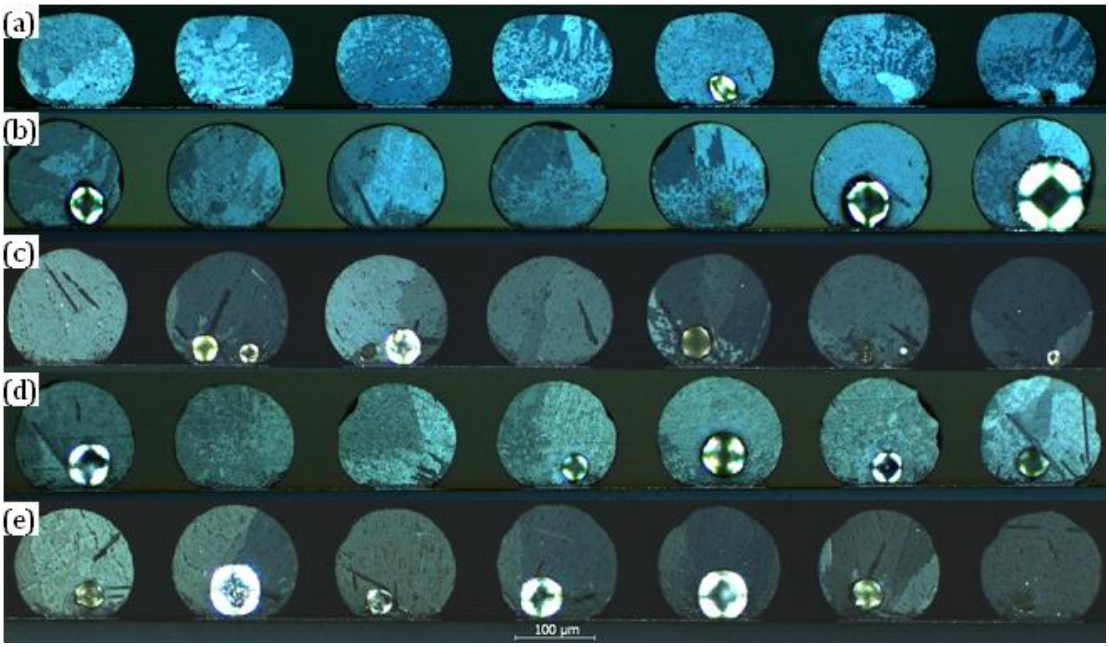

Figure 1.42: Cross polarized images of prepared sample (in Fig. 1.38). Same observation as Fig. 1.39, the difference in microstructure of samples is resulted from different solidification temperatures. The undercooling for reflowed (a), (b), (d) samples was much larger than that of isothermally solidified samples (c) and (e).

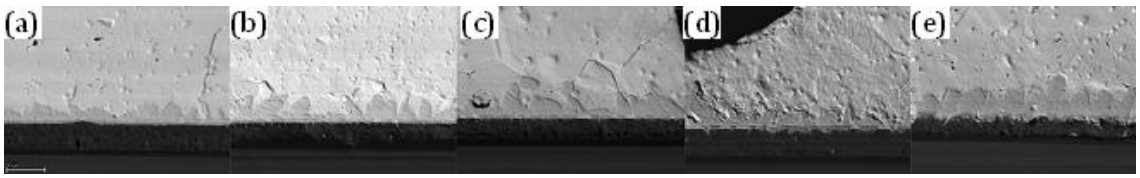

Figure 1.43: SEM images of prepared sampe (in Fig. 1.36). The images show the microstructure of prepared samples on Ni(V)/Al/Si substrate. The composition of IMC in as received sample is Cu_6Sn_5 with a small amount of Ni. The amount of Ni in the IMC will increase and as a result the composition will shift to $(Cu\ Ni)_6Sn_5$.

Different cross sectioned, SnAgCu flip chip solder balls were examined by means of electron microscopy at five different stages of a given thermal history ((a) through (e) in Fig. 1.43 and 1.44, corresponding to points A through E in Fig. 1.36, respectively). Due to their different atomic numbers, it is possible to distinguish bright Ag_3Sn from darker Cu_6Sn_5 particles in these backscattered electron microscopy images. Confirmation of this supposition was confirmed at various points in the bulk of the solder by means of chemical analysis using energy dispersive analysis (EDS). It was confirmed that Sn is in fact the major constituent of the solder matrix. Small precipitates with compositions corresponding to Ag_3Sn were visible in all five solder balls. Large IMCs (bigger than 20µm in length) with compositions close to that of the stoichiometric compound, Cu_6Sn_5, were most commonly found in samples C and E (Fig. 1.43). Fig. 1.45 provides an intermediate magnification scanning electron microscopy micrograph of a sample from set D which reveals large precipitates near the solder/substrate interface.

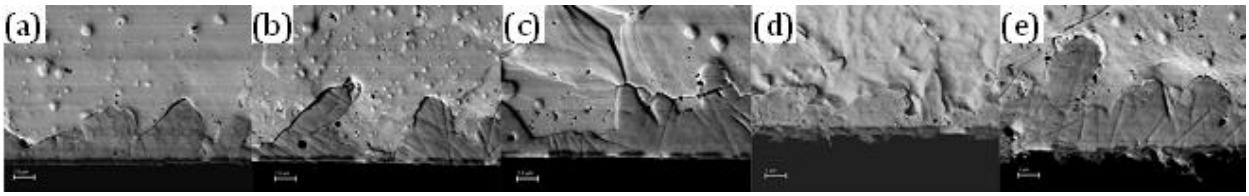

Figure 1.44: SEM images of prepared sample (in Fig. 1.36) at higher magnification. The Ni(V) looks almost intact in as received sample (a). The presence of white patches of Sn is observed even after the first reflow (b). The UBM layer will be consumed during the subsequent reflow and isotherms (c – e).

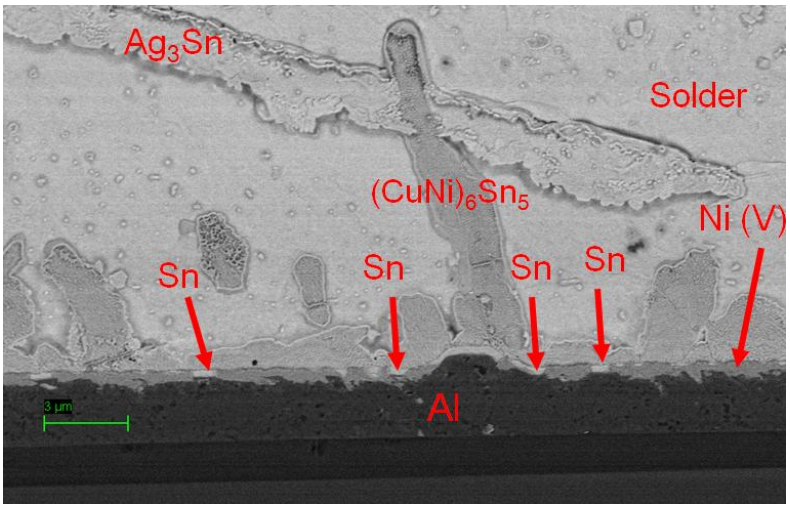

Figure 1.45: SEM image of prepared sample D at higher magnification. EDS results proved the presence of Sn in the UBM layer.

Microstructure evolution

The Sn grain morphology of these SAC solder balls was observed to be correlated with the solidification temperature of each ball; solder balls which undercooled the most revealed more interlaced Sn than those which solidified at higher temperatures [1.69, 1.74, 1.77]. The solder balls which were isothermally held and solidified at fairly high temperature (e.g. 195^{o}C in Fig. 1.42(c) and Fig. 1.42(e)) revealed Sn grain morphologies which primarily consisted of large Sn grains. In contrast, solder balls which were cooled from the melt at a rate of 60^{o}C/min after reflow and solidified at or near a temperature of approximately 172^{o}C, such as those of Fig. 1.42(b), generally displayed a large region of interlaced Sn; up to half of the visible area of the solder balls in Fig. 1.42(b) are interlaced. Solder balls which were cooled from the melt at a rate of 60^{o}C/min after two reflows and solidified at or near a temperature of approximately 183^{o}C generally displayed a smaller but significant region of interlaced Sn (Fig. 1.42(d)). Finally, all the as-received solder balls (Fig. 1.42(a)) revealed an interlaced Sn structure.

The observation of a correlation between the Sn grain morphology of SAC solder balls and the solidification temperature of the solder ball upon cooling from the melt [1.77] is consistent with previous observations of a correlation between Sn grain morphology in SnAgCu

solder balls and their size [1.72]. Beach ball type Sn grain morphologies are generally observed in larger (500 micron diameter) SnAgCu solder balls, while interlaced Sn grain morphologies are most generally seen in small (150 micron diameter) SnAgCu solder balls. Previous work has shown an inverse correlation between SnAgCu solder ball size and solidification temperature, for standard cooling rates near 60^{o}C/min [1.71, 1.77]. That is to say, larger solder balls generally solidify near 200^{o}C, and flip chip solder balls solidify closer to 175^{o}C. Thus, these previous observations are consistent with a correlation between the beach ball Sn grain morphology and higher solidification temperatures (temperatures greater than approximately 180^{o}C), and with a correlation between the interlaced Sn grain morphology and lower solidification temperatures, as seen in Fig. 1.43. Arfaei et al. showed that both the interlaced and the beach ball Sn grain morphologies are consistent with growth from a six fold, cyclically twinned nucleus. The change in the Sn grain morphology was correlated with changes in growth directions with temperature [1.77].

The interface between the SAC solder and the UBM in a given flip chip solder joint systematically evolved during a given thermal history in our laboratory [1.86-1.88]. The original UBM in these flip chip solder balls consisted of a Cu/Ni(V)/Al tri-layer (cf. Fig. 1.36); copper was consumed and dissolved in the molten solder during the initial reflow by the vendor (Fig. 1.36(a)) The SEM images of the cross section of an as-received sample (Figs. 1.44(a) and 1.45(a)) shows a distinct Ni(V) layer with a thickness of about 350 nm, just below a $(CuNi)_6Sn_5$ intermetallic layer. This Ni(V) layer initially acts as a barrier to interdiffusion between Sn and Al. After the first reflow in our laboratory, the morphology of the Ni(V) layer starts to change; white patches are visible inside the Ni(V) layer (they could also be observed in all of the other solder balls, B to E, Figs. 1.43-1.45). Previous studies of similar reactions concluded that similar white patches consist primarily of Sn (cf. Fig. 1.36) [1.86-1.88]. It was reported that Ni(V) is replaced by Sn from the matrix that penetrates through the channels formed between the IMC grains [1.86-1.88]. Furthermore, in the present study it is evident in the backscattered images that these white patches approach the Al interface (Fig. 1.44). This occurs as early as after the first reflow in our laboratory (Figs. 1.43(b) and 1.44(b)), while Sn in the Ni(V) layer in contact with Al is much more prevalent after further heating and cooling (Figs. 1.43(c-e) and Figs. 1.44(c-e)). Thus, while Al was able to dissolve in to Sn as early as after the first reflow in our laboratory, further interpenetration at the Al interface, with more channels open to dissolution of Al in to Sn, occurred after the second reflow ((Figs. 1.43(d-e) and Figs. 1.44(d-e)) [1.86-1.88].

The morphology and composition of intermetallics at the solder/Ni(V) interface of different solder joints were examined (Figs 1.43-1.45). Energy-dispersive X-ray spectroscopy (EDS) indicated that the intermetallic compound at the SnAgCu solder/Ni(V) interface in the as received sample had a composition of 47.5 atomic percent Sn, 4.9 atomic percent Ni and 47.4 atomic percent Cu, consistent with the formation of $(CuNi)_6Sn_5$. This layer had a scalloped morphology, as previously observed [1.86-1.88]. After reflow, the Ni concentration in the $(CuNi)_6Sn_5$ layer was observed to slightly increase; EDS measurements revealed a concentration of 5.6 atomic percent Ni after one reflow (point B in Fig. 1.36) and a concentration of 7.9 atomic percent after the second reflow (point D in Fig. 1.36). The presence of Ni in the intermetallic compound in the as received sample is consistent with dissolution of Ni in to the solder matrix during manufacture, as would be expected, given that the entire Cu layer reacted during manufacture [1.86-1.88].

Isothermal Solidification

The observed rates of nucleation of Sn in SAC solder joints and their variations with temperature can be compared to classical nucleation theory. It is generally observed that the rate of nucleation of a supercooled liquid increases exponentially as the degree of undercooling increases, for undercooling of up to $0.2T_m$ and more [1.78-1.81, 1.89, 1.90]. In fact, classical nucleation theory [1.89, 1.90] provides an expression for the heterogeneous nucleation rate, I_{het}, in an undercooled liquid which indicates that these rates rapidly increase as undercooling initially increases:

$$I_{het} = I_o \exp\ \frac{-W}{\Delta T^{\,2}\, T} = \frac{nKT}{h}\ exp\ \frac{-\Delta F_A}{KT}\ \exp[\frac{-16\,\pi\,\gamma^3\,T_m{}^2\,S(\theta)}{3\Delta H_f^2\ \Delta T^{\,2}\,KT}] \quad \text{nuclei } m^{-3}\,s^{-1} \quad (1.1).$$

Here n is the number of atoms in the solid-liquid interface per square meter, ΔF_A is the free energy of activation for transport across the solid-liquid interface, γ is the interfacial energy between crystal nucleus and liquid, T_m is the melting temperature in Kelvin, ΔH_f is the heat of fusion per unit volume, and $S(\theta)$ is the shape factor, determined by the wetting angle, θ.

Here $W = \frac{16\,\pi\,\gamma^3\,T_m{}^2\,S(\theta)}{3\Delta H_f^2\,K}$. For a spherical cap shaped nucleus, $S(\theta)$ is given by:

$$S\ \theta\ =\ 2 + cos\theta\ \ (1 - cos\theta)^2/4 \quad (1.2).$$

Examination of the solidification times of a large number of similarly prepared solder balls, held at a constant temperature after undercooling from the melt, provides the means to measure rates of nucleation for Sn in these SAC solder balls [1.79, 1.91, 1.92]. At a given temperature, the rate of nucleation, R, in N similar solder balls in the liquid state at time t can be written in terms of the volume, ν, of a single sample and the heterogeneous nucleation rate, I_{het}:

$$R = N\, I_{het}\, \nu = N\, \alpha \qquad \text{where } \alpha = I_{het}\, \nu \quad (1.3)$$

As the growth rate of the solid Sn in one sample after nucleation is very high, it is assumed that only one nucleant forms in each sample, and the measured rate of solidification of solder balls, dN/dt, can be assumed to be proportional to I_{het}, and to N:

$$dN/dt = -\,\alpha\, N \quad (1.4)$$

A simple calculation leads to:

$$\ln (N/N_t) = -\,\alpha\, t \quad (1.5)$$

where N_t is the total number of solder balls in the liquid state at t = 0.

Plots of $-\ln(N/N_t)$ versus time, at a given constant temperature, were constructed with the solidification data from each set of flip chip SAC solder balls (Figs. 1.46(a) and (b)). These plots are for isothermal holds after one reflow in our laboratory (Fig. 1.46(a)), or after two reflows in our laboratory (Fig. 1.46(b)). Linear fits to each data set were performed, and a value of α (where $\alpha = I_{het}\nu$) for each isothermal holding temperature was determined from the slope of the line (cf. Eq. 1.5). In accordance with Eq. 1.1, Fig. 1.47 shows plots of log I_{het} versus $[1/ (T \times \Delta T^2)]$ for the values of α calculated from isothermal holds in the range of 185 to 205ºC, for both the first and the second isotherms at a given temperature. As can be seen in Fig. 1.47, nucleation rates of Sn in liquid SnAgCu solder balls were higher during the second isotherm than during the first isotherm. Each set of data was fit with a straight line; the slope corresponding to the first

isotherms was 1.6×10^5 K^3, and that for the second isotherms was 8.9×10^4 K^3, while the value of the y intercept for both plots was 2×10^9 $m^{-3}s^{-1}$.

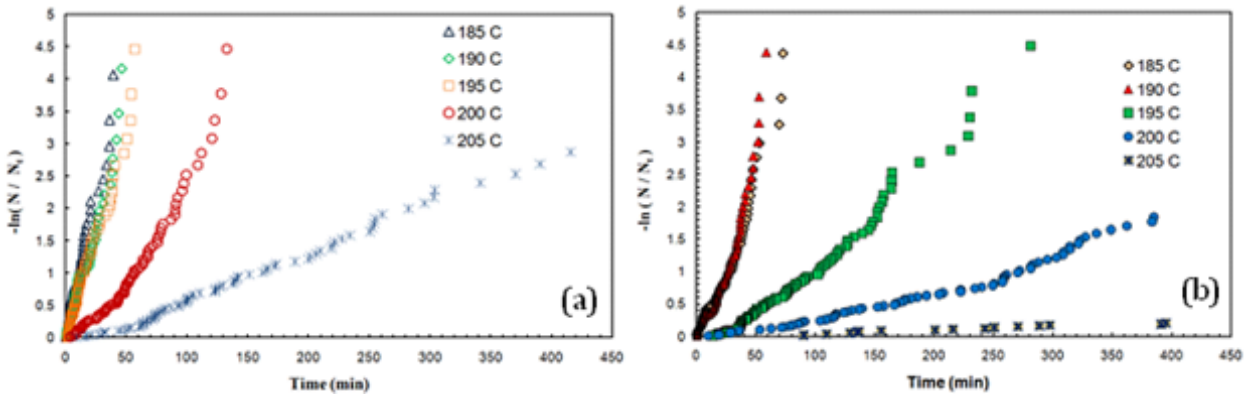

Figure 1.46: Plots of $-\ln(N/N_t)$ versus time for different flip chip samples, where N is the number of samples in the liquid state, and N_t is the number of samples in the liquid state at time t=0. The samples were heated up to a temperature of 250°C and then cooled to a given temperature and annealed for up to 420 minutes. Specific anneal temperatures are indicated in the figure. (a) is after the first isotherm in our laboratory and (b) is after the second isotherm in our laboratory.

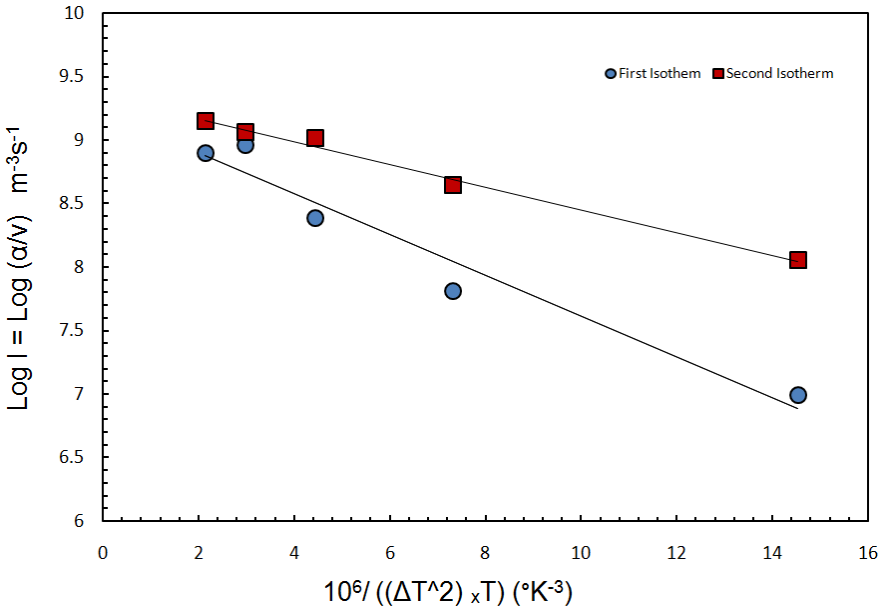

Figure 1.47: Plots of $-\ln(\alpha)$ versus $1/(\Delta T^{-2})$ T for different flip chip samples. The nucleation rate is faster in the second isotherm and it generally decreases by increasing the isothermal temperature. The slope of each line represents the value of W.

The data and fits of Fig. 1.47 indicate that the equations of classical nucleation theory (cf. Eq. 1.1) provide a means to characterize nucleation rates in this system. The equations corresponding to the straight line fits in Fig. 1.47 reflect with a fair degree of precision the temperature dependence of the nucleation rate; logI was found to vary linearly with respect to

$1/(\Delta T^2 T)$, consistent with Eq. 1.1. Thus an expression can be provided for nucleation rates, and for calculation of solidification temperatures, via standard techniques [1.79, 1.91, 1.92], for similar solder balls in the field. In fact, although classical nucleation theory considers a single component system and assumes that the nucleus has the same structure as the equilibrium solid, adaptations of this theory for the case of multicomponent systems (e.g. SAC) generally do result in equations of the same general form as Eq. 1.1 [1.90]. Such treatments of multicomponent systems assume that the system will utilize the degree of freedom provided by the composition to minimize the energy barrier to nucleation, such that the nucleus may have a different structure than the equilibrium solid. Such models assume that the structure of sub critical clusters in muliticomponent supercooled liquids is generally different than that of the equilibrium solid [1.94-1.98].

The nucleation rate of Sn in these SnAgCu samples was sensitive to thermal history. A distinct change in the nucleation kinetics (a 44% decrease in the value of W in Eq. 1.1) occurred after the second reflow (cf. Fig. 1.47). This observed increase in the nucleation rate of Sn in these SAC samples is most likely associated with the increase in the level of impurities, such as Al, in the solder. Previous work has shown that the introduction of Al, or of Ni, in to SnAgCu reduces the degree of undercooling of the SnAgCu melt upon cooling from the melt [1.83, 1.84]. In the present work, it is evident that some Ni and Al impurities had dissolved in to solder before the first isothermal hold, and that the second reflow allowed additional Al and Ni atoms to diffuse in to the SnAgCu. Ni had dissolved in to the SnAgCu solder in the as-received samples, as these samples already had $(CuNi)_6Sn_5$ in contact with the SnAgCu solder (Fig. 1.43-1.45). This $(CuNi)_6Sn_5$ phase was in contact with the SAC solder during the entirety of the first isothermal hold. Furthermore, some Al may have been allowed to diffuse in the solder matrix during the first reflow, as patches of Sn were observed in contact with the Al after the first relow (point B). An additional reflow could allow the amount of Al in the Sn to increase (Figs. 1.44(d, e)). The implication is that the nucleation rate of Sn in these solder alloys is sensitive to the concentration of impurities such as Ni and Al, at least over some range of concentrations.

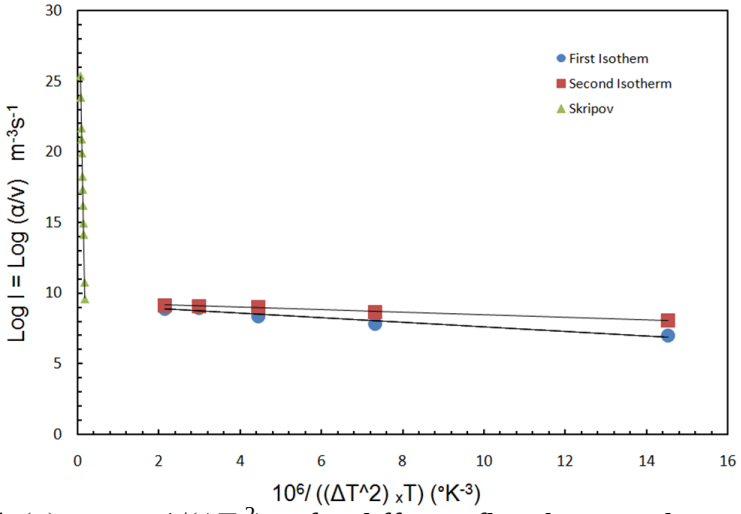

Figure 1.48: Plots of $-\ln(\alpha)$ versus $1/(\Delta T^{-2})$ T for different flip chip samples with the subset of data from Skripov's experiment.

The observed rates of nucleation of Sn in SnAgCu in undercooled flip chip solder joints are distinctly different than those of Sn in undercooled, high purity Sn melts [1.78-1.81, 1.93]. Data from previous work (describe as homogeneous nucleation by Skripov et al.) for high purity

Sn samples are represented in Fig. 1.48 with a best fit line [1.93]. Extrapolations of this line to temperatures of the present study indicate negligible nucleation rates for high purity Sn samples such as those utilized in Skripov's study at temperatures near 200°C. Furthermore, the temperature dependences of nucleation rates of Sn in small, high purity Sn droplets and in SnAgCu flip chip solder joints are very different (Fig. 1.48). The slope of the line fit to the data corresponding to high purity Sn samples is approximately 1.4×10^8 K^{-3}, while for the present study with SnAgCu solder balls on UBM layers, the observed slopes were 1.6×10^5 K^{-3} and 9.0×10^4 K^{-3}, for solder balls in the first and second isothermal hold, respectively. The linear fits for the data for the dependence of the nucleation rate on temperature both had similar values of y-intercepts, 2×10^9 $m^{-3}s^{-1}$, very different from measured values of y intercepts for similar plots for the data from high purity Sn droplets, approximately 10^{37} $m^{-3}s^{-1}$.

The temperature dependence of the nucleation rate for the SAC solder balls provides some insight in to the nature of the nucleation mechanism of Sn in these solder balls. Classical nucleation theory predicts that the value of the prefactor, N_o in Eq. 1.1, will be approximately 10^{37} $m^{-3}s^{-1}$. Within the context of classical nucleation theory, if nucleation occurs only at certain surfaces (heterogeneous nucleation), then the rate of nucleation should be multiplied by a factor reflecting the fraction of atoms which can comprise nucleation surfaces; large reductions in the prefactor N_o (many orders of magnitude) have been previously observed and associated with heterogeneous nucleation[1.79, 1.80, 1.91]. Given the large impurity content and exposure to oxygen of the SAC samples under study, it is reasonable to expect that the Sn nucleation events observed in the present study were heterogeneous. The observed value of the prefactors, 2×10^9 $m^{-3}s^{-1}$, is in fact much lower than 10^{37} $m^{-3}s^{-1}$. But if one assumes that this large difference in N_o is due solely to a reduction in the number of the atoms which potentially may nucleate the solid phase, (i.e. to the fraction of atoms at heterogeneous nucleation surfaces), then the indication is unphysical, i.e. that less than one atom per sample comprises such surfaces. It may be that the observed reduction in N_o is combined with other factors that also reduce the value of N_o. In fact, previous calculations for multicomponent systems [1.90, 1.94, 1.96] have indicated that while the equations for nucleation rates have similar forms as those indicated by classical nucleation theory, specific values of terms in corresponding equations are different, such as the prefactor in Eq. 1.1. Thus the small value found for these SAC solder solder balls (cf. y intercept in the plots of Fig. 1.48) may also be the result of the initial growth of nuclei of different structure than that of the equilibrium solid.

The large difference between the values of W (cf. Eq. 1.1 and the slopes in the curves in Fig. 1.48) for the high purity Sn samples of Skripov's study and the SAC solder solder balls of the present study is difficult to explain, in the context of classical nucleation theory (cf. Eq. 1.1), with only changes in the wetting angle θ. Although variations in θ result in large changes in W (cf. Eq. 1.2), even if one assumes that nucleation events in Skripov's study of Sn were homogeneous (that S = 1 in Eqs. 1.1 and 1.2 for these samples) the observed difference in slopes still indicates quite small values of θ for curves corresponding to the SAC solder balls. Specifically, a variation of S(θ) from a value of one (assuming homogenous nucleation of Skripov's samples) to 0.0021 ($\theta = 19^o$) would be required to account for the decrease in the slope observed. A similar analysis for the data of the second isotherm results in a value of S(θ) equal to 0.0012 ($\theta = 16^o$). Such angles are much less than those observed experimentally (approximately 30^o) for the contact angle of SnAgCu on Cu on a much larger length scale [1.99, 1.100].

It is more likely that the large difference in slopes in Fig. 1.D16 for Skripov's samples and those of the present study is due to changes in other factors that make up W in Eq. 1.1, in addition to a change in θ. The energy of formation of a nucleus of a different structure than equilibrium beta Sn in this multicomponent solder system, such as a six fold, cyclically twinned nucleus [1.74], with Al or Ni atoms present in relatively high concentrations, would be different than that of a pure beta Sn nucleus. In this context (cf. Eq. 1.1), the implication is that the nucleus adopts a structure with a larger value of ΔG_v than that of the equilibrium solid, in order to minimize the energy barrier to nucleation.

Sn Nucleation Rate Quantification Section D Summary

The isothermal nucleation of Sn from the melt in commercial SnAgCu flip chip solder joints was monitored at a number of different temperatures. Nucleation rates for 440 solder balls after one reflow were well epitomized with an expression based upon classical nucleation theory. After an additional reflow, the nucleation rates of the same 440 solder balls were observed to be faster; an equation of the same form, based upon classical nucleation theory, was found to adequately reflect the new nucleation kinetics, but with a lower energy barrier. This change in nucleation kinetics was correlated with a probable introduction of additional Al and Ni in to the Sn matrix. While the nucleation kinetics in all of these solder balls were consistent with the general form of classical nucleation theory, calculated parameter values were dramatically different than this single component theory predicts. Variations were consistent with previous considerations of multicomponent systems that assume that the structure of the nucleus is different than the equilibrium solid, such as a six fold cyclically twinned nucleus. The Sn grain morphology of these SnAgCu solder balls was also consistent with growth from a six fold cyclically twinned nucleus.

E. Conclusions

We have established a quantitative, predictive capability of the microstructure of near eutectic SnAgCu solder joints, in particular precipitate spacing and Sn grain morphology. Nucleation kinetics have been quantified through direct calorimetric measurements in combinatorial experiments at fixed temperatures for a number of different metallizations, solder compositions and geometries. We have identified the equation for this process, found specific values for a number of different solder joints, and shown that it works reliably.

The effects of reflow times and temperatures, as well as cooling rate, on the size, composition and distribution of precipitates in the bulk of the solder have been characterized as well (Fig. 1.49 and 1.50). An understanding of this is linked to the dissolution of metals and formation of intermetallics at interfaces, as these processes tend to add to and/or deplete the solder of certain species. Our studies have shown that small variations in peak reflow temperature to lead to marked changes in the precipitate distributions, as do variations in the solidification temperature. Any of these effects may cause significant changes in the initial mechanical properties of the solder. We have identified the equations to characterize precipitate size versus time and temperature for these reflow processes. For instance, for SAC305 solder $\lambda_o^2 = 0.17 + 0.26/(dT/dt)$.

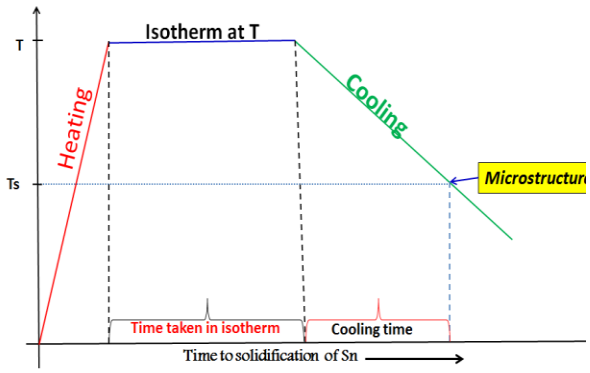

Figure 1.49: The melting and solidification processes in the reflow profile strongly affect solder joint microstructure. In this sketch of temperature, T versus time the solidification temperature, Ts, is noted.

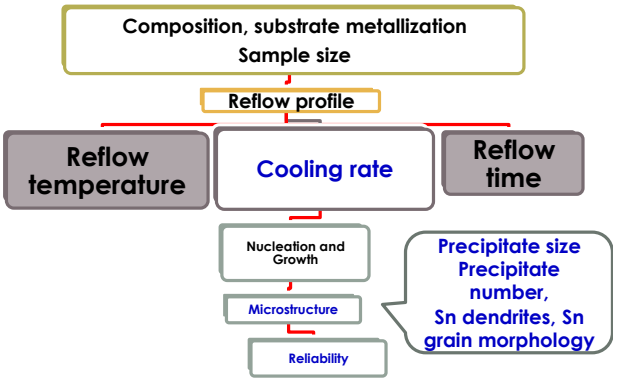

Fig. 1.50: The effects of original solder joint microstructure and composition and geometry in conjunction with the thermal history of the solder joint determine the sample microstructure. These dependencies can be quantified.

Task 2: Microstructure/Properties vs. Microstructure

Professor Dutta (Washington State University) is responsible for this task. The subtasks are here as follows: (2.1) Identify primary microstructural parameters, and develop unified coarsening model for aging and thermo-mechanical cycling; (2.2) Correlate Mechanical properties (creep and fracture) with microstructural coarsening.

One PhD student, Mr. Babak Talebanpour (expected graduation: May 2015) is involved in this project. Another student, Ms. Zhe Huang, who completed her PhD in August 2013, worked on this project as part of her dissertation. Two assistant research professors, Dr. Praveen Kumar and Dr. Uttara Sahaym, also worked on this project during 2009-2011 and 2011-2013, respectively.

Sub-Task 2.1: Microstructural characterization and coarsening kinetics

Technical Approach

Sample preparation and treatment: Experiments were conducted using two SnAgCu based lead-free solder alloys, Sn-1.0wt%Ag–0.5wt%Cu (SAC 105) and Sn-3.0wt%Ag–0.5wt%Cu (SAC 305). The samples were of cylindrical shape with 5mm diameter and 5mm height. In order to prepare the samples, SAC alloys were melted in graphite crucibles with inner diameter of 5mm and length of 12mm. The crucibles were heated to a reflow temperature of 260°C, kept at this temperature for 10 minutes, and then rapidly cooled by placing them over an aluminum chill-plate partly submerged in liquid nitrogen. The resulting cooling rate was approximately 10°C/s. The cast samples were then cut using a low speed diamond saw to produce cylindrical test specimens of 5mm length. Following casting and subsequent machining, the samples experienced the following thermo-mechanically excursions: (i) isothermal aging (IA) at 150^{o}C at ~10^{-4}Torr pressure for 110, 194, 220 and 330 hours and (ii) thermo-mechanically cycling (TMC) between -25^{o}C and 125^{o}C for 100, 200, 600 and 800 cycles with an imposed shear strain (γ) of 0.196 per cycle. The TMC experiments were conducted by affixing the sample to a bimetallic frame made of Al and Invar, and cycling the temperature. A schematic of the bimetallic frame is shown in Figure 2.1 [2.1]. The difference between the thermal expansion coefficients of Al and Invar (α_{Al} = 23 x 10^{-6}/K and α_{Invar} = 1.2 x 10^{-6}/K) resulted in loading of the solder sample in shear, imposing a shear strain proportional to the temperature excursion ΔT (=T-$T_{ambient}$).

Microstructural analysis: Following thermo-mechanical excursions, samples were metallographically polished to a 0.05μm finish to reveal the microstructure. The sample microstructures were characterized using scanning electron microscopy (SEM), followed by direct measurement of precipitate sizes for statistical analysis. The microstructural parameters measured are shown in Figure 2.2. For observing the impact of the isothermal aging on the precipitate coarsening, SEM micrographs were taken from well-identified regions and then the sample was subsequently aged in high vacuum (10^{-4}Torr) for longer periods of time. After a subsequent isothermal aging treatment, the sample was lightly polished using 0.05μm colloidal silica and SEM micrographs were always taken from the same regions as in the previous stage. Tracing a precipitate size through direct comparison of the micrographs following an additional aging treatment allowed visualization of the mass transport phenomenon during the Ostwald Ripening. *This is the first time that the effect of aging on microstructure coarsening has been studied by examining same regions before and after aging*. TMC excursions were conducted on different samples. To improve the statistics, two batches of samples of each alloy were prepared and tested under overlapping experimental conditions. Proeutectic grain size (D_β), proeutectic colony size (L_β) and the particle size of precipitates (d_p) were directly measured from the micrographs. D_β was measured by linear intercept method. L_β was determined by measured by using: $L_\beta = \sqrt{4A/\pi}$, where A is the area of proeutectic colony. The particle size, d_p was determined by using: $d_p = \sqrt{6A_p/\pi}$, A_p is the area of precipitate.

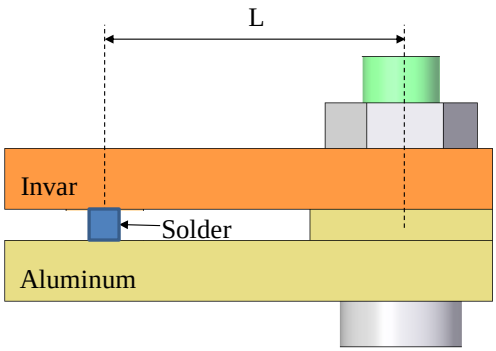

Figure 2.1: A schematic of the bimetallic frame which was used for thermo-mechanical cycling. Shear strain induced in a solder sample is equal to

$\gamma = \alpha_{Al} - \alpha_{invar} \Delta T L/h$

where *h* is the gap between the bimetallic frames.

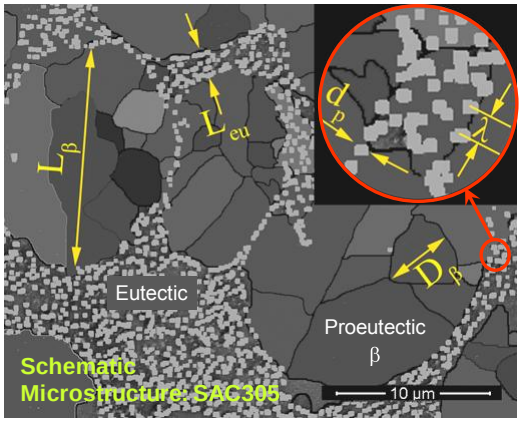

Figure 2.2: Schematic microstructure of SAC 305 showing microstructure parameters measured; Diameter of proeutectic colonies (L_β), Diameter of proeutectic grains (D_β) within proeutectic colonies, Eutectic channel width (L_{eu}), Particle size of precipitates (d_p) within eutectic, Inter-particle spacing between precipitates (λ)

Results and Discussion

Microstructure evolution during various thermo-mechanical excursions

Isothermal aging of SAC 305: Figures 2.3 and 2.**4** show the effect of isothermal aging at 150°C on microstructural evolution of SAC 305 solder alloy. In the as-reflowed condition (Figures 2.3a), the microstructure comprises of proeutectic β-Sn dendrites and an interdendritic eutectic comprising of a fine dispersion Ag_3Sn and Cu_6Sn_5 in β-Sn. Aging leads to progressive loss in the definition of the β-Sn dendrites, with commensurate coarsening of the eutectic leading to a more uniform distribution of precipitates in the solder (Figures 2.3b-d).

Back-scattered electron (BSE) imaging and energy dispersive spectroscopy (EDS) were employed to distinguish between Cu_6Sn_5 and Ag_3Sn particles and it was observed that the number fraction of Ag_3Sn particles was substantially larger than that of Cu_6Sn_5. Furthermore, the Cu_6Sn_5 particles coarsen much faster than Ag_3Sn due to the higher diffusivity of Cu in Sn as compared to Ag in Cu [2.2]. As a result, it is adequate to consider only the coarsening of Ag_3Sn precipitates when quantifying the coarsening of kinetics of SnAgCu solders [2.3]. In order to compare the effects of aging, the median value of the particle size was employed because it better represents the Ag_3Sn particle size (rather than the mean value, which may be affected by a few but rapidly growing Cu_6Sn_5 particles). The particle size monotonically increases with the severity of the aging for these thermo-mechanical excursion conditions.

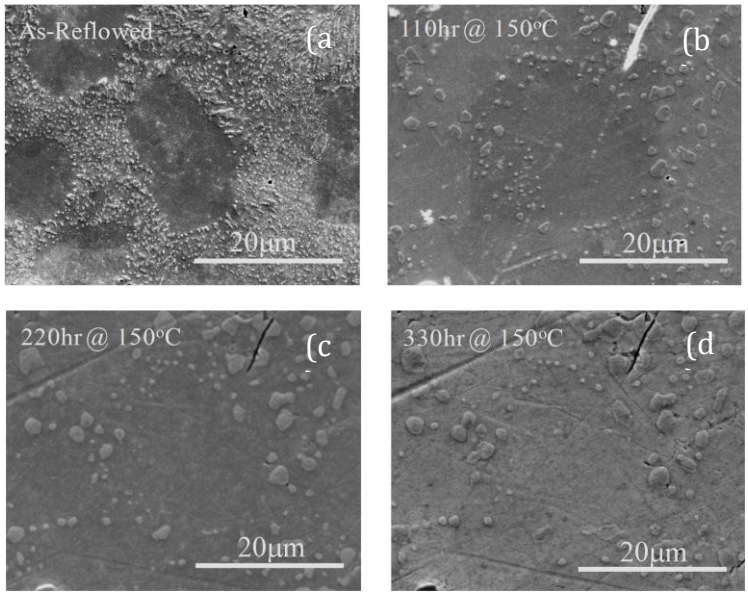

Figure 2.3: Representative secondary electron SEM micrographs from SAC 305 bulk solder sample with different thermal history: (a) as-reflowed, (b) isothermally aged at 150°C for 110 hr, (c) isothermally aged at 150°C for 220 hr, and (d) isothermally aged at 150 °C for 310 hr.

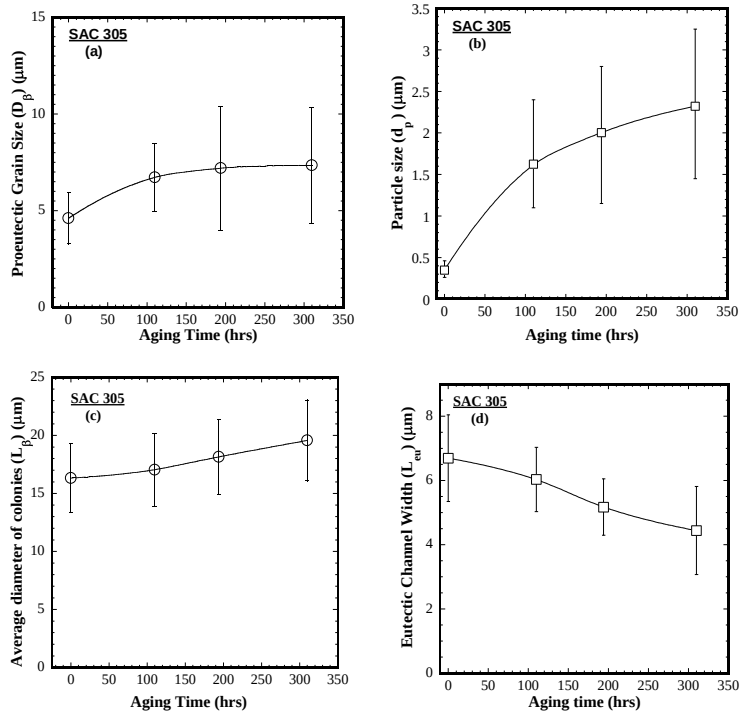

Figure 2.4: Variation of (a) proeutectic grain size, $D_{\square}$; (b) particle size, $d_{\square}$; (c) proeutectic colony size, $L_{\square}$; and (d) eutectic channel width, L_{eu} with elapsed aging time at 150°C in SAC 305.

The β-Sn grain size of SAC 305 increased from ~4.5μm to ~7.5μm and the precipitate size increased from ~0.35μm to ~2.5μm after aging for 310 hr at 150°C. Figure 2.4 shows variations of different microstructural parameters with elapsed aging time at 150°C. Proeutectic

β-Sn colonies coarsen slightly and eutectic channel width shrinks slightly with aging time. β-Sn grain size and Ag_3Sn precipitate size undergo significant coarsening with elapsed aging time.

Isothermal Aging of SAC 105: Figures 2.5 and 2.6 show the effect of isothermal aging at 150°C on microstructural evolution of SAC 105 solder alloy. Like SAC 305, in the as-reflowed condition (Figures 2.5a), the microstructure comprises of proeutectic β-Sn dendrites and an interdendritic eutectic comprising of a fine dispersion Ag_3Sn and Cu_6Sn_5 in β-Sn matrix. Aging leads to progressive loss in the definition of the β-Sn dendrites, with commensurate coarsening of the eutectic leading to a more uniform distribution of precipitates in the solder (Figures 2.5b-d).

Figure 2.6 shows variations of different microstructural parameters with elapsed aging time at 150°C. Proeutectic β-Sn colonies coarsen slightly and eutectic channel width shrinks slightly with aging time. β-Sn grain size and Ag_3Sn precipitate size undergo significant coarsening with elapsed aging time. The β-Sn grain size of SAC 105 increased from ~3μm to ~6μm and the precipitate size increased from ~0.35μm to ~1.4μm after aging for 310 hr at 150°C. As mentioned in the previous section, coarsening of only Ag_3Sn particles was considered.

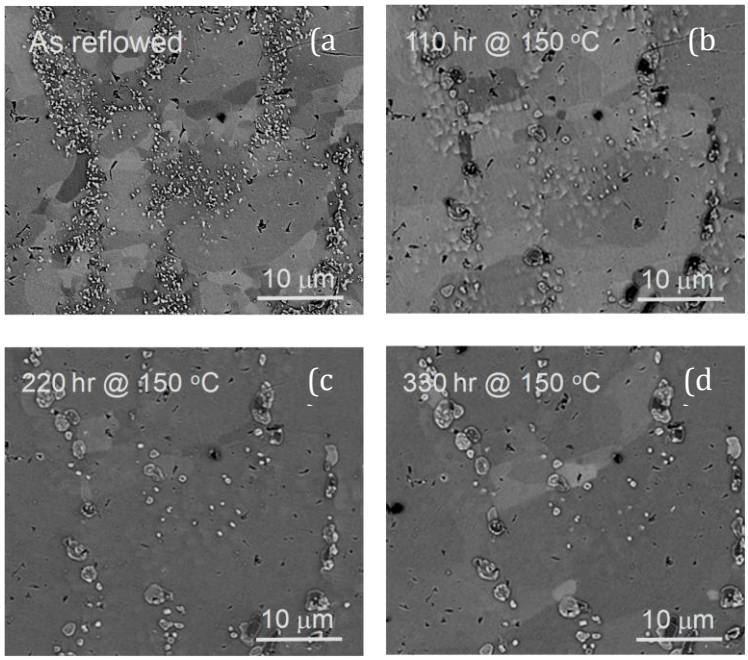

Figure 2.5: Representative secondary electron SEM micrographs from SAC 105 bulk solder sample with different thermal history: (a) as-reflowed, (b) isothermally aged at 150°C for 100 hr, (c) isothermally aged at 150°C for 220 hr, and (d) isothermally aged at 150 °C for 310 hr.

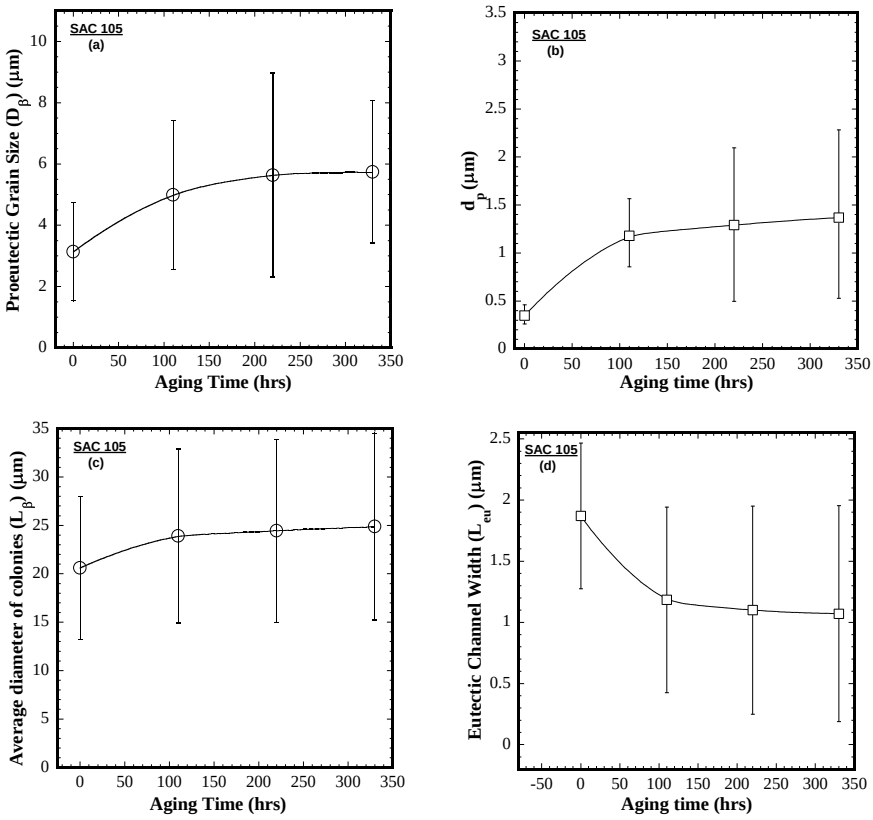

Figure 2.6: Variation of (a) proeutectic grain size, $D_{\square}$; (b) particle size, $d_{\square}$; (c) proeutectic colony size, $L_{\square}$; and (d) eutectic channel width, L_{eu} with elapsed aging time at 150°C in SAC 105.

Unusual recrystallization in eutectic region: In addition to this coarsening, some recrystallization was also observed near the precipitate clusters in the eutectic regions. The recrystallized grains are shown by white arrows in Figure 2.7b. The volume fraction of recrystallized grains is rather small (<10%). This recrystallization occurred within the first 50 hours of aging at 150°C, and then the recrystallized grains underwent relatively little growth, and no new recrystallization occurred, as seen in Figure 2.8. In fact, the number of recrystallized grains appears to decrease because of coalescence of growing grains. It is also noteworthy that the growth of recrystallized grains was more pronounced in the regions adjacent to the prior dense clusters of particles. For example, the grain marked A in Figure 2.7b shows a more pronounced growth as compared to the grain marked B (See Figures 2.7b-d)**.** *This is the very first time such a recrystallization behavior within the eutectic channels has been observed in SAC solder alloys during isothermal aging* [2.4]. However, it is not expected to have any significant effect on the mechanical properties of the solder because the fraction of these recrystallized grains is very small. It is expected that the coarsening of particles will dominate the microstructural effects on mechanical properties.

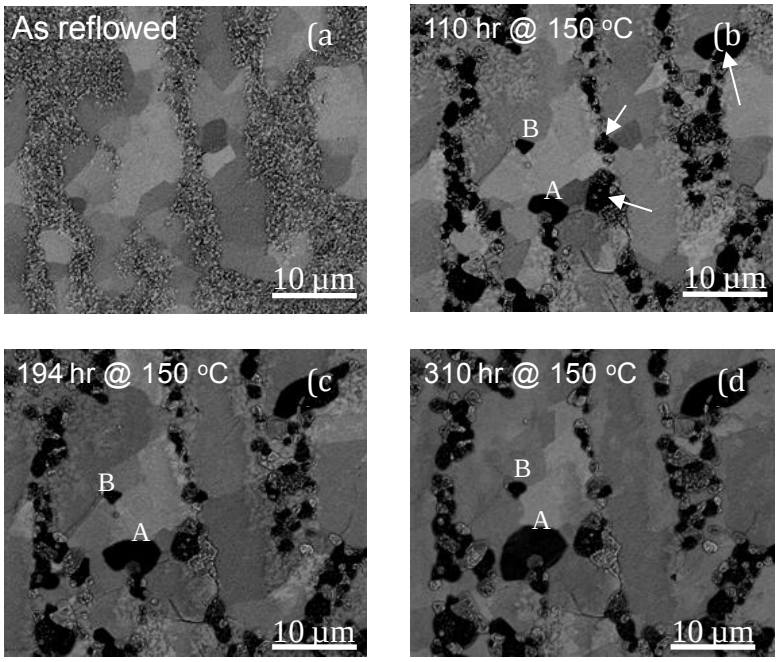

Figure 2.7: Representative backscattered electron SEM micrographs from SAC 305 bulk solder sample with different thermal history: (a) as-reflowed, (b) isothermally aged at 150°C for 110 hr, (c) isothermally aged at 150°C for 194 hr, and (d) isothermally aged at 150 °C for 310 hr. White arrows in (b) indicate some of the recrystallized grains within the eutectic channels. [2.4]

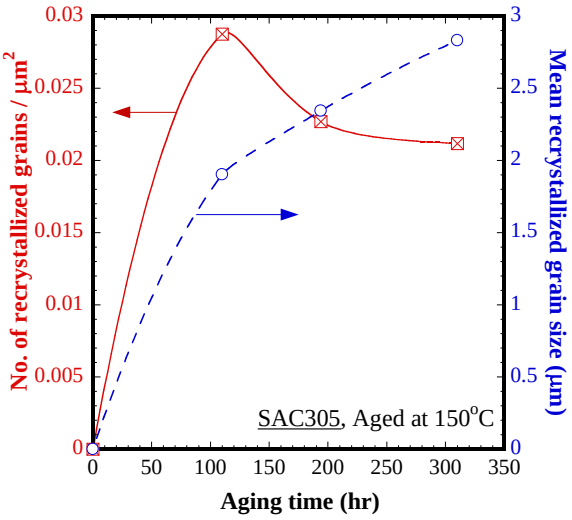

Figure 2.8: Variation of the number of recrystallized grains and the mean recrystallized grain size as function of aging time during isothermal aging at 150 °C. The mean recrystallized grain size, d, was estimated using the following equation: $d^2 = \frac{4}{\pi}\left(\frac{A_{reX}}{N_{reX}}\right)$, where A_{reX} and N_{reX} are the area fraction and areal number density of recrystallized grains at a given aging time. [2.4]

Since all of the recrystallized grains were confined to the prior eutectic channels and growth was more pronounced in the regions where the particles are clustered, it is proposed here that this recrystallization process is promoted by the coarsening of the Ag_3Sn precipitates within the eutectic channels. It is likely that this recrystallization occurs because of particle-stimulated nucleation (PSN) of new grains adjacent to growing precipitates, which may induce strain into the surrounding β-Sn matrix. In general, PSN is seen in alloys containing precipitates that are >1µm in size when they are cold worked at high strain rates (>10^{-2} s^{-1}) and subsequently annealed [2.5-2.8]. Although the solder alloys in the present investigation were not cold worked,

the strain induced by a number of neighboring particles undergoing coarsening could provide sufficient driving force for recrystallization in eutectic channels during aging at 150°C. Similar microstructural evolution was also observed in SAC 105 solder alloys. However, the extent of recrystallization in the prior eutectic channels in SAC 105 was much smaller than that in SAC 305. Furthermore, the volume fraction of Ag_3Sn particles in SAC 105 is lower than that in SAC 305. This is consistent with the hypothesis that recrystallization in eutectic channels is caused by the rapid growth of Ag_3Sn particles in the eutectic channels.

Thermo-mechanical cycling of SAC 305 and 105: Figure 2.9 shows the representative microstructures of SAC 305 from the central region of the samples (defined as 1mm wide, free to deform region along the middle) in as-reflowed condition and following 200 and 800 thermo-mechanical cycles. With increasing number of thermo-mechanical cycles, the particle size of Ag_3Sn increased rapidly up to 200 cycles due to both static and strain enhanced coarsening [2.9]. The average particle size increased from 0.35μm in as-reflowed condition to 0.9μm after 200 thermo-mechanical cycles. Between 200 and 600 thermo-mechanical cycles, eutectic channels break down and the precipitates are observed to have dissolved and re-nucleated, with a fine, even precipitate distribution throughout most of the solder along with few coarse particles. Figure 2.9c shows a representative micrograph of a sample subjected to 800 thermo-mechanical cycles. As shown, the microstructure consisted of a few coarsened pre-existing and growing Ag_3Sn particles along with fine dispersion of re-precipitated particles. Figure 2.10 shows the variation of Ag_3Sn precipitate size and proeutectic grain size with number of elapsed cycles. The shaded area in the graph indicates the regime of Sn grain recrystallization and precipitate redistribution.

After about 200 heating-cooling cycles with a shear strain range of 19.6%, when significant plastic strain has been stored in the solder, the β grains also recrystallized (dynamic recrystallization) resulting in the decrease in the average grain size. This recrystallization was observed in several but localized regions in the solder. Recrystallization during TMC is believed to be the result of formation and rotation of subgrain boundaries [2.10].

Similar aging behavior was observed in SAC 105 alloy. Figure 2.11 shows a representative microstructure after 800 thermo-mechanical cycles consisting of a few coarsened pre-existing Ag_3Sn particles along with a fine dispersion of re-precipitated particles. As observed in SAC 305, the β- Sn grains in SAC 105 also recrystallized and the recrystallization was observed in several but localized regions. The regions showing localized recrystallization are shown by white arrows in Figure 2.11. Figure 2.12 shows the variation of Ag_3Sn particle size and β-Sn grain size in SAC 105 with the number of elapsed cycles. The shaded area in the graph indicates the regime of Sn grain recrystallization and precipitate redistribution. As shown in Figure 2.12, the median particle size decreased after about 200 cycles.

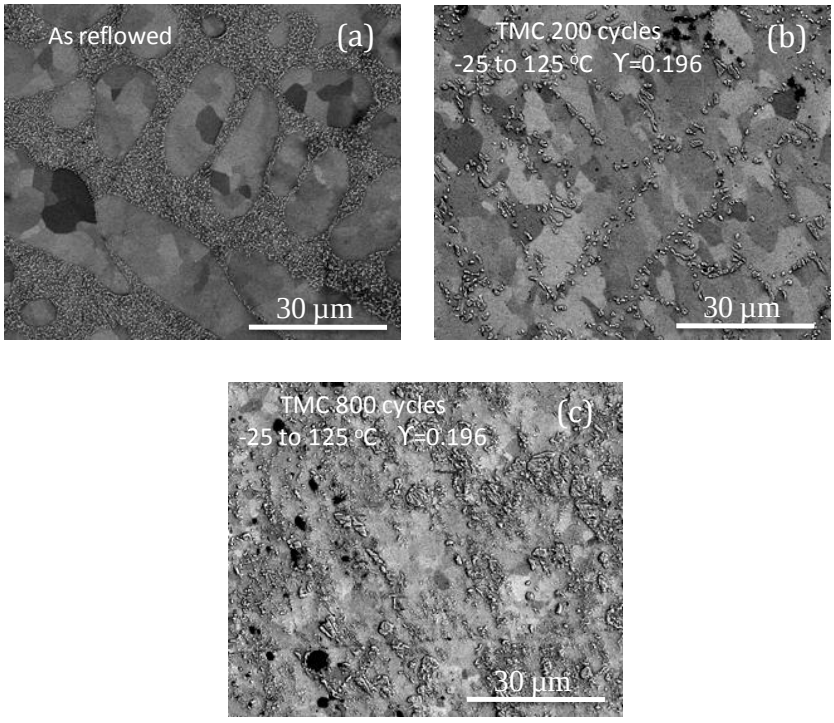

Figure 2.9: Representative micrographs from SAC 305 bulk solder samples subjected to thermo-mechanical cycling between -25 and 125°C and imposed strain of 0.196: (a) as-received, (b) 200 cycles, and (c) 800 cycles. [2.1, 2.4]

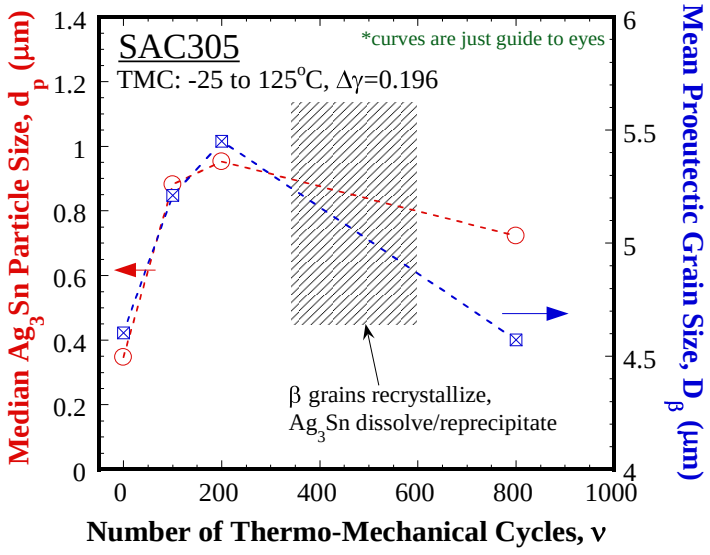

Figure 2.10: Effect of the number of elapsed thermo-mechanical cycles on median Ag_3Sn particle size and average proeutectic grain size of SAC 305 solder allov

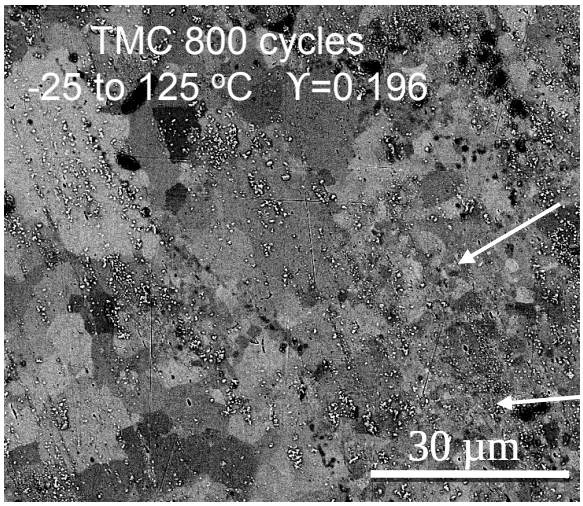

Figure 2.11: Backscatter electron SEM image of SAC 105 bulk solder alloy after 800 TMC cycles. Localized □-Sn grain recrystallization is indicated by white arrows. [2.1]

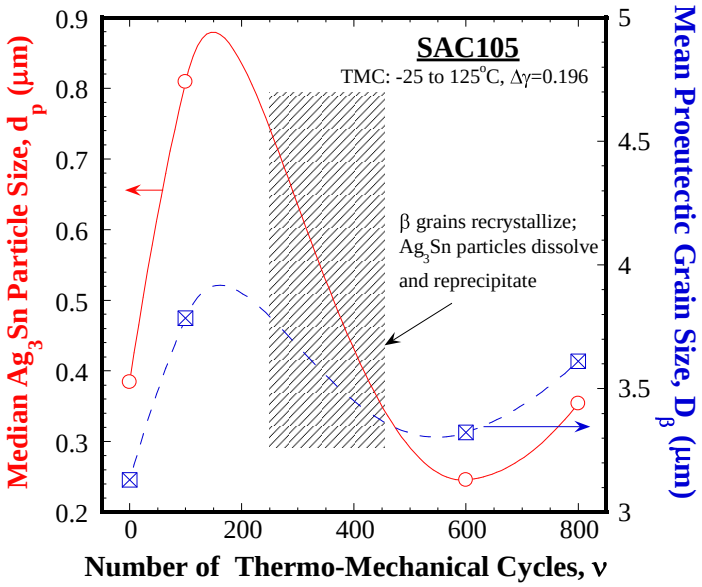

Figure 2.12: Effect of the number of elapsed thermo-mechanical cycles on median Ag_3Sn particle size and average proeutectic grain size of SAC 105 solder alloy

Strain enhanced dissolution and dynamic modification of microstructure and mechanical properties in precipitate containing alloys, e.g., Al alloys, has been long known. However, the operating mechanism for this phenomenon is not very well understood. Several researchers have shown that precipitate shearing takes place during cyclic straining which may result in dissolution of the precipitates [2.11-2.14]. Hutchinson et al. [2.11] have suggested that very small (<1 nm) particles do not dissolve in the matrix. This was based on the fact that under identical loading conditions, the alloy containing ~ 5 nm particles showed dissolution whereas the alloy containing <1 nm did not show any precipitate dissolution. Mathematical models for dissolution of precipitates based on precipitate shearing under homogeneous plastic strain have also been established by several authors [2.11, 2.15, 2.16]. No work has been done till date regarding dissolution of precipitates during TMC. The general belief is that TMC of lead-free SAC solder alloys results in strain enhanced coarsening.

Based on the experimental observation of this study, we suggest that during TMC, there are two concurrent and competing operating mechanisms: *strain enhanced coarsening* and *strain assisted dissolution* [2.4]. Coarsening would be accelerated during ramp up of thermo-mechanical cycle whereas the dissolution and re-precipitation likely occurs during ramp down. Some of the pre-existing precipitates undergo strain enhanced coarsening due to excess vacancy concentration during TMC, at the expense of shrinking precipitates. Such a process takes place during ramp up of the thermo-mechanical cycle when the temperature is high enough for rapid diffusion of Ag atoms from the shrinking particles to the growing particles. It has also been well established that during TMC, plastic strain accrues in solders during each ramp down [2.17] resulting in subsequent increase in dislocation density. When a critical amount of strain has been accumulated in the matrix, the shrinking precipitates may get sheared by moving dislocations and hence become thermodynamically unstable. These unstable precipitates will dissolve in the solid solution resulting in increase in Ag concentration in the β-Sn matrix. Indeed, the dissolution of precipitates was not observed at the onset of TMC but only after a certain critical amount of strain had been accumulated in the sample.

When the concentration of the solute in the β-Sn becomes large enough and solubility decreases with decreasing temperature, Ag_3Sn precipitates re-nucleate, preferably heterogeneously on randomly distributed dislocations. This would result in redistribution of precipitates in the solder. Such a process will take place during the ramp down of TMC when the temperature is low and diffusion distance is small. Instead of diffusing to the coarsening particles, excess Ag precipitates out as Ag_3Sn via heterogeneous nucleation of the precipitates on randomly distributed dislocations. Prior studies have shown that cyclic strain can induce precipitation in solution treated Al alloys under conditions that would normally not result in precipitation [2.18-2.20].

Particle coarsening kinetics Based on the Lifshitz-Slyolov-Wagner (LSW) model [2.21, 2.22], the kinetics of 3-dimensional coarsening of spherical second phase particles is given by [2.9, 2.23]:

$$\frac{dr}{dt} = B_1\left(\frac{\gamma_{ss} V_m C_{sol}}{RT}\right)\frac{D_{sol}}{3r^2} \tag{2.1}$$

where r is radius of the spherical particle, t is time, B_1 is a constant, γ_s is the specific energy of the particle-matrix interface, V_m is the molar volume of the second phase, C_{sol} is the equilibrium concentration of the solute in the matrix, R is gas constant, T is temperature and D_{sol} is the effective solute diffusivity in the matrix.

Integrating Equation 2.1, we have, for the kinetics of spherical precipitate coarsening undergoing 3-dimensional growth [2.9, 2.23]:

$$r^3 - r_o^3 = B_1\left(\frac{\gamma_s V_m C_{sol}}{RT}\right)D_{sol}t \tag{2.2}$$

where r_o is the initial radius of the precipitate. Typically, Ag_3Sn particles coarsen as platelets even though the initial shape may be spherical [2.14, 2.28, 2.29]. Therefore their coarsening is better described as 2-dimensional radial growth of disc shaped precipitates of constant thickness, h. Equation 2.1 can be modified to represent the rate of change of platelet radius, r, as [2.24]:

$$\frac{dr}{dt} = \frac{4B_1}{3h}\left(\frac{\gamma_{ss} V_m C_{sol}}{RT}\right)\frac{D_{sol}}{2r} \tag{2.3}$$

Integrating Equation 2.3, gives us the kinetics of platelet radius growth as [2.24]:

$$r^2 - r_o^2 = \frac{4B_1}{3h}\left(\frac{\gamma_s V_m C_{sol}}{RT}\right) D_{sol} t \qquad (2.4)$$

Where r_o is the initial radius of the precipitate and h is the thickness of the platelet. Here, h can be assumed to be approximately equal to r_o. A comparison of Equations 2.2 and 2.4 suggests that platelets (2-D growth) will coarsen faster than spherical particles (3-D growth).

Unified coarsening kinetics model for isothermal aging and thermo-mechanical cycling Assuming 2-dimensional platelet growth of Ag_3Sn precipitates in SAC solders, Equation 2.4 can be rewritten as:

$$d_p^{\ 2} - d_o^2 = \frac{K}{h}\left(\frac{C_{sol}}{T}\right) D_{sol} t \qquad (2.5)$$

where the constant $K=16B_1\gamma_s V_m/3R$ and d_o and d_p are the initial and instantaneous particle size, h is the platelet thickness.

Here, the term $C_{sol}D_{sol}t/T$ represents an explicit parameter signifying the critical parameters of Ostwald Ripening, namely the equilibrium solubility of the diffusing atom in the solvent and the diffusion distance of the solute atoms in the solvent, which depends on the thermo-mechanical history of the solder. For thermal and thermo-mechanical cycling conditions, where the temperature varies, $C_{sol}D_{sol}t/T$ may be replaced by an effective explicit parameter, $\overline{C_{sol}D_{sol}t/T}$ which depends on the temperature and strain range to which the sample is subjected, as well as the number of elapsed cycles. For ν_c cycles, $\overline{C_{sol}D_{sol}t/T}$ is given by:

$$\overline{C_{sol}D_{sol}t/T} = n_c.\left[\left(\overline{C_{sol}D_{sol}t/T}\right)_{ramp\,up} + \frac{C_{sol}^{\max}}{T_{\max}} D_{sol}^{T_{\max}} t_{dwell,T_{\max}} + \left(\overline{C_{sol}D_{sol}t/T}\right)_{ramp\,down} + \frac{C_{sol}^{\min}}{T_{\min}} D_{sol}^{T_{\min}} t_{dwell,T_{\min}}\right] \qquad (2.6)$$

where the terms within the brackets on the right hand side represent the above parameter during different segments of the thermal cycle (ramp-up of temperature, dwell at the maximum temperature, ramp-down of temperature and dwell at the minimum temperature). $D_{sol}^{T_{\max}}$ and $D_{sol}^{T_{\min}}$ are the solute diffusivities in Sn at the maximum and minimum temperatures, respectively, $C_{sol}^{\max}$ and $C_{sol}^{\max}$ are the solubility limit of solute in Sn at the maximum and the minimum temperatures (in mole fraction), respectively, $t_{dwell,T_{\max}}$ and $t_{dwell,T_{\min}}$ are the dwell times at the maximum temperature and the minimum temperatures, respectively, and $\overline{C_{sol}D_{sol}t/T}_{ramp\,up}$ and $\overline{C_{sol}D_{sol}t/T}_{ramp\,down}$ are the mean explicit parameters during the up and down ramps of one thermal cycle.

$\overline{C_{sol}D_{sol}t/T}_{ramp\,up}$ and $\overline{C_{sol}D_{sol}t/T}_{ramp\,down}$ may now be expressed as:

$$\overline{C_{sol} D_{sol} t/T}^{\,ramp\,up} = \int_0^{t_{ramp\,up}} D_{o,sol} \frac{C_{o,sol}}{T(t)} \exp\left[-\frac{Q_{sol} + Q'_{sol}}{RT(t)} \right] dt \tag{2.7a}$$

$$\overline{C_{sol} D_{sol} t/T}^{\,ramp\,down} = \int_0^{t_{ramp\,down}} D_{0,sol} \frac{C_{0,sol}}{T(t)} \exp\left[-\frac{Q_{sol} + Q'_{sol}}{RT(t)} \right] dt \tag{2.7b}$$

where, R is the universal gas constant, $D_{o,sol}$ and Q_{sol} are the frequency factor and activation energy, respectively, for diffusion of the solute atoms in Sn, and $C_{o,sol}$ and Q'_{sol} are the associated pre-exponent and activation energy, respectively, for the equilibrium solubility of solute (i.e., Ag) in Sn, which can be written as: $C_{sol}=C_{o,sol}.exp(-Q_{sol}'/RT)$. During the up and down ramps of a thermal cycle, the temperature is assumed to vary linearly with time at the rate of β_1 (i.e., $T = T_{min} + \beta_1 t$). Hence, for *thermal cycling conditions* (no mechanical strain), Equation 2.7 can be re-written as:

$$\overline{C_{sol} D_{sol} t/T}^{\,ramp,\,TC} = \int_0^{t_{ramp}} \frac{D_{o,sol} C_{o,sol}}{T_{\min}\left(1 + \frac{\beta_1 t}{T_{\min}}\right)} \exp\left[\left(-\frac{Q_{sol} + Q'_{sol}}{RT_{\min}\left(1 + \frac{\beta_1 t}{T_{\min}}\right)} \right) \right] dt \tag{2.8}$$

$$\overline{C_{sol} D_{sol} t/T} = \frac{D_{o,sol} C_{o,sol}}{T_{\max} - T_{\min}} \left[Ei\left(\frac{Q_{sol} + Q'_{sol}}{RT_{\max}} \right) - Ei\left(\frac{Q_{sol} + Q'_{sol}}{RT_{\min}} \right) \right] t_{ramp} \tag{2.9}$$

where Ei() is the exponential integral function.

For thermo-mechanical cycling, where strains accumulate during the up and down ramps, the effect of strain may be incorporated by considering an effective ramp time ($t_{ramp,eff}$), which accounts for strain-enhanced diffusion through the following equation [2.9]:

$$t_{ramp,eff} = t_{ramp}\left(1 + N\dot{\gamma}_{TMC}\phi\right) \tag{2.10}$$

where N (in seconds) is a kinetic constant that scales the vacancy concentration to the strain rate and hence represents strain-enhanced aging (~ 10^4 s [2.23]), $\dot{\gamma}_{TMC}$ is the shear strain rate to which the joint is subjected during the ramps of the thermo-mechanical cycle, and ϕ is the plastic fraction of the total strain (for typical TMCs with large strain ranges, $\phi \sim 1$). Equation 2.1. 10 suggests that under strain-enhanced aging conditions, the effective time of the ramp may be significantly greater than the actual ramp time t_{ramp}, depending on the magnitudes of the constant N and the strain rate $\dot{\gamma}_{TMC}$. The effective diffusion length during the ramps (up or down) during thermo-mechanical cycling may now be written simply as the product of the mean $C_{sol}D_{sol}/T$ over the temperature range of the cycle and $t_{ramp,eff}$, as follows:

$$\overline{C_{sol}D_{sol}t/T}_{ramp,\,TMC} = \frac{D_{o,sol}C_{o,sol}}{T_{\max}-T_{\min}}\left[Ei\left(\frac{Q_{sol}+Q'_{sol}}{RT_{\max}}\right)-Ei\left(\frac{Q_{sol}+Q'_{sol}}{RT_{\min}}\right)\right]t_{ramp,eff} \tag{2.11}$$

This can then be substituted in Equation 2.6 to get the value of $\overline{C_{sol}D_{sol}t/T}$ for ν_c thermo-mechanical cycles, as follows:

$$\begin{aligned}\overline{C_{sol}D_{sol}t/T} = \nu_c\{&\frac{D_{o,sol}C_{o,sol}}{T_{\max}-T_{\min}}\left[Ei\left(\frac{Q_{sol}+Q'_{sol}}{RT_{\max}}\right)-Ei\left(\frac{Q_{sol}+Q'_{sol}}{RT_{\min}}\right)\right]\left(1+N\dot{\gamma}_{TMC}\varphi\right)t_{ramp\ up}\\ &+\frac{D_{o,sol}C_{o,sol}}{T_{\max}-T_{\min}}\left[Ei\left(\frac{Q_{sol}+Q'_{sol}}{RT_{\max}}\right)-Ei\left(\frac{Q_{sol}+Q'_{sol}}{RT_{\min}}\right)\right]\left(1+N\dot{\gamma}_{TMC}\varphi\right)t_{ramp\ down}\\ &+\frac{C_{sol}^{\max}}{T_{\max}}D_{sol}^{T_{\max}}t_{dwell,T_{\max}}+\frac{C_{sol}^{\min}}{T_{\min}}D_{sol}^{T_{\min}}t_{dwell,T_{\min}}\}\end{aligned} \tag{2.12}$$

Figure 2.13 shows the variation in the effective particle diameter of Ag_3Sn with $\overline{C_{sol}D_{sol}t/T}$, where the relevant solute atom is Ag. Therefore, henceforth, the subscript 'sol' is replaced by 'Ag'. The diffusion constants used in the calculations are: $D_{o,Ag} = 7 \times 10^{-7}\ m^2/s$, $Q_{Ag} = 51.5$ kJ/mol, $C_{o,Ag} = 0.294$ *mole fraction* and $Q'_{Ag} = 26.57$kJ/mol [2.2]. The diffusivity value corresponds to the diffusion of Ag atoms in the direction perpendicular to the c-axis of Sn and give the fastest diffusion rates as compared to other directions.

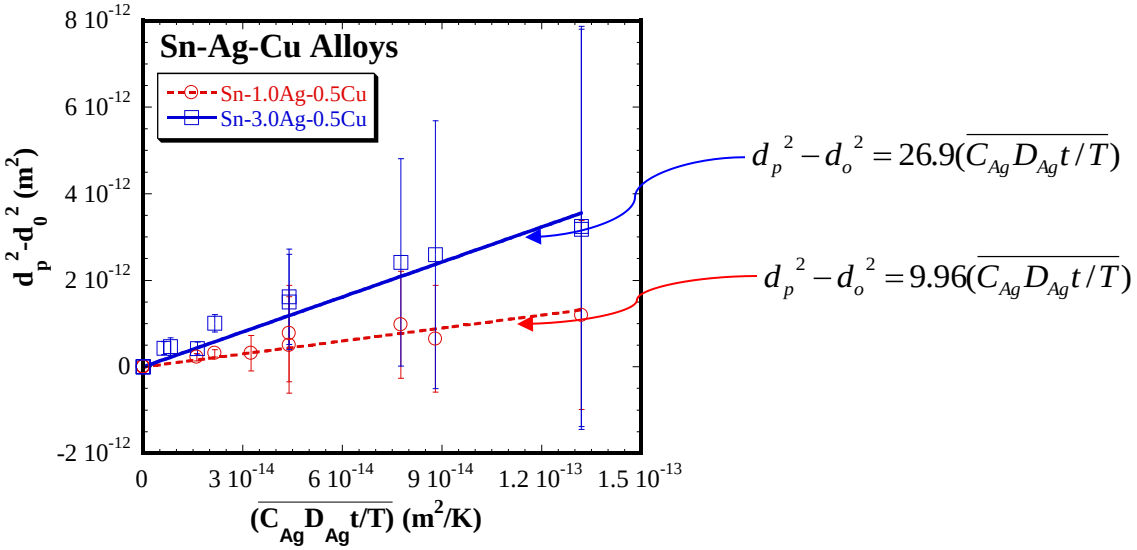

Figure 2.13: The variation in the particle size in SAC 105 and SAC 305 with the explicit parameter, $\overline{C_{Ag}D_{Ag}t/T}$

It is apparent from Figure 2.13 that the Ag_3Sn particles coarsen continuously with $\overline{C_{Ag}D_{Ag}t/T}$ according to the 2-dimensional platelet coarsening law:

$$d_p^{\,2} - d_o^{\,2} = K'(\overline{C_{Ag} D_{Ag} t/T})$$

(2.13)

where *K'* (*=K/h*) is the proportionality constant equal to ~ *9.96K* and *26.92K* for SAC105 and SAC305, respectively [2.1]. This demonstrates that the parameter $\overline{C_{Ag} D_{Ag} t/T}$ adequately describes the thermo-mechanical history dependence of the usual coarsening of Ag_3Sn precipitates in the Sn-Ag based solders. *Equation 2.13 can be used to predict the microstructure (in terms of Ag_3Sn particle size) if the initial microstructure of the solder and the thermo-mechanical history is known.* A new model needs to be developed for predicting the microstructure in the regime of unusual recrystallization, dissolution and re-precipitation of Ag_3Sn particles.

Typically, the Ag_3Sn particles are concentrated within bands of the eutectic microconstituent (Ag_3Sn + β-Sn) in the interdendritic spaces of primary β-Sn. Assuming a cubic array of precipitates within the eutectic, the average interparticle spacing may be estimated as:

$$\lambda = \sqrt[3]{\frac{\pi}{6V_{Pre\ in\ Eu}}}\, d \qquad (2.14)$$

where, d_p is the particle size and $V_{pre\ in\ Eu}$ is the volume fraction of precipitates in the eutectic.

Figure 2.14 shows the relationship between the inter-particle spacing and $\overline{C_{Ag} D_{Ag} t/T}$ for the various thermo-mechanical histories. Since inter-particle spacing is related to particle size through a constant (Equation 2.14), λ shows the same dependence on $\overline{C_{Ag} D_{Ag} t/T}$ as d_p:

$$\lambda = \sqrt{\lambda_o^{\,2} + M(\overline{C_{Ag} D_{Ag} t/T})}$$

or,

$$\lambda^2 - \lambda_o^2 = M(\overline{C_{Ag} D_{Ag} t/T}) \qquad (2.15)$$

where, λ_o is the initial inter-particle spacing and *M* is the proportionality constant which is equal to 47.54 K for SAC 105 and 38.42 K for SAC 305. *The inter-particle spacing data for both these alloys can also be estimated by using a value of 43.013K for M*. Just like the particle size, inter-particle spacing can also be predicted for various thermo-mechanical histories in the usual coarsening regime using Equation 2.15.

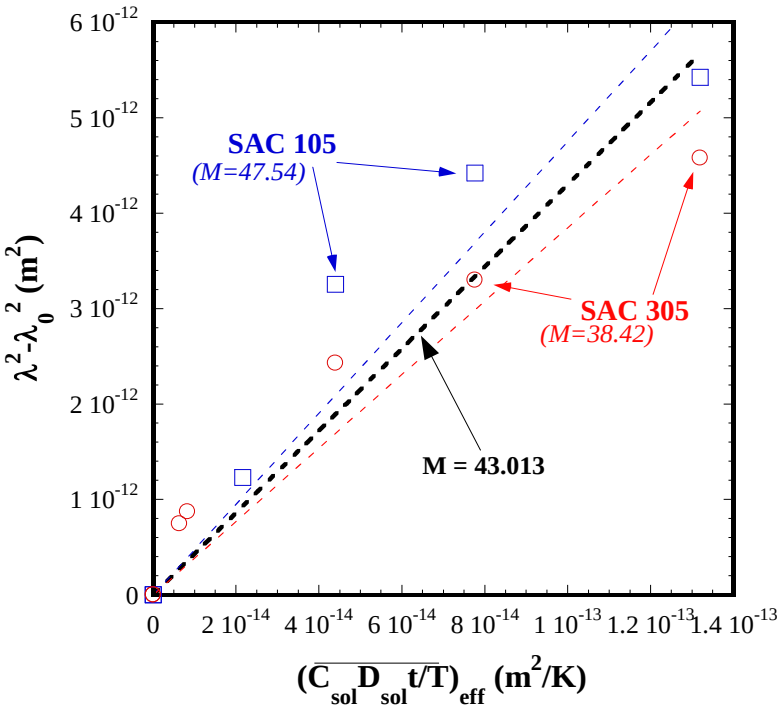

Figure 2.14**:** The variation in Ag_3Sn inter-particle spacing in SAC 105 and 305 with the explicit parameter, $\overline{C_{Ag} D_{Ag} t/T}$.

Conclusions for Sub-Task 2.1

Extensive microstructural characterization of SAC 105 and 305 has been conducted. The salient results found are:

(1) During isothermal aging, not only do the precipitates grow, but some recrystallization of Sn grains close to precipitate clusters within the eutectic regions is observed. Recrystallization occurs within the first 20 hours of aging at 150°C, and then the recrystallized grains undergo relatively little growth, and no new recrystallization occurs. The volume fraction of recrystallized grains is small (<5%). This recrystallization occurs because of particle-stimulated nucleation (PSN) of new grains adjacent to growing precipitates, which induce strain into the surrounding Sn-matrix. Since the volume fraction of recrystallized grains is small, this effect, although interesting and new, does not need to be accounted for in the microstructurally adaptive creep model.

(2) During thermo-mechanical cycling (TMC), precipitates initially undergo strain-enhanced coarsening. After about 200 or so cycles with a shear strain range of ~19.6%, when significant plastic strain has been stored in the solder, the β grains undergo localized recrystallization, but the particles continue to coarsen. Close to 600 cycles, the precipitates are observed to have dissolved and re-nucleated, with a fine, even precipitate distribution throughout the solder. The dissolution-reprecipitation-redistribution of the particles may have significant impact on the mechanical properties, and hence the thermo-mechanical cycling response, of the solder. Once again, this is a new effect that has not been observed before. Further work is needed to develop models for predicting microstructure in the regime of strain assisted recrystallization and dissolution and re-precipitation of Ag_3Sn, and to incorporate these effects in the

microstructurally adaptive creep models. This will require complete understanding of the operating mechanism for this phenomenon and can be a subject of future studies.

A unified coarsening model has been developed and a temperature-dependent parameter, $\sqrt{C_{Ag} D_{Ag} t / T}$, has been defined that adequately describes the thermo-mechanical history dependence of the usual coarsening of Ag_3Sn precipitates in the Sn-Ag based solders during both aging and thermo-mechanical cycling. The model can be used to predict the microstructure (in terms of Ag_3Sn particle size) if the initial microstructure solder and the thermo-mechanical history is known. A new model needs to be developed for predicting the microstructure in the regime of unusual recrystallization, dissolution and re-precipitation of Ag_3Sn particles.

Sub-Task 2.2: Creep and Fracture

A. Fracture behavior of SAC alloys

Background and Technical Approach Most portable devices undergo thermo-mechanical cycling during service, accelerating the formation of tiny low-cycle fatigue interfacial cracks in the solder joints. These pre-existing cracks may propagate under a combination of tensile and shear loading when the package sustains a drop. Therefore, the resistance of solder joints to high strain rate fracture is critical to the reliability of electronic packages. A few studies have addressed the quasi-static fracture behavior of Sn-Ag based solder joints, outlining the effects of mode-mixity, bond-pad metallization, interfacial IMC composition and thickness, etc on the fracture toughness of the solder joints [2.25-2.30]. It has been generally observed that at relatively low strain-rates (~8.3×10^{-3} /s), longer solder-reflow times shift the dominant failure mode from ductile (i.e., through bulk solder) to brittle (i.e., interfacial delamination of different layers of IMCs, e.g. Cu_3Sn and Cu_6Sn_5) [2.30]. However, there is a lack of systematic study on the relationship between solder microstructure, the IMC morphology and the fracture behavior of solder joints at high strain rate as well as the evolution of the relative contributions of these mechanisms with increasing loading mode-mixity.

The effects of joint-processing parameters, aging and loading conditions on the microstructure and fracture response of Sn-3.8%Ag-0.7%Cu (SAC387) solder joints attached to Cu substrates at high strain rate loading has been studied in our previous work [2.31-2.34]. In general, a higher strain rate and increased mode-mixity resulted in decreased G_C. G_C also decreased with increasing dwell-time at reflow temperature, which produced a thicker intermetallic layer at the solder-substrate interface. Softer solders, produced by slower cooling following reflow, or post-reflow aging, enhanced G_C. Fracture mechanism maps (FMM) for Sn-3.8%Ag-0.7%Cu (SAC387) solder joints attached to Cu-substrates have been generated. Separate maps are presented for nominally Mode I and equi-mixed mode loading conditions (loading angle $\phi = 0^o$ and 45^o, respectively), as shown in Figure 2.15a and 2.15b. *The FMMs allow rapid assessment of the operative fracture mechanism(s) along with an estimate of the expected joint fracture toughness value for a given loading condition (strain rate and loading angle) and joint microstructure without conducting actual tests, and may serve as both predictive and microstructure-design tools*. SAC 305 is also utilized widely in electronic industry, yet its high strain rate fracture behavior has not been systematically studied.

The solder used in this study is commercially available Sn-3.0%Ag-0.5%Cu (SAC305). Fracture mechanics tests were conducted on samples comprising of a 0.5mm thick solder joint between two copper substrates in the modified compact mixed mode (CMM) configuration[1], where the joint-length (W) equals 9mm (Figure 2.16a). For a sharp interfacial crack (length a), a 4.5mm long and 500 nm thick Al thin film (which is not wetted by solder) was deposited on one of the Cu substrates (polished up to 0.05μm colloidal silica) by vacuum evaporation prior to joint-formation, giving a/W=0.5. Solder joints were formed by sandwiching rolled solder sheets between the Cu substrates and placing the sandwich in a specially designed mold which allowed precise control of the joint thickness by the use of two triangular wedges of appropriate

[1] The CMM geometry, first proposed by M. Arcan, Z. Hashin and A. Voloshin [2.35], is for a monolithic material with a cohesive crack. This geometry has been modified in the present work to incorporate an adhesive joint with an interfacial (i.e., adhesive) crack, while retaining all the capabilities of controlled mixed-mode loading afforded by the CMM configuration.

dimensions. It is necessary to determine the stress-state in the sample during a typical fracture test. Therefore, a few double crack samples (Figure 2.16b) were also prepared to observe the crack propagation behavior and to ascertain the role of plasticity during fracture through observation of the regions near the tip of the partially propagated crack (also termed as secondary crack) [2.33]. Double crack solder joints were mechanically polished up to 0.05μm colloidal silica before fracture tests. After the test, the region ahead of the partially propagated crack was observed under scanning electron microscope (SEM). The region ahead of the crack tip, where plastic deformation took place, showed apparent surface undulations including short slip traces or grain boundary sliding, whereas the regions without plastic deformation remained flat. The reflow parameters used in the study were as follows: (a) reflow temperature: 260°C, (b) dwell time: 30s, 180s or 300s, and (c) cooling rate: ~10°C/s (water cooled, WC) or ~3°C/s (air cooled, AC).

Figure 2.17 shows the fracture test set-up for the CMM arrangement. Tests were conducted using a servo-hydraulic test frame at ram speeds of ~0.5 to ~50 mm/s (corresponding to joint strain rates of 1 to 100s^{-1}). The loading fixture, shown in Figure 2.17a, enables changing the loading angle from 0° to 90° relative to the specimen axis in 15° increments. For high-strain rate tests, during the acceleration period, the displacement of the ram can be on the order of or greater than the thickness of the joint, thereby resulting in joint failure prior to the ram reaching the requisite velocity. Thus, a piston- cylinder design was adopted, which is shown in Figure 2.17b. Such a configuration ensures that the sample is loaded only after the ram velocity reaches the set velocity.

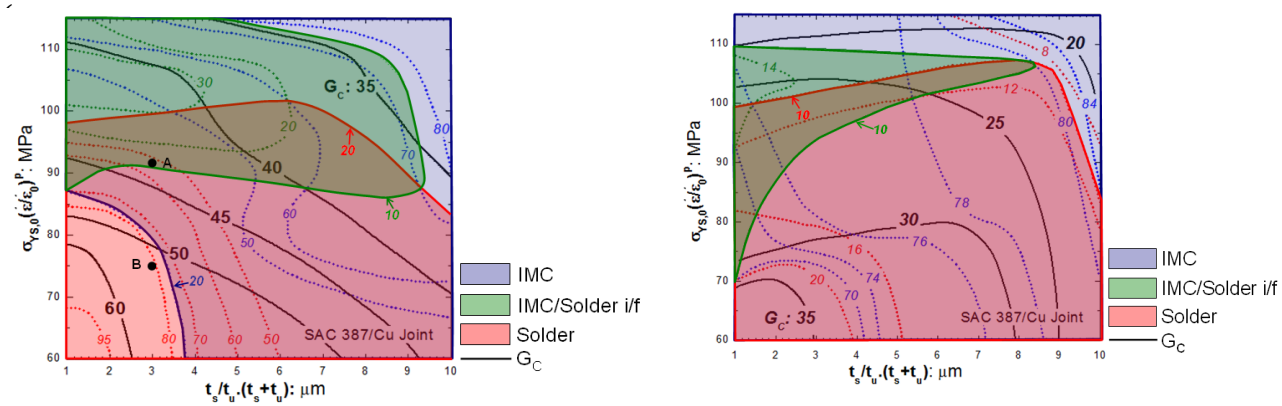

Figure 2.15: Fracture mechanism map showing the contribution of different fracture types as a function of t_{eff} and σ_{YS}. Contour lines corresponding to constant values of G_C (solid lines) and the various fracture types (dashed lines) are shown. G_C values are in large, black letters, and the percent fracture values for each fracture type are in small letters, in the same color as the mechanism-field; (a) Mode I FMM; (b) equi-mixed mode FMM.

Figure 2.16: CMM sample configuration: (a) single crack sample; (b) double crack sample. This study does not utilize any special surface finish.

(a)

(b)

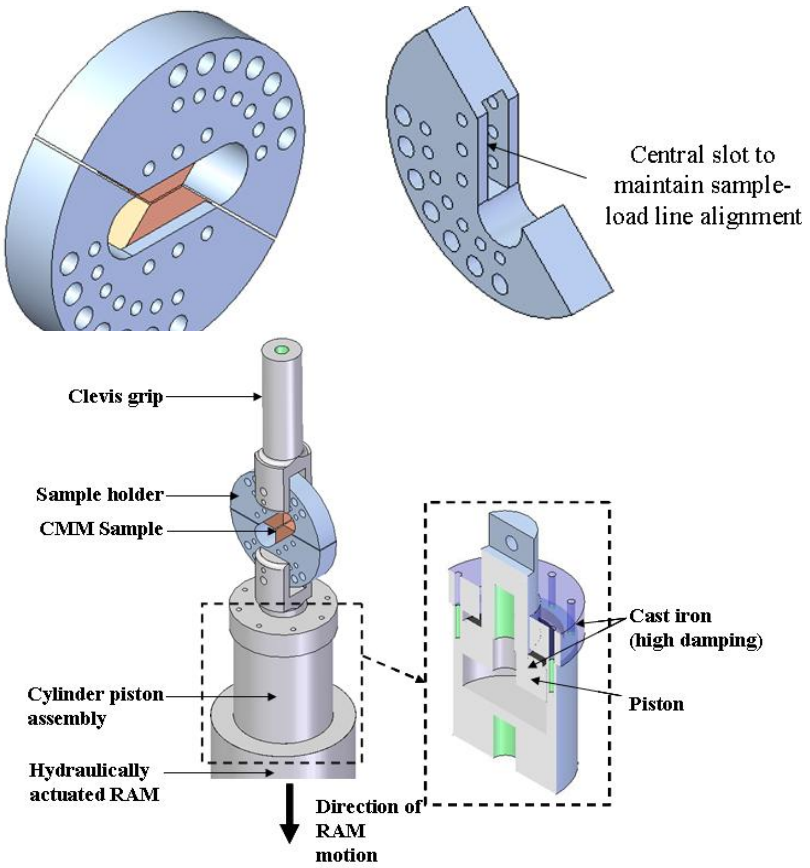

Figure 2.17: (a) A schematic showing the sample holder. It is a modified Arcan design which allows changing the loading angle by rotating the sample holder with respect to the loading axis. (b) A schematic showing a cylinder/piston design which allows the loading of the sample only when the ram attains the desired velocity.

Methodology for calculating G_C: Figure 2.18 shows the crack profile of a sample processed with typical reflow parameters (WC, dwell time 30s, as-reflowed condition) and tested at strain rate

$100s^{-1}$. By measuring the regions up to which the plasticity induced surface undulation was extended, the size of the plastic zone was estimated to be ~90 μm for this condition. Similarly, plastic zone for other cases were also measured, and it was concluded that the plastic zone extended only up to 100 to 200μm ahead of the tip for all test conditions. The plastic zone ahead of the crack tip, hence, was always much smaller than the crack length (a_0=4.5 mm) and the thickness of the specimen (t=6.35mm). This, therefore, qualifies all the test conditions used in this study to be in the plane strain condition. For small-scale yielding problems, where failure is catastrophic, the fracture toughness can be expressed as the critical strain energy release rate, G_C.

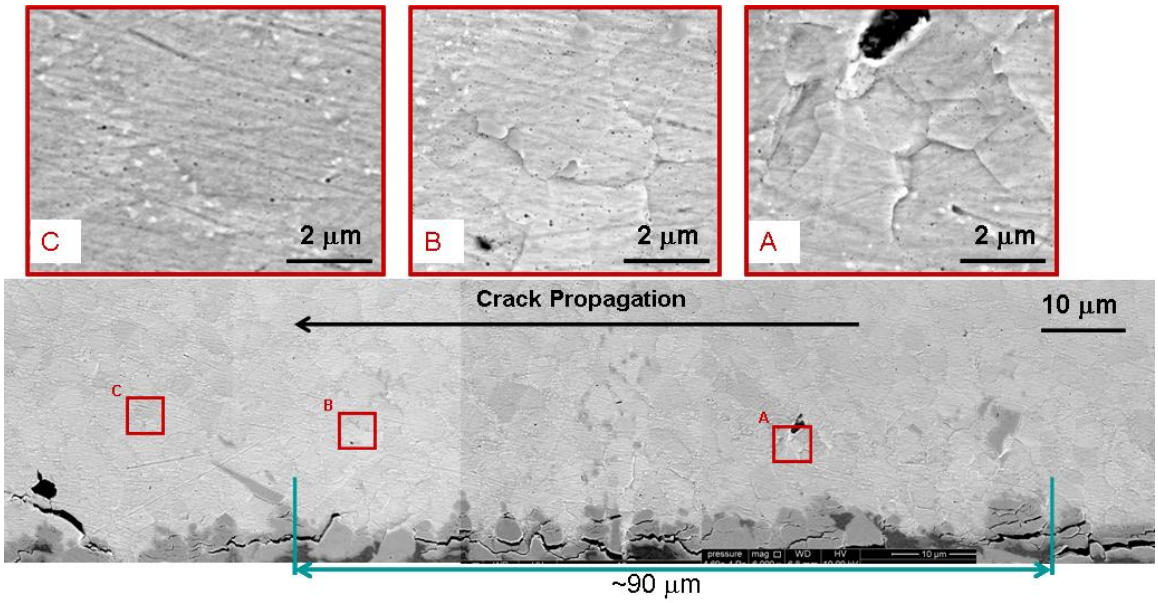

Figure 2.18: The crack profile of a sample processed with typical reflow parameters (WC, dwell time 30s, without aging) and tested at 100 s^{-1}. Ahead of the crack tip, the size of region which shows apparent surface relief and undulation including slip traces and grain sliding in Sn dendrites is about 90 μm.

The strategy utilized for computing G_C comprised two steps: (i) estimate the actual crack length just prior to fracture by accounting for any sub-critical crack growth, and (ii) utilize available formulations for the stress intensity factors for adhesive joints in CMM samples under mode I and II, K_{1a} and K_{2a} [2.36]:

$$K_{1a}(\text{CMM}) = \frac{P\cos\phi\sqrt{\pi a_c}}{Wt} f_{1a}\left(\frac{a_c}{W}\right)$$
$$K_{2a}(\text{CMM}) = \frac{P\sin\phi\sqrt{\pi a_c}}{Wt} f_{2a}\left(\frac{a_c}{W}\right) \qquad (2.16)$$

where P is the applied load, ϕ is the loading angle, a_c is the critical crack length (at which unstable crack propagation initiates), W is the joint width, t is the thickness of the Cu pieces, and f_{1a} and f_{2a} are factors depending on the sample geometry and the crack length. The values of f_{1a} and f_{2a} are reported in reference [2.33].

To estimate the actual crack length just prior to catastrophic crack propagation (accounting for any sub-critical crack growth, which can be significant), a methodology based on ASTM standard E561-05 [2.37] was employed. This involved comparing the secant modulus just prior

to fracture from the load-displacement plot with the initial modulus during loading to determine the fractional decrease in modulus (or increase in compliance C). For this, a master plot of the fractional compliance change ($\Delta C/C_0$) versus the fractional crack-length increase ($\Delta a/a_0$) was developed using finite element modeling (FEM), and the experimentally obtained $\Delta C/C_0$ value was utilized to determine $\Delta a/a_0$, and hence the critical crack length a just prior to fracture. G_C can then be expressed as [2.38]:

$$G_C = \frac{K_{1a}{}^2 + K_{2a}{}^2}{E_a' \cosh^2(\pi\varepsilon)} \tag{2.17}$$

where ε is a constant depending on Dundurs parameter, β, and E_a' is given by:

$$E'_a = 2\frac{E_1' . E_2'}{E_1' + E_2'} \tag{2.18}$$

where E_1' and E_2' are the plane strain Young's moduli [$=E/(1-\nu^2)$] of substrate and adhesive, respectively, E and υ being the Young's modulus and Poisson's ratio, respectively, and ε and β are:

$$\varepsilon = \frac{1}{2\pi}\ln\frac{1-\beta}{1+\beta} \tag{2.19a}$$

and

$$2\beta = \frac{\mu_1(1-2\nu_2) - \mu_2(1-2\nu_1)}{\mu_1(1-\nu_2) + \mu_2(1-\nu_1)} \tag{2.19b}$$

where μ_1 and μ_2 are the shear modulus of the substrate and the adhesive layer, respectively, and ν_1 and ν_2 are Poisson's ratio of the substrate and the adhesive layer, respectively. The mode-mixity ψ (which may be different from the loading angle, ϕ) for interfacial fracture [2.39, 2.40] is:

$$\psi = \tan^{-1}\frac{K_{2a}}{K_{1a}} \tag{2.20}$$

Results and Discussion

The effect of strain rate and mode mixity Figure 2.19 shows the effect of strain rate on the fracture toughness of SAC305/Cu joints for dwell time of 30s and water cooled condition with the reflow temperature (260ºC). It is noted that the fracture toughness monotonically decreases with strain rate. This can be explained by the higher solder yield strength and work hardening rates at higher strain rates, causing a smaller yielding region at the crack tip [2.33, 2.41]. Compared with SAC 387/Cu joints for the same reflow and testing condition, SAC 305/Cu joints show higher G_C for strain rates ranged from $1s^{-1}$ to $100s^{-1}$ because of the lower yield strength of SAC305 alloys [2.42]. Figure 2.20 shows the effect of mode mixity on the G_C. G_C decreases with increasing the mode mixity. In the previous work, it was found that for SAC 387/Cu joints, the decrease of G_C is because the crack is more prone to propagate into the IMC than the solder at higher ψ,, which is less energy-expensive [2.33, 2.34]. However, for SAC305/Cu joints, the mechanism for such phenomenon still needs to be clarified by both the crack profile and fractography.

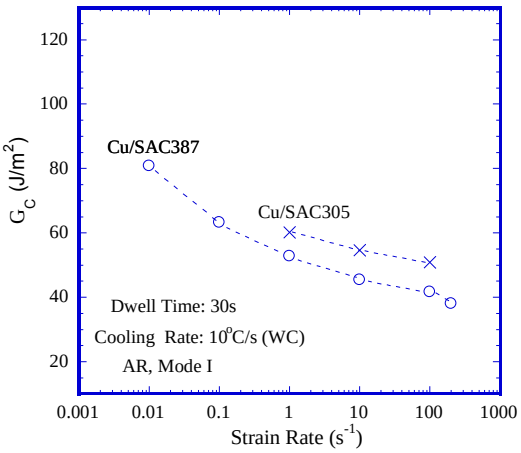

Figure 2.19: Effect of strain rate on the mode I fracture toughness of the solder joints. An increase in the strain rate monotonically reduces G_C.

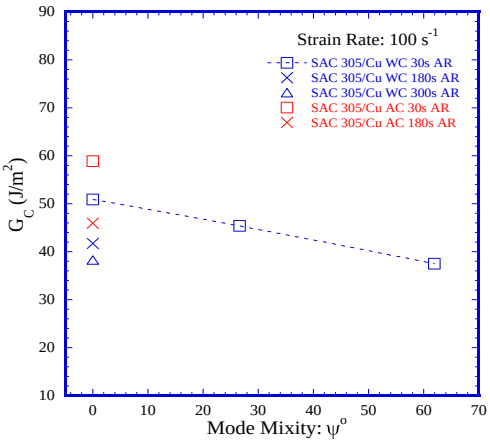

Figure 2.20: Effect of reflow parameters (cooling rate and dwell time) on the mixed mode fracture toughness of the solder joints. [Key: WC=water-cooled; AC=air-cooled; Dwell times = 30s, 180s, 300s; AR=as-reflowed]

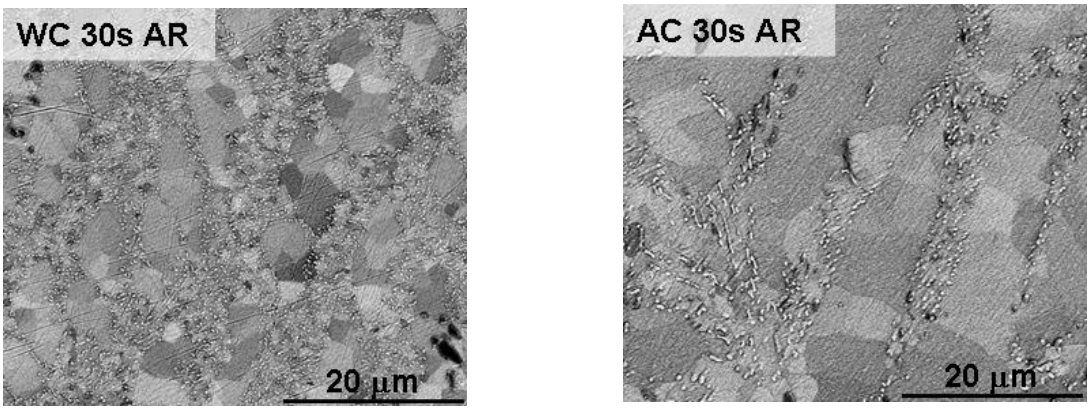

Figure 2.21: Effect of processing conditions on solder microstructure, where (a) 30s,WC,AR (b) 30s,AC,AR.

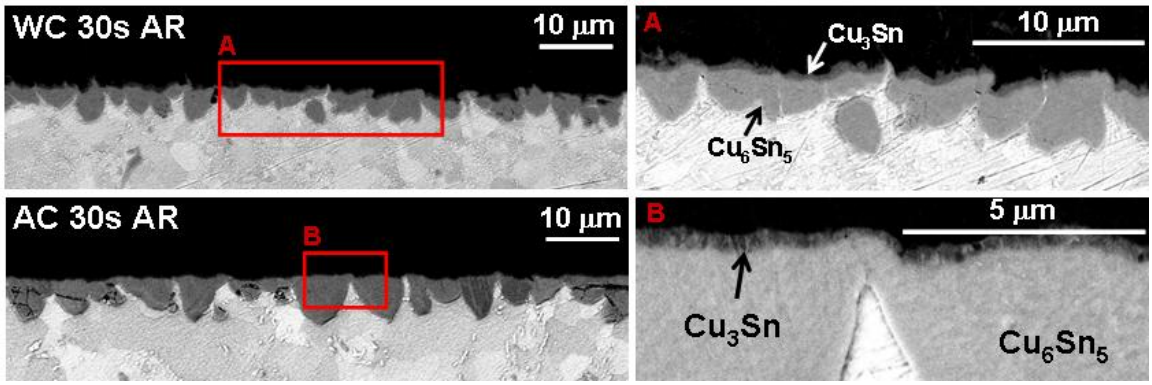

Figure 2.22: Effect of processing conditions on interfacial IMC layer, where the images in the right row are the magnifications of those in the frames in the left images.

The effect of dwell time and cooling rate Both water cooled and air cooled samples with different dwell time (30s, 180s and 300s) were tested at the strain rate of 100 s^{-1} for mode I loading. Figure 2.20 shows that G_C decreased with an increase in the dwell time. This is attributable to the formation of coarser IMC scallops and greater overall IMC thickness at longer dwell times, which increases the probability of the crack to remain confined to the IMC. A thicker IMC layer not only increases the fraction of brittle material near the crack tip but also increases the elastic-plastic stresses at the solder/IMC interface, arising due to the elastic mismatch between IMC and solder. This proffers a faster nucleation rate of micro-voids, resulting in degradation of fracture toughness [2.32, 2.33].

G_C decreases with increase of cooling rate (Figure 2.20) for mode I. Higher cooling rate (i.e. WC) samples have finer microstructures as shown in Figure 2.21, which leads to higher yield strength. Thus, a smaller plastic zone at the crack tip results in smaller G_C as compared to a sample produced using a slower cooling rate. On the other hand, cooling rate also plays a role on the IMC morphology. Figure 2.22 represents the IMCs at the interface for both cooling rates are composed of scallop-like Cu_6Sn_5 layer and planar-like Cu_3Sn layer, respectively. The AC sample represents much larger Cu_6Sn_5 scallops as well as higher ratio of Cu_6Sn_5 thickness over Cu_3Sn thickness, yet its effect on the fracture behavior has not been completely understood.

It is noted that for the same testing and reflow condition, the G_C values of SAC 305 joints are always higher than those of SAC 387 joints, as shown in Table 2.1, which may be partly related to the fact that SAC 305 alloy is softer than SAC 387 [2.42]. However, the specific effect of solder composition on the formation and growth of interfacial IMC layer as well as solder properties needs to be explained in detail in the future work.

Table 2.1: Comparison of G_C between SAC305/Cu and SAC387/Cu joints under Mode I loading

	WC, 30s, AR	WC, 180s, AR	WC, 300s, AR	AC, 30s, AR	AC, 180s, AR
SAC305/Cu	50.904	41.752	38.270	58.898	45.920
SAC387/Cu	41.690	34.226	32.163	47.567	43.285

* All the units in Table 2.1 are J/m^2.

Modified Fracture Mechanism Maps for SnAgCu / Cu Joints [2.45] Previously [2.33, 2.34], we presented detailed analysis of the fracture behavior of Sn-3.8Ag-0.7Cu solder joints attached to Cu substrates under both quasi-static and dynamic loading conditions (strain range of 0.01 to 100s^{-1}) and at various mode-mixities, ranging from mode I to equi-mixed mode (loading angles of 0^o to 45^o), and the results were finally assembled in the form of a fracture mechanism map. The main observations are summarized below.

It was found that irrespective of the condition, the fracture path was always close to (i.e., associated with) the solder-Cu interfacial region, although the relative contributions of the various fracture mechanisms changed substantially. Among the three prevalent mechanisms of joint failure (solder fracture, IMC fracture, or solder-IMC interface fracture), solder and IMC fractures were observed to be the most and the least energy absorbing, respectively. Typically, all three mechanisms operated simultaneously in a given sample, although the relative proportions of their contributions varied, depending on the test conditions and sample history.

The key parameters which determined the mix of different fracture mechanisms were the strain-rate compensated solder yield strength ($\sigma_{ys,eff}$) and a roughness-compensated IMC thickness (t_{eff}). The effective (roughness-compensated) IMC thickness was expressed as [2.34]:

$$t_{eff} = \frac{t_s}{t_u}\left(t_u + t_s\right) = t_s + \frac{t_s^2}{t_u} \tag{2.21}$$

where t_s, t_u and t_t are the IMC scallop-height, uniform IMC thickness, and the total IMC thickness. The formulation of t_{eff}, and the functional dependency of the fracture path on t_{eff} was qualitatively validated based on observations on the solder-Cu system. An inspection of equation 2.21 reveals that as the t_{eff} increases with increasing roughness (i.e., the ratio of scallop height t_s to the uniform IMC thickness t_u) and total thickness (t_u + t_s). However, the particular formulation for t_{eff} as given by equation 2.2 suggests that when the IMC layer becomes smooth (i.e., when $t_s/t_u \rightarrow 0$), $t_{eff} \rightarrow 0$, even when the layer is very thick. Thus, a joint with a very thick IMC layer would result in a very high propensity for solder fracture (low likelihood of IMC fracture), as long as the layer is smooth. In solder-Cu joints, this situation almost never arises. However, for SAC solder joints on Ni substrates, the IMCs are often smooth, and yet, the failure is through the IMC, as long as it is thick. This necessitated re-formulation of the mathematical description of t_{eff}.

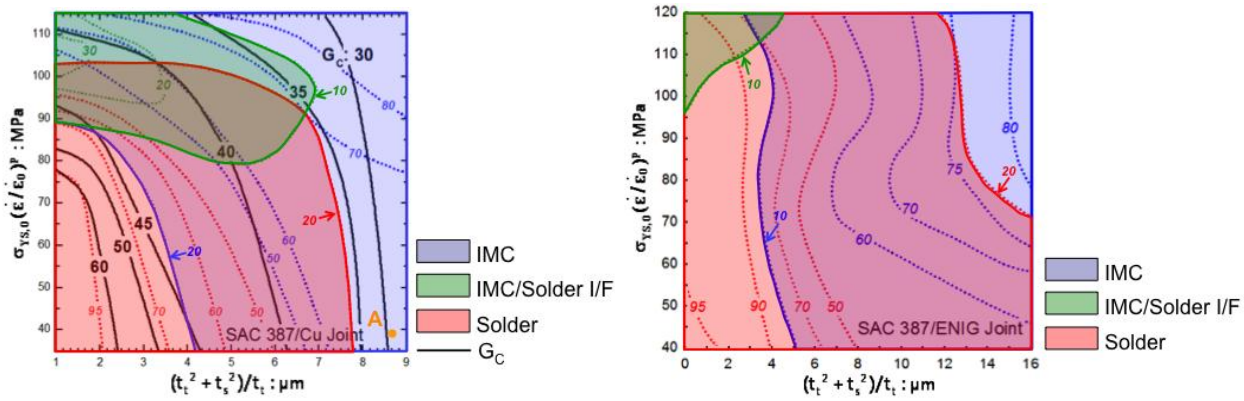

Figure 2.23: Modified Mode I Fracture Mechanism Maps for SAC387/Cu and SAC387/ENIG joints

The definition of t_{eff} must satisfy the following requirements. First, t_{eff} should be finite and significant in the two limiting cases, corresponding to $t_s \rightarrow 0$ or $t_u \rightarrow 0$ (i.e, very smooth or very thin IMC). Secondly, t_{eff} should be dominated by t_u when t_u is very large relative to t_s, and by t_s when $t_s >> t_u$. Based on these considerations, a modified expression for t_{eff} was proposed, where the term t_u in equation 2.21 was replaced by the total thickness t_t, as follows:

$$t_{eff} = t_t + \frac{t_s^2}{t_t} = t_u + t_s + \frac{t_s^2}{t_u + t_s} \tag{2.22}$$

This modified definition of t_{eff} satisfies all of the criteria set forth above. When $t_s = 0$ and $t_u \neq 0$, then t_{eff} is determined by t_u ($t_{eff} = t_u$). On the other hand, when $t_u = 0$, but $t_s \neq 0$, then t_{eff} is dependent only on t_s ($t_{eff} = 2t_s$). It is further noted that the effects of all these limiting conditions on the joint fracture behavior are consistent with the experimental data on both Cu and Ni substrates obtained to date.

New the fracture mechanism maps for SAC387/Cu and SAC387/ENIG joints were developed, using the modified definition of t_{eff} given by equation 2.22, as depicted in Figure 2.23. Consistent with the FMM in Figure 2.15a, the new FMM in Figure 2.23a also indicates that a combination of low $\sigma_{ys,eff}$ and low t_{eff} result in a tougher solder joint. To validate the effectiveness of the updated definition of t_{eff} even for the joints containing a thick and smooth IMC layer, a few samples were aged at 180°C for 144 hrs, and tested. Point A on Figure 2.23a represents this solder joint, for which the FMM predicts a G_C value of slightly less than 30 J/m^2, and crack propagation primarily through the interfacial IMC layer. Consistent with the modified FMM, the experimentally measured value of G_C for this joint was 28 J/m^2. Furthermore, the crack, as well as the damage-zone ahead of the crack tip, remained predominantly in the IMC layer in this sample, as expected from the FMM. This validates the modification proposed for the definition of t_{eff}, and suggests that it is valid for both smooth, thick IMCs, as well as rough, thin IMCs. Compared with the Mode I FMM for SAC387/Cu joints, the span of solder-fracture field becomes more extensive for SAC387/ENIG joints (Figure 2.23b). Since the IMC in the solder/ENIG joint is smoother than that in solder/Cu joints, this suggests that a much thicker IMC is needed in the solder/Ni joint to have the same mix of fracture mechanisms as in a solder/Cu joint.

Conclusions of Sub-Task 2.2A

A generalized procedure for mixed-mode fracture toughness testing of elasto-plastic joints attached to two elastic substrates was developed [2.46]. The fracture toughness of 500μm thick solder joints was measured for a range of loading rates, and reflow and aging parameters [2.33]. The associated fracture mechanisms were studied in detail, and fracture mechanisms maps were constructed in a field defined by strain rate compensated yield strength vs. an effective interfacial IMC morphology t_{eff} [2.34]. The original definition of t_{eff} [2.34] was subsequently modified to make it consistent with physical mechanistic trends observed in both solder-Cu and solder-Ni joints [2.45]. The new definition of t_{eff} resolves discrepancies noted for smooth interfaces in the previously used definition of t_{eff}, by attaching proper emphasis on the *total* thickness of IMC layer, and makes it compatible with both thin, rough IMC layers, as well as thick, smooth IMC layers. Fracture mechanism maps were plotted using this new definition of t_{eff} for both solder-Cu and solder-Ni systems [2.45, 2.47].

B. Impression Creep tests of SAC 105 and 305

Technical Approach

The solder alloys used in this test were SAC 105 and SAC 305 in as-reflowed condition as well as under differently aged conditions. Reflow procedure and aging conditions are described in detail under Sub-Task 2.1. The experimental samples were cylindrical with a height of 5mm and a diameter of 5 mm. Both ends of the cylinders were ground and polished and care was taken to ensure that the two surfaces were parallel. This is crucial to ensure that the indenter is normal to the surface and the whole area of the indenter's tip touches the sample.

Impression creep tests were conducted using a specially developed technique in a dynamic mechanical analyzer (DMA) machine. DMA was chosen for impression creep tests due to its accurate force and displacement control and measurements. Figure 2.24 shows a sample set up for impression creep test. A flat tipped cylindrical tungsten carbide indenter of 100 μm diameter was used for impression creep tests. The sample is positioned on the fixed clamp and the indenter is set to rest on it. A force-controlled module is used for the creep tests. Initially, a load of 0.001N is applied on the sample to make sure a physical touch exists between the indenter. The temperature is increased to the test temperature and then load is further increased to 0.1N to make a full-circle contact between the indenter and the sample. The indenter then penetrates the sample with a force of 0.8 N. The sample is immediately unloaded to 0.05 N and the sample is allowed 200 min for recovery. After recovery, force is ramped up to the reach the desired test stress, and is kept constant for a period of up to 200 min. Time, displacement, and forces are recorded at regular intervals. Impression creep tests were done over a temperature range of 50^{o}C and 150^{o}C and the normalized punch stress (σ_p/G) range of 1.1 x 10^{-3} to 6 x 10^{-3}.

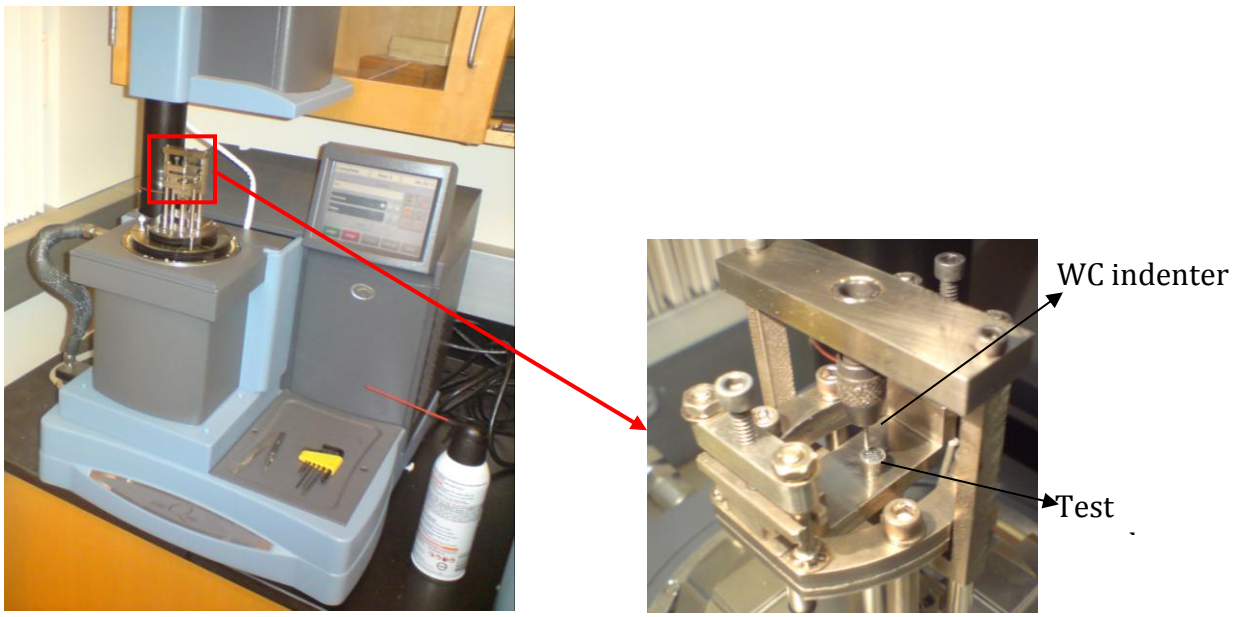

Figure 2.24: Experimental setup in DMA used for impression creep tests.

For power law creep, the steady state impression velocity, V, is related to the punch stress σ_p as follows:

$$V = A' f(\phi)\left(\frac{Gb}{kT}\right)\left(\frac{\sigma_p}{G}\right)^n e^{-Q/RT} \tag{2.23}$$

where the equivalent expression for the steady state creep strain rate is:

$$\dot{\varepsilon} = A\left(\frac{Gb}{kT}\right)\left(\frac{\sigma}{G}\right)^n \exp\left(-\frac{Q}{RT}\right) \tag{2.24}$$

where σ is the applied stress, G is the shear modulus, n is the creep stress exponent, b, k and T are Burger's vector, Boltzmann's constant, and the absolute temperature, respectively, Q is the activation energy for creep, R is the universal gas constant, and A is the creep pre-exponent. The punch stress σ_p is related to the equivalent stress as: $\sigma=\sigma_p/\kappa$, where κ is a constant that depends on geometry of the plastic zone under the indenter, and is ~3. The effective creep strain rate is related to the impression velocity V as $\dot{\varepsilon} = V/C\varphi$, where the constant C~1. As a result, the pre-exponents A' and A are related as follows: $A'=A.C\phi/\kappa^n$.

The creep stress exponent n can be determined from the slope of the VT/G vs. σ_p/G plot, whereas the activation energy Q may be obtained from the slope of ln(VT/G) vs. 1/RT. The experimentally determined values for V, n and Q were then used to develop creep constitutive laws, which, in conjunction with the particle coarsening model discussed in Sub-Task 2.1, were utilized to develop the microstructurally adaptive model for creep of these solder alloys, as discussed in Sub-Task 5.1.

Results and discussion:

Figure 2.25 shows typical impression depth vs. t plots for a SAC305 under various aging and thermo-mechanically cycled conditions.

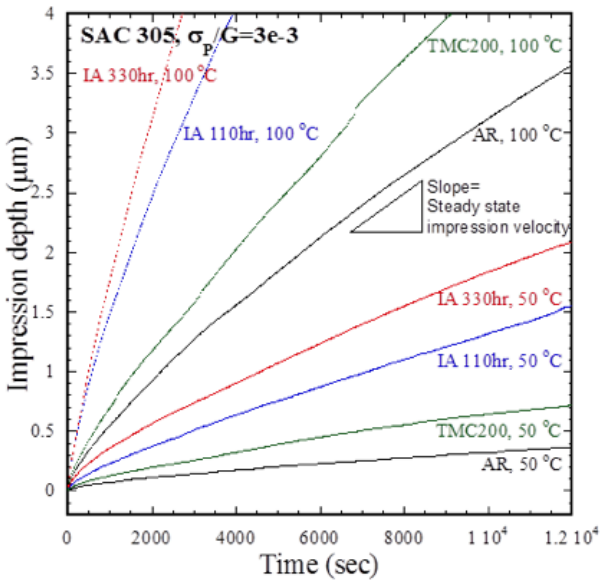

Figure 2.25 Impression depth vs. time for SAC305.

Figure 2.26 shows plots of VT/G versus σ_p at constant temperatures for Sn, SAC 105 and SAC 305 in the as-reflowed condition, from which the n values are determined. For pure Sn, the stress exponent was calculated to be 5, while for the alloys it was determined to be 6.

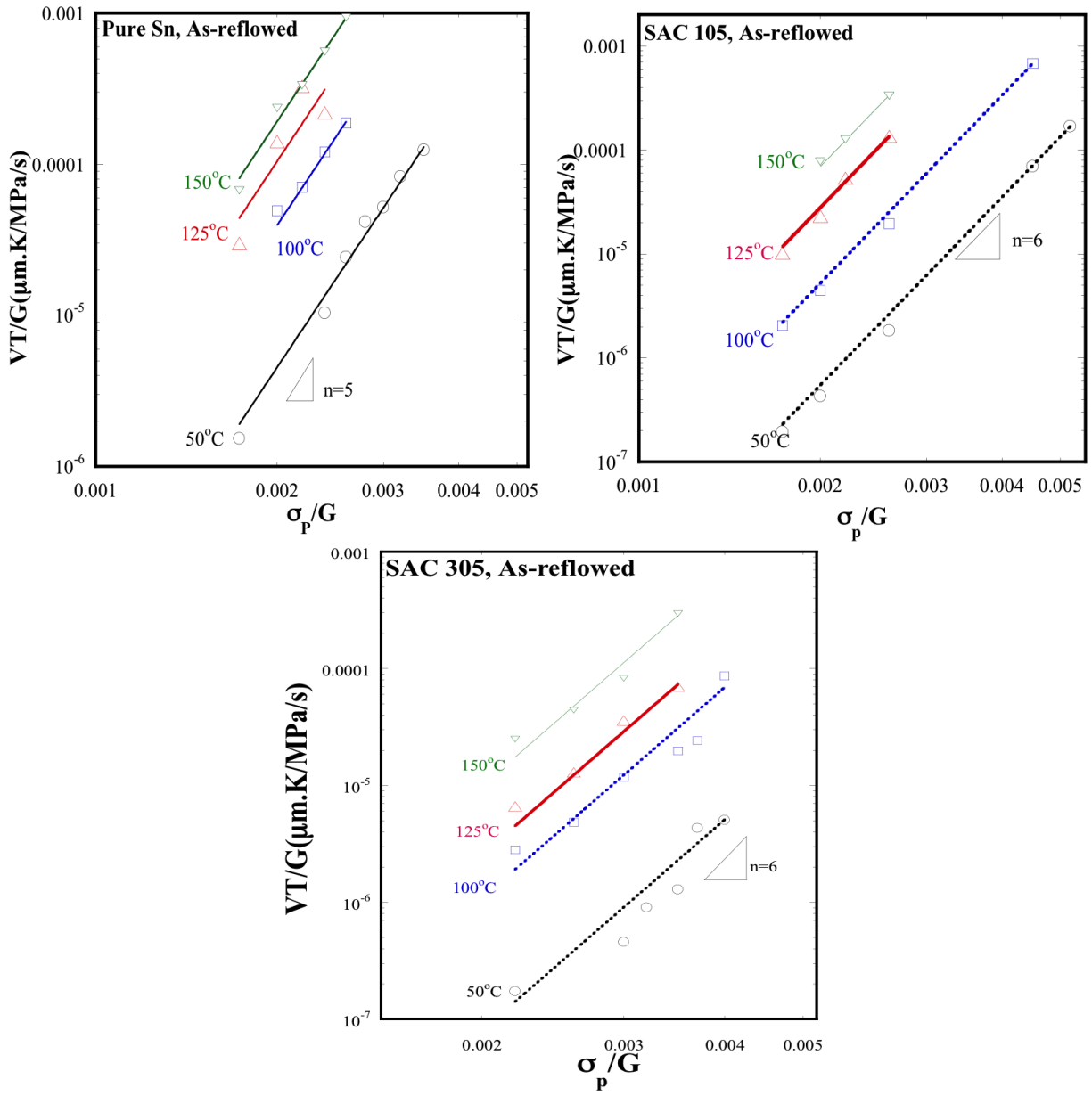

Figure 2.26 Plots of VT/G versus σ_p/G for pure Sn, SAC105, and SAC 305. The graphs present a comparison between the steady state creep rates and the stress exponents of the three materials.

The activation energy *Q* was calculated by plotting the logarithm of strain-rate vs. reciprocal of the temperature, as shown in Figure 2.27. The Q value is 43kJ/mole for pure Sn, and 50 kJ/mole for the SAC alloys (SAC105 and SAC305). These values are comparable to those found for pure Sn previously [2.47], but a little smaller than previously reported values for Q in SAC alloys [2.43, 2.48]. The difference between the present Q values for the SAC alloys (50kJ/mole)

and those reported previously (~60kJ/mole) is probably related to the fact that the present work was based on bulk samples rapidly cooled from the reflow temperature, whereas the previous work was on commercial BGA joints attached to Cu substrates. This presents two potential compositional differences near dislocation cores. First, the BGA joints are likely to have a higher amount of Cu due to dissolution from pads during reflow, potentially leading to a larger Cu segregation near dislocation cores. Secondly, since the solubility of both Cu and Ag in Sn is very small, segregation of Cu atoms near cores is likely to displace Ag solute atoms [2.24] from the vicinity of the core because of the higher binding energy of Sn-Cu (3.5eV) relative to Sn-Ag (2.83eV) [2.49], thereby substantially altering the coordination of the near-core Sn atoms. This in turn is likely to result in a measurable difference in the Q for core diffusion. The measured n values, on the other hand, are consistent with previous results, suggesting that despite the difference in measured Q, the operative creep mechanism is the same.

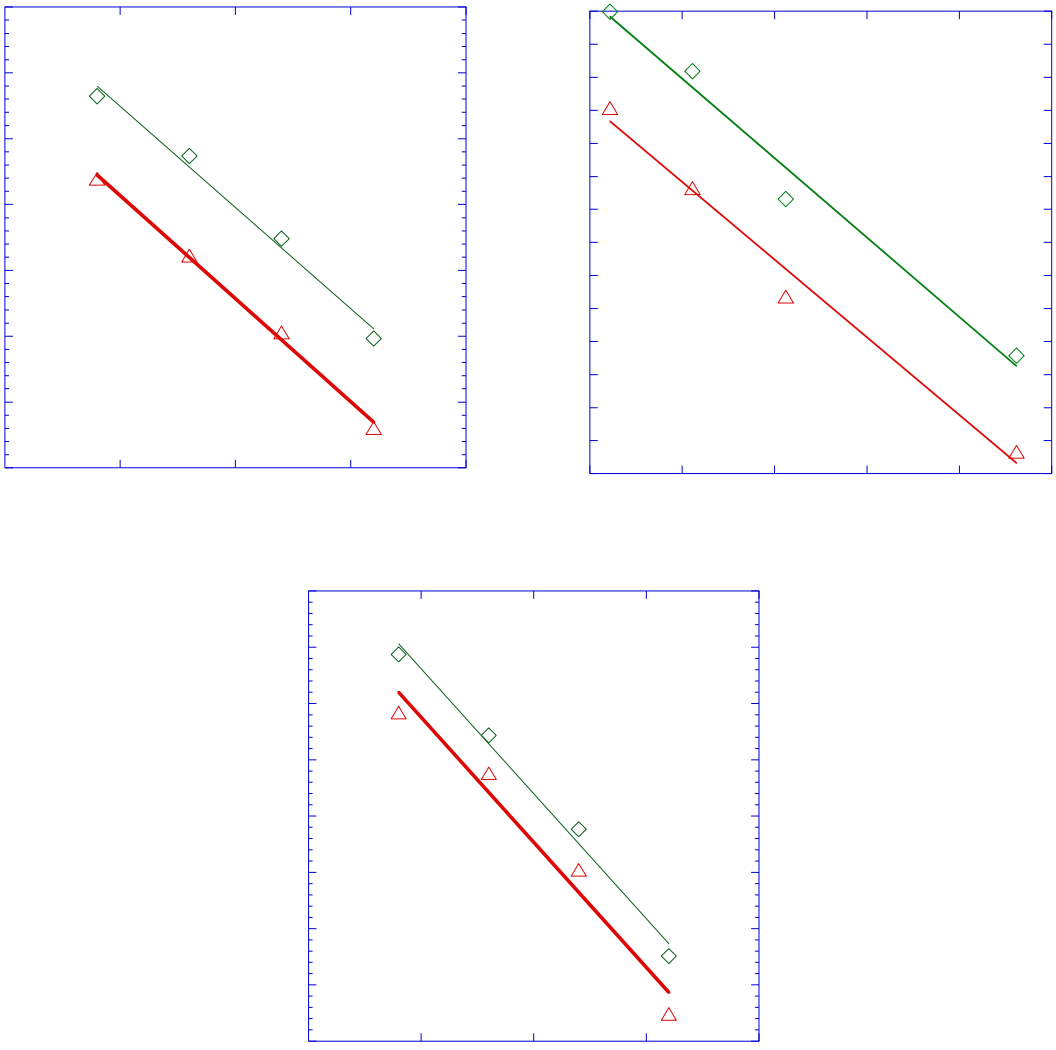

Figure 2.27 Plots of ln(VT/G) versus 1/RT at constant stress, showing the activation energies (Q) for Sn, SAC105, and SAC 305.

Figure 2.28 shows plots of temperature compensated impression velocity vs. modulus compensated punch stress for the SAC alloys following different treatments, using n=6 and Q=50kJ/mole. Clearly, the n and Q values are valid under all conditions, indicating that the creep mechanism remains the same isothermal after aging (IA) and thermo-mechanical cycling (TMC) as in the as-reflowed state. Importantly, increasing aging, which is commensurate with increasing Ag_3Sn coarsening, increases the creep rate of the solder. Table 2.2 summarizes the creep rate for both Sn and the SAC alloys under different conditions.

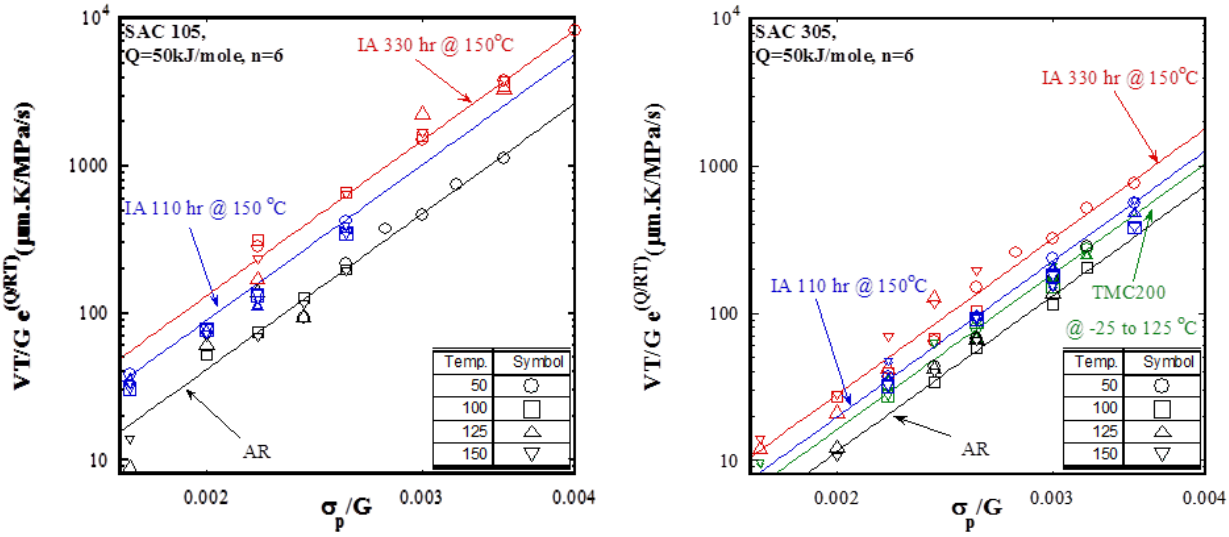

Figure 2.28 Plots of temperature compensated creep rate vs. modulus compensated stress for SAC105 and SAC305 under different conditions (as-reflowed, aged at 150°C for 110h and 220h, and thermo-mechanically cycled for 200 cycles).

Table 2.2. Creep stress exponent n and activation energy Q for various conditions

Alloy	Condition	Inter-particle spacing (μm)	n	Q (kJ/mole)	$\frac{VT}{G}$ at T=50°C, σ_p/G=2.6e-3 $(\mu m.\frac{K}{MPa}/s)$
Pure tin	AR	-	5	43	2.436e-5
SAC 105	AR	1.165215	6	50	1.23e-6
	IA 110hr	4.218082	6	50	3.49e-6
	IA 330hr	5.174574	6	50	3.91e-6
SAC 305	AR	0.629827	6	50	4.30e-7
	TMC 200	0.95235	6	50	5.08e-7
	IA 110hr	2.706486	6	50	1.26e-6
	IA 330hr	3.697727	6	50	1.47e-6

As noted in section 2.1, increasing aging and TMC leads to particle coarsening (higher d_p), and commensurately, greater inter-particle spacing (λ). Figure 2.29 shows a plot of temperature-compensated impression velocity vs. inter-particle spacing λ, showing that creep rate increases linearly with λ in SAC305. This is consistent with previously developed creep models [2.9, 2.23, 2.50-2.52], where the creep rate is proportional to the particle diameter or the inter-particle spacing for SAC405 and SAC387. For SAC105, however, the proportionality between creep rate and λ was not observed in this study, suggesting that when the particle content (i.e., the

amount of eutectic) in the microstructure is low, a deviation from the simple proportionality between creep rate and λ occurs. This warranted the development of a new model, which considers the pro-eutectic phase in addition to the eutectic, and is reported in **Sub-Task 5.1**.

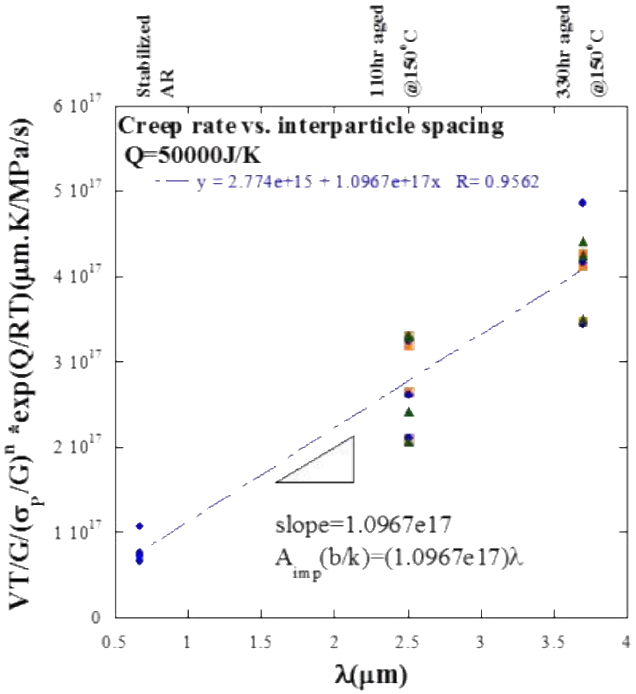

Figure 2.29 Plot of temperature-compensated impression velocity vs. inter-particle spacing λ, showing that creep rate increases linearly with λ

Task 3: Damage/Reliability vs. Microstructure

Professor Borgesen was responsible for this task. The experimental details and a substantial part of our results have been published or submitted for publication, with acknowledgement of SERDP support.

The development of constitutive relations for damage due to fatigue required first of all correlations of fatigue damage with the evolution of the solder microstructure and, of course, with stresses, strains and temperature. A great deal has here been learned from considerations of the totality of a range of different isothermal and thermal cycling tests. A separate effort focused on SnAgCu solder joints with a few percent of Pb. The results of this are included in this section because of their special nature.

Technical Approach

Testing was conducted at both the single joint and the assembly level. In the former case coupons were fabricated by soldering SnAgCu solder spheres onto corresponding organic solderability preservative (OSP) coated Cu contact pads on print circuit boards [3.1]. A no-clean tacky flux was printed onto the pads before placement of the solder balls. Reflow was done in a nitrogen ambient with less than 50 ppm O_2 in a Vitronic-Soltec 10-zone full convection oven with a typical lead-free temperature-time profile (peak temperature 242^{o}C, 45-60 seconds above liquidus). The most common samples were prepared from 30 mil diameter SAC305 solder balls on 22 mil diameter pads. Mixed solder samples were prepared by soldering the SAC305 balls with a SnPb paste [3.2, 3.3]. The effects of Pb addition on solidification after reflow were characterized by differential scanning calorimetry [3.3].

The resulting joints were tested for strength and shear fatigue resistance in a Dage 4000 Bond Tester or an Instron micro tensile tester with a shear tool movement speed of 1mm/s [3.2, 3.1, 3.3]. Figure 3.1 shows the fatigue tool and sketches of how the hollow cylinder makes contact with a joint.

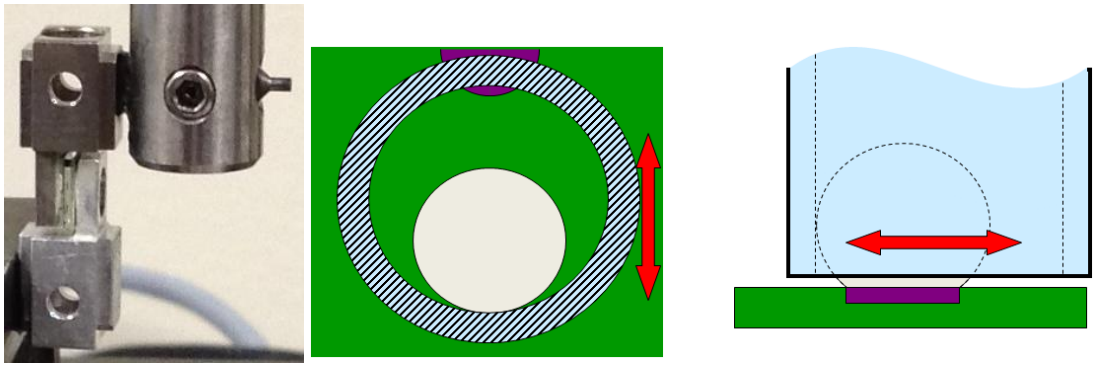

Figure 3.1: (a) Shear fatigue tool attached to Dage or Instron; (b) top view sketch showing how the hollow cylinder contacts a solder joint in cycling; (c) side view sketch.

Thermal cycling tests were conducted on a wide range of commercial and specially prepared model components [3.4 - 3.7]. Systematic studies made particularly effective use of special model components designed to have uniform in-plane properties and negligible warpage during thermal excursions [3.4]. The thermomechanical properties of these components and the

corresponding printed circuit board (PCB) were carefully characterized. The coefficient of thermal expansion (CTE) of the components was very low, 5.5ppm/^{o}C, but the resulting mismatch with the PCB scales with the product of the CTE difference and the component dimensions (distance to neutral point). The results are thus immediately relevant to more realistic larger components with higher CTE values, except that results for realistic components are often affected by component warpage.

A unique experiment was developed to allow for the independent control of important parameters under conditions representative of thermal cycling. In this experiment joints were loaded in shear at low temperature and then exposed to a high temperature dwell. The original strain was reversed either at the low temperature or the high temperature to exclude or include the effect of loading at high temperature [3.8, 3.9].

Solder joints were carefully potted and cross sectioned for characterization by [3.10, 3.11] bright field and cross polarizer microscopy, as well as by Scanning Electron Microscopy (SEM), while Sn grain orientations in selected samples were also measured by Electron Backscatter Diffraction (EBSD).

Results and Discussion

Systematic testing and characterization of the resulting damage and microstructure revealed different damage mechanisms in thermal cycling than in accelerated isothermal cycling. Failure in isothermal cycling tends to occur by transgranular crack growth through the large Sn grains typical of most realistic SnAgCu joints. In contrast, failure in thermal cycling is found to almost always occur by recrystallization of the Sn in the high strain region of the joint, followed by crack growth along the network of new grain boundaries. The reasons for this difference were elucidated through experiments combining isothermal cycling with different thermal treatments before, during and after cycling [3.9].

The above observations allow for mechanistically justified models of damage evolution and failure (see Sub-Task 5.2). The extension of the thermal cycling model to typical long term service conditions was assessed separately, but the picture is not universal, in fact it doesn't even apply to all realistic SAC305 solder joints in typical microelectronics assemblies. As discussed below we have identified types of solder joints where the microstructure is different, or where the configuration leads to a different evolution of damage. The present effort is however focused on SnAgCu solder joints typically found in Ball Grid Array (BGA) and Chip Scale Package (CSP) assemblies, i.e. joints with only a single Sn grain or a few cyclically twinned grains in a so-called 'beach ball' structure (see Task 1**)**. In previously published papers we reported on the strong variations in solder joint strength and fatigue resistance in both isothermal [3.12] and thermal cycling [3.13] with the orientations of the strongly anisotropic Sn grains. These orientations appear to vary in a random fashion in realistic solder joints and tend to dominate statistical variations.

Isothermal Cycling Induced Fatigue of SnAgCu In a previously published study we showed isothermal shear fatigue cycling of SAC305 solder joints to lead to little or no detectable recrystallization before failure [3.14]. This is also consistent with extensive isothermal cycling experiments across a very broad range of temperatures by Korhonen et al. [3.15]. In a separately published work we showed detectable recrystallization after cycling of SAC205 joints to failure [3.12], albeit still not to an extent suggesting a similar damage mechanism as the one found to dominate in thermal cycling (see **Thermal Mismatch Induced Fatigue of SnAgCu** below). Indeed, as documented below recrystallization is enhanced for greater precipitate spacings, as is

fatigue crack growth, and it may well be that crack growth it associated with local recrystallization immediately in front of the crack tip.

Precipitate Coarsening. Aside from recrystallization the only other aspects of the solder microstructure evolution accessibly with the tools and resources available for the present work are coarsening of the secondary precipitates and eventual crack growth. This is of concern in terms of aging of the solder, as addressed in our publication [3.10]. Long term aging leads to reductions in hardness and ultimate strength. Figure 3.2 shows the effects of short term aging at three different temperatures on the subsequent room temperature shear strength for 30 mil SAC305 joints on Cu pads.

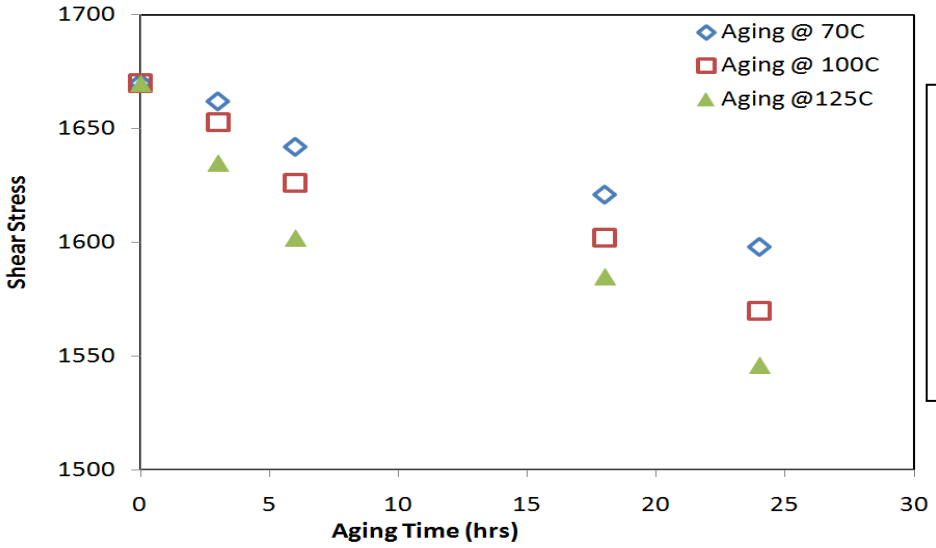

Figure 3.2: Room temperature shear strength at speed of 1mm/sec for 30 mil SAC305/Cu joints after various pre-aging treatments.

Coarsening of the precipitates also led to a reduction in the fatigue resistance of the joints. Figure 3.3 shows the life of 30 mil SAC305 and SAC105 joints on Cu pads in load controlled cycling with a fixed amplitude of 300gf at 100^{o}C as a function of time of pre-aging at 125^{o}C. Cycling to a fixed load does of course lead to a strong increase in inelastic deformation and work per cycle as the solder softens, so it is not surprising that the life is reduced. However, no realistic cycling of an actual assembly leads to a constant load amplitude as far as the solder joints are concerned.

Cycling of assemblies also does not lead to displacement controlled cycling of the joints. Rather, practical situations lie somewhere between the two. If component and substrate are extremely rigid compared to the solder joint the cycling of the latter might approach displacement control, but the difference remains significant in all realistic cases. If component or substrate is extremely compliant, say for a leaded device, variations in the load amplitude on the solder will be much smaller, but usually both load and displacement amplitude still change as the solder softens (precipitates coarsen).

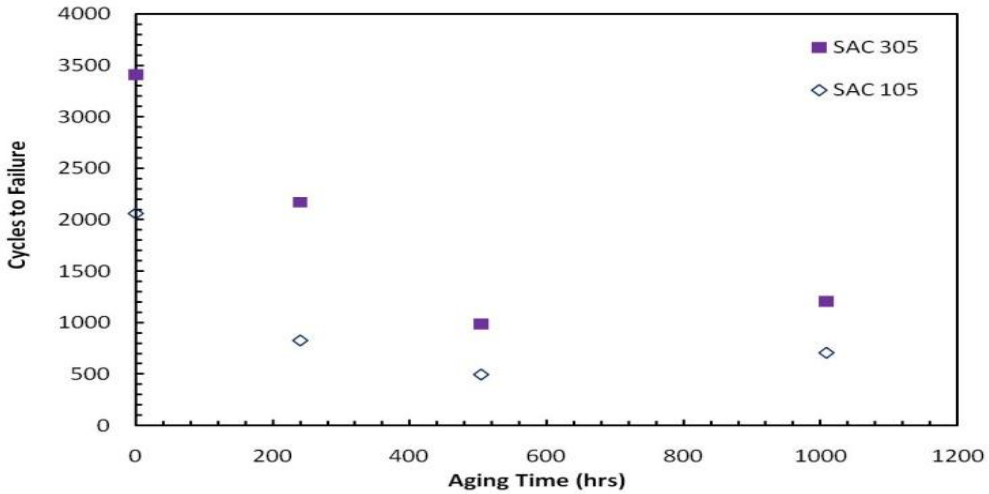

Figure 3.3: Number of cycles to failure in load controlled shear fatigue testing with a 300gf amplitude vs. aging time at 125°C for 30 mil SAC305 and SAC105 solder joints.

A systematic study [3.11] showed that the rate of damage in SnAgCu solder joints during room temperature cycling scales with inelastic energy deposition. We may therefore assess fatigue resistance in terms of the amount of damage caused by a given amount of inelastic energy (work). Figure 3.4 shows the average rate of damage (inverse life time) vs. the average work per cycle for 30 mil SAC305 joints on Cu pads before and after aging for 2 weeks at 125°C. In either case the rate of damage does appear to be proportional to the rate of inelastic work, but a given amount of work is seen to do more damage after coarsening of the precipitates.

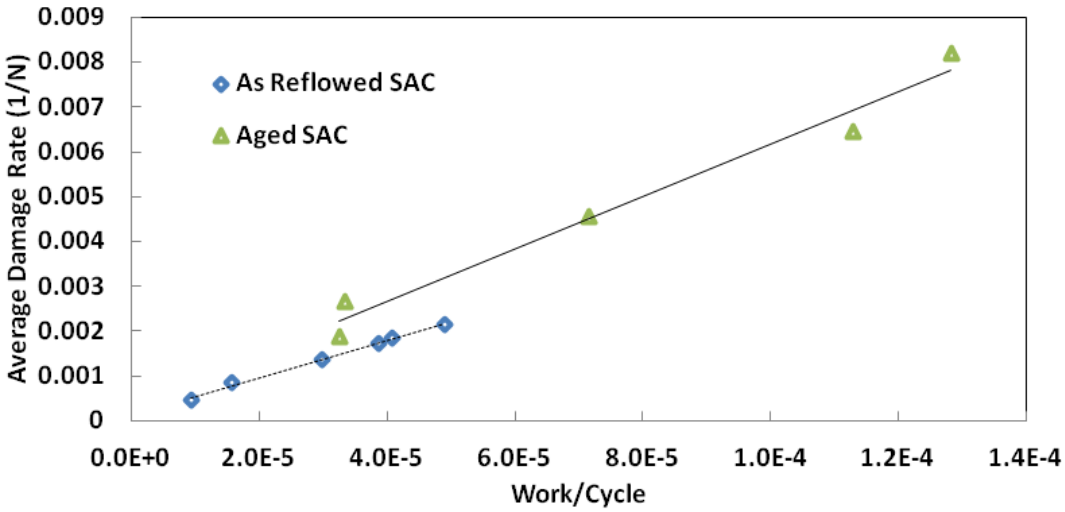

Figure 3.4: Average rate of damage (inverse life) vs. work per cycle for 30 mil SAC305/Cu joints before and after aging for 2 weeks at 125°C.

Dislocation Cell Structures and Slip Bands. As reported in our previously published study [3.16], unlike in thermal cycling (see **Sub-Task 2.1**) strain enhanced precipitate coarsening is not a significant factor during a typical accelerated room temperature cycling test. A special experiment on partially cross sectioned joints did allow us to observe localized slip bands in 30mil diameter SAC405 joints on Cu pads after room temperature shear fatigue cycling. As

expected the evolution of these bands varied quite strongly with Sn grain orientation. Very high peak loads led to slip through several Sn dendrites and the secondary precipitate regions between them, whereas most cycling amplitudes of concern in long term service led to slip bands that remained confined within individual dendrites for a long time [3.16]. We expect such slip bands to serve as nucleation sites for eventual crack growth. Unfortunately, much earlier detection of slip bands would require TEM as would direct observation of dislocation cell structures. This goes beyond the resources of the present effort. Still, important effects could be inferred from a systematic study in which loads and cycling amplitudes were varied for a given joint. This experiment also allowed for an increased sensitivity to systematic trends since a large amount of scatter in the data is eliminated by the study of effects on an individual joint as opposed to comparing different joints. An ongoing NSF sponsored research effort has recently shown these effects not to correlate with the dislocation structures generated in the cycling, and work is ongoing to determine if slip bands are in fact responsible.

Figure 3.5 shows the displacement vs. number of cycles in load controlled shear fatigue cycling of 30 mil SAC305 joints on Cu pads with a peak load of 400gf. Initial hardening of the solder leads to a rapid drop in peak displacement, but this is followed by an extended 'cyclic saturation' stage. The eventual rapid increase in displacement has been shown to coincide with the initiation and growth of an external crack [3.17], but we argue that this is accompanied by softening due to ongoing changes in the stress amplitude.

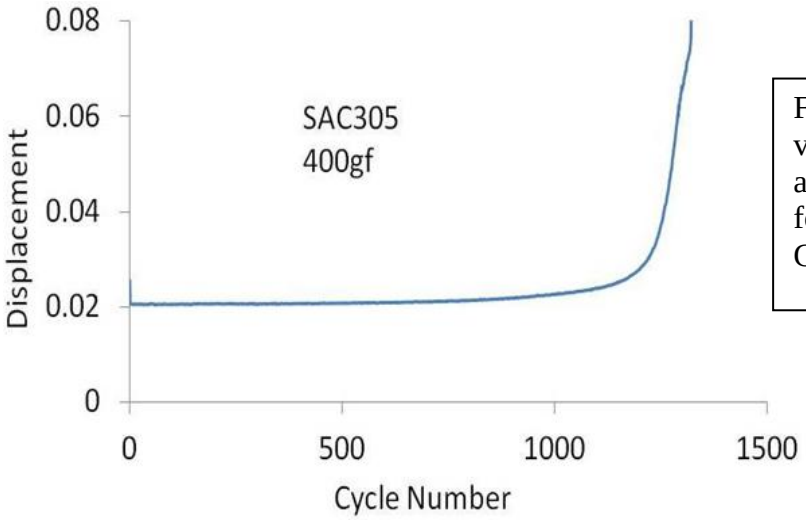

Figure 3.5: Peak displacement vs. number of shear cycles with a fixed load amplitude of 400gf for 30 mil SAC305 joints on Cu pads.

The same trend is reflected in the 'effective stiffness' of the joint represented by the initial slope of the load-displacement curve from the point of zero load in each cycle. At any given stage this value must be reduced to below that characteristic of purely elastic deformation by dislocation multiplication due to critical bowing between obstacles. Figure 3.6 shows both the initial increase in effective stiffness (hardening) and the eventual reduction due to crack growth and softening.

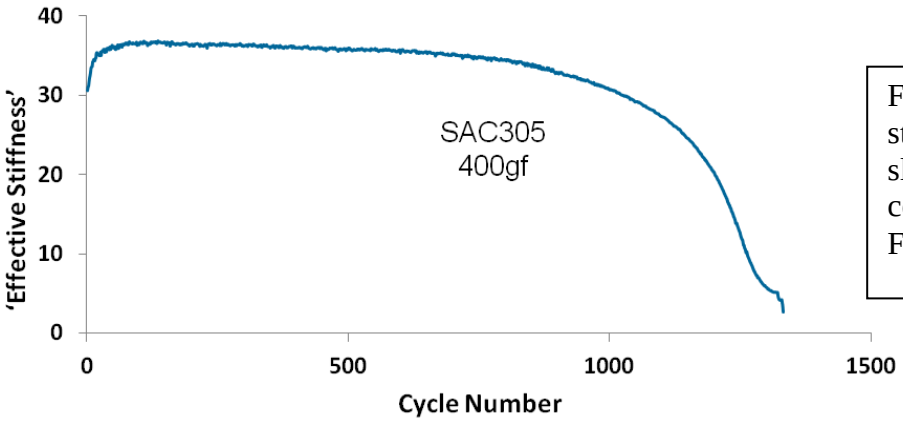

Figure 3.6: Effective stiffness (initial loading slope) vs. cycle number corresponding to Figure 3.5.

As expected, the initial hardening appeared to be faster for higher loading amplitudes. Both the initial value of the stiffness and the saturation level did, however, vary strongly from joint to joint. This is not surprising given the well established variability of solder joint properties with the orientation of the highly anisotropic Sn grains and, to a lesser extent, with the equally uncontrollable degree of undercooling in cool-down from reflow (**Task 1**). Figure 3.7a shows the average ***increase*** in the 'effective stiffness' factor for 30 mil SAC305 joints on Cu pads vs. number of cycles for peak loads of 400gf and 500gf. Values for each load were averaged over 20 joints, suggesting that the establishment of a higher stiffness with a lower peak load is statistically significant. As shown in Figure 3.7b this is a systematic trend over a larger range of amplitudes for different SnAgCu based alloys [3.18].

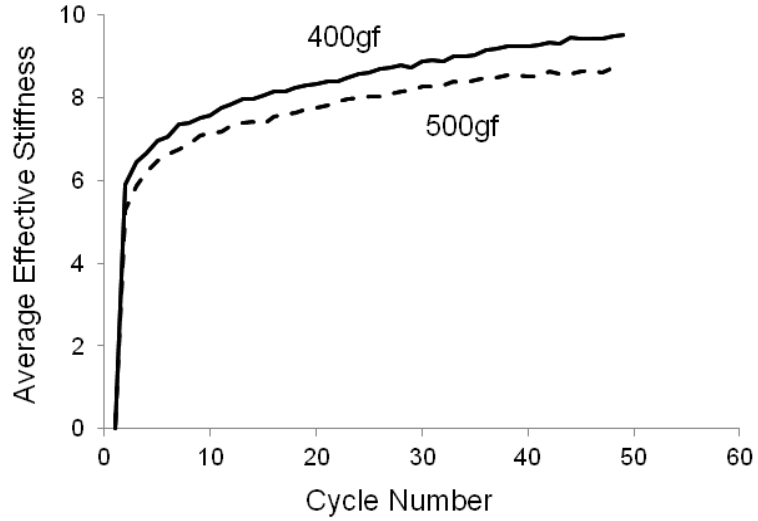

Figure 3.7a: Effective stiffness, averaged over 20 samples each, vs. number of shear cycles with peak loads of 400gf and 500gf, respectively, for 30 mil SAC305 on Cu.

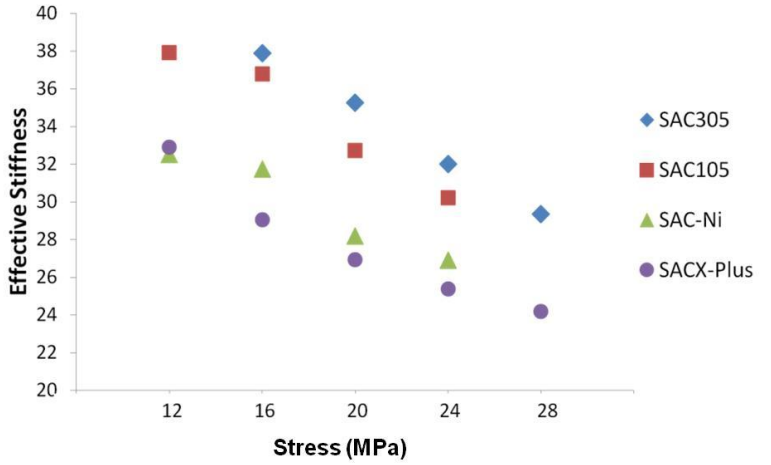

Figure 3.7b: Effective stiffness at 'saturation' vs. stress amplitude for 30 mil bumps of 4 different alloys

The problem with the large statistical variations was largely circumvented by varying the amplitude during cycling of individual joints instead. Figure 3.8 shows the effective stiffness vs. number of cycles in an experiment starting out with a peak load of 300gf. After initial hardening the stiffness levels off at a value of approximately 34. After 1000 cycles the amplitude was raised to 500gf, leading to an almost immediate drop in stiffness. After 50 cycles the peak load was lowered back to 300gf, and the stiffness started to increase again. It did, however, never reach much above 30, i.e. it remained reduced by more than 10% compared to before the harsher cycles. After an additional 1000 cycles with a peak of 300gf another 50 cycles with a peak of 500gf led to a further reduction. The effective stiffness never recovered from this either (Fig. 3.8).

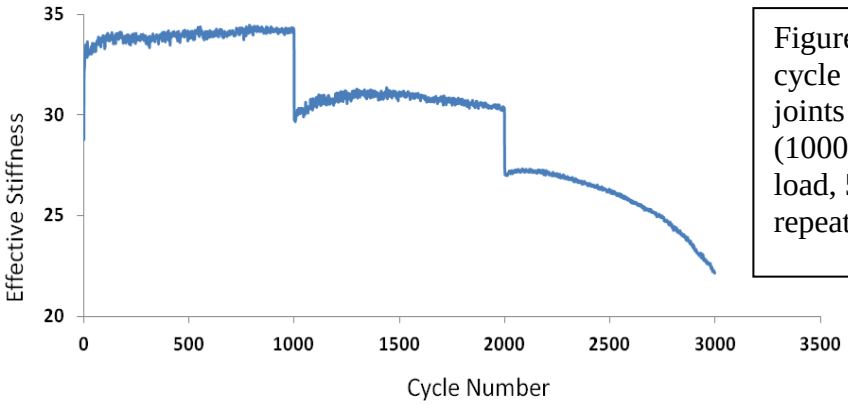

Figure 3.8: Effective stiffness vs. cycle number for 30 mil SAC305 joints on Cu pads. Sequence (1000 cycles with 300gf peak load, 50 cycles with 500gf) repeated 3 times.

The abrupt reduction in solder joint stiffness when the loading amplitude was reduced could not be ascribed to microcracking. Figure 3.9 shows the variation in stiffness with number of cycles for a peak load of 300gf. In this case that cycling was interrupted after 100 cycles and the joint subjected to 100 cycles with a peak of 500gf. The resulting (lower) stiffness values during the 500gf cycling are not included in the figure, but the stiffness can be seen to start about 5% lower and then ***increase*** slightly again during another 100 cycles at 300gf.

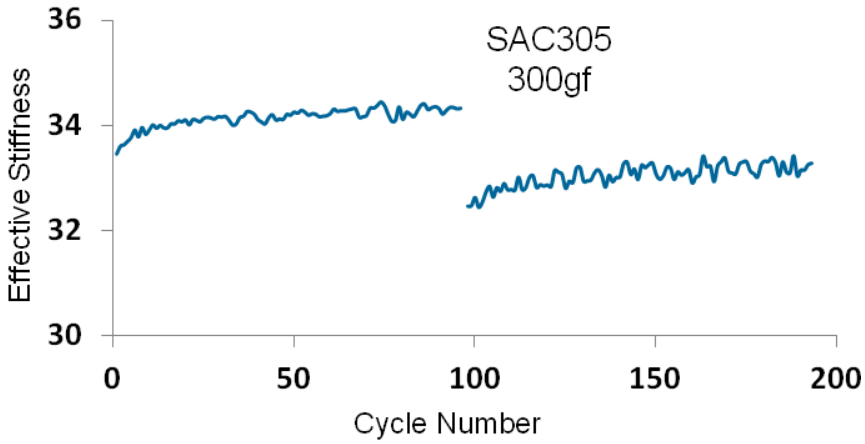

Figure 3.9: Effective stiffness vs. cycle number for 30 mil SAC305 joints on Cu pads cycled with a peak load of 300gf. After 100 cycles the peak load was raised to 500gf for 100 cycles (not shown) before returning to 300gf for another 100 cycles (included)

It is commonly recognized that the initial hardening step during the cycling of a ductile metal with a constant loading amplitude reflects the build-up of a steady state dislocation cell structure, while slow but significant microstructural changes must continue, in spite of the near-balance between dislocation multiplication and annihilation, during the cyclic saturation stage. These changes eventually lead to persistent slip band formation and crack initiation. However, according to the mesh length theory of strain hardening [3.19], and most commonly observed experimentally, larger cycling amplitudes should lead to smaller dislocation cells. Indeed, TEM analysis conducted as part of an ongoing NSF sponsored effort revealed a denser distribution of smaller dislocation loops in SAC305 joints after cycling with a higher amplitude. The suggestion of less hardening for larger peak loads in the case of SnAgCu is therefore non-trivial.

'Memory' effects have in fact been observed in cycling of other metals when amplitudes were varied enough to create completely different dislocation structures, say persistent slip bands vs. cells. In such a case Christ et al. [3.20] found samples to remain ***harder*** after cycling at a higher amplitude, as would be expected. Huang [3.21], on the other hand, did find polycrystalline Cu to be ***softer*** after cycling at a higher amplitude. This trend was ascribed to the evolution of three dimensional dislocation cell structures due to the multiple slip processes activated by the larger amplitude followed by the collapse of these into denser two dimensional loop patches under a lower amplitude where only a single slip plane is involved [3.21, 3.22]. That explanation is however not credible for the SnAgCu system in which multiple planes are expected to remain active at cycling amplitudes much below the present ones. It is not consistent with the systematic trend for different combinations of amplitudes or, notably, with the abovementioned TEM results.

We suggest that some other, competing, modification of the lattice structure, perhaps the formation of slip bands, is responsible for the general trend.

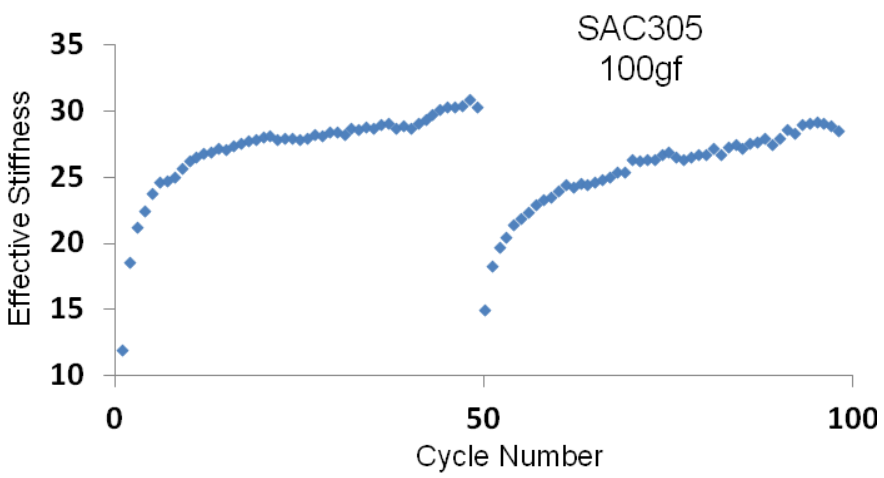

Figure 3.10:
Effective stiffness vs. cycle number for 30 mil SAC305 joints on Cu pads cycled with a peak load of 100gf. After 50 cycles the peak load was raised to 300gf for 25 cycles (not shown) before returning to 100gf for another 50 cycles (included)

Given that the rate of damage varies with the work per cycle, any effect of loading history on the deformation properties is of concern.

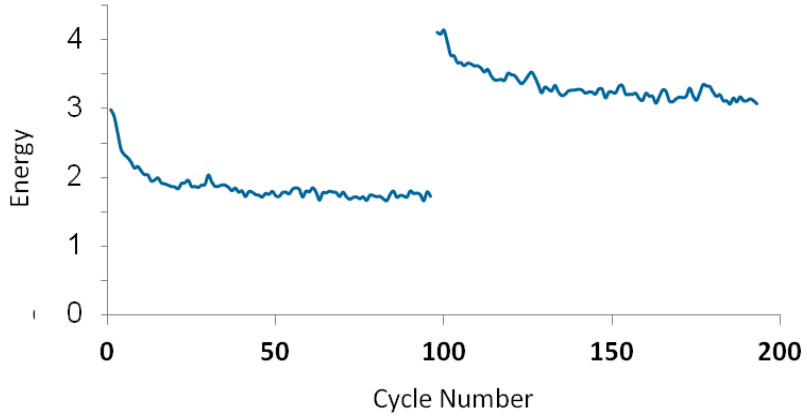

Figure 3.11:
Work per cycle vs. cycle number for 30mil SAC305 joints cycled with a peak load of 300gf, corresponding to figure 3.9. After 100 cycles the peak load was raised to 500gf for 100 cycles (not shown) before returning to 300gf for another 100 cycles (included)

Figure 3.11 shows the inelastic work in each cycle for the experiment first addressed in Figure 3.9. Relatively small changes in stiffness (Fig. 3.9) lead to considerably stronger changes in inelastic energy deposition (Fig. 3.11). In cycling with a peak load of 300gf the joint first hardens slightly and the inelastic energy per cycle drops by about 30%. After 100 cycles with a peak of 300gf the joint was subjected to 100 cycles with a peak of 500gf (not shown). Returning to a peak load of 300gf after that the joint has been softened and the energy deposition per 300gf cycle is now doubled. This is reduced somewhat as the joint hardens again, but it never returns to the same stiffness (Fig. 3.9) and the energy deposition per cycle remains higher (Fig. 3.11). Accordingly, we expect the damage evolution to be faster.

The reverse effect was much smaller. Cycling with a peak load of 300gf led to more hardening than would have occurred in cycling with a 500gf peak (Fig. 3.8), so the energy deposition per 500gf cycles was reduced but not enough to balance out the increases in energy deposition in the subsequent 300gf cycling. Certainly, this explains the observation of strong deviations from Miner's rule of linear damage accumulation documented in [3.18].

The stiffness and the work per cycle vary differently with Sn grain orientation, but for a given joint changes in the two are linearly correlated [3.18]. Given that the work is inelastic

while the stiffness reflects reversible (elastic and anelastic) deformation this correlation may offer an important clue as to the lattice structure changes involved. Resolving this does, however, go beyond the present effort.

Thermal Mismatch Induced Fatigue of SnAgCu It is well established that thermal cycling of SnAgCu based BGA or CSP assemblies tends to lead to dynamic recrystallization of the Sn grains (Fig. 3.12a) and the formation of a network of grain boundaries across the high strain region in the most highly loaded joints [3.23- 3.28]. As documented in detail in our publication [3.29] failure analysis shows fatigue cracks to propagate through the same region (Fig. 3.12b) along or very near the new grain boundaries, as also suggested by others [3.27, 3.28, 3.30], favoring high-angle boundaries.

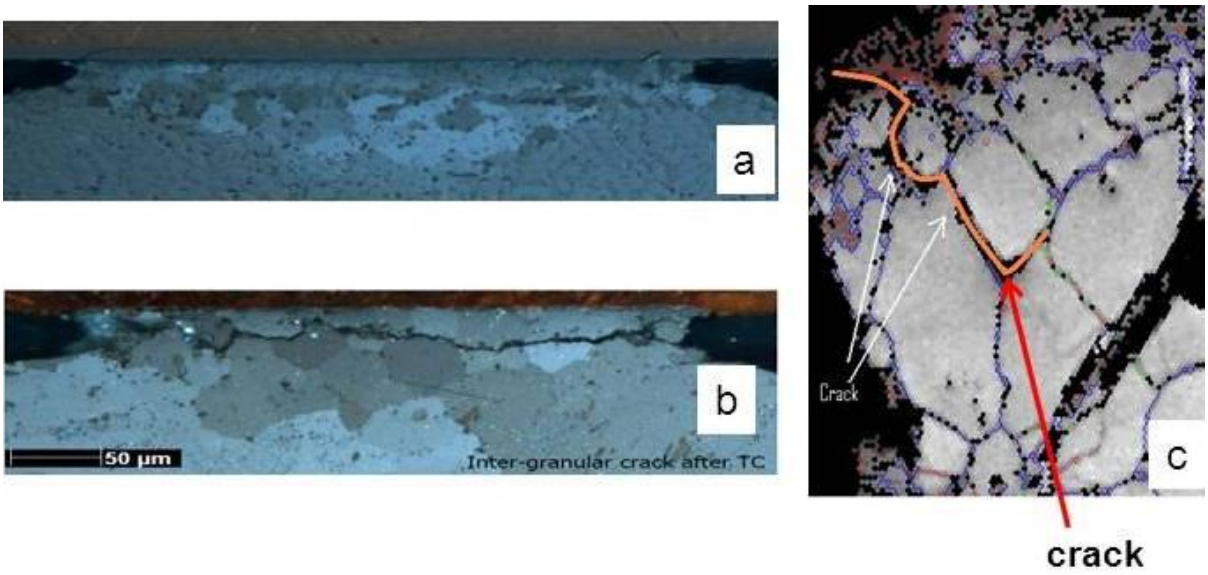

Figure 3.12: Cross polarizer images of solder joint cross sections after different levels of thermal cycling. (a) Recrystallized region with crack in SnAgCu solder joint that started out as single Sn grain after thermal cycling; (b) Fatigue crack through recrystallized region; (c) EBSD of part of SnAgCu sample showing crack growth along high angle grain boundaries.

We found a tendency for the recrystallization process to precede the crack growth. Figure 3.13 shows an example where the bright field image (Fig. 3.13a) reveals a relatively small crack while the cross polarizer image (Fig. 3.13b) reflects extensive recrystallization ahead of the crack. More detailed studies [3.29] showed subgrains to first form within the individual β-Sn dendrites, and eventually in between the densely spaced precipitates as well, after which these subgrains would then rotate during ongoing cycling.

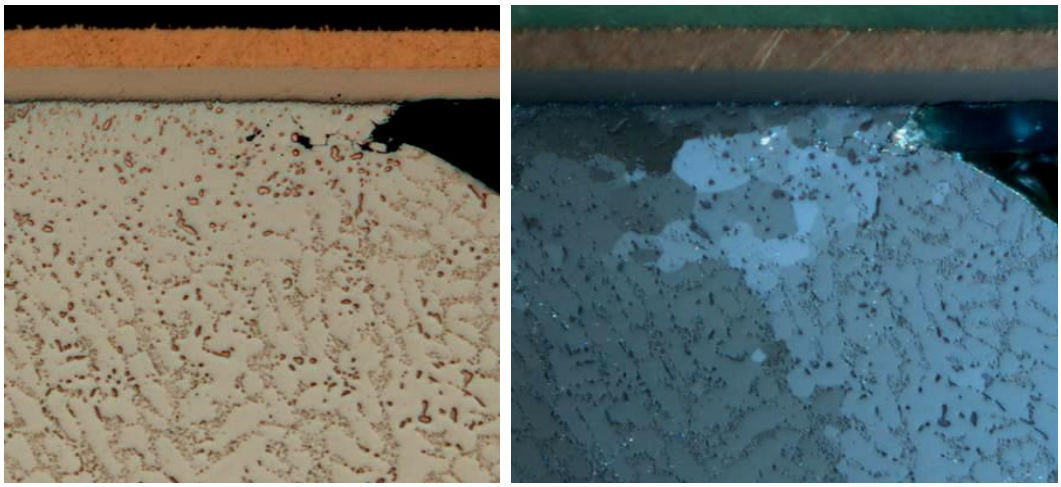

Figure 3.13: Cross section of SAC305 solder after a limited amount of 0/100°C thermal cycling with 10 minute dwells. (a) Bright field image showing the beginning of a fatigue crack; (b) Cross polarizer image showing extensive recrystallization of the original 2-Sn grain structure in the same region.

A separate study, documented in detail in our publication [3.31], quantified the crack growth in some of the same assemblies by interrupting after various numbers of cycles and subjecting them to 'dye and pry'. An improvement over the conventional approach involved replacing the 'prying' step by thermal shock cycling to failure. This ensured the detection of small cracks at a very early stage, and we found crack initiation to occur almost immediately while initial crack growth remained relatively slow. However, the crack growth suddenly accelerated considerably after 25-35% of the total fatigue life (Fig. 3.14). We found this increase in crack growth rate to be consistent with the completion of a network of high angle grain boundaries across the high strain region of the joint [3.29].

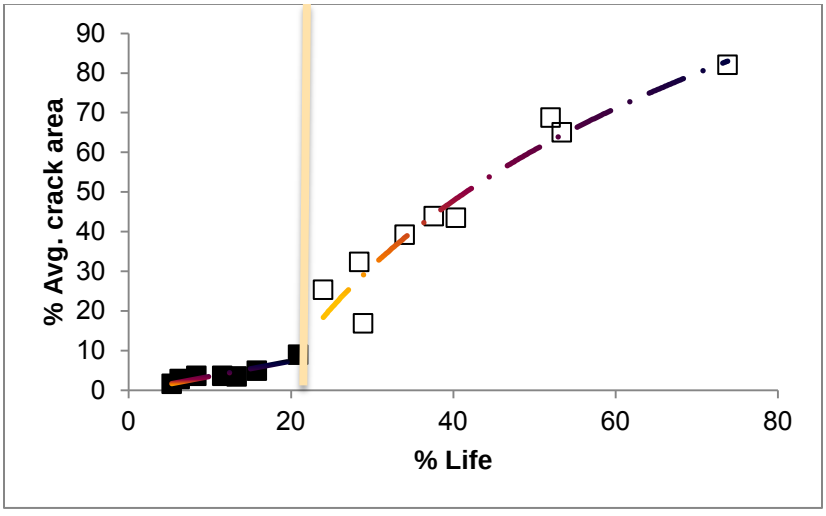

Figure 3.14:
Average crack area (%) in SAC305 solder joints such as those in Figure 3.13 vs. number of cycles in 0/100°C with 10 minute dwells (% of characteristic number of cycles to failure for this assembly)

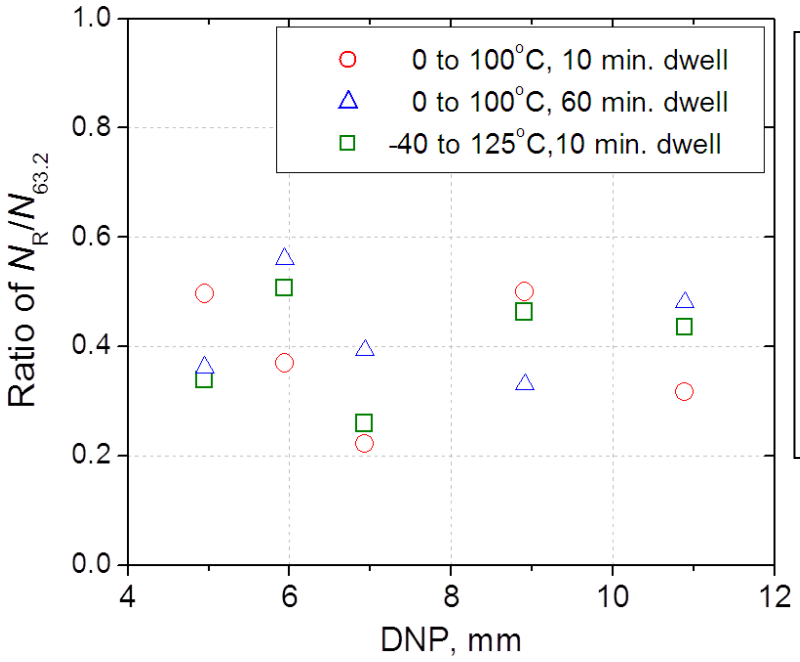

Figure 3.15:
The number of cycles, expressed as fraction of total life, after which cross sectioning revealed a complete network of grain boundaries across the high strain region of the SAC305 solder joint for different cyclic strain ranges (DNPs), temperatures and dwell times.

Figure 3.15 shows results of interrupting thermal cycling of 20mil diameter SAC305 joints at different intervals and characterizing the degree of recrystallization. Each data point reflects the number of cycles, relative to the characteristic life N_{63}, after which recrystallization appeared to be complete. As such, the values consistently overestimate the number of cycles required and offer an uncertainty related to the interval between the present and the previous interruption (after which recrystallization was not yet complete). Five different versions of our model assemblies were tested, with five different distances to the neutral point and corresponding N_{63} values varying by a factor of 6-7 for given thermal cycling parameters. Two different dwell times were considered, 10 minutes and 60 minutes, for the same cycling temperatures, as were two different sets of cycling temperatures. While the uncertainty on each individual data point was considerable, we find no systematic effect of any of the parameters varied. In view of the values all being upper limits we thus conclude that the formation of a complete network of grain boundaries across the high strain region tends to be complete after about 1/3 of the total life. Based on our mechanistic understanding (below) we expect that the completion of such network may take closer to ½ of the total life for smaller joints and/or much milder cycling conditions.

We suggest that the proportionality for a given joint size, where the dominant crack growth stage is in fact longer than the time to recrystallization, suggests a common rate limiting mechanism behind the two. Indeed, EBSD analysis of sub-grain orientations after different numbers of cycles showed that sub-grains continue to rotate after the apparent completion of the recrystallized band [3.29]. This rotation may thus be the crack growth rate limiting mechanism. The actual crack growth may involve thermal mismatch induced stresses between anisotropic Sn grains [3.17], grain boundary sliding induced microvoid formation [3.29], or the increase in grain boundary angle beyond a limiting value. We are currently investigating this within an NSF funded effort, but from the perspective of life prediction it appears that all we have to do to predict the thermal mismatch induced fatigue life is to predict the number of cycles to 'completion' of the recrystallized region.

Recrystallization. A series of experiments was conducted to identify the parameters controlling the Sn recrystallization process in SnAgCu joints. Individual parameters and effects were isolated through combinations of isothermal cycling with different thermal treatments before, during and after cycling.

In a previously published study we showed isothermal shear fatigue cycling of SAC305 solder joints to lead to little or no detectable recrystallization before failure [3.14]. In a separately published work we showed clearly detectable, albeit still minor, recrystallization after cycling of SAC205 joints to failure [3.12]. Motivated by this observed difference and theoretical considerations we characterized the effects of pre-annealing our SAC305 joints to induce coarsening before shear fatigue cycling at room temperature.

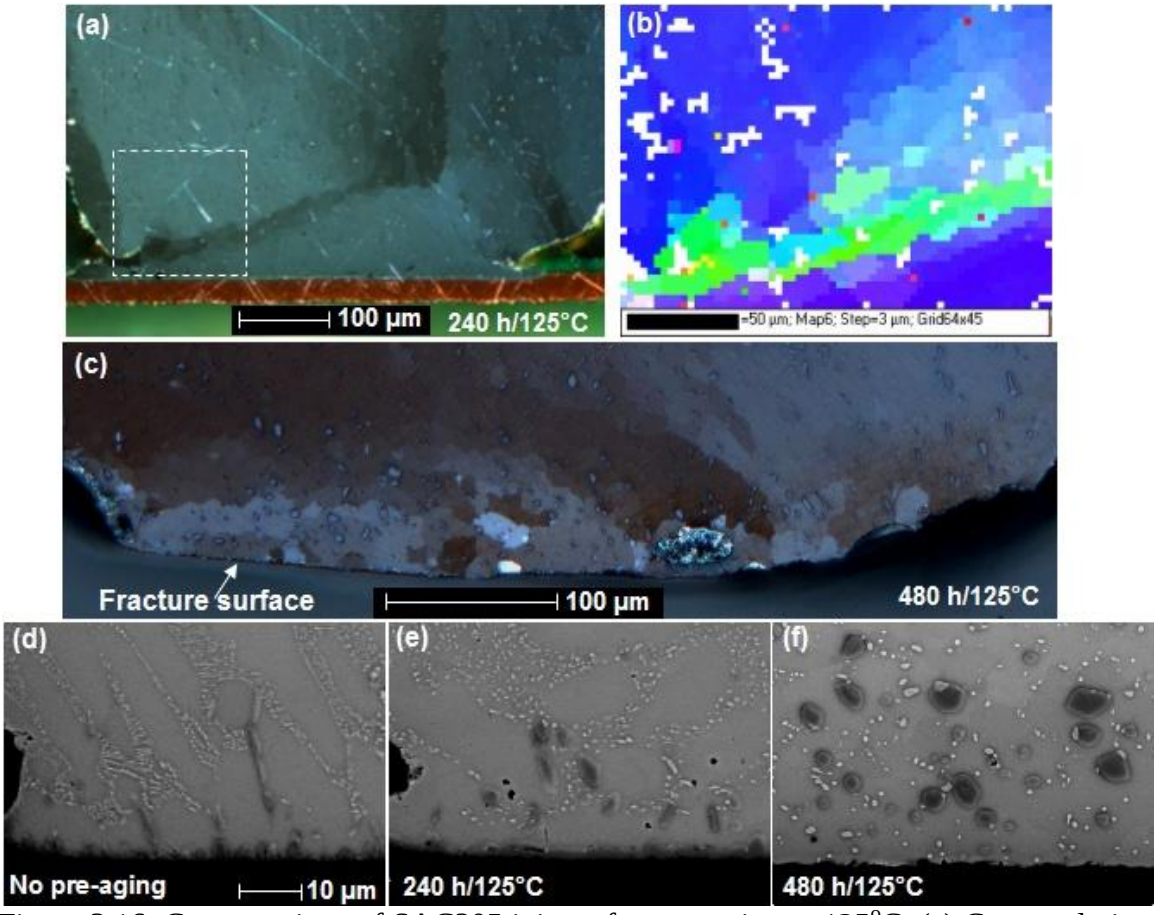

Figure 3.16: Cross sections of SAC305 joints after pre-aging at 125^{o}C. (a) Cross polarizer image of joint after 240hr aging followed by 750 shear fatigue cycles at RT; (b) EBSD image of the enclosed area in (a) confirming recrystallization; (c) Cross polarizer image of joint after 480hr aging and RT cycling; (d) SEM image of joint without aging showing small secondary precipitates; (e) Image of joint after 240hr aging shows precipitate coarsening; (f) Image after 480hr aging shows further coarsening.

In an experiment documented in detail in [3.29] we reflow soldered 0.76mm diameter SAC305 balls onto 0.56mm Cu pads and then pre-aged them for 0, 240 and 480 hours at 125^{o}C. Figures 3.16d-f show typical examples of the resulting secondary precipitate distributions. After aging the individual solder joints were shear fatigued at 100^{o}C with a peak load of 300g. Without

pre-aging there was no obvious sign of recrystallization after 750 cycles. In contrast, joints pre-aged for 240 hours exhibited a visible deformation zone (Fig. 3.16a). EBSD analysis showed this to reflect the formation of new grain boundaries with misorientation angles up to 22^{o} in that region (Fig. 3.16b). Figure 3.16c shows a cross polarizer image of a joint cycled to failure after pre-aging for 480 hours. A clear but still limited amount of recrystallization is evident along the fracture surface. As also evident from the following and experiments documented in our publication [3.2] the enhanced recrystallization is associated with the coarsening of the secondary precipitates.

The question remains whether the effect of precipitate coarsening on recrystallization is related to the precipitate sizes or to the spacings. Figure 3.17a shows a cross polarizer image of an as-reflowed SAC305 joint on Cu after 750 shear fatigue cycles at room temperature. There is no obvious sign of recrystallization. However, joints subjected to the same number of cycles after pre-aging for 240 hours at 125^{o}C showed clear evidence of recrystallization (Fig. 3.17b). This is consistent with our observations above, but this time we are concerned with the extent of recrystallization.

30 mil SAC105 joints on Cu pads recrystallized more readily than SAC305 joints did in the same cycling. Figure 3.18a shows minor recrystallization even without pre-aging. At this point the recrystallization appears to have progressed slightly less than in the pre-aged SAC305 joints (Fig. 3.17b), while it was clearly more extensive after pre-aging (Fig. 3.18b).

Figure 3.19 shows examples of the corresponding precipitate distributions. The precipitate sizes start out comparable in the two alloys. After aging of the SAC305 joint the precipitates are clearly larger than the initial sizes in unaged SAC105 or SAC305 joints.

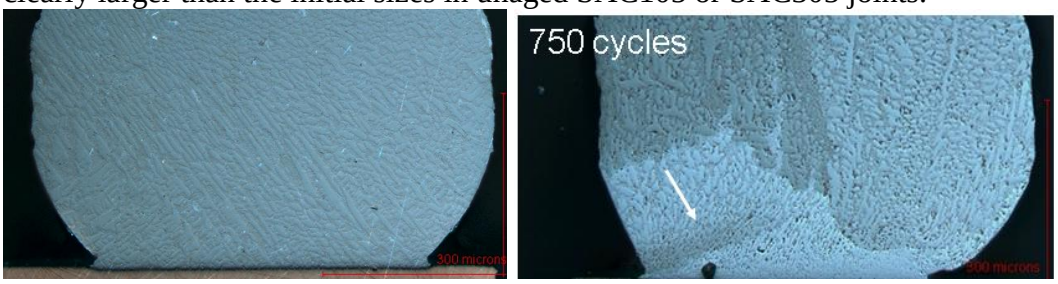

Figure 3.17: Cross polarizer images of cross sections of 30 mil diameter SAC305 joints on Cu pads after 750 shear fatigue cycles. (a) No pre-aging; (b) cycled after 240hrs @ 125^{o}C.

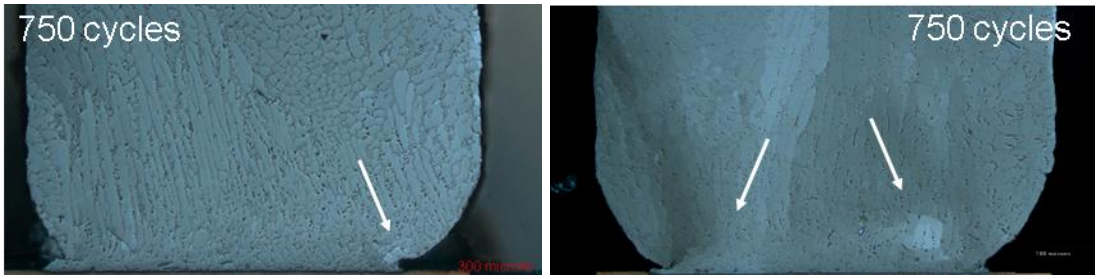

Figure 3.18: Cross polarizer images of cross sections of 30 mil diameter SAC105 joints on Cu pads after 750 shear fatigue cycles. (a) No pre-aging; (b) cycled after 240hrs @ 125^{o}C.

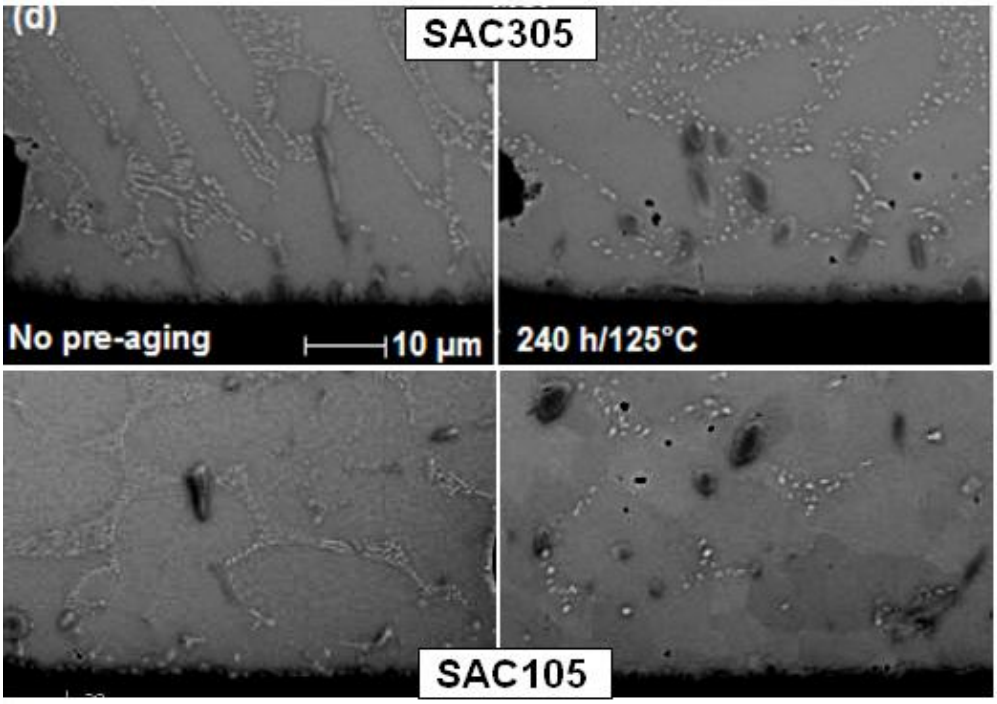

Figure 3.19: SEM of cross sections of SAC305 and SAC105 joints before and after pre-aging for 240hr at 125^{o}C. (a) SAC305 before aging; (b) SAC305 after aging; (c) SAC105 before aging; (d) SAC105 after aging.

Image analysis over considerably greater areas allowed for quantification of both average precipitate sizes and the associated densities (Table 3.1), and it becomes readily evident that the rate of recrystallization varies with the precipitate spacing rather than with the size.

Table 3.1: Effects of aging 30mil SAC305 and SAC105 joints on Cu pads for 240 hours at 125^{o}C on the average sizes and number densities of secondary precipitates.

	Avg. precip. size (µm)	**Precipitates per 1000 µm^2**
SAC305	**0.31**	**767**
SAC105	**0.33**	**299**
SAC305 Aged	**0.46**	**198**
SAC105 Aged	**0.42**	**97**

Turning now to the other factors affecting recrystallization an attempt was made to simulate the conditions known to lead to extensive recrystallization in thermal cycling ***except*** for the repeated excursions to low temperatures. In a simple experiment 30 mil SAC305 solder balls on Cu pads were first aged for 2 weeks at 125^{o}C and then shear fatigue cycled at 100^{o}C using nominal strain rates on the order of $10^{-4}s^{-1}$, i.e. close to those encountered in some accelerated thermal cycling tests. Even though the accumulated time at 100^{o}C was also similar to that in

thermal cycling tests that lead to extensive recrystallization, very little was observed. This was consistent with work by Korhonen et al. [3.15] who used strain rates, dwells and loads typical of thermal cycling in isothermal cycling at 100^{o}C and 125^{o}C without finding any recrystallization. We conclude that the level of recrystallization common in thermal cycling does require loading of the solder to build up dislocation cell structures at lower temperatures.

A systematic experiment, documented in detail in our paper [3.2], addressed different combinations of thermal aging and isothermal shear fatigue testing of 20mil diameter SAC305 solder joints. The apparent systematic can be summarized as follows. In the case of 20 mil SAC305 joints on Cu pads pre-aging for 2 weeks at 125^{o}C may be close to maximizing subsequent recrystallization. Shorter and longer pre-aging was less effective. After a certain amount of pre-aging and subsequent shear fatigue cycling recrystallization was further enhanced by post-annealing at 100^{o}C. Annealing for longer than 15 minutes did not further enhance recrystallization. This does, however, not necessarily suggest that a longer high temperature dwell in thermal cycling, where the joint is still subject to ongoing loading, will not lead to more effective recrystallization. Post-annealing at 150^{o}C led to a strong reduction in recrystallization, an effect that may have consequences for the interpretation of highly accelerated thermal cycling tests. Post-annealing at 70^{o}C led to visible recrystallization but less than annealing at 100^{o}C did. The introduction of a short dwell at maximum load during room temperature cycling was found to further enhance subsequent recrystallization.

Notably, alternating between room temperature cycling and annealing at 100^{o}C was more efficient in producing recrystallized joints. It thus appears that the effective recrystallization across the high strain region of the joint controlling life in thermal cycling is a result of the build-up of dislocation cell structures at or near the low temperature dwell alternating with the coalescence and rotation of the cells, eventually evolving into subgrains that continue to rotate, at the high temperatures. A significant contributing factor is the ongoing temperature and strain enhanced coarsening of the secondary precipitates (see **Sub-Task 2.1**).

'Simulated thermal cycling' experiments showed the low temperature dislocation cell structure to have largely stabilized after a few minutes [3.8], and indeed extensions of the low temperature dwell in actual thermal cycling to beyond 15 minutes had relatively little effect on the number of cycles to failure [3.7]. This, as well as the absence of extensive recrystallization in ***isothermal*** cycling at temperatures typical of the high temperature dwell in regular ***thermal*** cycling (above), would seem to suggest that the life should vary with the steady-state dislocation cell structure established during the low temperature dwell. However the effect of lowering the minimum temperature by 20^{o}C, which should affect this structure significantly, was very limited [3.8]. Lowering the maximum temperature by 20^{o}C had a much stronger effect, but this is consistent with the effect of post-annealing in the absence of a simultaneous load (above) although the magnitude of that effect may be less. More telling is that the life in 0/100C thermal cycling continues to drop as the 100C dwell is extended up to 2 hours [3.7].

All of this led to the suspicion that the dislocations generated during the high temperature dwell may be temporarily 'stabilized' by the low temperature dislocation cell structure and thus continue to contribute to the simultaneous recrystallization. Indeed, a final 'simulated thermal cycling' experiment [3.9] showed that only when a load is maintained during the high temperature dwell is a continuous network of grain boundaries established across the high strain region in the joint. It follows that the rate of recrystallization must be determined by the balance between the generation of dislocations and the coalescence and rotation of them at the high temperature (dynamic recrystallization).

Effect of Coarsening. We showed that the rate of recrystallization is sensitive to the density of the secondary precipitates. This explains both the increase in acceleration factors as solder joint size is reduced and the lower acceleration factors for mixed SnAgCu/Pb joints. For purposes of quantitative modeling the question then remains whether precipitate coarsening is the rate controlling factor, i.e. is recrystallization completed when the temperature and cycling induced coarsening reaches a certain level, or is it significantly affected by other factors?

In order to assess this, two different of our model BGA assemblies were both subjected to 0/100°C thermal cycling with dwell times of 10 minutes and samples were removed after different numbers of cycles before measurement of the precipitate densities. Figure 3.20 shows the densities of secondary precipitates vs. number of cycles for packages with maximum distances to neutral point (DNP) of 10.9mm and 4.95mm, respectively, i.e. for very different cyclic strain ranges. The precipitate coarsening is seen to have progressed considerably less at the time recrystallization is complete (indicated by arrows) for the higher cyclic strain (Package E). While precipitate coarsening does have an effect the rate of recrystallization clearly increases with the cyclic strain (or some parameter that varies with it).

Package A assemblies were also subjected to 0/100°C thermal cycling with two different dwell times. Figure 3.21 shows the evolution of precipitate densities with number of cycles for dwell times of 10 minutes and 60 minutes, respectively. The precipitate coarsening appears to have progressed considerably less at the time recrystallization is complete (indicated by arrows) for the shorter dwell.

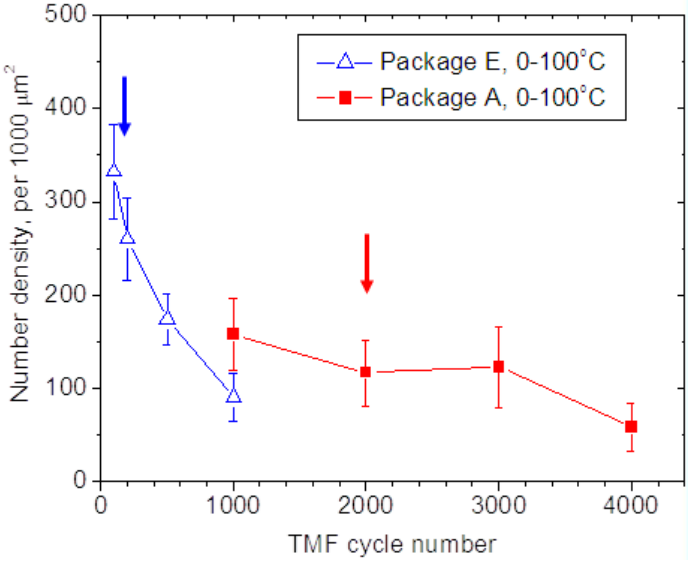

Figure 3.20: Secondary precipitate densities in corner joints of SAC305 based model BGA assemblies vs. number of 0/100°C cycles with 10 minute dwells. Package E has DNP=10.9mm; Package A has DNP=4.95mm. Arrows indicate 'completion' of recrystallized region.

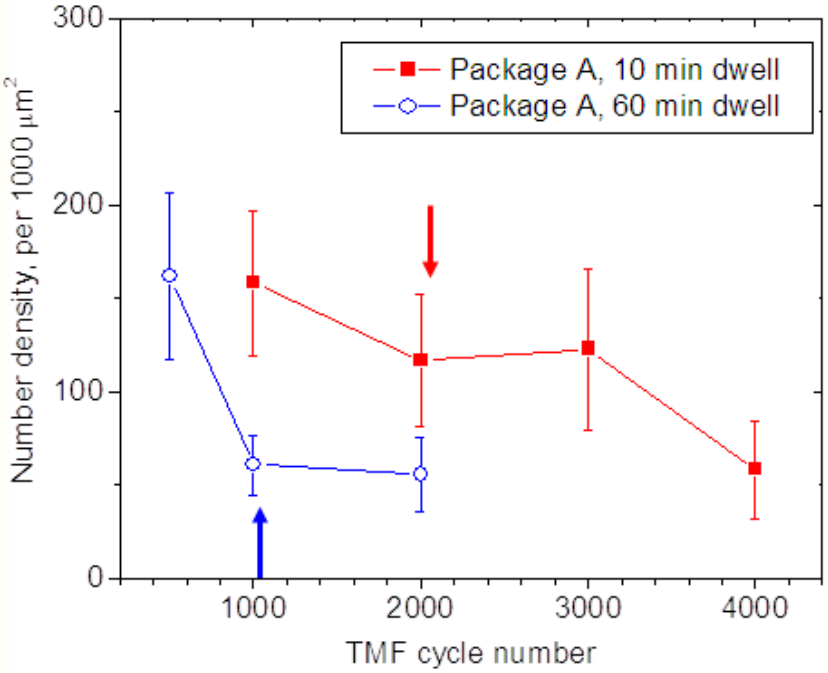

Figure 3.21: Secondary precipitate densities in corner joints of SAC305 based model BGA assemblies vs. number of 0/100°C cycles with 10 minute dwells and 60 minute dwells, respectively. Package A has DNP=4.95mm. Arrows indicate 'completion' of recrystallized region.

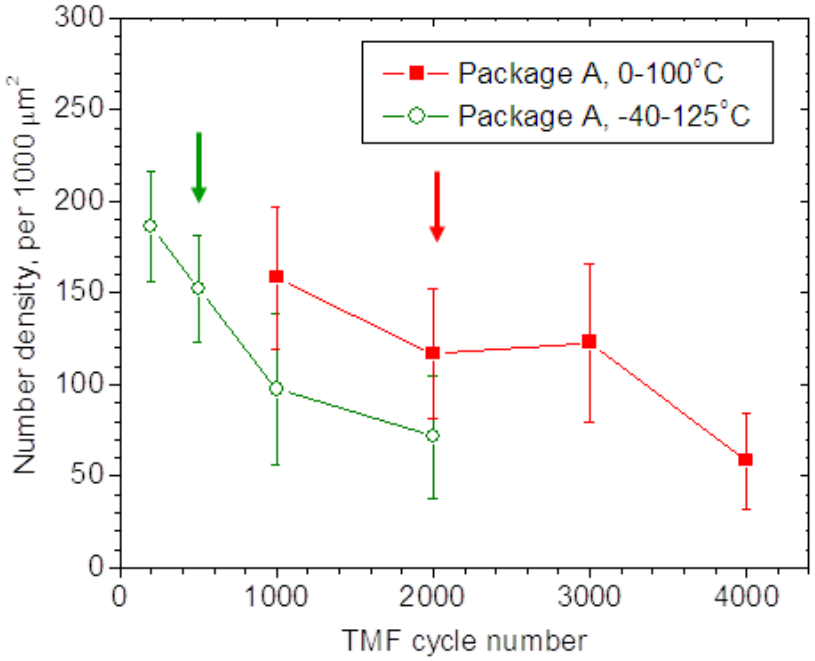

Figure 3.22: Secondary precipitate densities in corner joints of SAC305 based model BGA assemblies vs. number of 0/100°C cycles with 10 minute dwells and -40/125°C cycles with 60 minute dwells, respectively. Package A has DNP=4.95mm. Arrows indicate 'completion' of recrystallized region.

Finally, Figure 3.22 shows the combined effect of cycling temperatures and dwell times on the precipitate coarsening. -40/125^{o}C cycles with 60 minute dwells appear to cause more recrystallization than 0/100^{o}C cycles with 10 minute dwells for the same precipitate densities. Comparing this to the results in Figure 3.21 we see that the effect of the cycling temperatures alone is quite strong, in agreement with the previous assertion that the rate of recrystallization is dominated by a parameter that varies with the cyclic strain (Fig. 3.20).

Relevance to life in service? An immediate concern then becomes whether the same damage mechanism will dominate under realistic long term service conditions as well. An experiment was conducted [3.32] in which our BGA assemblies were cycled between -40^{o}C and 60^{o}C, leading to about twice the life of that observed in 0/100^{o}C cycling. This is consistent with the above observation [3.8] that a reduction in the maximum temperature has a stronger (positive) effect on life than the negative effect of a reduction in minimum temperature. Importantly, failure in -40/60^{o}C cycling was also found to occur by recrystallization followed by crack growth along the new grain boundaries.

Figure 3.23a shows a cross polarizer image of a solder joint removed after 400 cycles between -40^{o}C and 60^{o}C. At this stage there is no obvious indication of recrystallization. In contrast, a similar joint subjected to 400 cycles in 0/100^{o}C cycling showed clear evidence of recrystallization (Fig. 3.23b).

Figure 3.23: Cross polarizer images of SAC305 solder joint cross sections after 400 thermal cycles. (a) No sign of recrystallization in joint cycled from -40^{o}C to 60^{o}C; (b) Clear recrystallization in joint cycled from 0^{o}C to 100^{o}C.

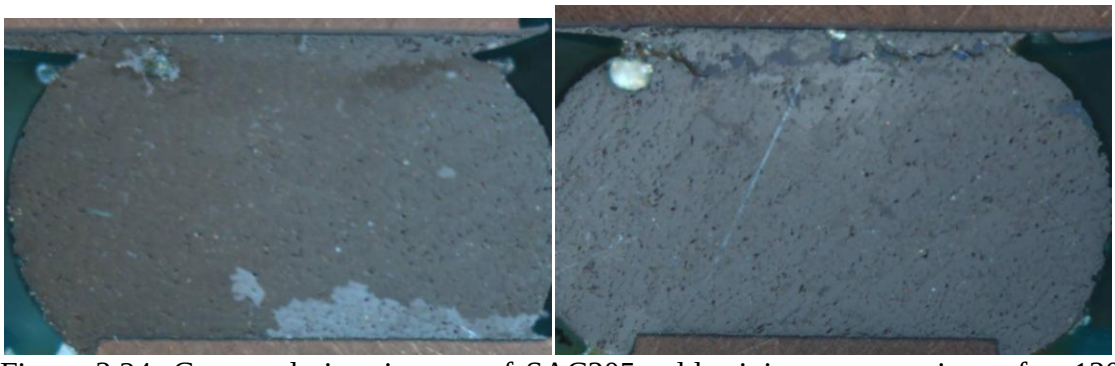

Figure 3.24: Cross polarizer images of SAC305 solder joint cross sections after 1300 thermal cycles. (a) Limited recrystallization in joint cycled from -40^{o}C to 60^{o}C; (b) Complete recrystallization and major crack in joint cycled from 0^{o}C to 100^{o}C.

Similarly, Figure 3.24 shows images of solder joints removed from the two tests after 1300 cycles. At this stage the joint subjected to 0/100^{o}C cycling has completed recrystallization and formed a major crack. Meanwhile, the joint that was subjected to the lower cycling temperatures has started to recrystallize but there are no significant cracks yet.

Finally, Figure 3.25 shows an example of a joint after 1730 cycles from -40^{o}C to 60^{o}C. At this stage recrystallization is complete and a significant crack has formed.

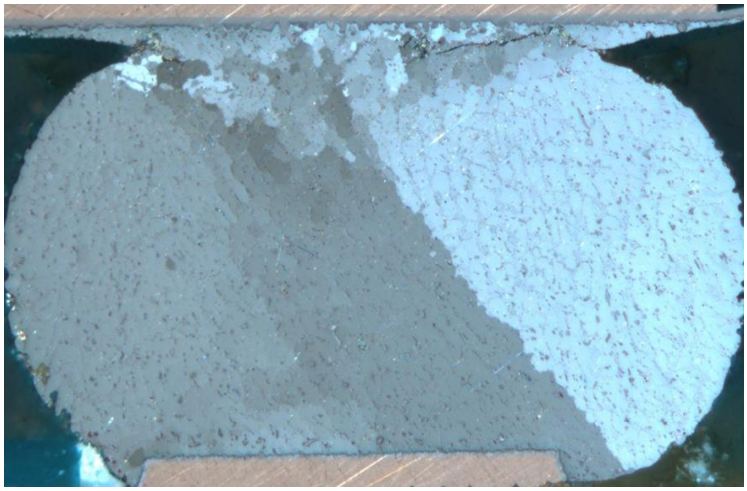

Figure 3.25: Cross polarizer image of SAC305 solder joint cross section after 1730 thermal cycles from -40^{o}C to 60^{o}C.

Figure 3.26: Cross polarizer images of SAC305 solder joint cross sections after 971 thermal cycles from 25^{o}C to 100^{o}C.

Another question that arises is thus whether dwells at room temperature, which would often be the minimum temperature in service, are sufficient to ensure extensive recrystallization. Our BGA assemblies were therefore also cycled from 25^{o}C to 100^{o}C with 10 minute dwells at both extremes [3.32]. Figure 3.26 shows two cross polarizer images of solder joints cross sectioned after completion of 971 thermal cycles. The joints are still far from failure but extensive recrystallization is already evident.

Since this experiment a proprietary industry experiment led to recrystallization and crack growth along the grain boundaries in 0/20C cycling. Only for very high strain ranges is transgranular crack growth so fast that it is completed before the development of significant recrystallization. This was the case for a high strain assembly cycled in -40/125^{o}C where failure

occurred after only 149 cycles [3.8], but not so for other cases where the characteristic life was on the order of 350 cycles or more.

At this point we conclude that thermal mismatch induced fatigue failure of SnAgCu solder joints in typical BGA or CSP assemblies under common long term service conditions is also likely to be controlled by the Sn recrystallization process.

Other Solder Joint Configurations. As far as damage and failure in thermal cycling is concerned the present picture is not universal, in fact it doesn't even apply to all realistic SAC305 solder joints in typical microelectronics assemblies. We have identified types of solder joints where the microstructure is different, or where the configuration leads to a different evolution of damage.

Like most other relevant studies in the literature our systematic investigations have focused on BGA and CSP assemblies. Aside from this configuration considerable efforts have been focused on a similar one with smaller dimensions, e.g. so-called flip chips.

Figure 3.27 shows cross sections of SAC387 flip chip joints between Cu pads on the substrate and NiV pads on the chip before and after 2500 cycles of liquid-to-liquid thermal shock between -55^{o}C and 125^{o}C with 30s ramps and 5 minute dwells at both extremes. Before cycling the joints typically exhibited a so-called interlaced twinning structure near the substrate pads (Fig. 3.27a). Like the 'beach ball' structure interlaced twinning is also the result of a single solidification event and involves only 3 (twinned) Sn grains oriented at approximately 60^{o} to each other. However, the average grain-boundary to grain-boundary distance within the interlaced region, as measured by the line intercept method, was only about 7 μm in this case. We notice also some very large primary Ag_3Sn precipitates in the shape of platelets because of the relatively large Ag content and the strong undercooling associated with the small solder dimensions (see Task 1). After cycling the whole joint was found to have recrystallized (Fig. 3.27b) and fatigue cracks had propagated along some of the new grain boundaries. However, cracks were also found to propagate along interfaces with the large Ag_3Sn and Cu_6Sn_5 precipitates (Fig. 3.27c). This together with possible effects of the original interlacing on the joint properties and recrystallization makes it unlikely that the damage functions developed within the present effort will apply to such flip chip joints. The deformation properties of the interlaced structure are definitely different. Notably, interlaced twinning structures are harder and creep less readily than the beach ball structures [3.33] so the constitutive relations developed based on Task 2 cannot apply.

The interlaced twinning structure is also encountered in other solder joint configurations. Figure 3.28a shows an example for a so-called Land Grid Array (LGA) joint. In this case the average grain boundary to grain boundary distance within the interlaced region was greater, about 30 μm. Because of the large number of grain boundaries, observation of the early stages of recrystallization by polarized light imaging is difficult, but Figure 3.28b shows clear recrystallization after ~3600 cycles of -40/125^{o}C cycling with 60 minute dwells, while fatigue crack development is still limited. At this stage the grain boundary to grain boundary distance had grown to ~ 70 μm. It is not surprising that thermal cycling may lead to the growth of grains as well as precipitates as long as either haven't reach their limits.

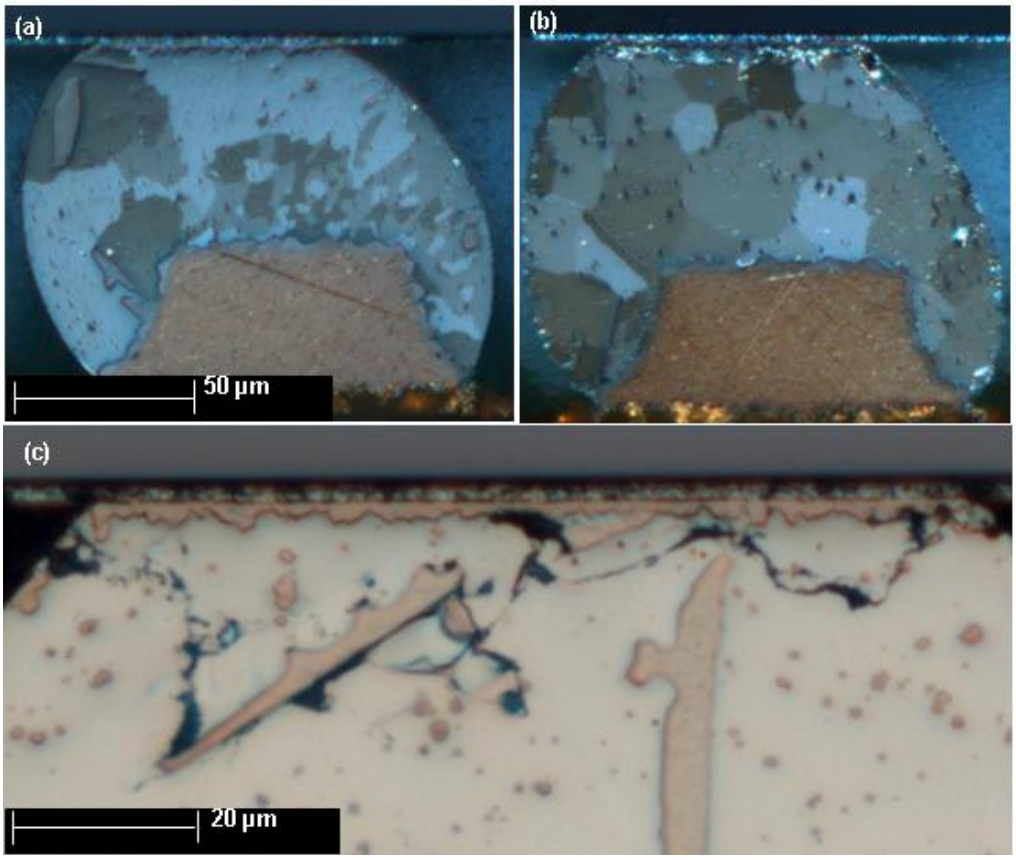

Figure 3.27: Cross sections of SAC387 flip chip joints. (a) Cross polarizer image of as-reflowed joint; (b) cross polarizer image after 2500 cycles of -55°C/125°C with 30s ramps and 5 minute dwells; (c) bright field after same cycling.

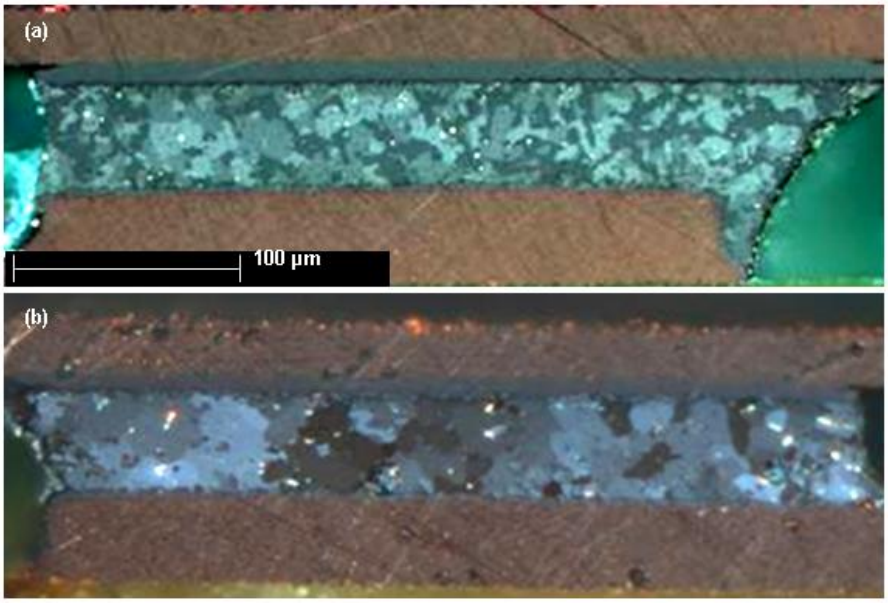

Figure 3.28: Cross sections of SAC387 flip chip joints. (a) Cross polarizer image of as-reflowed joint; (b) cross polarizer image after 2500 cycles of -55°C/125°C with 30s ramps and 5 minute dwells; (c) bright field after same cycling.

The eventual failure mechanism is found to be the same as for BGA and CSP joints (above), but a significant amount of the initial inelastic work goes into simultaneous growth of the Sn grains. This and the different properties of the initial interlaced structure are assumed to be the reason for a rather unique behavior. Figure 3.29 shows a Weibull plot of the cumulative failure distributions for three of our model BGA assemblies in thermal cycling between -20°C and 100°C with 30 minute dwells [3.33]. In this case, three different SAC305 solder ball sizes (10mil, 12mil, and 16mil diameters) were attached to the same components leading to three significantly different solder joint heights (Fig. 3.30). Normally, one would expect the life in thermal cycling to increase systematically with the height of the solder joints, and indeed the 16mil spheres gave a significantly longer life than the 12mil ones (Fig. 3.29). However, the smallest spheres gave the longest life in cycling. Close inspection of the associated microstructures suggest that the smallest spheres tend to give interlaced twinning (Fig. 3.30), similarly to the LGA joints above.

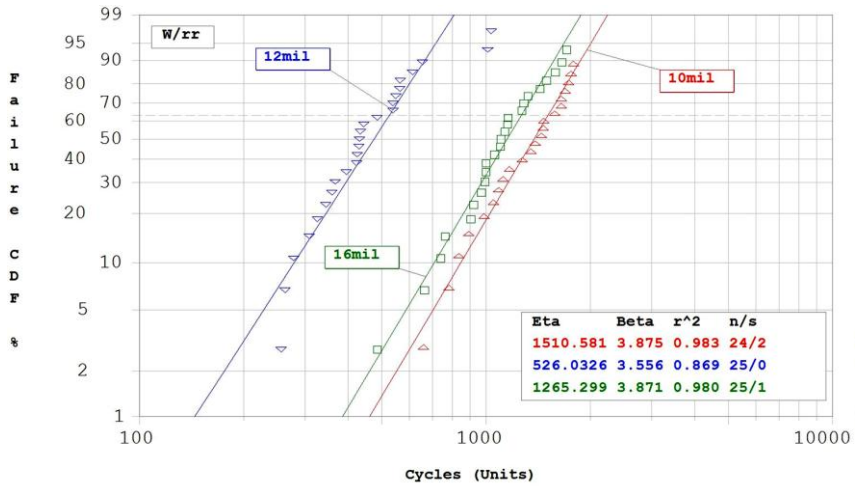

Figure 3.29: Weibull plot of cumulative failure distributions for BGA assemblies made with three different size SAC305 solder spheres in -20/100°C cycling with 30 minute dwells.

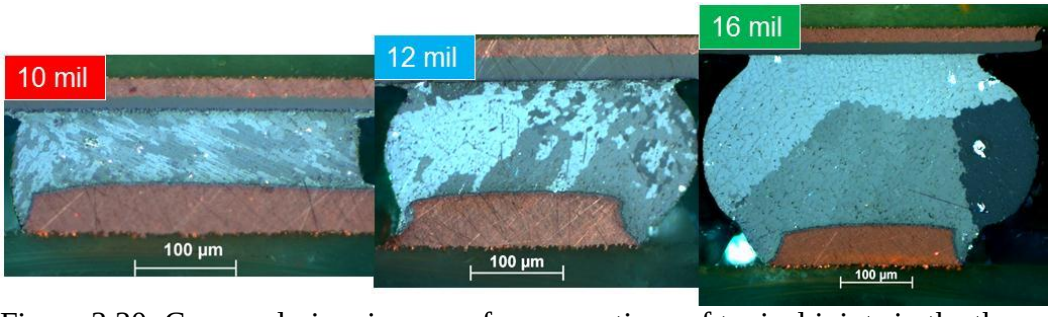

Figure 3.30: Cross polarizer images of cross sections of typical joints in the three different BGA assemblies in Figure 3.29.

Clearly, the approach to damage and life assessment for interlaced joints will have to be modified slightly from that developed for BGA and CSP joints. Variations in life with accelerated thermal cycling parameters were found to be very similar to those observed for BGA

assemblies [3.34], but the interlaced twinning structures are also not stable under thermal aging [3.35] so we expect that acceleration factors to long term service conditions will be different.

Task 1 addresses the question as to when the assumption of a single Sn grain or beach ball structure is going to break down. Interlaced twinning is associated with greater undercooling, and is enhanced by reductions in solder joint size, as well by increases in Ag content and the use of electroless nickel immersion gold (ENIG) solder pad finishes [3.36].

As documented in detail in our publication [3.34], the initial microstructures of so-called Thin Small Outline Package (TSOP) and Quad Flat No-Lead (QFN) package solder joints tended to be single Sn grain or beach ball structure. This is consistent with a dependence of undercooling on the total solder volume and, in particular, the total interface area with Cu surfaces on component and printed circuit board.

In the case of the leaded TSOP devices the evolution of the microstructure to recrystallization and eventual fatigue crack growth along the new grain boundaries in thermal cycling was very similar to the one observed in BGA and CSP joints (above), except for the very final stage where the crack would grow along the intermetallic bond to either the lead or the PCB pad. The latter had a very limited effect on the overall life and indeed variations in life with accelerated thermal cycling parameters were found to be very similar to those observed for BGA assemblies.

The typical QFN joints did, as said, start out with a similar microstructure but in this the damage evolution was quite different. Cracks usually started where the contact pad wraps around the edge of the package within the solder joint and grew considerably before significant recrystallization is observed. A lip or burr at the component edge was thought to introduce a stress concentration that may have facilitated crack initiation, and the crack evolution was clearly not dependent on recrystallization kinetics. Obviously, this means that a different damage function is needed.

It is not clear that QFNs always have such a lip or burr at the edge, but we don't expect our damage constitutive relations to apply anyway. Figure 3.31 shows cross sections of solder joints for a surface mount resistor after different numbers of -40/125^{o}C thermal cycling with 10 minute dwells. The typical fatigue life was approximately 2600 cycles, but significant cracks not observed until after about 20% of that. These first cracks were internal (Fig. 3.31a), originating in the same region as for the TSOP assemblies [3.34], although there was neither a lip/burr nor a sharp corner to concentrate stresses. The initiation and growth of the fatigue cracks from the corner region is in fact not surprising considering the stress distributions associated with this solder joint configuration. Further cycling did eventually lead to recrystallization (Fig. 3.31c), but prediction of this is clearly not going to be sufficient to predict overall life.

In summary, damage mechanisms in thermal cycling are different for solder joint configurations involving an edge, such as in QFN and surface mount resistor assemblies. Our mechanistic picture of microstructure and damage evolution appears to apply to flip chip and LGA assemblies as well, except that the recrystallization of interlaced twinning structures seems to be delayed by initial grain growth. In cases without interlaced twinning our constitutive relations may apply. Solder joints in leaded assemblies such as TSOP appear to fail by the same mechanism as BGA and CSP joints, and our constitutive relations may be expected to apply.

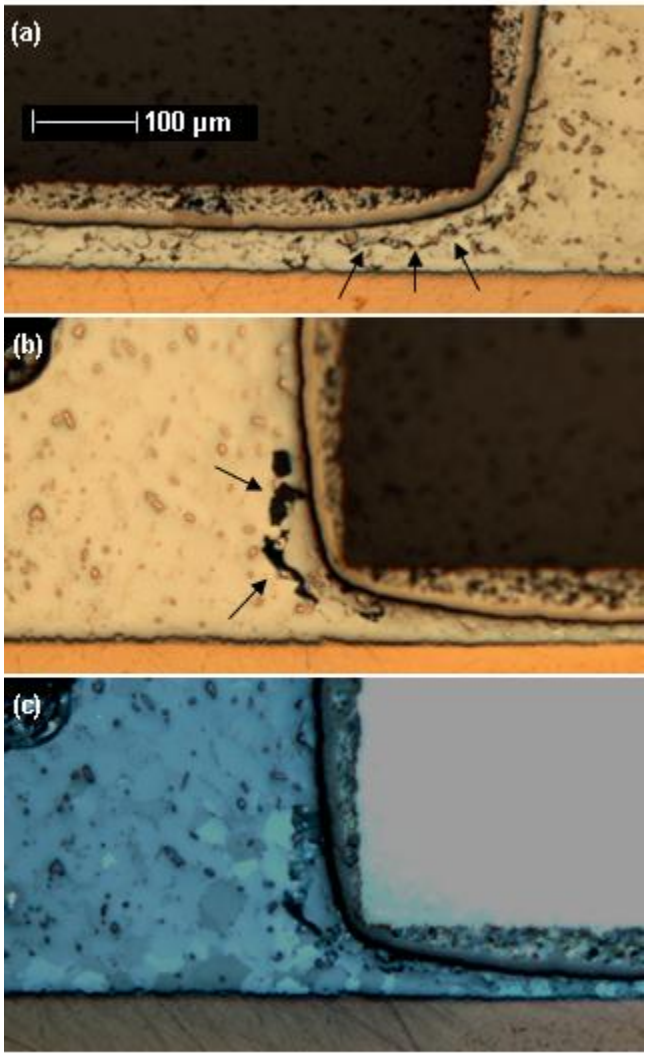

Figure 3.31: Cross sections of surface mount resistor assembly SAC305 solder joints after -40/125^{o}C thermal cycling with 10 minute dwells. (a) and (b) bright field images of internal cracks near component edge after 20% of total life; (c) cross polarizer image after about 50% of life.

SnAgCu Solder Joints Mixed with Pb The addition of a few percent Pb to SnAgCu solder joints in BGA assemblies leads to profound consequences for the microstructure and its evolution. This aspect of our work is covered in detail in our publications [3.2, 3.3].

Mixed BGA and CSP joints still start out with single Sn grain or beach ball structures (Fig. 3.32), but the presence of Pb allows minor eutectic SnPb regions in the joint to stay liquid while the majority of the Sn solidifies. As a result, we end up with larger Sn dendrites and fewer regions with Pb and larger secondary precipitates (Fig. 3.33).

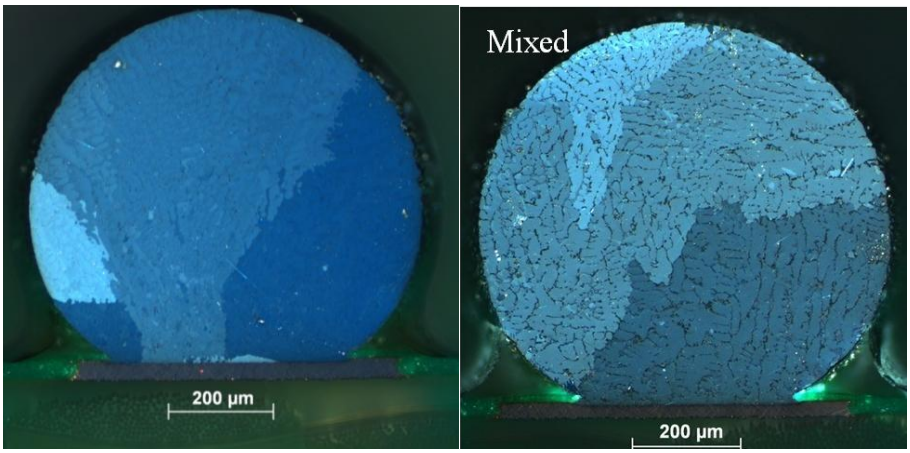

Figure 3.32: Cross polarizer images of cross sections of SAC305 joint (a) and SAC305 joint with approximately 4% Pb after cool down from reflow.

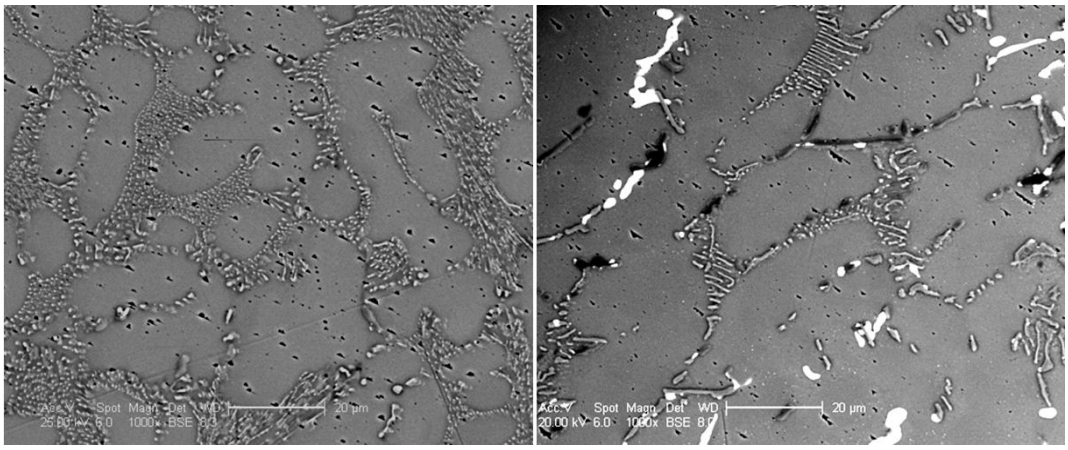

Figure 3.33: SEM images of the cross sections in Figure 3.32. (a) SAC305; (b) SAC305(4%Pb).

Isothermal Cycling.

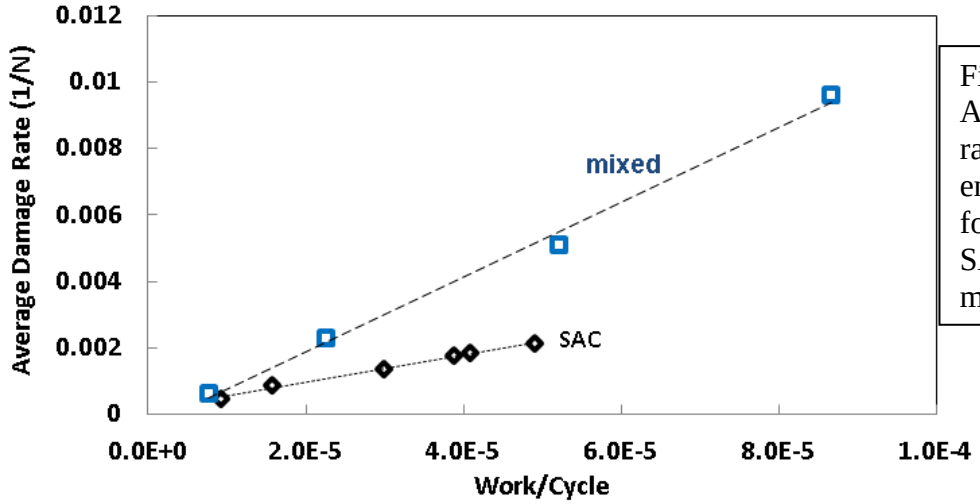

Figure 3.34: Average damage rate ($1/N_f$) vs. energy per cycle for 30 mil SAC305 and mixed joints.

The inclusion of very fine Pb particles within the dendrites is believed [3.3] to be the main reason for the mixed joints to be harder, more brittle and slightly stronger than the pure SAC305. Isothermal cycling of mixed joints with a given peak load leads to less inelastic work

per cycle than for the pure joints. However, the same amount of work does more damage to mixed joints (Fig. 3.34) so they still tend to fail faster even under load controlled conditions.

On the other hand, the mixed microstructure is much more stable under long term aging than the pure solder. Precipitate coarsening is extremely slow and the Pb inclusion density is not visibly reduced. The only noticeable effect of aging are an initial break down of the relatively long Ag_3Sn platelets characteristic of the structure (Fig. 3.33b) and a minor increase in the typical size of the Pb inclusions within the dendrites (without an accompanying reduction in density). It is not clear which of these are responsible for the small increase in solder hardness, but overall the hardness remained stable in aging at 125°C for up to 1.5 years (Fig. 3.35). Unlike for pure SAC305 neither the ultimate strength nor the fatigue resistance changed appreciably in aging either (Fig. 3.36).

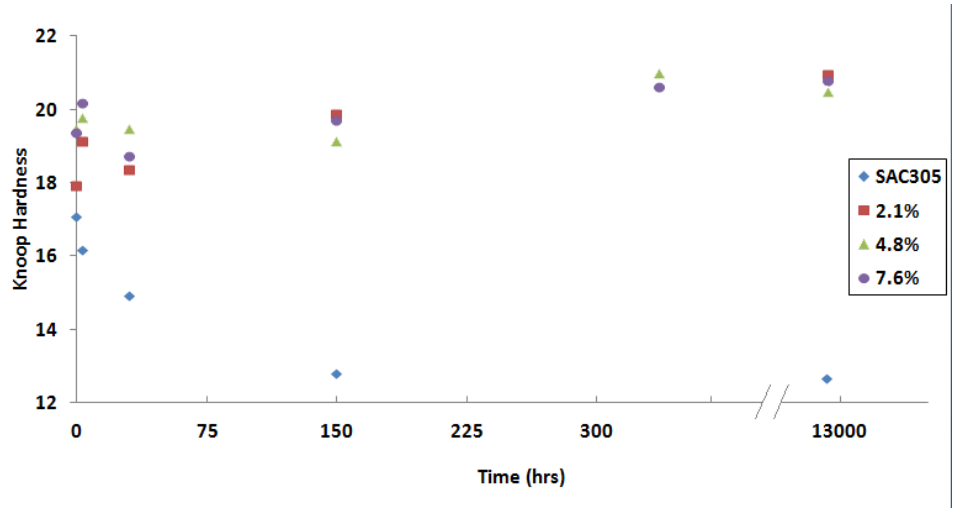

Figure 3.35: Room temperature Knoop hardness of 30 mil SAC305/Cu joints with different Pb contents vs. time of aging at 125°C.

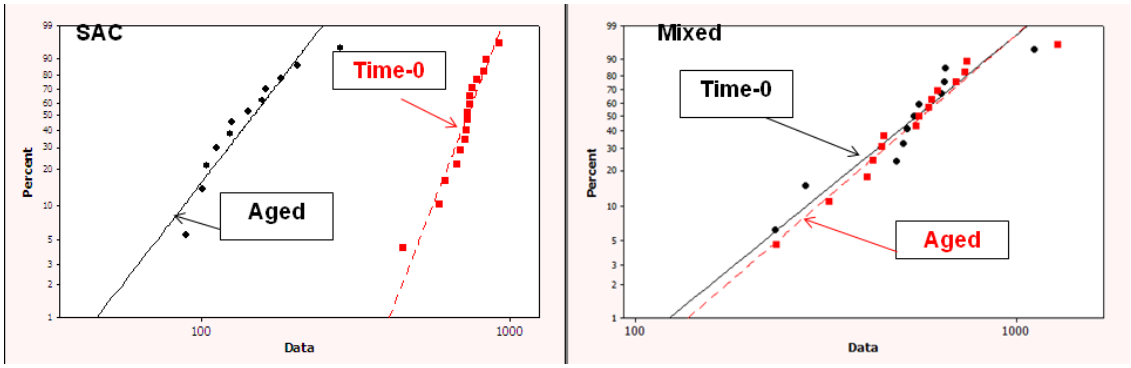

Figure 3.36: Weibull plots of cumulative failure distributions for 30 mil SAC305 joints in room temperature cycling with a constant peak load of 500gf before and after aging for 2 weeks at 125°C. (a) pure SAC305; (b) mixed SAC305(4.8%Pb).

Aging reduced the fatigue resistance of SAC305 joints (Fig. 3.4) but the same amount of work still does more damage to the mixed joints after aging (Fig. 3.37). Nevertheless, as noted above the work per cycle in load controlled cycling is less for mixed, and after 2 weeks at 125°C the pure SAC305 joints now fail faster than the mixed ones (compare Figure 3.36a and b). This

difference increases as the peak load is reduced towards values more typical of long term life (Fig. 3.38).

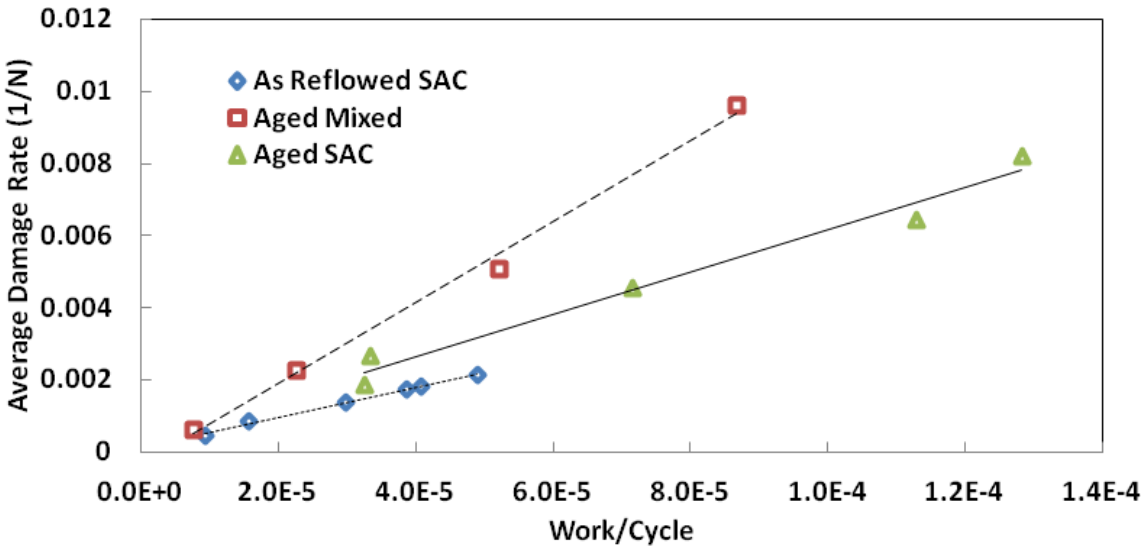

Figure 3.37: Average rate of damage (inverse life) vs. work per cycle for 30 mil SAC305/Cu joints before and after aging for 2 weeks at 125°C.

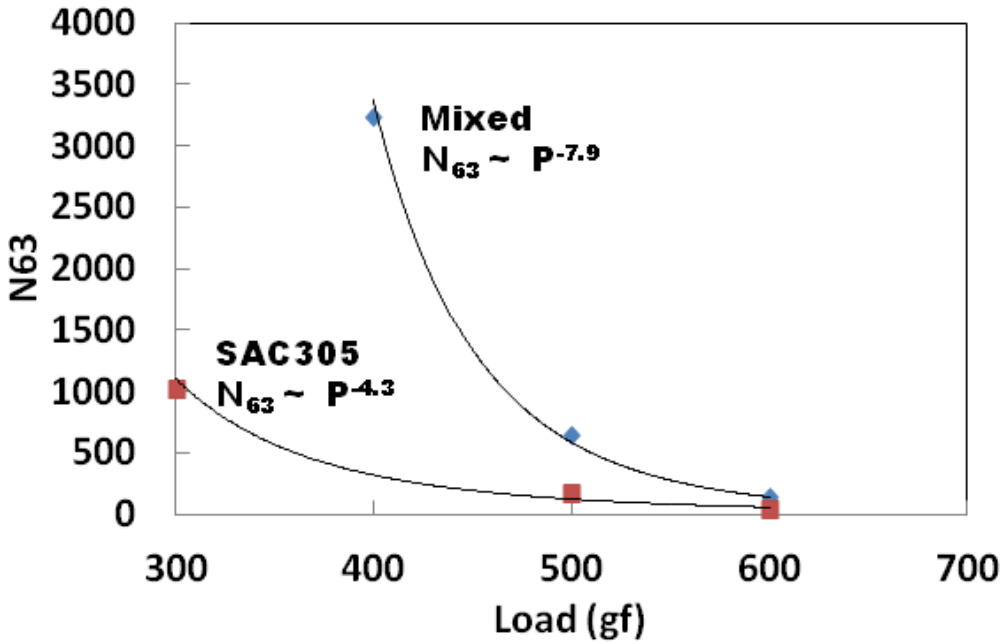

Figure 3.38: Room temperature fatigue life of mixed and pure SAC305/Cu joints after aging for 2 weeks at 125°C vs. peak load in load controlled cycling.

In fact, only if the joints are compared at the same peak displacement do the pure SAC305 joints still outperform the mixed ones after aging (Fig. 3.39). Even then the life of the mixed joints appears to increase slightly faster as the displacement is reduced. Overall, indications are thus that isothermal cycling of an assembly after moderate aging should lead to longer fatigue life for SAC305 joints with a few percent Pb. Exceptions might be for harsh

cycling (life of only a few thousand cycles) of assemblies with extremely rigid component and printed circuit board. Of course, the assembly life may actually end up shorter if failure is dominated by intermetallic bond failure or solder pad cratering as the mixed joints are less compliant. The same would be true for interlaced twinning structures, of course.

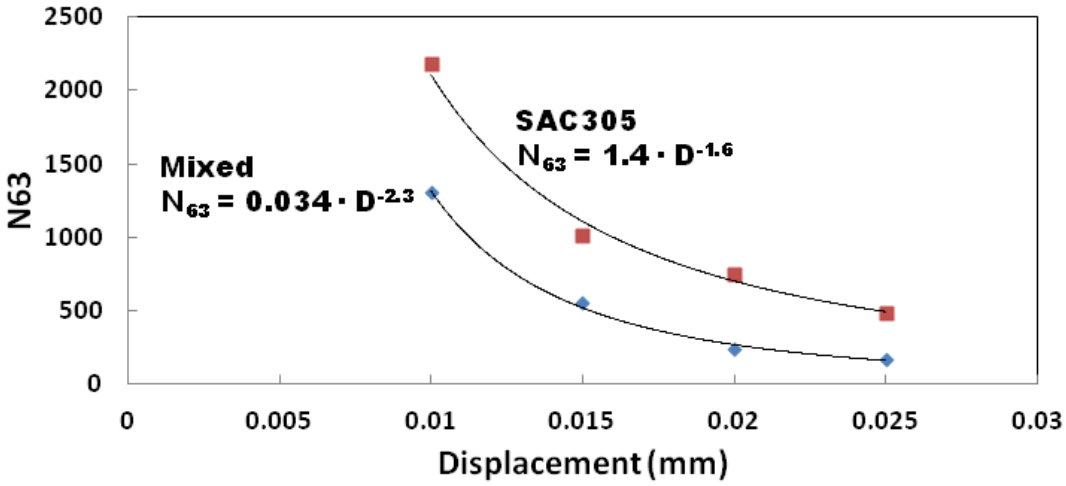

Figure 3.39: Room temperature fatigue life of mixed and pure SAC305/Cu joints after aging for 2 weeks at 125°C vs. peak displacement in displacement controlled cycling.

Thermal Cycling. As noted above (see Thermal Mismatch Induced Fatigue of SnAgCu) and in our paper [3.2] initial precipitate spacings in high Ag alloys such as SAC305 tend to not favor effective recrystallization. Indications are that recrystallization in thermal cycling is enhanced by thermal and cycling induced precipitate coarsening. In the case of mixed joints coarsening remains negligible, but on the other hand the average precipitate density is already lower. The question is whether recrystallization is actually sensitive to the average precipitate spacing, the dendritic arm sizes, or the local spacing between precipitates in the surrounding regions.

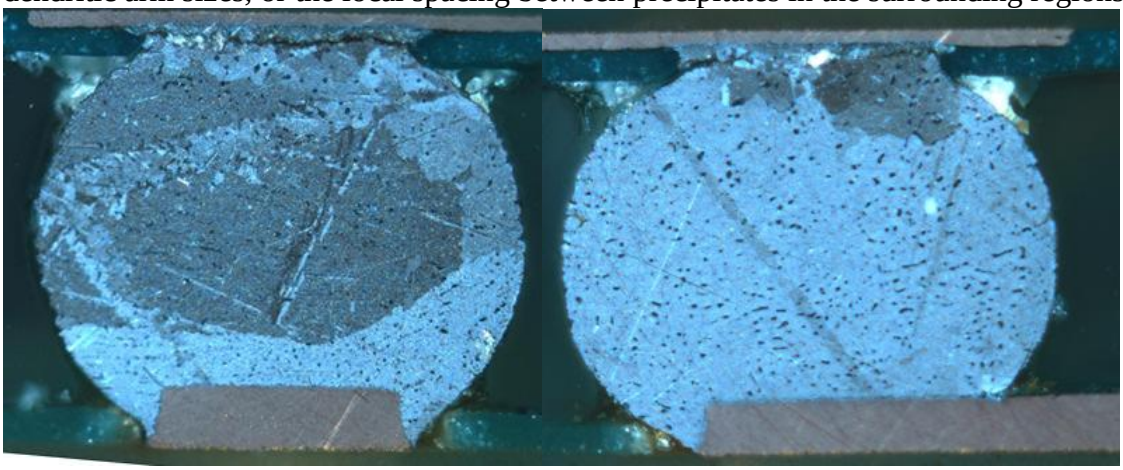

Figure 3.40: Cross polarizer images showing recrystallization of 30 mil SAC305(Pb) solder joints. (a) After 4000 cycles of 0/100°C with 10 minute dwells; (b) after 2600 cycles of -40/125°C with 10 minute dwells.

In fact, indications are that thermal cycling induced recrystallization may be delayed in mixed joints but as also noted in our paper [3.2] it does eventually happen (Fig. 3.40), albeit less

extensively than in pure SAC305. The fatal crack also does appear to grow along the new grain boundary network, but the time it takes to do that may be a considerably smaller fraction of the total life (which is often shorter than for pure SAC305).

Taken together a series of thermal cycling experiments described in detail in our publications [3.4, 3.5, 3.6] revealed systematic trends as far as the effects of mixing is concerned, as well as contributing to our general understanding of the damage mechanisms leading to failure of SnAgCu based solder joints in thermal cycling (see Sub-Task 5.2).

Conclusions

A systematic mechanistic understanding has been developed of the damage and failure of SnAgCu solder joints in both isothermal and thermal cycling. Our picture applies to single Sn grain or 'beach ball' solder structures in BGA, CSP and TSOP assemblies. The general picture also applies to smaller joints in LGA and flip chip assemblies, and to SnAgCu joints with a few percent of Pb, but separate constitutive laws will be required for predictions of life. QFN and SMT resistor joints have similar structures, but the damage mechanism in thermal cycling is different.

Isothermal Cycling. Cycling of a SnAgCu solder joint with a fixed loading amplitude leads to the rapid build-up to steady state deformation properties after which the joint hardness and work per cycle remains almost constant until the peak stress changes. One reason for a change in stress amplitude, even for a fixed peak load, would be the growth of a crack. The deformation properties depend on the peak stress, a ***larger*** amplitude leading to a ***lower*** hardness of typical BGA scale Sn3Ag0.5Cu joints. This happens even though the higher amplitude leads to a denser distribution of dislocation loops. Anyway, the deformation properties keep changing during crack growth. During cycling of an assembly the changes will depend on, among other, the rigidities of component and substrate. If component and substrate are both extremely rigid compared to the solder joint the stress amplitude may decrease, and the solder hardness thus increase, during crack growth. If the component or substrate is extremely compliant, on the other hand, variations in the load amplitude on the solder will be much smaller, so the stress amplitude is likely to increase and the solder will soften. These trends will affect the work per cycle in opposite directions. These effects need to be overlaid on the commonly recognized changes in peak loads and displacements due to the reductions in load bearing area by the crack growth.

Current indications, subject to further verification, are that the rate of damage evolution is given by the work per cycle (see also sub-section 5.2a). This relationship does vary with precipitate coarsening, however.

Thermal Cycling. Thermal mismatch induced loading leads to almost immediate initiation of a fatigue crack, but this grows relatively slowly until the completion of dynamic recrystallization across the high strain region of the joint. Cracks then grow much faster along the network of new high angle grain boundaries. Although the latter takes longer than the recrystallization stage we can predict life as 2-3 times the number of cycles to 'completion' of the recrystallization. Recrystallization of high-Ag alloys like SAC305 is delayed somewhat by the high density of secondary precipitates and thus enhanced by precipitate coarsening in aging or cycling, particularly for small joints and/or the low strain ranges typical of long term service.

Extensive recrystallization requires the effective build-up of dislocation cell structures at low temperatures, but the rate is dominated by the simultaneous generation and the coalescence and rotation of dislocation structures at high temperatures. The repeated alternations between high and low temperatures account for recrystallization dominating damage and failure in

thermal cycling while it does not in isothermal cycling (even with intermittent excursions to high temperatures).

This allows for identification of the parameters of a damage function (see Sub-Task 5.2). The same picture applies even if the temperatures never drop below room temperature and the maximum (operating) temperature is as low as 60^{o}C.

Mixed Solder. The addition of a few percent Pb leads to significantly different secondary precipitate distributions and the inclusion of very fine Pb particles within the Sn dendrites. This makes the solder harder and more brittle than in the corresponding pure SnAgCu joint and there is no indication of softening in long term aging.

The mixed solder is less fatigue resistant (the same amount of work does more damage to it) but it may end up lasting longer in isothermal cycling of realistic assemblies after moderate aging. In thermal cycling the eventually damage and failure mechanism is the same as for the pure SnAgCu, recrystallization and crack growth along the network of new grain boundaries.

Task 4: Interim Report

An interim report was submitted in March 2012.

Task 5: Constitutive Laws

The development of dynamic constitutive laws required first a mechanistic understanding of the relationships between deformation properties or damage function and the evolution of solder microstructure. These laws are specifically intended for single Sn grain or 'beach ball' solder structures as typically found in BGA, CSP and TSOP assemblies (see Task 3). These types of assemblies are commonly the first to fail in cycling of a printed circuit assembly. QFN and SMT resistor joints tend to have the same structures, but our damage function will not apply there. LGA and flip chip joints may have interlaced twinning structures, in which case our microstructurally adaptive deformation (creep) models do not apply. Thermal cycling leads to recrystallization with the formation of a polycrystalline region across the high strain part of the joint, at which point the overall joint deformation properties are certain to change. However, we shall base our predictions of life in thermal cycling on the prediction of the recrystallization step, i.e. we won't need the properties after that. Isothermal cycling by itself does not affect the precipitate distributions, so in that respect all we have to do is account for effects of thermal aging. Unfortunately, variations in stress amplitude do have permanent effects on the deformation properties. This goes beyond the scope of the present work, so we will focus on isothermal cycling with a fixed amplitude.

On a special note, it was never the goal to develop constitutive laws for SnAgCu solder joints mixed with Pb. One reason is that these laws are certain to vary with Pb content as well as with almost all the other factors affecting the properties of SnAgCu joints. The systematic studies discussed under Task 3, and in more detail in our publication [3.3], suggest systematic changes in the deformation properties of SAC305 joints as the Pb content increases up to about 4%. After that the properties did not seem to be affected by further Pb addition, but as we shall see below damage accumulation and failure in thermal cycling continues to vary with Pb content up to at least 5-8% [3.5]. Anyway, there will be no need for the constitutive laws for mixed joints to be dynamic since the materials properties do not appear to change during cycling or aging. Our systematic work does, however, allow us to predict important trends and offer practical guidelines.

Sub-Task 5.1 Microstructurally Adaptive Model for Creep

Professor Dutta is responsible for this sub-task.

Background and Technical Approach:

The creep behavior of Sn-Ag based solders is generally thought to be controlled by the eutectic microconstituent, which is the harder of the two microstructural components (proeutectic β and the eutectic) [5.1]. Furthermore, the creep response of the eutectic is controlled by dislocation interaction with precipitate particles (Ag_3Sn and/or Cu_6Sn_5), giving rise to a particle size/spacing dependent threshold stress [5.1-5.3], as well as a direct dependence of the creep rate on the interparticle spacing (λ) [5.4 - 5.6]. Hence, obtaining a mathematical description of the history dependence of particle size (or interparticle spacing) is a pre-requisite to developing microstructurally adaptive creep models [5.4-5.8]. This has already been done for SAC 105 and 305 solder alloys in Task 2.1.

A microstructurally adaptive model for steady state dislocation creep in a matrix with precipitates was previously proposed by Dutta et al [5.4-5.6]. Based on that approach, a new microstructurally adaptive model for primary-cum-secondary creep of SAC 387 has also been proposed by our group assuming that there is a random distribution of particles throughout the solder microstructure [5.7, 5.8]. The model is valid for dislocation climb controlled creep, which is the dominant mechanism in Sn-based solders during typical use conditions [5.1-5.3, 5.9]. The model assumes that the creep rate of the solder is controlled by the eutectic microconstituent, which comprises a random particulate dispersion in a β-Sn matrix.

The total creep strain is expressed as the sum of primary and secondary creep, using an exponential formulation for primary creep as follows [5.10, 5.11]:

$$\gamma_{creep} = \alpha\left(1 - e^{-\beta t}\right) + \dot{\gamma}_{ss} t \tag{5.1.1}$$

where γ_{creep} is the total shear creep strain, α is the saturation primary creep strain, β is the exhaustion rate of primary creep and $\dot{\gamma}_{ss}$ is the steady state shear creep strain rate. The first part of the right hand side of Equation 1 gives the primary creep and its second term gives the steady state creep. The exponential expression utilized here for primary creep gives a finite creep rate even at small times, and is therefore advantageous over conventional expressions with power dependence on time. To develop the model, creep tests were conducted on SAC 387 using a double lap-shear geometry at shear stresses ranging from 26.1 to 52.2 MPa at temperatures ranging from 25 to 125^{o}C. In addition to the as-reflowed samples, joints isothermally aged at 125^{o}C for 30, 60 and 90 days were also tested.

In addition to the above model for primary-cum-secondary creep, which is valid when the creep rate is controlled entirely by the eutectic microconstituent, a new model for steady-state creep, where both the proeutectic β and the dispersion-containing eutectic contribute in proportion to their volume fractions (i.e., when the solder behaves like a composite of β and eutectic), has been developed. While the former model is valid only when the eutectic volume fraction is appreciable (e.g., in SAC387 or SAC405), the new model is valid even when the

eutectic volume fraction is very small (e.g., in SAC105). Details of this 'composite model' are given below.

Results and discussion:

Case A. Eutectic-Controlled Solder Creep (Primary-cum-secondary creep model) [5.7, 5.8]

In order to develop a microstructurally adaptive model for primary creep, it was necessary to develop a physical basis for the constants α and β, and relate them to the microstructure and the steady state creep rate $\dot{\gamma}_{ss}$. $\dot{\gamma}_{ss}$ may be expressed as:

$$\dot{\gamma}_{ss} = A' \frac{Gb}{kT} \left(\frac{\tau_{eff}}{G} \right)^n e^{-\frac{Q}{RT}} \tag{5.1.2}$$

where A' and n are constants, b is the Burgers vector, k is Boltzmann's constant, and τ_{eff} is the effective shear stress, given as τ-τ_{th}, where τ is the applied stress on the joint and τ_{th} is threshold stress below which creep is negligible.

Now, by subtracting the steady state creep strain $\dot{\gamma}_{ss} t$ from the total creep strain, the primary creep strain γ_{pri} may now be plotted and fitted to the first term of Equation 1, as shown in Figure 5.1.1, thereby yielding the values of α and β for each test condition. For as-reflowed SAC 387, the values of α and β were determined to be $\alpha = 1.04 \times 10^{-3}$ and $\beta = 3.05 \times 10^{-5}$ s^{-1}.

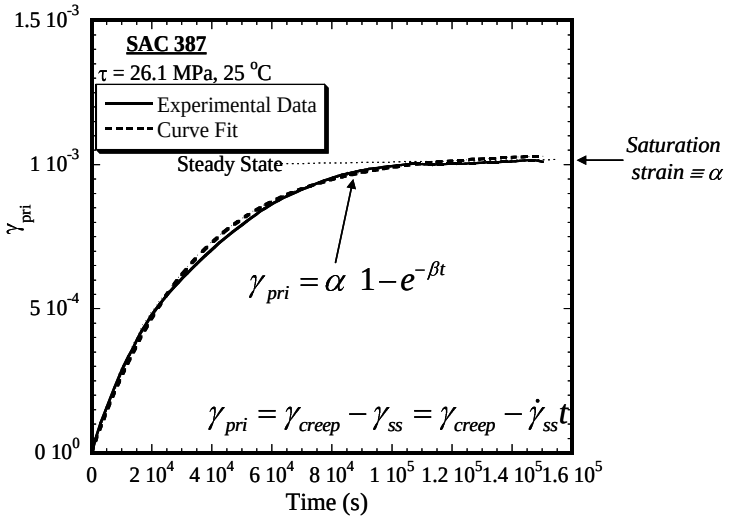

Figure 5.1.1: A typical primary creep curve (continuous line) for SAC 387 [5.7].

It was established that α, β and $\dot{\gamma}_{ss}$ are related to each other as:

$$\dot{\gamma}_{ss} = (\alpha * \beta) / 3 \tag{5.1.3}$$

It was also established that the saturation primary creep strain α is independent of temperature and depends on stress as:

$$\alpha = C_1 \left[\tau_{eff} / G \right]^2 \tag{5.1.4}$$

and β, the exhaustion rate of primary creep, shows similar dependencies on temperature and applied stress as $\dot{\gamma}_{ss}$:

$$\beta = C_2 \left[\tau_{eff} / G \right]^n (1/T) e^{-Q/RT} \tag{5.1.5}$$

Dependence of $\dot{\gamma}_{ss}$ on microstructural coarsening can be written as [5.4]:

$$\dot{\gamma}_{ss} = B \frac{Gb}{kT} \left[\frac{\tau_{eff}}{G} \right]^n \lambda e^{-Q/RT} \tag{5.1.6}$$

where λ is the inter-particle spacing. Since β is independent of aging condition and hence λ, α must have the same λ dependence as $\dot{\gamma}_{ss}$ (i.e., $\alpha \propto \lambda$). Further, knowing that $\dot{\gamma}_{ss} \approx \alpha\beta/3$, equation 4 and 5 can be rewritten as:

$$\alpha = \frac{3B}{C} \left[\tau_{eff} / G \right]^2 \lambda \tag{5.1.7}$$

$$\beta = C \frac{Gb}{kT} \left[\tau_{eff} / G \right]^{n+2} e^{-Q/RT} \tag{5.1.8}$$

The constants B and C were determined using experimental data and the inter-particle spacing can be predicted using the unified growth kinetics model. For SAC 387, the value of B was 2.16 x 10^8 m/s and that for C was 7.36 x 10^{-3} m^2/s. The comparison of experimental creep data over a range of microstructural and test conditions showed good agreement with the predictions of the model (Figure 5.1.2).

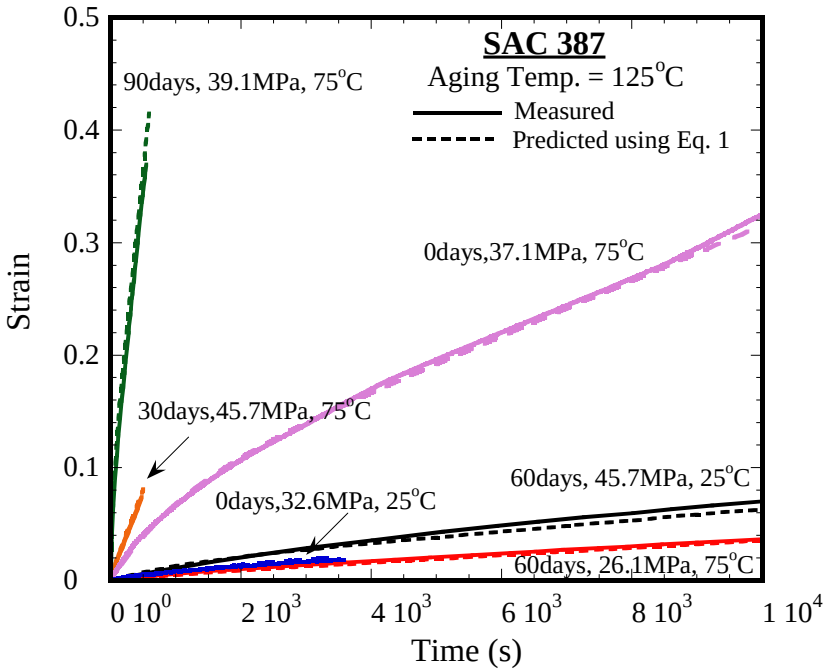

Figure 5.1.2: Experimental creep curves for SAC387 from the double lap-shear creep specimens, along with predicted curves based on the proposed model [5.7].

Case B. Composite Model for Solder Creep [5.12, 5.13]

As discussed before, this model *assumes that the particles are randomly distributed throughout the entire microstructure*. Therefore it fits well to the creep data of SAC 405 and SAC 387, which have a large volume fraction of the eutectic microconstituent (comprising a random particulate dispersion in a β-Sn matrix). Compared to SAC 387, SAC 105 and 305 have a much smaller volume fraction of the eutectic. Microstructure of SAC 105 and 305 bulk solder alloys, shown in Figure 5.1.3, indicates that the particles are concentrated in well defined channels separating proeutectic colonies rather than being dispersed in Sn. In SAC 105, the volume fraction of the eutectic channels is small enough that the proeutectic β phase provides a nearly continuous matrix, periodically interrupted by the eutectic. For such microstructures, the creep rate of the solder cannot be assumed to be controlled by the eutectic only, and it is necessary to develop a 'composite model', where both the proeutectic and the eutectic contribute to the overall creep rate. The development of this model and comparison with experimental results is reported below.

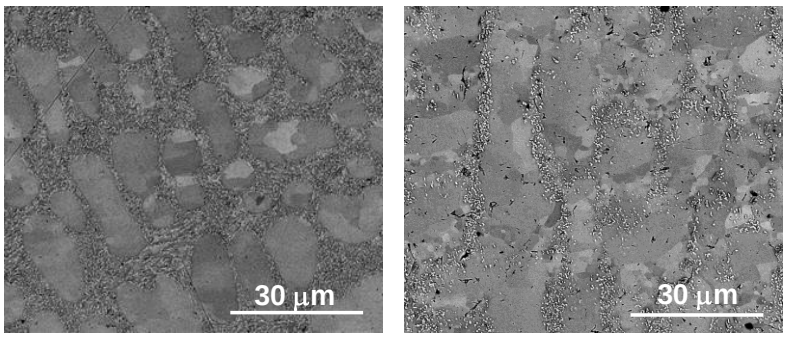

Figure 5.1.3: Representative micrographs showing relative volume fractions of eutectic and proeutectic microconstituents in (a) SAC 305 and (b) SAC 105.

The composite model combines the creep characteristics of both the constituents, eutectic and pro-eutectic, and uses their morphological dimensions as well as the distribution of the reinforcements (second phase particles) to calculate the creep rates of the solders. Figures 5.1.4a & 5.1.4b show the actual microstructure of SC305 as well as the one assumed for the microstructurally adaptive model.

A repeatable unit cell, which may be used to represent the entire microstructure, is shown in Figure 5.1.5. The unit cell may be thought to comprise 3 parts: two parts, A and B, which are in iso-strain condition when loaded, and another part (C) which is in iso-stress condition with A+B, when loaded. Parts A and C are eutectic while part B is pro-eutectic.

The displacement rate of the unit cell can be obtained by adding the displacement rates of part A and C:

$$\dot{\delta} = \dot{\delta}_A + \dot{\delta}_C \tag{5.1.9}$$

$\dot{\delta}, \dot{\delta}_A, \dot{\delta}_C$ are the displacement rates of the alloy, part A and Part C, respectively.

Equation 5.1.3 can be rewritten in terms of the strain rate as:

$$\dot{\varepsilon} = \dot{\varepsilon}_A \frac{L_\beta}{L_\beta + L_{Eu}} + \dot{\varepsilon}_C \frac{L_{Eu}}{L_\beta + L_{Eu}} \tag{5.1.10}$$

$\dot{\varepsilon}$, $\dot{\varepsilon}_A$, $\dot{\varepsilon}_C$ are the strain rates of the alloy, part A and Part C, respectively, and L_β, L_{Eu} are the geometrical parameters shown in Figure 5.1.5.

$$\text{then } \dot{\varepsilon} = A_{Eu}\left(\frac{G_{Eu}b}{kT}\right)\left(\frac{\sigma_A}{G_{Eu}}\right)^{n_{Eu}} \exp\left(-\frac{Q_{Eu}}{RT}\right)\frac{L_\beta}{L_\beta + L_{Eu}} + A_{Eu}\left(\frac{G_{Eu}b}{kT}\right)\left(\frac{\sigma}{G_{Eu}}\right)^{n_{Eu}} \exp\left(-\frac{Q_{Eu}}{RT}\right)\frac{L_{Eu}}{L_\beta + L_{Eu}} \tag{5.1.11}$$

σ, σ_A are the stresses on the alloy, and part A. $A_{Eu}, G_{Eu}, Q_{Eu}, n_{Eu}$ are pre-exponential constant, shear modulus, creep activation energy, and stress exponent of the eutectic phase.

In equation (5.1.11) σ_A and A_{Eu} are unknown. To calculate σ_A, two equations, arising from the assumption of (a) iso-strain condition of parts A and B, and (b) the equilibrium of forces, can be used:

$$\dot{\delta}_A = \dot{\delta}_B \quad or, \quad A'_{Eu}\left(\frac{G_{Eu}b}{kT}\right)\left(\frac{\sigma_A}{G_{Eu}}\right)^{n_{Eu}} \exp\left(\frac{-Q_{Eu}}{RT}\right) = A'_{Sn}\left(\frac{G_{Sn}b}{kT}\right)\left(\frac{\sigma_B}{G_{Sn}}\right)^{n_{Sn}} \exp\left(\frac{-Q_{Sn}}{RT}\right) \tag{5.1.12}$$

and

$$F = F_A + F_B \Rightarrow \sigma(L_\beta + L_{Eu})^2 = \sigma_A((L_\beta + L_{Eu})^2 - L_\beta{}^2) + \sigma_B L_\beta{}^2 \tag{5.1.13}$$

In the above equations, the subscripts A and B represent the eponymous regions in the unit cell (**Figure 5.1.4**), where A is the eutectic, and B is the proeutectic Sn.

By simultaneously solving the above equations, σ_A is obtained as follows:

$$\sigma_A = \frac{\sigma}{\left(\frac{(L_{Eu}+L_b)^2 - L_b^2}{(L_{Eu}+L_b)^2} + \left(\frac{A'_{Eu}}{A'_{Sn}}\left(\frac{G_{Sn}^{n_{Sn}-1}}{G_{Eu}^{n_{Eu}-1}}\right)\exp\left(\frac{Q_{Sn}-Q_{Eu}}{RT}\right)\right)^{\frac{1}{n_{Sn}}} \frac{L_b^2}{(L_{Eu}+L_b)^2}\right)} \tag{5.1.14}$$

$A_{Sn}, G_{Sn}, Q_{Sn}, n_{Sn}$ are the creep pre-exponential constant, shear modulus, creep activation energy, and stress exponent of the proeutectic phase (Sn).
Substituting (5.1.14) in to (5.1.11) gives:

$$\dot{\varepsilon}_{Solder} = \frac{A_{Eu}}{L_\beta + L_{Eu}}\left(\frac{G_{Eu}b}{kT}\right)\exp\left(-\frac{Q_{Eu}}{RT}\right)\left(\frac{\sigma}{G}\right)^{n_{Eu}} \times \left[\left(\frac{1}{\left(\frac{(L_{Eu}+L_\beta)^2 - L_\beta^2}{(L_{Eu}+L_\beta)^2} + \left(\frac{A_{Eu}}{A_{Sn}}\left(\frac{G_{Sn}^{n_{Sn}-1}}{G_{Eu}^{n_{Eu}-1}}\right)\exp\left(\frac{Q_{Sn}-Q_{Eu}}{RT}\right)\right)^{\frac{1}{n_{Sn}}} \frac{L_\beta^2}{(L_{Eu}+L_\beta)^2}\right)}\right)^{n_{Eu}} L_\beta + L_{Eu}\right] \tag{5.1.15}$$

Equation (5.1.15) can be solved numerically to obtain the creep pre-exponent of the eutectic, A_{Eu}, using the solder creep rates of a concentrated alloy (e.g., SAC 387 or 305), where the creep rate is controlled by the eutectic. As noted in previous models, within the eutectic region (i.e., where particles are uniformly distributed throughout the constituent), the creep pre-exponent is directly proportional to the inter-particle spacing, which in turn depends on the extent of microstructural coarsening, as follows [5.4-5.8].

$$A_{Eu} = B_{Eu}\left(\sqrt{\lambda_o + M\left(C_{sol}D_{sol}t/T\right)}\right) \tag{5.1.16}$$

By substituting equation (16) into equation (15), the final creep equation for the solder becomes:

$$\dot{\varepsilon}_{Solder} = B_{Eu}\left(\sqrt{\lambda_o + M\left(C_{sol}D_{sol}t/T\right)}\right)\left(\frac{G_{Eu}b}{kT}\right)\exp\left(-\frac{Q_{Eu}}{RT}\right)\left[\left(\frac{\sigma_A}{G}\right)^{n_{Eu}}\frac{L_\beta}{L_\beta + L_{Eu}} + \left(\frac{\sigma}{G}\right)^{n_{Eu}}\frac{L_{Eu}}{L_\beta + L_{Eu}}\right] \tag{5.1.17}$$

where σ_A is given by equation (5.1.14).

Inspection of equation 5.1.17 reveals that in addition to the applied stress and temperature, the solder creep rate depends on: (i) the the particle spacing, (ii) properties of the eutectic, (iii) the dimensions of the eutectic channels (L_{eu}) and the proeutectic grain size (L_β), and the term σ_A, which represents the stress on the component A in the unit cell. From equation (14), σ_A depends on the properties of both proeutectic Sn and the eutectic, as well as the applied stress and the dimensions (i.e., the volume fractions) of the eutectic and proeutectic. Clearly, as evident from

equation 17, the solder creep rate is simply equal to the creep rate of the eutectic when $L_\beta=0$, since the first term in the square brackets disappears. Depending on the amount of proeutectic phase present (i.e., the relative magnitudes of L_β and L_{eu}), this term becomes increasingly important, and the creep behavior of the solder starts deviating from that of the eutectic. This is the reason why the previous model [5.4-5.8] is able to simulate SAC 405 and SAC 387 very well, but is less effective when the eutectic volume fraction is small, as in SAC 105.

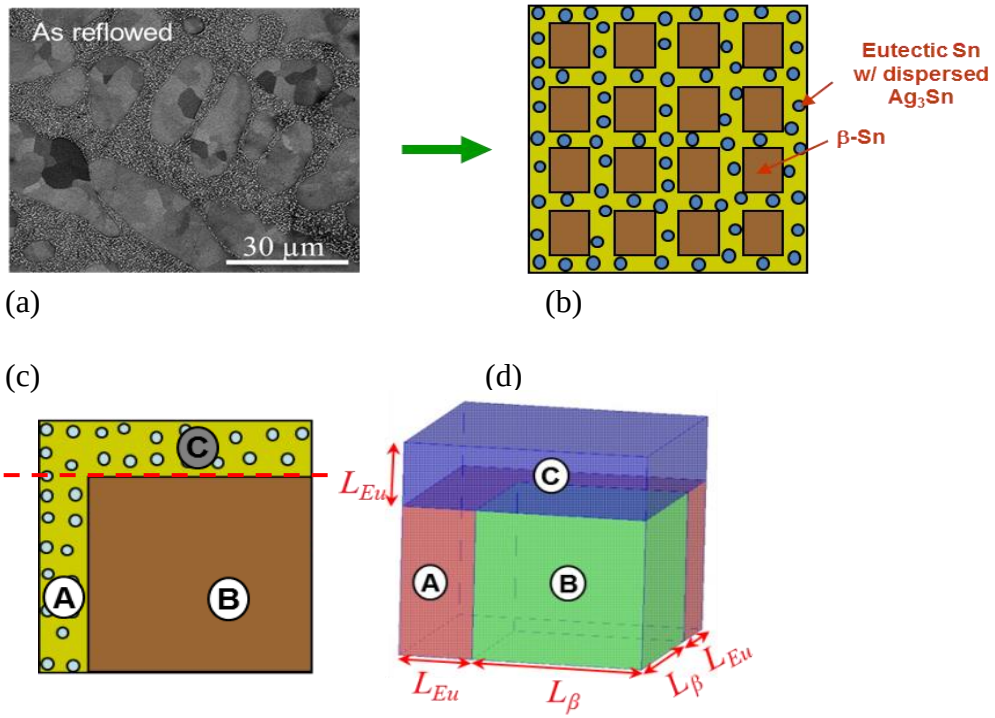

Figure 5.1.4 (a) Microstructure of as-reflowed SAC305; (b) Schematic representation of the assumed composite structure; (c) Schematic of a unit cell of the composite; and (d) 3-D representation of the unit cell, showing the appropriate dimensions.

Figure 5.1.5 shows plots of experimental impression velocity vs. stress (VT/G vs. σ_p/G) data for SAC105 (hollow symbols) at several temperatures, and compares these values with those predicted by the two models: the eutectic only model of refs. [5.4-5.8], and the newly-developed composite model (solid symbols). For SAC305, which has significantly more eutectic content (i.e., less proeutectic content), the eutectic model does adequate work of predicting the creep behavior, as previously noted for SAC405 and SAC387. However, for SAC105, where the proeutectic content is large, the predictions of the eutectic only model are less accurate, and the composite model gives better predictions that are closer to the experimental results.

Conclusions

Two microstructurally adaptive creep models were developed as part of this work.

First, a unified model for primary and secondary creep in SAC solders was developed. This model considers that the creep rate of the solder is controlled by the eutectic microconstituent, the particulates (e.g., Ag_3Sn) in which undergo coarsening during service. The model accounts for this coarsening, due to both isothermal aging and thermo-mechanical cycling, and incorporates explicit parameters accounting for it in a closed form creep law given by eqn 5.1.1. Predictions of the model provide good agreement with experimental results for SAC alloys containing a significant volume fraction of eutectic, such that the eutectic comprises a continuous network around the proeutectic. As such, it is effective for SAC 305, 387 and 405.

Secondly, a composite model was developed for solders, such as SAC105, where the solute (Ag) concentration is low enough that the amount of eutectic is insufficient to result in a continuous matrix. This model, which is valid for secondary or steady-state creep, considers that both the proeutectic and the eutectic contribute to the overall strain rate, their contributions scaling with their volume fractions in the microstructure. This composite model fits the data for SAC105 better, and it is proposed that this model is more universally applicable in predicting the steady state creep behavior of solders, irrespective of the Ag content.

An Excel spreadsheet is available for users to utilize the composite model to predict the steady state creep behavior of SAC solders.

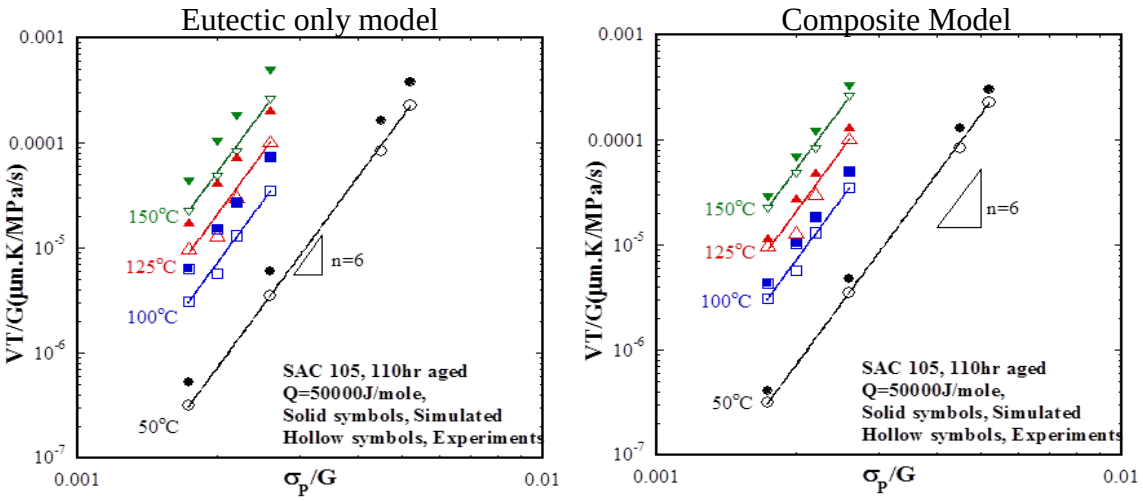

(a) (b)

Figure 5.1.5. Comparison of *experimentally obtained* impression velocity vs. punch stress data (hollow symbols) with *simulated results* at the same stress levels (solid symbols), for SAC105, using (a) previous model assuming that the solder creep rate is controlled by the eutectic only, and (b) composite model assuming that both eutectic and proeutectic determine solder creep rate.

Sub-Task 5.2 Phenomenological Damage Models

Professor Borgesen is responsible for this sub-task. As intended, a mechanistic picture of damage and failure under various cyclic loading conditions has been established (see **Task 3**). This leads to two different damage models.

Results and Discussion

Isothermal Cycling Induced Fatigue Indications are that as long as precipitate coarsening remains negligible, the number of isothermal cycles to solder fatigue failure is inversely proportional to the inelastic work per cycle. This allows for a scaling that takes a lot of the inherent variability out of our data.

The crack growth stage tends to be a relatively small fraction of the total life in load controlled cycling (Figs. 3.5 and 3.6), so the fact that the average damage rate (1/N) or the total life (N) appears to scale with work per cycle might only reflect a scaling of the crack initiation stage. That would be a concern in displacement controlled or realistic assembly cycling where the crack ***growth*** stage may be dominant. We therefore also conducted experiments in which SAC305 joints were cycled with different load amplitudes while monitoring the accumulated inelastic energy deposition in each joint. Cycling was interrupted at various stages and the crack area measured by our dye and pry technique [3.31]. A plot of the crack size (percent of joint cross section) vs. number of cycles (Fig. 5.2.1) shows substantial joint to joint variations even for the same peak load.

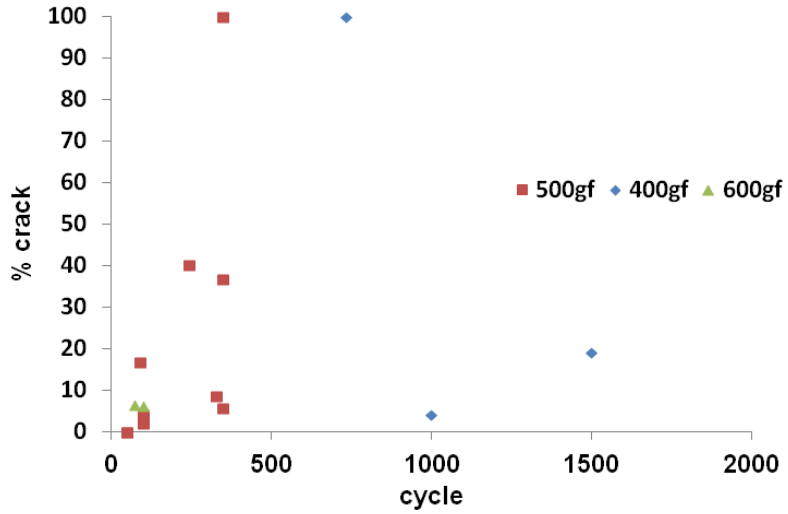

Figure 5.2.1: Crack size (percent of total area) vs. number of load controlled shear fatigue cycles at room temperature for SAC305 joints on Cu.

Figure 5.2.2 shows the same data plotted as crack size vs. accumulated energy. There is no longer any systematic effect of cycling amplitude and the scatter is strongly reduced, i.e. it appears that a major reason for some Sn grain orientations to be less fatigue resistant is that given cycling conditions lead to greater inelastic work. Notably, the scaling with accumulated work appears to continue in the crack growth stage.

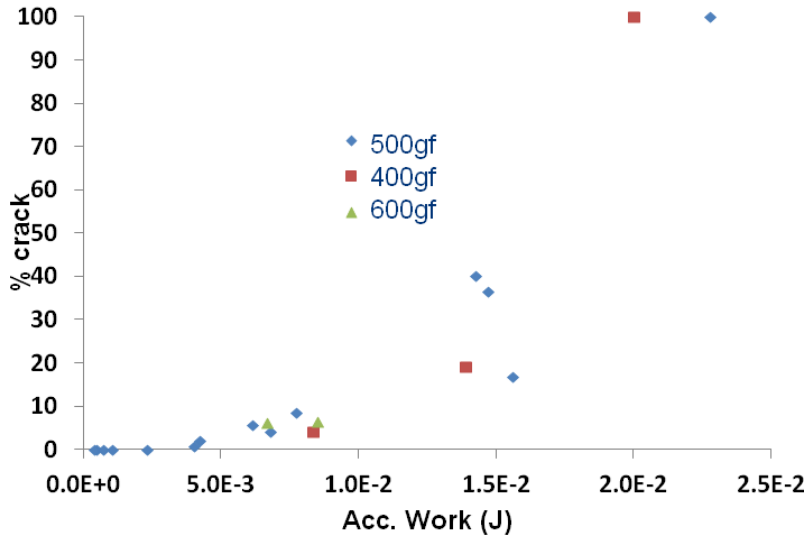

Figure 5.2.2: Crack size (percent of total area) vs. accumulated energy in load controlled shear fatigue cycling at room temperature for SAC305 joints on Cu.

Modifications to the Cu pad and reflow process, together with a different batch of SAC305 spheres, led to significant changes in shear fatigue resistance. These modifications were not intentional and the detailed reasons for the changes were not pursued at this time (see **Task 1** for systematic studies). However, new data generated on these samples revealed an encouraging fact: All samples were pre-annealed for 4 hours at 125°C to somewhat stabilize the microstructure. Some were then subjected to shear cycling at room temperature, others at 100°C. Figure 5.2.3 shows both sets of results to fit the same scaling of crack length vs. accumulated work.

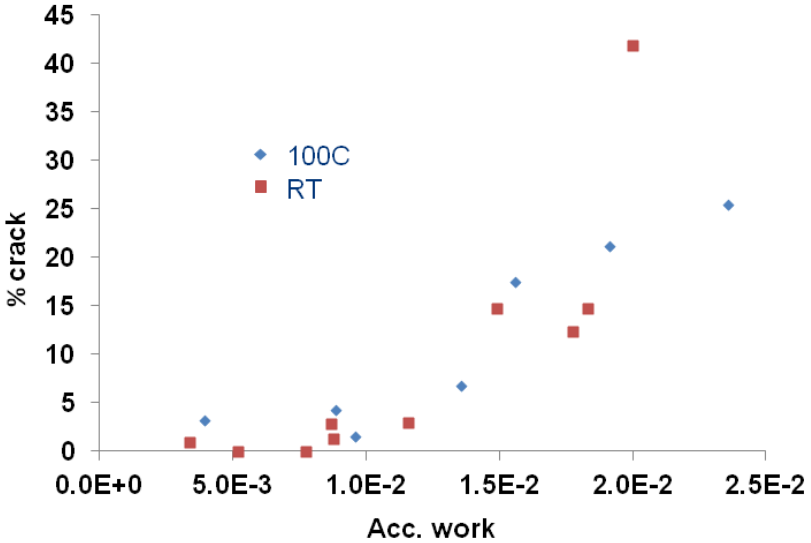

Figure 5.2.3: Crack size (percent of total area) vs. accumulated energy in load controlled shear fatigue cycling at room temperature and at 100°C for pre-annealed SAC305 joints on Cu.

So far it thus appears that we can predict life in isothermal cycling for a given set of solder joints based on the accumulated work required for failure. This work does not vary significantly with cycling amplitude, and it varies very slowly with strain rate [3.11]. The scaling

is not good near the end of load controlled cycling. This may be a result of the extremely rapid catastrophic crack growth and inelastic work at that point, large differences in accumulated energy reflecting only a few cycles, or it may be unique to the shear test method. However, the number of cycles to develop a major crack may be predicted quite accurately [3.11].

The scaling with accumulated work does vary, albeit to a limited extent, as the secondary precipitates coarsen over time (Fig. 3.4). The work leading to our microstructurally adaptive models allows us to predict such coarsening over the course of any thermomechanical history (see **Task 2**). In the case of mixed SAC305(Pb) joints the same damage function applies even after long term aging.

Dynamic recrystallization is often modeled based on the fraction of the overall deformation energy (work) stored in dislocations [5.14-5.18], so the indication that the rate of damage scales with work per cycle may be consistent with the assumption that damage involves local recrystallization right in front of the crack tip.

Thermal Cycling Induced Fatigue As documented under Task 3 the thermal cycling induced failure of BGA and CSP type solder joints occurs by continuous recrystallization of the Sn followed by rapid crack growth along the newly formed network of high angle grain boundaries across the high strain region of the joint. In fact, from the practical perspective of life prediction we concluded that all we have to do to is to predict the 'completion' of the recrystallized region. The life in long term service will be over after approximately twice the number of cycles.

As outlined above and documented in detail in [3.9], the rate of recrystallization in a typical thermal cycle with dwells of 10 minutes or more is controlled by dynamic recrystallization during the high temperature dwell. This recrystallization is sensitive to the spacing between the Ag_3Sn precipitates, becoming increasingly easier as these coarsen. For a given spacing we expect the recrystallization to vary with the work stored in dislocations, just like in isothermal cycling, but only during the high temperature dwell. This stands in strong contrast to current models based on the total work done per cycle! The stress, and thus the strain rate, goes through a peak at the beginning of this dwell, dropping and leveling off to a near-steady state within a few minutes. We therefore propose a rate of recrystallization (damage) per cycle that can be approximated as

$$\partial D/\partial N = \beta + \alpha * t_{dwell} \qquad (5.2.1)$$

where t_{dwell} is the length of the high temperature dwell, α is the rate of work in steady state and β accounts for the higher rate of work during the first few minutes. Rewriting this as

$$1/N_{63} = \beta * (1 + \xi * t_{dwell}) \qquad (5.2.2)$$

and plotting the 'average damage rate' $1/N_{63}$ vs. t_{dwell} for a large number of data we find the parameter ξ to be insensitive to the temperatures and strains [3.9].

This leads us to propose a damage function

$$\partial D/\partial N = \beta * (1 + \xi * t_{dwell}) \qquad (5.2.3)$$

where β accounts for the dependencies on temperatures, strains and precipitate spacings. To the extent that ξ is indeed constant, we furthermore notice that β must be proportional to the rate of work during the steady state part of the dwell. This means that we can use steady state creep properties to calculate it.

Damage Function

The above finally leads us to damage functions for use in the extrapolation of thermal and isothermal cycling test results to life under the much milder cycling conditions typical of long term service.

The rate of damage in an isothermal cycle is well approximated as proportional to the product of the inelastic work in the cycle and the strain rate to the power of 0.13:

$$\partial D/\partial N = D_o * \Delta W * \dot{\varepsilon}^{0.13} \qquad (5.2.4)$$

The rate of damage in thermal cycling varies as

$$\partial D/\partial N = \beta * (1 + \xi * t_{dwell}) \qquad (5.2.5)$$

where β is proportional to the work done during the steady state part of the high temperature dwell but also varies with the temperature there as well as increasing with the spacing of the Ag_3Sn precipitates. Analysis of systematic thermal cycling test results suggests that β may be approximated as following an Arrhenius dependence with an activation energy ΔE = 0.4-0.5eV [3.9, P3.13].

A plan has been developed for a systematic effort, based on our 'simulated thermal cycling experiment', to quantify the interacting effect of precipitate spacings, but that goes beyond the scope of the present effort. For now we therefore propose an approximation:

$$(\partial D/\partial N)_{eff} = \Phi_o * \psi^n * e^{-\Delta E/kT} * (1 + \xi * t_{dwell}) \qquad (5.2.6)$$

where ΔE = 0.4-0.5eV, Φ_o is a constant, and ψ equals the ***rate*** of work (per time) during the 'steady-state' part of the high temperature dwell (after the first couple of minutes). The power 'n' and the constant ξ are best extracted by matching predictions to available experimental results (see Task 6). This would also help account for the specific creep properties assumed and FEM techniques employed. In the absence of this we propose the following crude approximations, for SAC305 joints on Cu pads:

$$\xi = 0.016 \text{ min}^{-1} \qquad (5.2.7a)$$

and

$$n = 4.2 - 4 * D \qquad (5.2.7b)$$

where D is the BGA joint diameter in mm.

The variation of the power 'n' with solder joint size here accounts for the effect of that size on the acceleration factor.

Mixed SnAgCu(Pb) joints

It was, as mentioned above, not our goal to develop constitutive laws for SnAgCu solder joints mixed with Pb. However, the inclusion of SAC305 solder joints with an average of 2.6%Pb in the above testing, as documented in detail in our publication [3.4], provided for important systematic observations.

First of all, the mixed solder joints clearly tend to last longer than the pure SAC305 ones in -40/125C cycling but shorter in 0/100C (Fig. 5.2.4 – 5.2.6). Also, the mixed joints may be less sensitive to the dwell than the pure ones in the harsher cycling but the effects of dwell time are very similar to each other in the milder cycle. The weaker sensitivity of the mixed joints to cycling temperature would be consistent with the elimination of any effects of precipitate coarsening on recrystallization for these. The smaller acceleration factor is therefore also expected to continue as we extrapolate accelerated test results towards typical long term service conditions.

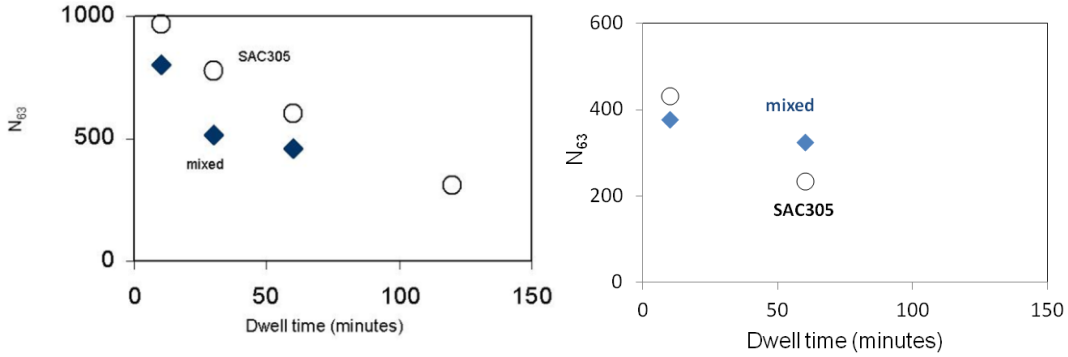

Figure 5.2.4: Characteristic life vs. dwell time for TV64C with 20 mil SAC305 solder joints (a) in 0/100^{o}C cycling with 10, 30, 60 and 120 minute dwells, and (b) in -40/125^{o}C cycling with 10 and 60 minute dwells.

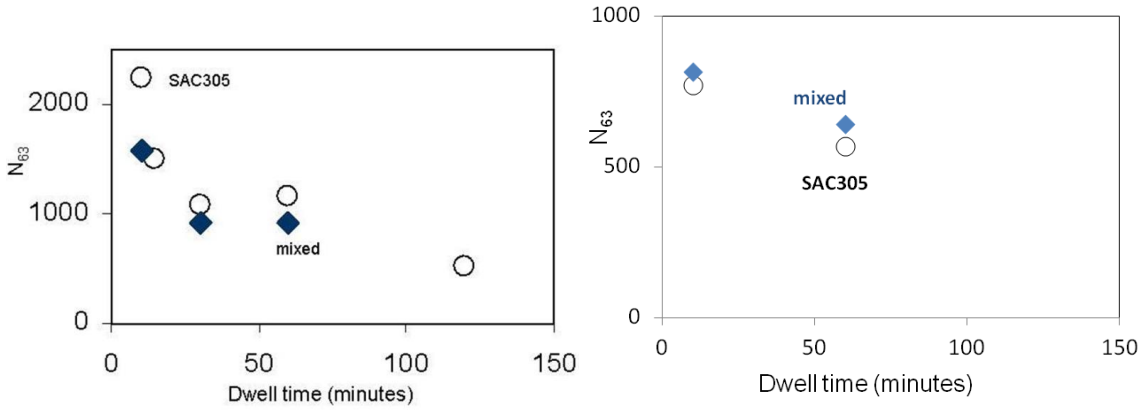

Figure

Figure 5.2.5: Characteristic life vs. dwell time for TV64B with 20 mil SAC305 solder joints (a) in 0/100^{o}C cycling with 10, 15, 30, 60 and 120 minute dwells, and (b) in -40/125^{o}C cycling with 10 and 60 minute dwells.

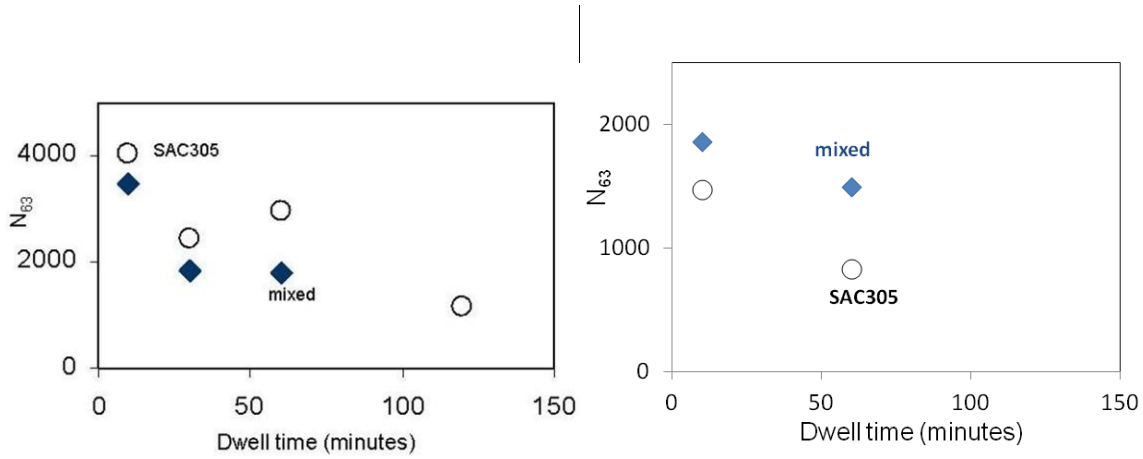

Figure 5.2.6: Characteristic life vs. dwell time for TV64A with 20 mil SAC305 solder joints (a) in 0/100°C cycling with 10, 30, 60 and 120 minute dwells, and (b) in -40/125°C cycling with 10 and 60 minute dwells.

In a separate experiment documented in detail in our publication [3.5] we compared the performance of SnPb, mixed and different high-Ag SnAgCu alloys for 6 different commercial BGAs and CSPs with very different constructions and mechanical properties ranging from flexible to very rigid in 0/100°C with 5 and 10 minute dwells. Consistently with the trend above the life of the mixed joints was 15-60% lower than that of the corresponding pure SnAgCu alloy for any of these assemblies. Importantly, the life continued to drop as the Pb content increased from 2.1% through 5.3% to 8.5%. This is noteworthy because our mechanical testing at room temperature did not show any effect of the Pb content increasing above about 4% (Fig. 3.35 and [3.3]). We speculate that the differences in thermal cycling performance may be associated with the increase in Pb solubility at higher temperatures.

Finally yet another experiment, documented in detail in our publication [3.6], compared mixed joints to eutectic SnPb in 0/100°C thermal cycling with 15 minute dwells. This kind of comparison is less meaningful from a scientific perspective as the failure mechanisms are believed to be very different, but it is often of considerable practical importance. Three different components were available with both eutectic SnPb and SnAgCu solder balls. Both were assembled using a eutectic SnPb solder paste. Because of the fine pitches involved, 0.4mm and 0.5mm, realistic SnPb solder paste printing led to large Pb concentrations in the final mixed joints.

Figure 5.2.7 shows a Weibull plot of the failure distributions for 7mm wafer level CSP assemblies with SnPb and mixed SAC405(18%Pb) joints on an 0.4mm pitch. The latter are seen to last about 26% longer than the SnPb ones.

Another 0.4mm pitch assembly, based on a so-called Very Thin ChipArray package, gave a 90% longer life with mixed SAC305(18%Pb) joints and an 0.5mm pitch assembly, based on a so-called Thin ChipArray package, gave 70% longer life with SAC305(11%Pb) joints. The better performance of the mixed joints compared to eutectic SnPb in all three cases is not surprising. It is also quite common for pure SnAgCu joints to last longer than SnPb in such tests.

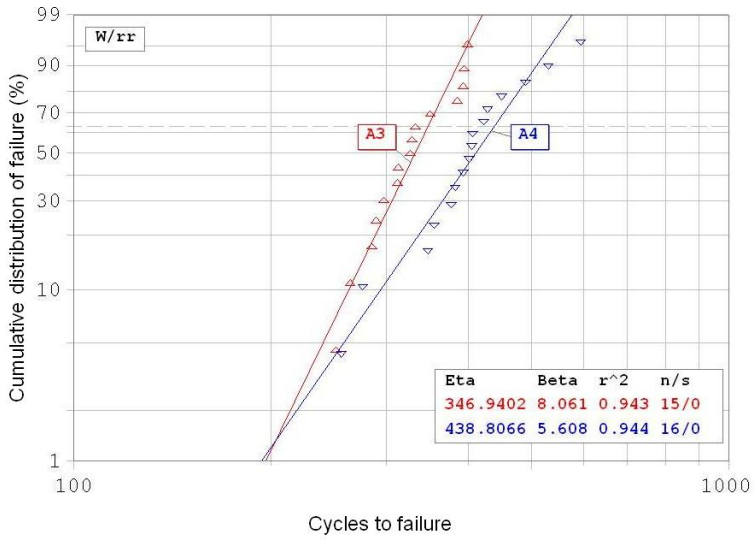

Figure 5.2.7: Weibull plot of failure distributions for 0.4mm pitch wafer level CSP assemblies with SnPb (A3) and mixed (A4) joints.

Sub-Task 5.3 Model Validation

Validation of the overall models relies largely on the agreement with all the different systematic trends and insights developed above. The fact that the damage function proposed for isothermal cycling explains the otherwise confusing effects of amplitude variations on damage accumulation may be seen as validating this.

The most controversial part of our model is the damage function for thermal cycling. Thermal cycling experiments are expensive and time consuming. Available systematic data therefore usually (a) are not all conducted by the same group, (b) are not accompanies by thorough failure analysis, (c) involve a limited number of different thermal cycling parameters for the same component, (d) do not always involve testing to failure, and/or (e) involve commercial components for which important parameters are not well characterized. We had access to a unique set of fully characterized systematic data and complemented this with further tests for completeness (see our publications). Based on this we showed that none of the current models can account for systematic effects of cycling parameters [P3.13]. They are also not compatible with our mechanistic understanding (**Task 3**). The fact that our model predicts the observed trends and is capable of explaining other published trends would thus seem to qualify it as the best currently available model:

The model first of all predicts the observed inverse linear dependence on the high temperature dwell time as well as the absence of a similarly strong effect of the low temperature dwell [3.9, P3.13]. The model also predicts the effects of solder joint size on the interactive dependencies on strain range, dwell time and temperatures, and thus on the acceleration factors [P3.13], even though Equation 5.2.7b only accounts for this in an approximate fashion.

The model may also be viewed as explaining the observation of a comparable or longer life of LGA assemblies than of BGA assemblies in spite of the much larger strains associated with the shorter joints [3.33].

The model finally explains the confusing effects of aging assemblies before thermal cycling reported by Cisco and HDPUG. In simple terms, precipitate coarsening during cycling has two sets of counteracting effects:

1) It softens the solder, reducing stress build-up in the heating and cooling ramps and during the first few minutes of the dwells. This has the strongest effect for very stiff components and boards where the displacements remain almost the same.
2) It enhances the rate of recrystallization for a given stress. This is less important for larger joints (which start out with larger initial precipitate spacings) and/or at higher strains (where the spacing matters less).

These counteracting effects add up to reducing the life most for small joints, low strains, and soft components, seemingly explaining the trends reported by Cisco. In fact, HDPUG found aging to ***improve*** the life for particularly rigid components in accelerated thermal cycling.

Task 6: Protocols and Models

Professor Borgesen is responsible for this task. Tasks 2, 3 and 5 provided the necessary understanding and constitutive laws required for the development of proper protocols for accelerated aging as well as isothermal and thermal cycling. These all go together with our practical models which are all approximations but believed to be by far the best available at this point.

We emphasize again that the goal is to conduct accelerated tests and extrapolate the results to much milder cycling conditions ('life in service'), not to make a priori predictions of accelerated test results. Also, the vast majority of accelerated tests are so-called 'engineering tests' not intended to lead to an actual prediction of life. Instead, the primary concern for such tests should be whether a comparison between results for different materials, designs or processes can be interpreted to say which would be best ***in service***. As we have shown this is far from always as obvious as commonly believed.

In the following we first make general recommendations with respect to the different calculations and models involved. This is followed by recommended protocols for various levels of testing. In general, our models involve the prediction of inelastic work during parts or all of a cycle, based on which we then predict the rate of damage or the total life.

Deformation (Creep) Properties

Our microstructurally adaptive models allow for the rapid calculation of the inelastic strain rate corresponding to a given stress and temperature for any SnAgCu alloy at any stage of aging and thermal cycling. They only predict the steady-state strain rate in thermal cycling, but this is sufficient for use with the damage function proposed. The associated inelastic work done on a solder joint is best predicted by FEM.

As far as deformation properties are concerned the only practical challenge is therefore to account for the ongoing evolution of deformation properties, something that can rapidly become computationally prohibitive in FEM. The creep rates for a fixed stress may change by orders of magnitude over the course of a typical thermal cycling experiment, or during aging times and cycling typical of a long term service environment. However, just like for thermal aging (**Task 5**) this is counteracted by a drop in stress as the solder softens. That effect depends on the relative rigidities of solder, component and substrate, but the actual consequences for the fatigue life may be significant but should be quite finite.

Overall, we may take advantage of the fact that aging and cycling induced coarsening of the precipitates is not expected to ever lead to a strong ***reduction*** in the rate of damage per cycle. A conservative estimate of life may thus be based on assuming major thermal aging and cycling induced coarsening and then calculating the work. Otherwise, for purposes of computing economy we recommend the following steps, in each simulating 4 cycles in order for the stress/strain vs. time hysteresis loop to stabilize:

i. Predict the average precipitate spacing before and by the end of aging and cycling. For the purpose
ii. Simulate the first 4 cycles and the last 4 cycles. Compare the values of the damage function.
iii. Based on the difference and available computing resources results may be refined by the simulation of 4 cycles at one or more intermediate levels of precipitate spacing.

Damage Function

The proposed damage function predicts the rate of damage per cycle based on the calculated work. The function is slightly different for thermal than for isothermal cycling, but in either case it involves a constant pre-factor which needs to be extracted by calibration to an accelerated test result.

Isothermal Cycling The rate of damage in isothermal cycling is proportional to the product of the inelastic work per cycle, ΔW, and a factor that varies as the strain rate to the power of 0.13:

$$\partial D/\partial N = D_o * \Delta W * \dot{\varepsilon}^{0.13} \quad (6.1)$$

Below, we recommend an accelerated test protocol in which life is measured for a fixed cycling amplitude (fixed input and frequency in vibration). Calculation of the work per cycle for the same experiment then provides the pre-factor D_o and the life can be extrapolated to any other fixed amplitude.

The prediction of life in cycling with varying amplitude is complicated by our inability to predict effects of variations on the deformation properties. This may be dealt with by a completely different approach (below).

Thermal Cycling As discussed (**Task 5.2**) the rate of damage in thermal cycling may be approximated as

$$(\partial D/\partial N)_{eff} = \Phi_o * \psi^n * e^{\Delta E/kT} * (1 + \xi * t_{dwell}) \quad (6.2)$$

where ψ equals the rate of work during the 'steady state' part of the high temperature dwell and t_{dwell} is the duration of that dwell. We shall address the parameters 'n' and ξ in connection with the test protocols below, but we recommend $\Delta E = 0.45eV$, and the constant Φ_o should be extracted by comparing predictions to an accelerated test result.

Simple Acceleration Factor Models

Simple extrapolations of a measured number of cycles to failure may be accomplished using

$$N = N_o * \Delta W^{-1} * \dot{\varepsilon}^{-0.13} \quad (6.3)$$

for isothermal cycling and

$$N = N_o * \psi^{-m} * e^{-\Delta E/kT} / (1 + 0.016 * t_{dwell}) \quad (6.4a)$$

for thermal cycling with the duration of the high temperature dwell t_{dwell} in units of minutes and

$$m = 4.2\text{-}4\cdot10^{-3} * D \quad (6.4b)$$

where D is the BGA joint diameter in units of μm.

Test Protocols

Recommended accelerated test protocols depend on the purpose of the test, the service conditions expected, and the available capabilities. Comprehensive protocols would for example apply to the qualification of a solder material or for an R&D laboratory to establish important model parameters, while much simpler protocols would apply to the ongoing quantification and reliability assessment of specific designs, products, ...

Aging The creep properties of SnAgCu solder joints change rapidly within the first few days after the last reflow and may change by orders of magnitude during storage at room temperature for periods of half a year or more. This may have clear consequences for life in isothermal cycling and may complicate the extrapolation of thermal cycling test results to long term service conditions.

Effects of aging may be accelerated by heating, but at the risk of introducing a slightly different microstructure rather than achieving the same microstructure faster. This is primarily of consequence for the intermetallic structure on Cu pad surfaces, where the ratio of the thickness of the Cu_3Sn to that of the Cu_6Sn_5 layer will be different [6.1]. The effects on intermetallic bond properties and the risk of Kirkendall void formation do, however, remain limited. Acceleration factors may be calculated based on an activation energy of 50kJ/mol (**Task 2**).

Thermal aging may be required before or in between periods of cycling to simulate a particular environment of concern. In the absence of a more specific requirement we recommend aging assemblies for 2 weeks at 100^oC before cycling to stabilize the solder properties (precipitate distributions) somewhat and to account for absence of regular aging during a typical accelerated cycling test.

NOTE, however, that aging may ***enhance*** the life of rigid assemblies in subsequent thermal cycling. This is an effect unique to high strain ranges and complicates interpretations in terms of life in long term service further. A better approach is therefore to test assemblies both with and without pre-aging and ignoring any improvements in life by aging. Comparisons between alternatives (designs, materials, processes) should be made in terms of the worst performance for each (pre-aged or not).

Isothermal Cycling The most common isothermal cycling of concern in long term service is vibration. We argue that as far as solder fatigue is concerned, at least, comparisons made in random vibration may be misleading [3.18] and actual extrapolations of results to a value for life in service is certainly not possible.

a) For a quantitative estimate of 'life in service' it is recommended that life be measured in accelerated testing with one or more fixed amplitudes and the results extrapolated to a representative 'service level' amplitude according to Equation 6.3. It is quite common for the resonant frequency to shift during vibration testing. This may be the indication of a problem and should be investigated (see below). The best approach may be to sweep the frequency across a narrow range to compensate for a limited shift.
b) For comparisons between alternatives, testing at fixed amplitudes should be complemented by testing with a varying amplitude. Some alternatives may be much more sensitive than others to variations in amplitude and thus be expected to compare less favorably under realistic service conditions. We do not yet have a model allowing us to predict actual life under such conditions. For a qualitative measure of the sensitivity to variations we recommend choosing two substantially different amplitudes that both give practical life times in accelerated testing. Alternate between a number of cycles equal to 0.1% of cycles to failure at each amplitude until actual failure. Expectations are that this will cause failure well before the life predicted based on Miner's rule.

Resonance shift: There are at least three potential reasons for a shift in the resonant frequency in vibration. (i) there may be changes in how firmly the board is fixed, (ii) changes in the solder properties may cause a shift, (iii) the board may be damaged by cycling.

After a limited number of cycles at the very beginning, cycling induced changes in the solder properties are only expected when the amplitude is changed or cracks become significant. Anyway, the first two effects are acceptable and may be accounted for to a large extent by sweeping across a narrow range of frequencies as suggested above.

Damage to the board is a major concern. Microscopic damage may not be otherwise detectable, but a resulting softening of the board will reduce the loads on the solder joints and lead to overestimates of the solder fatigue life. As such damage is most likely at high amplitudes, extrapolations to long term service may become non-conservative and effects of amplitude variations may be underestimated. If a resonance shift is detected, it is recommended that this be investigated by, for example, measurement of the board rigidity before and after cycling.

Thermal Cycling Failure of a BGA, CSP or TSOP joint in thermal cycling between a low temperature dwell at 25C or less and a high temperature dwell at 60C or more is normally preceded by recrystallization to form a network of grain boundaries across the high strain region of the joint. This may not occur in highly accelerated cycling, so the accelerated thermal cycling test should not lead to failure in less than 200 cycles.

It is recommended that both the prediction of actual life in service and comparisons between alternatives in a so-called 'engineering test' be based on accelerated testing ***together with*** extrapolation of the test results to conditions typical of service conditions. **NOTE** that comparisons may easily become misleading without such extrapolations, i.e. the alternative doing best in test may not do best in service.

It would be preferable that three or more accelerated thermal cycling tests be conducted on the assemblies of interest. If this is possible, these should include two different maximum temperatures and two different dwell times at the maximum temperature. However, life assessment can be based on a single test. The maximum temperature should not exceed 125C unless higher temperatures are anticipated in long term service. The dwell time should not exceed 2 hours, unless a longer dwell time is anticipated in service (the dwell time dependence in Equation 6.2 or 6.4 may be conservative for longer dwells).

A characteristic life of more than 200 cycles may be extrapolated to life in service based on Equation 6.4 or, better, by FEM modeling using our constitutive relations and the damage function in Equation 6.2. In either case we can calculate the rate of work, ψ, during the 'steady state' part of the high temperature dwell. However, we need the values for the parameters 'n' and ξ. Different levels of testing efforts will lead to different levels of accuracy and confidence in these values.

The most accurate approach is for the user to conduct a large set of accelerated tests and match the results to predictions based on FEM using Equation 6.2, varying 'n' and ξ to get the best fit. The second best approach is to use $\xi = 0.016\ \text{min}^{-1}$ and conduct FEM with Equation 6.2, to calibrate 'n' to the experimental trends reported in this work. This means simulating model assemblies for which the component properties do not vary laterally and with dimensions to ensure that the nominal shear strain range is on the order of 1%. Different component designs should be modeled for which the only change is in the Distance to the Neutral Point (DNP) for the corner joints. The solder joint dimensions should equal the dimensions of actual concern. 'n' should be varied until the predicted life varies with the DNP to a power equal to $4.2\text{-}4\cdot10^{-3} * D$, where D is the solder joint diameter in units of μm.

It is recommended that the user conduct the FEM, rather than we, even when reproducing experimental trends reported by us, is that a large number of approximations are invariably involved and everybody will do this a little differently. Not only will meshing and the use of local-global models be different, individual users will also approximate effects of precipitate coarsening to different levels of accuracy (see **Deformation Properties** above). The parameter 'n' will effectively account for these as well as for the effects of joint size.

NOTE that we do not currently have data to enable the assessment of 'n' for pre-aged assemblies. It is conceivable that the value may drop towards unity after pre-aging at 125C for a couple of weeks. A conservative prediction of life in long term service would therefore be achieved by extrapolation of accelerated test results for pre-aged assemblies based on n = 1 (see also **Aging** above).

Combined Loading Many applications involve combinations of thermal excursions and, for example, vibration. Conventional accelerated testing for either typically involves a few hours of highly accelerated vibration or several weeks of less accelerated thermal cycling. The few experiments published did not appear to accelerate realistic combinations. A qualitative impression of the effect of ***simultaneous*** thermal cycling and vibration might be achieved by combining cycling conditions that would, each, on their own, give about the same life.

The effect of alternating between thermal cycling and vibration depends strongly on the order. For a conservative assessment of the 'worst that can happen' we recommend thermal cycling first, followed by vibration. Miner's rule may strongly overestimate life in this.

ESS Environmental Stress Screening typically relies on some combination of vibration and thermal cycling to a level that does not reduce the life of non-defective parts by more than 10%. The problem is that the 10% can only be checked by comparing the results of accelerated testing of parts that have and have not been subjected to ESS. However, a procedure that reduces life in subsequent accelerated testing by 10% may easily reduce life in long term service by 90% or more.

The worst we can do in this respect is screening in thermal cycling (see **Combined Loading** above). Independently on the actual long term service conditions of concern we recommend screening in vibration ***only***. We furthermore recommend that the vibration be as gentle as possible, i. e. take as long as is practical. Fatigue life is invariably more sensitive to defects than strength is, so there is no reason to screen with a higher load amplitude than necessary.

Conclusions and Implications for Future Research/Implementation

As specified in the original proposal the focus of the present research effort was on two deliverables:

1) Constitutive relations (creep equations and a damage function) for use in modeling of the damage and failure of lead free solder joints in cycling.
2) Recommendations as to reliability assessment protocols based on the mechanistic understanding that was established in order to develop the constitutive relations. This part included special consideration of lead free solder joints mixed with a SnPb paste in reflow.

Both of these deliverables were successfully achieved and documented in detail in the present report.

After completion of a significant fraction of the work we were requested to extend the second deliverable to include efforts to incorporate the constitutive models into industry standard practices and models. That was attempted to the extent possible based on the available resources, but as discussed below our conclusion is that significant further funding would be required to complete this. Efforts are ongoing to find and secure such funding.

The assessment of the long term life of lead free solder joints is commonly based on accelerated testing and the explicit or implicit extrapolation of the test results to service conditions. Explicit extrapolations require the knowledge of acceleration factors which can only be predicted on the basis of models that need to be mechanistically justified as predictions cannot be validated empirically in time. Implicit extrapolations may 'only' be based on the assumption that acceleration factors are the same as last time, or the same for different materials, designs or processes being compared. Even this assumption is, however, not as easily justified as commonly believed. Examples of acceleration factors varying with solder joint design were documented and we predict systematic effects of reflow process parameters on acceleration factors as well. Overall, a fundamental mechanistic understanding is thus required.

Constitutive Relations

Acceleration factors are best predicted by Finite Element Modeling (FEM). This can be done by individual practitioners for their own use, or by select experts for use in the establishment of tabulations and/or the formulation of industry standards and protocols. In either case the critical part is the definition of constitutive relations or models for use in the FEM. Both the deformation (creep) properties and the damage function vary strongly with the initial microstructure and its evolution over time.

The critical microstructural factors are the Sn grain morphology, the Sn grain orientation(s), and the average spacing between the secondary Ag_3Sn precipitates. Small solder volumes, relatively high Ag contents and certain combinations of pad sizes and finishes tend to favor a so-called interlaced twinning morphology that is generally more reliable, although the benefits of this are reduced by long term aging. The most common is, however, a single Sn grain or a so-called 'beach ball' structure. In either case joint properties vary strongly with the orientation of the Sn grain(s) relative to the loading direction. Orientations are random so for practical purposes effects of this should be included in the general statistics of damage and failure.

The effects of precipitate spacing on the creep properties are accounted for by our constitutive relations. The expressions look complex but can in fact be used even in a simple Excel spreadsheet. A mechanistic understanding of solidification allows for qualitative and

quantitative predictions of trends in initial spacing vs. solder volume, pad sizes and pad finishes as well as process parameters. A quantitative expression for the subsequent evolution of the spacing in cycling and aging was developed.

Separate, quantitative damage functions were developed and documented for thermal and isothermal cycling. These express the average rates of damage in cycling in terms of temperatures and the inelastic work in specific parts of the cycle.

Reliability Assessment Protocols

In the case of thermal cycling the average damage rate can be calibrated experimentally and acceleration factors predicted by FEM based on the constitutive relations. Recommendations were made with respect to accelerated testing and the interpretation of results.

In the case of isothermal cycling (vibration, cyclic bending) predictions are complicated by effects of variations in cycling amplitude on the deformation properties. Practical test protocols and an approach to account for this were developed.

Special recommendations were made for SnAgCu joints with small amounts of Pb.

Implementation

Recommendations were made as to the incorporation of the constitutive models into industry standard practices and models. These were presented at conferences, at a SERDP webinar, at meetings of the AREA consortium and, notably, at meetings of the PERM consortium. Detailed discussions with individual members of PERM did, however, lead to an identification and understanding of the critical barriers to implementation.

In simple terms it is clear that only large companies have the resources to implement the use of the new constitutive models. Industry experts agreed that smaller companies will focus on following industry standards and customer requirements. The members of PERM are all large companies but these will also not be willing to implement the models without the establishment of an industry wide consensus and standards. That will first of all require more effective communication with the overall community. While the constitutive relations do not need further validation a consensus will also require a validation of FEM models ***using*** the constitutive relations together with quantification of the benefits relative to current practices. It is anticipated that such quantification will lead to the identification of service conditions for which the use of the new constitutive relations will be critical, as well as to the formulation of further recommendations as to test protocols.

The development and optimization of FEM models goes beyond the resources of the present effort. An ESTCP proposal is currently being prepared with a PERM member to support the effective communication with stake holders and transfer of constitutive relations and recommendations. We are also looking for funding for an effort to develop and use FEM models for further quantification. It is envisioned that results would be shared with the community among other as a tabulation of representative acceleration factors together with predictions of current models. This would also help justify updates to industry standards.

Future Research

Aside from the development and optimization of FEM models using the new constitutive relations as mentioned above, there is also a need for further research to improve on predictions.

Quantitative modeling will allow for the extraction of a quantitative description of the relationship between precipitate spacing, rate of work and the rate of recrystallization from

accelerated test results. Complementing existing test results with specifically designed experiments will lead to an improved damage function.

An ongoing NSF sponsored research effort is leading to an understanding of the effect of amplitude variations on the properties of solder in cycling. Follow-up research will be required to translate this into improved constitutive relations.

Appendix

Literature Cited

[1.1] M. Kerr, N. Chawla, Acta Materialia 52 (2004) pp. 4527

[1.2] T. R. Bieler, H. Jiang, L. P. Lehman, T. Kirkpatrick, E. J. Cotts, 56th IEEE Transactions on Components and Packaging Technology vol. 31 (2006) pp. 370

[1.3] B. Arfaei, Y. Xing, J. Woods, J. Wolcotts, P. Tumne, P. Borgesen, and E. Cotts, 58th Electronic Components and Technology Conference (2008), pp. 459

[1.4] M. Lu, D. Y. Shih, P. Lauro, C. Goldsmith, D. W. Henderson, Applied Physics Letters 92 (2008) pp. 211909.

[1.5] K. Lee, K.S. Kim, Y. Tsukada, K. Suganuma, K. Yamanaka, S. Kuritani, M. Ueshima, Journal of Materials Research 26 (2011) pp. 467.

[1.6] G. Powell, G. Colligan, V. Surprenant, A. Urquhart, Metallurgical and Materials Transactions A 8 (1977) pp. 971.

[1.7] A. Hellawell, P.M. Herbert, Proceedings of the Royal Society of London. Series A, Mathematical and Physical Sciences 269 (1962) pp. 560.

[1.8] F. Weinberg and B. Chalmers, Can J Phys 30 (1952) pp. 488.

[1.9] L.P. Lehman, S.N. Athavale, T.Z. Fullem, A.C. Giamis, R.K. Kinyanjui, M. Lowenstein, K. Mather, R. Patel, D. Rae, J. Wang, Y. Xing, L. Zavalij, P. Borgesen, E.J. Cotts, Journal of Electronic Materials 33 (2004) pp. 1429.

[1.10] L.P. Lehman, Y. Xing, T.R. Bieler, E.J. Cotts, Acta Materialia 58 (2010) pp. 3546.

[1.11] B. Arfaei, E. Cotts, Journal of Electronic Materials 38 (2009) pp. 2617.

[1.12] P. Borgesen, T. Bieler, L. Lehman, and E. Cotts, MRS Bull. 32 (2007) pp. 360.

[1.13] B. Arfaei, M. Benedict and E. J. Cotts, Acta Materialia (submitted).

[1.14] D.N. Lee, K.-h. Kim, Y.-g. Lee, C.-H. Choi, Materials Chemistry and Physics 47 (1997) pp. 154.

[1.15] J. Warner, J. Verhoeven, Metallurgical and Materials Transactions B 3 (1972) pp. 1001.

[1.16] S.E. Battersby, R.F. Cochrane, A.M. Mullis, Journal of Materials Science 34 (1999) pp. 2049.

[1.17] J. Gong, C. Liu, P.P. Conway, V.V. Silberschmidt, Scripta Materialia 61 (2009) pp. 682.

[1.18] A.M. Mullis, K.I. Dragnevski, R.F. Cochrane, Materials Science and Engineering A 375-377 (2004) pp. 157

[1.19] T. Haxhimali, A. Karma, F. Gonzales, M. Rappaz, Nat Mater 5 (2006) pp. 660

[1.20] C.F. Lau, H.W. Kui, Acta Metallurgica et Materialia 41 (1993) pp. 1999

[1.21] S. O'Hara, Acta Metallurgica 15 (1967) pp. 231.

[1.22] V. O. Esin, G. N. Pankin, R. H. Nasyrov, Sov. Phys. Crystallogr. 18 (1973) pp. 246

[1.23] A. Rosenberg and W. C. Winegard, Acta Metallurgica 2, 2242 (1954), pp. 2242

[1.24] B. E. Sundquist, L. F. Mondolfo, Trans Met Soc AIME 221 (1961) pp. 157.

[1.25] I. Anderson, J. Walleser, J. Harringa, F. Laabs, A. Kracher, J Electron Mater 38 (2009) pp. 2770.

[1.26] M. G. Cho, S. K. Kang, S. Seo, D. Shih, H. M. Lee, J Mater Res. 24 (2009) pp. 534.

[1.27] A. Ohno, T. Motegi, Nippon Kinzoku Gakkaishi/ J JPN I MET 37 (1973) pp. 777.

[1.28] M. Li, F. Zhang, W. T. Chen, K. Zeng, K. N. Tu, H. Balkan, P. Elenius, J Mater Res. 17, (2002) pp. 1612.

[1.29] P. Borgesen, T. Bieler, L. Lehman, E. Cotts, MRS Bulletin 32 (2007) pp. 360.

[1.30] Y. Kariya, T. Hosoi, S. Terashima, M. Tanaka and M. Otsuka, J. Electron. Mater. 33 (2004) pp. 321

[1.31] K. S. Kim, S. H. Huh, K. Suganuma, Materials Science and Engineering A 333 (2002) pp. 106

[1.32] F. Ochoa, X. Deng, N. Chawla, J. Electron. Mater. 33 (2004) pp. 1596

[1.33] M. Kerr, N. Chawla, Acta Materialia 52 (2004) pp. 4527.

[1.34] F. Ochoa, J.J. Williams, N. Chawla, J. Electron. Mater. 32(2003) pp. 1414.

[1.35] P. W. Bridgman, Proc. Amer. Acad. Arts Sci. 60 (1925) pp. 305.

[1.36] J.A. Rayne, B.S. Chandrasekhar, Phys. Rev. 120 (1960) pp. 1658.

[1.37] F. Yang, J. C. M. Li, J. Mat. Sci. Mat. Electronics 18 (2007) pp. 191.

[1.38] A. U. Telang, T. R. Bieler, Solid State Phenomena 105 (2005) pp. 219.

[1.39] A.U. Telang, T. R. Bieler, M. A. Crimp, Materials Science and Engineering A 421 (2006) pp. 22

[1.40] T. R. Bieler, H. Jiang, L. P. Lehman, T. Kirkpatrick, E. J. Cotts, 56th IEEE Transactions on Components and Packaging Technology (2006) pp. 370.

[1.41] S. Park, R. Dhakal, L. Lehman, E. Cotts, Acta Materialia 55 (2007) pp. 3253.

[1.42] B. Arfaei, Y. Xing, J. Woods, J. Wolcotts, P. Tumne, P. Borgesen, E. Cotts, 58th Electronic Components and Technology Conference (2008) pp. 459.

[1.43] T. M K. Korhonen, L. Lehman, M. A. Korhonen D. W. Henderson, J. Electron. Mater. 36, (27) pp. 173.

[1.44] M. Kerr, N. Chawla, Acta Materialia 52 (2004) pp. 4527.

[1.45] T. R. Bieler, H. Jiang, L. P. Lehman, T. Kirkpatrick, E. J. Cotts, 56th IEEE Transactions on Components and Packaging Technology vol. 31 (2006) pp. 370

[1.46] B. Arfaei, Y. Xing, J. Woods, J. Wolcotts, P. Tumne, P. Borgesen, and E. Cotts, 58th Electronic Components and Technology Conference (2008) pp. 459.

[1.47] M. Lu, D. Y. Shih, P. Lauro, C. Goldsmith, D. W. Henderson, Applied Physics Letters 92 (2008) pp. 211909

[1.48] K. Lee, K.S. Kim, Y. Tsukada, K. Suganuma, K. Yamanaka, S. Kuritani, M. Ueshima, Journal of Materials Research 26 (2011) pp. 467.

[1.49] G. Powell, G. Colligan, V. Surprenant, A. Urquhart, Metallurgical and Materials Transactions A 8 (1977) pp. 971.

[1.50] A. Hellawell, P.M. Herbert, Proceedings of the Royal Society of London. Series A, Mathematical and Physical Sciences 269 (1962) pp. 560.

[1.51] F. Weinberg and B. Chalmers, Can J Phys 30 (1952) pp. 488.

[1.52] L.P. Lehman, S.N. Athavale, T.Z. Fullem, A.C. Giamis, R.K. Kinyanjui, M. Lowenstein, K. Mather, R. Patel, D. Rae, J. Wang, Y. Xing, L. Zavalij, P. Borgesen, E.J. Cotts, Journal of Electronic Materials 33 (2004) pp. 1429.

[1.53] L.P. Lehman, Y. Xing, T.R. Bieler, E.J. Cotts, Acta Materialia 58 (2010) pp. 3546.

[1.54] B. Arfaei, E. Cotts, Journal of Electronic Materials 38 (2009) 2617.

[1.55] P. Borgesen, T. Bieler, L. Lehman, and E. Cotts, MRS Bull. 32 (2007) pp. 360.

[1.56] B. Arfaei, M. Benedict and E. J. Cotts, Acta Materialia (submitted).

[1.57] D.N. Lee, K.-h. Kim, Y.-g. Lee, C.-H. Choi, Materials Chemistry and Physics 47 (1997) pp. 154.

[1.58] J. Warner, J. Verhoeven, Metallurgical and Materials Transactions B 3 (1972) pp. 1001.

[1.59] S.E. Battersby, R.F. Cochrane, A.M. Mullis, Journal of Materials Science 34 (1999) pp. 2049.

[1.60] J. Gong, C. Liu, P.P. Conway, V.V. Silberschmidt, Scripta Materialia 61 (2009) pp. 682.

[1.61] A.M. Mullis, K.I. Dragnevski, R.F. Cochrane, Materials Science and Engineering A 375-377 (2004) pp. 157.

[1.62] T. Haxhimali, A. Karma, F. Gonzales, M. Rappaz, Nat Mater 5 (2006) pp. 660.

[1.63] C.F. Lau, H.W. Kui, Acta Metallurgica et Materialia 41 (1993) pp. 1999.

[1.64] S. O'Hara, Acta Metallurgica 15 (1967) pp. 231.

[1.65] V. O. Esin, G. N. Pankin, R. H. Nasyrov, Sov. Phys. Crystallogr. 18 (1973) pp. 246.

[1.66] A. Rosenberg and W. C. Winegard, Acta Metallurgica 2 (1954) pp. 2242.

[1.67] J. H. Hollomon and D. Turnbull, "Nucleation," Progress in Metal Physics 4 (1953) pp. 333.

[1.68] B. Arfaei, E. Cotts, J Electron Mater 38 (2009) pp. 2617.

[1.69] L. P. Lehman, Kinyanjui RK, Wang J, Xing XY, Zavalij L, Borgesen P, 55th Electronic components and technology conference (2005) pp. 674.

[1.70] Kerr M, Chawla N, Acta Mater 52 (2004) pp. 4527.

[1.71] Kinyanjui R, Lehman L, Zavalij L, Cotts E. J Mater Res. 20 (2005) pp. 2914.

[1.72] Lehman L, Athavale S, Fullem T, Giamis A, Kinyanjui R, Lowenstein M, Mather K, Patel R, Rae D, Wang J, Xing Y, Zavalij L, Borgesen P, Cotts E, J Electron Mater 33 (2004) pp. 1429

[1.73] Sundquist BE, Mondolfo LF, Trans Met Soc AIME 221 (1961) pp. 157.

[1.74] Lehman LP, Xing Y, Bieler TR, Cotts EJ, Acta Mater. 58 (2010) pp. 3546.

[1.75] Arfaei B, Xing Y, Woods J, Wolcotts J, Tumne P, Borgesen P, 58th Electronic components and technology conference (2008) pp. 459.

[1.76] Bieler TR, Jiang H, Lehman LP, Kirkpatrick T, Cotts EJ, and Nandagopal B, IEEE Transactions on Components and Packaging Technologies 31 (2008) pp. 370 .

[1.77] Arfaei B, Kim N, and Cotts E, Journal of Electronic Materials 41 (2012) pp. 362.

[1.78] Bonicelli, M, Ceccaroni, G, Gauzzi, F,Mariano, G., Thermochimica Acta 430 (2005) pp. 95.

[1.79] Kim WT, Cantor B, J Mat Sci. 1991 (1991) pp. 2868.

[1.80] Boswell PG, Chadwick GA, Acta Met 28 (1980) pp. 209.

[1.81] Pound, GM, La Mer, VK, J Am Chem Soc 74 (1952) pp. 2323.

[1.82] Swenson D, J Mater Sci: Mater Electron. 18 (2007) pp. 39.

[1.83] Anderson I, Walleser J, Harringa J, Laabs F, Kracher A, J Electron Mater. 38 (2009) pp. 2770.

[1.84] Cho MG, Kang SK, Seo S, Shih D, Lee HM, J Mater Res. 24 (2009) pp. 534.

[1.85] Ohno A, Motegi T, Nippon Kinzoku Gakkaishi/ J JPN I MET 37 (1973) pp. 777.

[1.86] Li M, Zhang F, Chen WT, Zeng K, Tu KN, Balkan H, Elenius P, J Mater Res. 17 (2002) pp. 1612.

[1.87] Jang G-Y, Duh J-G, Takahashi H, Lu S-W, Chen J-C, J Electron Mater. 35 (2006) pp. 1745.

[1.88] Zhang F, Li M, Chum CC, Shao ZC, J Electron Mater. 32 (2003) pp. 123.

[1.89] Porter D, Easterling KE,, *Phase Transformations in Metals and Alloys*, 2nd edition, Chapman & Hall, 1992.

[1.90] K. F. Kelton and A. L. Greer, *Nucleation in Condensed Matter*, Pergamon, 2010.

[1.91] Kim W, Zhang D, Cantor B, Metall Mater Trans A 22 (1991) pp. 2487.

[1.92] J. H. Perepezko, P. G. Hockel, J. S. Paik, Thermochimica Acta 388 (2002) pp.129.

[1.93] Koverda VP, Skokov VN, Skripov VP, Phys Status Solidi A 74 (1982) pp. 343

[1.94] Schmelzer JWP, J Non-Cryst Sol 356 (2010) pp. 2901.

[1.95] Solthin RT, Chadwick GA, Acta Metall. 26 (1978) pp. 223.

[1.96] G. Powell, G. Colligan, V. Surprenant, A. Urquhart, Metallurgical and Materials Transactions A 8 (1977) pp. 971

[1.97] Perepezko JH, Mater Sci Eng. 65 (1984) pp. 125.

[1.98] Schmelzer JWP, J.Non-Cryst Sol 354 (2008) pp. 269.

[1.99] Guignard M, Cormier L, Montouillout V, Menguy N, Massiot D, J Non-Cryst Sol. 356 (2010) pp. 1368.

[1.100] Gebauer D, Volkel A, Colfen H, Science 322 (2008) pp. 1819.

[1.101] Tatchev D, Hoell A, Kranold R, Armyanov S, Physica B 369 (2005) pp. 8.

[1.102] Hao Y, Kivilahti JK, IEEE Trans Compon Pack Technol 29 (2006) pp. 778.

[2.1] P. Kumar, B. Talenbanpour, U. Sahaym, C. H. Wen, I. Dutta, "Microstructural Evolution and Some Unusual Effects During Thermo-Mechanical Cycling of SnAgCu Alloys", Proc. 13th IEEE Inter-Society Conference on Thermal and Thermomechanical Phenomena in Electronic Systems (ITherm), June 2012, IEEE/ASME, pp. 880-887.

[2.2] Smithells Metals reference Book, in: E. A. Brandes, G. B. Brook (Eds.), 7th ed., Butterworth-Heinemann Ltd., 1992

[2.3] P. Kumar, Z. Huang, S. Chavali, D. Chan, I. Dutta, G. Subbarayan, V. Gupta "A Microstructurally Adaptive Model for Primary and Secondary Creep of Sn-Ag-based Solders", IEEE Trans. Comp. Packag. Technol. 2012, pp. 256 – 265.

[2.4] U. Sahaym, B. Talebanpour, S. Seekins, I. Dutta, P. Kumar, and P. Borgesen, "Recrystallization and Ag_3Sn Particle Redistribution during Thermo-mechanical Treatment of Bulk SnAgCu Solder Alloys", IEEE Trans. Comp. Pack. and Manuf. Tech., 3 (11), 2013, 1868-1875.

[2.5] F.J. Humphreys and M Heatherly, Recrystallization and related phenomena, Elsevier Science Ltd, 1995

[2.6] R.D. Doherty, D.A. Hughes, F.J. Humphreys, J.J. Jonas, D. Juul Jensen, M.E. Kassner, W.E. King, T.R. McNelley, H.J. McQueen, A.D. Rollett, "Current issues in recrystallization: a review", Mater Sci. Eng. A 238, 1997, pp. 219-274

[2.7] F.J. Humphreys and P.N. Kalu, "Dislocation-particle interaction during high temperature deformation of two phase alloys", Acta Metall., 35 1987, pp. 2815-2829

[2.8] F.J. Humphreys, "The nucleation of recrystallization at second phase particles in deformed aluminum", Acta Metall., 25, 1977, pp.1323-1344

[2.9] I. Dutta, "A constitutive model for creep of lead-free solders undergoing strain-enhanced microstructural coarsening: A first report", J. Elec. Mater., 32, 2003, pp. 201-207

[2.10] E. Kohler, E. Bischoff, V. Gerold, "Chemical analysis of persistent slip bands in age hardened Al-Ag alloys by means of EDS", Scripta Metall. 18, 1984, pp. 699-702

[2.11] W. Vogel, M. Wilhelm, V. Gerold, "Persistent slip bands in fatigues peak aged Al-Zn-Mg single crystals –1. development of dislocation microstructure and change of precipitation distribution" Acta Metall. 30 1982, pp.21.

[2.12] D. Steiner, R. Beddoe, V. Gerold, G. Kostorz, R. Schmelczer, "particle dissolution during fatigue of age hardened Cu-Co single crystals", Scripta Metall. 17, 1983, 733-736

[2.13] J. Lendvai, H.J. Gudladt, V. Gerold, “The deformation induced dissolution of delta precipitates in Al-Li alloys”, Scripta Metall. 22, 1988, pp. 1755-1760.

[2.14] M. Sundararaman, W. Chen, V. Singh, R.P. Wahi, “TEM investigation of gamma’-free bandsin nimonic PE16 under LCF loading at room temperature”, Acta Metall Mater. 38, 1990, pp.1813-1822.

[2.15] A.-W. Zhu, “Evolution of size distribution of shearable ordered precipitates under homogeneous deformation – application to an Al-Li alloy”, Acta Mater 45, 1997, pp. 4213-4223.

[2.16] A.-W. Zhu, “Strain localization and formation of heterogeneous distribution shearable ordered precipitates :application to an Al-10at% Li single crystal”, Acta mater. 46, 1998, pp. 3211-3220.

[2.17] X. Long, I. Dutta, R. Guduru, R. Prasanna, M. Pacheco, “A highly accelerated thermal cycling (HATC) test for solder joint reliability assessment in BGA packages”, Proceedings of IPACK, Vancouver, B.C. 2007, pp. 1-8

[2.18] H.D. Chandler and J.V. Bee. “Cyclic Strain Induced Precipitation in a Solution-Treated Aluminum Alloy.” Acta Metall. 35, 1987, pp. 2503-2510

[2.19] C. Laird, VJ Langelo, M Hollrah, NC Yang and R De Le Veaux, “The cyclic stress-strain response of precipitation hardened Al-15wt%Ag alloy.” Mat. Sci. Eng. A32, 1978, pp. 137-160

[2.20] A. Farrow and C Laird, “Precipitation in solution treated Al-4wt% Cu under cyclic strain”, Solid State Phenomena, 172-174, 2011, pp. 715-720

[2.21] M. Lifshitz and V. Slyolov, "The kinetics of precipitation from supersaturated solid solutions", J. Phys. Chem.Solids 19, 1961, pp. 35-50

[2.22] C. Wagner, "Theorie der Alterung von Niederschlagen durch Umlosen (Ostwald-. Reifung)", Zeitschrift Elektrochemie 65, 1961, pp. 581-591

[2.23] I. Dutta, D. Pan, R.A. Marks, and S.G. Jadhav, “Effect of thermo-mechanically induced microstructural coarsening on the evolution of creep response of SnAg-based microelectronic solders”, Mater. Sci. Eng., A 410–411C, 2005, pp.48-52

[2.24] P. Kumar, O. Comejo, I. Dutta, G. Subbarayan and V Gupta, “Joint scale dependence of aging kinetics in SnAgCu alloys”, 10th Electronics Packaging Technology Conference, 2008, pp. 903-909

[2.25] S. H. Choi, B. G. Song, K. J. Kang and N. A. Fleck, Fracture of a ductile layer constrained by stiff substrates, Fatigue Fract. Eng. M., 23, 2001, pp. 1-13

[2.26] H. Nayeb-Hashemi and P. Yang, Mixed mode I/II fracture and fatigue crack growth along 63Sn-37Pb solder/brass interface, Int J Fatigue, 23, 2001, pp. S325-S335

[2.27] K. J. Kang, D. H. Kim and S. H. Choi, Effects of mode mix upon fracture behavior of a solder joint, Int. J. Fracture, 113, 2002, pp. 195-212

[2.28] Y. Sun and J. H. L. Pang, Experimental and numerical in investigations of near-crack-tip deformation in a solder alloy, Acta Mater., 56, 2008, pp. 537-548

[2.29] K. S. Siow and M. Manoharan, Mixed mode fracture toughness of lead-tin and tin-silver solder joints with nickel-plated substrate, Mat. Sci. Eng. A-Struct., 404, 2005, pp. 244-250

[2.30] S. M. Hayes, N. Chawla and D. R. Frear, Interfacial fracture toughness of Pb-free solders, Microelectron. Reliab., 49, 2009, pp. 269-287

[2.31] P. Kumar, I. Dutta, V. Sarihan, D. R. Frear and M. Renavikar, "Effects of Strain Rate and Aging on Deformation and Fracture of SnAgCu solder joints", Thermal and Thermomechanical Phenomena in Electronic Systems, 2008. ITHERM 2008. 11th, 660-667.

[2.32] P. Kumar, Z. Huang, I. Dutta, "Roles of process and microstructural parameters of mixed mode fracture of SnAgCu solder joints under dynamic loading conditions", Proceedings of InterPACK2009, Paper no. 89205, IEEE/ASME CD-ROM.

[2.33] Z. Huang, P. Kumar, I. Dutta, J. H. L. Pang, R. Sidhu, M. Renavikar and R. Mahajan "Fracture of SnAgCu solder joints on Cu substrates: I. Effects of loading and processing conditions", J. Electron. Mater., 41, 2012, pp. 375-389

[2.34] P. Kumar, Z. Huang,, I. Dutta, R. Sidhu, M. Renavikar and R. Mahajan, "Fracture of SnAgCu solder joints on Cu substrates: II. Fracture Mechanism Map", J. Electron. Mater., 41, 2012, pp. 412-424

[2.35] M. Arcan, Z. Hashin and A. Voloshin, "A Method to Produce Uniform Plane- Stress States with Applications to Fiber-Reinforced Materials", Exp. Mech., 28, 1978, pp. 141-146

[2.36] H. L. J. Pang and C. W. Seetoh, "A compact mixed mode (CMM) fracture specimen for adhesive bonded joints", Eng. Frac, Mech., 57, 1997, pp. 57-65

[2.37] ASTM E561-05: Standard test method for K-R curve determination. Annual book of ASTM standards 04.01, 2008, pp. 593-611

[2.38] B. S. Majumdar and J. Ahmad, "Fracture of Ceramic-Metal Joints: Zirconia/Nodular Cast Iron System in. Metal-Ceramic Joining", P. Kumar and V. A. Greenhut, eds., TMS, 1991, pp. 67 – 97

[2.39] J. W. Hutchinson, Z. Suo, "Mixed mode cracking in layered materials", Adv. Appl. Mech., 29, 1991, pp. 63-191

[2.40] Z. Suo and J. W. Hutchinson, "Sandwich test specimens for measuring interface crack toughness", Mater. Sci. Eng. A, 107, 1989pp. 135-143

[2.41] X. Long, R. Guduru, I. Dutta, V. Sarihan and D. R. Frear, "Deformation Behavior of Sn3.8Ag0.7Cu Solders at Intermediate Strain Rates: Effect of Microstructure and Test Conditions", J. Electronic Mater., 37, 2008, pp. 189-200

[2.42] K. S. Kim, S. H. Huh and S. Suganuma, "Effects of cooling speed on microstructure and tensile properties of SnAgCu alloys", Mater. Sci. Eng. A333, 2002pp. 106-114

[2.43] T. Chen and I. Dutta, "Effect of Ag and Cu Concentrations on the Creep Behavior of Sn-Based Solders", Journal of Electronic Materials, 37, 2008 pp. 347-354.

[2.44] T Chen, I Dutta, S Jadhav, "Effect of Ag and Cu Concentrations on the Creep Behavior of Sn-Based Solders", IPACK 2007 Proceedings of the ASME INTERPACK Conference, 2007 vol. 2 2007, pp. 399-405.

[2.45] Z. Huang, P. Kumar, I. Dutta*, R. Sidhu, M. Renavikar and R. Mahajan, "Incorporation of Interfacial Intermetallic Morphology in Fracture Mechanism Map for SnAgCu Solder Joints", J. Electr. Mater., 2013 (DOI: DOI: 10.1007/s11664-013-2755-0).

[2.46] Z. Huang, P. Kumar, I. Dutta, J. H. L. Pang, R. Sidhu, M. Renavikar and R. Mahajan, "A General Methodology for Calculating Mixed Mode Stress Intensity Factors and Fracture Toughness of Solder Joints with Interfacial Cracks", Eng. Fract. Mech., accepted Sept. 2014.

[2.47] C. Park, X. Long, S. Haberman, S. Ma, I. Dutta, R. Mahajan and S. G. Jadhav, "A Comparison of Impression and Compression Creep Behavior of Polycrystalline Sn", J. Mater. Sci., 42, 2007, pp. 5182-5187

[2.48] I. Dutta, P. Kumar and G. Subbarayan, "Microstructural Coarsening in Sn-Ag based Solders and its Effects on Mechanical Properties", J. Materials (JOM), 61, no. 6, pp. 29-38, 2009.

[2.49] Sellers et al, J. Applied Physics, 110 (2011) 3528.

[2.50] I. Dutta, P. Kumar and G. Subbarayan, "Microstructural Coarsening in Sn-Ag based Solders and its Effects on Mechanical Properties", J. Materials (JOM), 61, no. 6, pp. 29-38, 2009

[2.51] P. Kumar, Z. Huang, S. Chavali, D. Chan, I. Dutta, G. Subbarayan, V. Gupta "A Microstructurally Adaptive Model for Primary and Secondary Creep of Sn-Ag-based Solders", IEEE Trans. Comp. Packag. Technol. 2(2012) 256 – 265.

[2.52] P. Kumar, Z. Huang, I. Dutta, G. Subbarayan, R. Mahajan, "Influence of Microstructure on Creep and High Strain Rate Fracture of Sn-Ag Based Solder Joints", Chapter 8 in Lead-free Solders: Materials Reliability for Electronics, edited by K. N. Subramanian, Wiley series in Electronic and Optoelectronic Materials, John Wiley, 1st edition, 2012, pp. 199-233.

[3.1] L. Yang, L. Yin, B. Arafei, B. Roggeman and P. Borgesen, "On the Assessment of the Life of SnAgCu Solder Joints in Cycling with Varying Amplitudes", IEEE Transactions on Components, Packaging and Manufacturing Technologies 3 (2013) pp. 430-440

[3.2] A. Qasaimeh, Y. Jaradat, L. Wentlent, L. Yang, L. Yin, B. Arfaei, and P. Borgesen, "Recrystallization Behavior of Lead Free and Lead Containing Solder in Cycling", Proc. 61st ECTC, (2011), pp. 1775-1781

[3.3] Y. Jaradat, A. Qasaimeh, P. Kondos, B. Arfaei, and P. Borgesen, "On the Evolution of the Properties of Backward Compatible Solder Joints during Cycling and Aging", Proc. 61st ECTC (2011), pp. 722-730

[3.4] M. Meilunas and P. Borgesen, "Effects of Cycling Parameters on the Thermal Fatigue Life of Mixed SnAgCu/SnPb Solder Joints", Journal of Electronic Packaging, vol. 133 (2011), 0210011-0210015

[3.5] P. Borgesen and M. Meilunas, "Effects of Solder Paste Volume and Reflow Profiles on the Thermal Cycling Performance of Mixed SnAgCu/SnPb Solder Joints", IEEE Transactions on Components and Packaging Technologies, Vol. 1, No. 8 (2011) 1205-1213

[3.6] D. Blass, M. Meilunas, and P. Borgesen, ”On the Incorporation of Fine Pitch Lead Free CSPs in High Reliability SnPb Based Microelectronics Assemblies”, IEEE Transactions on Components, Packaging and Manufacturing Technology, Vol. 1 (2011), 92-99

[3.7] M. Meilunas, A. Qasaimeh, S. Hamasha, and P. Borgesen, “Effects of Thermal Cycling Parameters on the Life of SnAgCu Solder Joints”, AREA Consortium report – to be included in forthcoming publication

[3.8] D. Schmitz, S. Shirazi, L. Wentlent, S. Hamasha, L. Yin, A. Qasaimeh, and P. Borgesen, “Towards a Quantitative Mechanistic Understanding of the Thermal Cycling of SnAgCu Solder Joints”, Proc. 64th ECTC 2014, pp. 371-378

[3.9] P. Borgesen, L. Wentlent, A. Qasaimeh, S. Hamasha, D. Schmitz, S. Khasawneh, Y. Jaradat, S. Shirazi, J. Jiang, J. L. Then Cuevas, and L. Yin, “Quantitative Prediction of the Thermal Fatigue Life of SnAgCu Solder Joints”, Mater. Sci. & Eng. A (in review)

[3.10] B. Arfaei, T. Tashtoush, N. Kim, L. Wentlent, E. Cotts, and P. Borgesen, “Dependence of SnAgCu Solder Joint Properties on Solder Microstructure”, Proc. 61st ECTC, (2011), pp. 125-132

[3.11] S. Hamasha, A. Qasaimeh, J. Younis, and P. Borgesen, “Correlation between Solder Joint Fatigue Life and Accumulated Work in Isothermal Cycling”, ”, accepted for publication in IEEE Transactions on Components, Packaging and Manufacturing Technologies

[3.12] B. Arfaei, Y. Xing, J. Woods, J. Wolcott, P. Tumne, P. Borgesen, and E. Cotts, “The Effect of Sn Grain Number and Orientation on the Shear Fatigue Life of SnAgCu Solder Joints”, Proc. 58th ECTC, 2008, 459-465

[3.13] T. Bieler, P. Borgesen, Y. Xing, L. Lehman, and E. Cotts: “Correlation of Microstructure and Heterogeneous Failure in Pb Free Solder Joints”, *Pb-Free and RoHS-Compliant Materials and Processes for Microelectronics,* C. A. Handwerker, K. Suganuma, H. L. Reynolds, J. Bath, eds., MRS Spring Meeting, April 2007

[3.14] A. Mayyas, L. Yin, and P. Borgesen, “Recrystallization of Lead Free Solder Joints – Confounding the Interpretation of Accelerated Thermal Cycling Results?”, Proc. 2009 ASME Int. Mech. Eng. Congr. & Exp., Nov. 2009, Lake Buena Vista, FL, IMECE2009-12749

[3.15] T-M. K. Korhonen, L. P. Lehman, M. A. Korhonen, and D. W. Henderson, “ Isothermal fatigue behaviour of the near-eutectic SnAgCu alloy between – 25°C and 125°C”, Journal of Electronic Materials. 36 (2007) pp. 173-178.

[3.16] L. Yang, L. Yin, B. Roggeman, and P. Borgesen, “Effects of Microstructure Evolution on Damage Accumulation in Lead Free Solder Joints”, Proc. ECTC 2010

[3.17] A. Qasaimeh, ‘Study of the Damage Evolution Function for SnAgCu in Cycling’, Ph. D. dissertation, Binghamton University, May 2012

[3.18] S. Hamasha, Y. Jaradat, A. Qasaimeh, M. Obaidat, and P. Borgesen, “Assessment of Solder Joint Fatigue Life under Realistic Service Conditions”, accepted for publication in J. Electron. Mater.

[3.19] D. Kuhlmann-Wilsdorf, “A new theory of workhardening”, Trans Met Soc AIME 224 (1962) 1047–61.

[3.20] H.-J. Christ, G. Hoffmann, and O. Oettinger, “History Effects in Metals During Constant and Variable Amplitude Testing. I: Wavy Dislocation Glide Behaviour”, Mater. Sci. & Eng. A201 (1995) 1-12

[3.21] H. L. Huang, “A Study of Dislocation Evolution in Polycrystalline Copper During Low Cycle Fatigue at Low Strain Amplitudes”, Materials Science and Engineering A342 (2003) 38-43

[3.22] C-C. Shih, N-J. Ho, and H-L. Huang, “Dislocation Evolution in Interstitial-Free Steel During Constant and Variable Amplitude Testing”, J Mater Sci (2010) 45:1809–1816

[3.23] D. W. Henderson, J. J. Woods, T. A. Gosselin, J. Bartelo D. E. King, T.M. Korhonen, M.A. Korhonen, L. P. Lehman, E.J. Cotts, S. K. Kang, P. Lauro, Da-Yuan Shih, C. Goldsmith and K. J. Puttlitz, “The microstructure of Sn in near-eutectic SnAgCu alloy solder joints and its role in thermomechanical fatigue”, J. Mat. Res. 19, 1608 (2004).

[3.24] S. Terashima, T. Kobayashi, and M. Tanaka, “Effect of crystallographic anisotropy of β-tin grains on thermal fatigue properties of Sn–1Ag–0.5Cu and Sn–3Ag–0.5Cu lead free solder interconnects”, Sci. Technol. Weld. Join. 13, 732 (2008).

[3.25] Terashima, S., Takahama, K., Nozaki, M., and Tanaka, M. Recrystallization of Sn Grains due to Thermal Strain in Sn-1.2Ag-0.5Cu-0.05Ni Solder, Mater Trans. 45 1383 (2004)

[3.26] U. Telang, T. R. Bieler, A. Zamiri, and F. Pourboghrat, “Incremental recrystallization/grain growth driven by elastic strain energy release in a thermomechanically fatigued lead-free solder joint”, Acta Mater. 55, 2265 (2007).

[3.27] J. Sundelin, S. Nurmi, and T. Lepistö, “Recrystallization behaviour of SnAgCu solder joints”, Mater. Sci. Eng. A- Struct. 474, 201 (2008).

[3.28] T. Mattila and J. Kivilahti, “The Role of Recrystallization in the Failure of SnAgCu Solder Interconnections Under Thermomechanical Loading”, IEEE Trans. Compon. Pack T., 33, 629 (2010).

[3.29] L. Yin, L. Wentlent, L. Yang, B. Arfaei, A. Qasaimeh, and P. Borgesen, “Recrystallization and Precipitate Coarsening in Pb-free Solder Joints during Thermo-mechanical Fatigue”, J. Electronic Materials 41, Issue 2 (2012) pp. 241-252

[3.30] B. Zhou, T. R. Bieler, T-K. Lee, and K-C. Liu, “Crack Development in a Low-Stress PBGA Package due to Continuous Recrystallization Leading to Formation of Orientations with [001] Parallel to the Interface”, Journal of Electronic Materials 39 (2010) 2669-2679.

[3.31] A. Qasaimeh, S. Lu, and P. Borgesen, “Crack Evolution and Rapid Life Assessment for Lead Free Solder Joints”, Proc. 61st ECTC, (2011), pp. 1283-1290

[3.32] P. Borgesen, L. Yang, A. Qasaimeh, L. Yin, and M. Anselm, “A Mechanistically Justified Model for Life of SnAgCu Solder Joints in Thermal Cycling”, Proc. SMTA PanPac Conf. 2013

[3.33] S. Joshi, B. Arfaei, M. Obaidat, A. Alazzam, M. Meilunas, L. Yin, M. Anselm, and P. Borgesen, “LGAs vs. BGAs – Lower Profile and Better Reliability”, Proc. SMTAI 2012

[3.34] L. Wentlent, L. Yin, M. Meilunas, B. Arfaei, and P. Borgesen, “Damage Mechanisms and Acceleration Factors for No-Pb LGA, TSOP, and QFN Type Assemblies in Thermal Cycling”, Proc. SMTA Int., (Oct. 2011), pp. 535-544

[3.35] B. Arfaei, M. Anselm, S. Joshi, S. Mahin-Shirazi, E. Cotts, P. Borgesen, J. Wilcox, and R. Coyle, “Effect of Sn Grain Morphology on Reliability of Lead-Free Solder Joints in Thermal Cycling Tests”, Proc. SMTAI 2013

[3.36] B. Arfaei, L. Wentlent, S. Joshi, M. Anselm, and P. Borgesen, “Controlling the Superior Reliability of Lead Free Assemblies with Short Standoff Height Through Design and Materials Selection”, Proc. IMECE 2012

[5.1] I. Dutta, C. Park and S. Choi, “Impression creep characterization of rapidly cooled Sn-3.5Ag solders”, Mat. Sci. Eng. A379, 238, 2004, pp. 401-410

[5.2] M. Kerr and N. Chawla, “Creep deformation behavior of Sn-3.5Ag solder/Cu couple at small length scales”, Acta Mater., 52, 2004, pp. 4527-4535

[5.3] M. L. Huang, L. Wang and C. M. L. Wu, “Creep behavior of eutectic Sn-Ag lead-free solder alloy”, J. Mater. Res. 17, 2002, pp. 2897-2903

[5.4] I. Dutta, “A constitutive model for creep of lead-free solders undergoing strain-enhanced microstructural coarsening: A first report”, J. Elec. Mater., 32, 2003, pp. 201-207

[5.5] I. Dutta, D. Pan, R.A. Marks and S.G. Jadhav, “Effect of thermo-mechanically induced microstructural coarsening on the evolution of creep response of SnAg-based microelectronic solders”, Mater Sci. Eng. A 410-411, 2005, pp. 48-52

[5.6] I. Dutta, P. Kumar and G. Subbarayan, “Microstructural coarsening in Sn-Ag-based solders and its effects on mechanical properties”, JOM-J Min. Met. Mat. S., 61, 2009, pp. 29-38

[5.7] P. Kumar, Z. Huang, S. Chavali, D. Chan, I. Dutta, G. Subbarayan, V. Gupta “A Microstructurally Adaptive Model for Primary and Secondary Creep of Sn-Ag-based Solders”, IEEE Trans. Comp. Packag. Technol. 2, 2012, pp. 256 – 265

[5.8] P. Kumar, Z. Huang, I. Dutta, G. Subbarayan, R. Mahajan, “Influence of Microstructure on Creep and High Strain Rate Fracture of Sn-Ag Based Solder Joints”, Chapter 8 in Lead-free Solders: Materials Reliability for Electronics, edited by K. N. Subramanian, Wiley series in Electronic and Optoelectronic Materials, John Wiley, 1st edition, 2012, pp. 199-233.

[5.9] M. D. Mathew, H. Yang, S. Movva and K. L. Murty, “Creep deformation characteristics of tin and tin-based electronic solder alloys”, Metall. Mater. Trans. A36, 2005pp. 99-105

[5.10] R. W. Evans and B. Wilshire, “Creep of metals and alloys”, The Institute of Metals, London, 1985

[5.11] F. Garofalo, C. Richmond, W. F. Domis and F. von Gemmingen, “Strain-time, rate-stress, and rate-temperature relations during large deformations in creep”, Proc. Joint Int. Conf. on Creep, Inst. Mech. Eng. London, 178, 1963, pp. 31-39

[5.12] B. Talebanpour, I. Dutta and U. Sahaym, "Effects of alloy composition and thermal-mechanical history on the creep behavior of SnAgCu Alloys: I. Experiments", J. Electron. Mater., in review (2014)

[5.13] B. Talebanpour, I. Dutta and U. Sahaym, "Effects of alloy composition and thermal-mechanical history on the creep behavior of SnAgCu Alloys: II. Model", J. Electron. Mater., in review (2014)

[5.14] J. Li, T. T. Mattila, and J. K. Kivilahti, “Multiscale simulation of recrystallization and grain growth of Sn in lead-free solder interconnections”, J. Electr. Mater. 39 (2010) pp. 77-84

[5.15] J. Li, H. Xu, T. T. Mattila, J. K. Kivilahti, T. Laurila, and M. Paulasto-Krockel, “Simulation of dynamic recrystallization in solder interconnections during thermal cycling”, Comput. Mater. Sci. 50 (2010) pp. 690-697

[5.16] A. D. Rollett and D. Raabe, “A hybrid model for mesoscopic simulation of recrystallization”, Comput. Mater. Sci. 21 (2001) pp. 69-78

[5.17] X. Song and M. Rettenmayr, “Modelling study on recrystallization, recovery and their temperature dependence in inhomogeneously deformed materials”, Mater. Sci. & Eng. A332 (2002) pp. 153-160

[5.18] Q. Yu and S. K. Esche, “A Multi-scale approach for microstructure prediction in thermo-mechanical processing of metals”, J. Mater. Processing Technol. 169 (2005) pp. 493-502

[6.1] P. Borgesen, L. Yin and P. Kondos, “Acceleration of the Growth of Cu_3Sn Voids in Solder Joints”, Microelectronics Reliability 55, Issue 6 (2012) 1121-7